ELECTRONIC STRUCTURE AND EXCITED STATE DYNAMICS OF CHROMIUM(III) COMPLEXES

VOLUME I

By

Joel Nicholas Schrauben

A DISSERTATION

Submitted to
Michigan State University
in partial fulfillment of the requirements
for the degree of

DOCTOR OF PHILOSOPHY

CHEMISTRY

2010

ABSTRACT

ELECTRONIC STRUCTURE AND EXCITED STATE DYNAMICS OF CHROMIUM(III) COMPLEXES

By

Joel Nicholas Schrauben

Interest in fundamental aspects of transition metal photophysics and photochemistry stems from potential application of such systems to technologies such as solar cells, photocatalysts and molecular machines. Chromium(III) offers a convenient platform for the fundamental study of transition metal photophysics due to its relatively simple ligand-field electronic structure. The work presented in this dissertation deals with understanding the ground and excited state electronic structure and dynamics of chromium(III) complexes, ranging from high-symmetry derivatives of tris(acetylacetonato)chromium(III) ($Cr(acac)_3$) to low symmetry chromium-semiquinone complexes of the form $[(tren)Cr(III)\text{-}SQ]^{+2}$ (where tren is tris(2-aminoethyl)amine, a tetradentate amine capping ligand enabling only one moiety of the orthosemiquinone (SQ) to chelate to the chromium(III) ion). This effort can be thought of in terms of building up the additional interactions (lowered symmetry and spin exchange) in a piecewise fashion by first considering the electronic structure and dynamics of high-symmetry systems, then lowering the symmetry while maintaining the quartet spin nature of the high-symmetry system by studying the chromium(III)-catechol systems. Finally, spin exchange can be introduced via the chromium(III)-semiquinone system. In general, these

complexes represent dramatic changes from the high-symmetry complexes in several ways: 1) the local symmetry of the chromium(III) ion is reduced from high-symmetry, pseudo-octahedral ligation to a C_{2v}-like N_4O_2 coordination, effectively breaking the degeneracy of the ligand field T and E states; 2) unpaired spin of the semiquinone ligand interacts via Heisenberg spin-exchange with the unpaired spins of the chromium(III) ion, resulting in substantial changes in the absorption spectrum indicative of radically different electronic structure of both the ground and excited states. Studies of the excited-state dynamics were first carried out on derivatives of the archetypal complex $Cr(acac)_3$ to gain an understanding of correlations between electronic structure, geometry, and excited state dynamics. These studies revealed an empirical correlation between low-frequency modes of the molecule and the rate of ultrafast intersystem crossing in the ligand field manifold. Efforts on the lower symmetry catechol and semiquinone complexes are focused mainly on synthesis and characterization of the electronic structure. The ground states of these systems are characterized primarily using electron paramagnetic resonance techniques, revealing the rich nature of these spin systems. For these studies, gallium(III)-semiquinones are employed as a structural analog to study spin density distribution in the absence of the chromium(III) ion. The concepts learned from these studies provide a useful backdrop to the eventual study of the excited state dynamics of the aforementioned chromium(III)-catechol and -semiquinone complexes.

For my mother, who made sure I did my homework.

ACKNOWLEDGEMENTS

I would first like to thank my boss, Jim, for setting me up with a project that encompasses so many of the aspects of inorganic chemistry that drew me to the area: electronic structure, magnetism, and synthesis, and mixing ultrafast spectroscopy into the equation. It's been a pleasure working with you.

Many members of the McCusker group have contributed to various aspects of the work presented in this dissertation through their expertise, hard work, and helpful discussions: Dr. Dong Guo (x-ray structures, synthetic mastermind), Dr. Richard Fehir, Jr. (synthetic and magnetism wizard, masterful tailgater), Allison Brown (femto enabler, travel buddy), Dr. Troy Knight (low-T experiments, 40's), Drew Kouzelos (low-T, calculations, protector of group traditions), Lisa (e-chem, Riv) as well as just about everyone else for listening at one time or another. I've also had the good fortune to collaborate with the McCracken group during my time at MSU, specifically Matthew Krzyaniak (expert home-brewer). Also thanks to Kevin Dillman (coherence!) from the Beck group for work on $Cr(acac)_3$.

My family and friends have done a good job of keeping me grounded and being patient during my grad school career. Thanks guys. Finally, thanks to Sarah for waiting.

TABLE OF CONTENTS

LIST OF TABLES

LIST OF FIGURES

Images in this dissertation are presented in color.

Chapter 1: Introduction, Historical Perspective and Theory

1.1 Introduction

This dissertation concerns itself with fundamental questions underlying the photophysical and physicochemical properties of transition metal compounds, and employs chromium(III) as a platform for these studies. This chapter will present the necessary background, both historical and theoretical, for understanding excited state photophysical processes in transition metal systems, including an overview of electronic structure and kinetics of chromium(III) complexes and nonradiative decay theory. Other theories pertaining to electronic structure, dynamics, and magnetism are covered throughout this dissertation as necessitated.

1.2 Historical Perspective

Rational design of applications such as solar cell technology, molecular machines, and artificial photosynthesis demands a strong understanding of the electronic structure and dynamics that constitute the photophysical properties of the molecules employed in these applications.[1,2] The study of these fundamental properties has a far reaching impact in the area of quantum chemistry and spectroscopy. The rich photochemistry and photophysics of transition metal complexes has attracted researchers for many years, with the oldest studies being performed primarily on ionic solids, such as chromium(III) impurities. The emission spectra of these salts were described by Becquerel in 1867,[3] whose

photochemical work on chromium salts was essential in the development of photoengraving and lithography techniques.[4] Since then, chromium(III) has been extensively studied and characterized both photophysically and photochemically,[5,6] and therefore makes an ideal probe for answering fundamental questions about the electronic structure of transition metal complexes.

After the work of Becquerel the field essentially lay dormant until 1940 when Van Vleck analyzed the absorption spectra potassium chrome alum ($KCr(SO_4)_2 \cdot 12\ H_2O$) in terms of crystal field theory.[7] Many more studies of this type were carried out, most notably Sugano and Tanabe's extensive study of Cr(III) in Al_2O_3.[8] Later on, after the advent of ligand field theory in the early fifties, many studies of transition metal complexes in solution were carried out, but it was not until the early sixties that the luminescence of a chromium(III) complex, $Cr(acac)_3$ (where acac is the monodeprotonated form of acetylacetone), was first reported by Forster and DeArmond.[9] The assignment of the low-energy narrow lineshape emission as originating from the lowest-energy ^2E state was based in part on single-crystal polarized absorption measurements on $Cr(ox)_3$ (ox = oxalate) carried out the previous year by Piper and Carlin,[10] who also later carried out the first polarized single-crystal spectrum of $Cr(acac)_3$.[11] Many other studies were carried out, most notably by Forster and DeArmond,[12,13] as well as theoretical advances such as the development of nonradiative decay theory that

began to lead to an understanding of the dynamical processes occurring in these complexes.

Of course, technological advances also play a role in this story, most notably with the development of the ruby laser by Ted Maiman in 1960[14]—a technological feat that not only changed the course of spectroscopy but also ignited a large amount of interest in chromium(III) photophysics (the gain medium, ruby, is chromium doped corundum—a form of aluminum oxide). Several decades afterward, in the 1990's, spectroscopy was again fundamentally altered with the advent of ultrafast spectroscopy, which enabled the scientist to observe chemical and photophysical events on the lifespan of molecular vibrations. Many early studies focused on organic[15-18] or fully inorganic systems, such as Zewail's gas-phase experiments on iodine and salts of iodine.[19-26] With the development of a dye-sensitized solar cell in 1991 employing nanoparticle TiO_2 by Grätzel, which employed complexes of ruthenium(II) as the dye species, interest in transition metal photophysics expanded.[27,28] In 1996, it was shown that electron injection into the conduction band of a dye-sensitized solar cell occurred with $\tau < 500$ fs.[29] At this time ultrafast transition metal photophysics became interesting not only from a purely scientific viewpoint, involving challenges in spectroscopy and theory, but also in the realm of applications. $[Ru(bpy)_3]^{2+}$, tris(2,2'-bipyridine)ruthenium(II), eventually became the paradigm for ultrafast spectroscopy of transition metal complexes, and has been extensively studied.[30-35]

While the excited state dynamics of second and third row transition metal complexes are concerned almost entirely with charge-transfer states, complexes of first-row transition metal elements have ligand-field based states as their lowest-energy electronic state. Therefore, unlike most other studies of excited state processes, the dynamics of the complexes presented herein are occurring entirely in the ligand field manifold, i.e. only d-orbital based multielectronic wavefunctions play a role in the observed dynamics. Up to this point, the extent of published ultrafast spectroscopic data of chromium(III) complexes has been confined to a handful of studies on tris(acetylacetonato)chromium(III),[36-39] as described in chapter 3, as well as some photochemical[40,41] and donor-acceptor studies.[42] Some unpublished results are also relevant, which are reviewed in chapters 3 and 4.[38] Indeed, the field of ultrafast dynamics of first row transition metal complexes remains largely uncultivated.[43,44]

1.3 Electronic Structure, Kinetics, and Application of Nonradiative Decay Theory to Complexes of Chromium(III).

1.3.1 Electronic Structure. Chromium(III) complexes of high symmetry are ideal for the study of photophysics and photochemistry of transition metal containing systems due to the simplicity of the ligand field manifold in an O_h environment (compare, for example, the Tanabe-Sugano diagrams of d^3 and d^6 transition ions, Appendix A).[45] Furthermore, the wealth of extant literature on

the photophysical properties[5,6,46] of this ion provides the researcher with an invaluable resource for evaluation and context in which to place one's results.

The Tanabe-Sugano diagram for a d^3 species in an octahedral environment is shown below in Figure 1-1. Using the common "one electron" molecular orbital representation, the relevant electronic states of chromium(III) are highlighted.

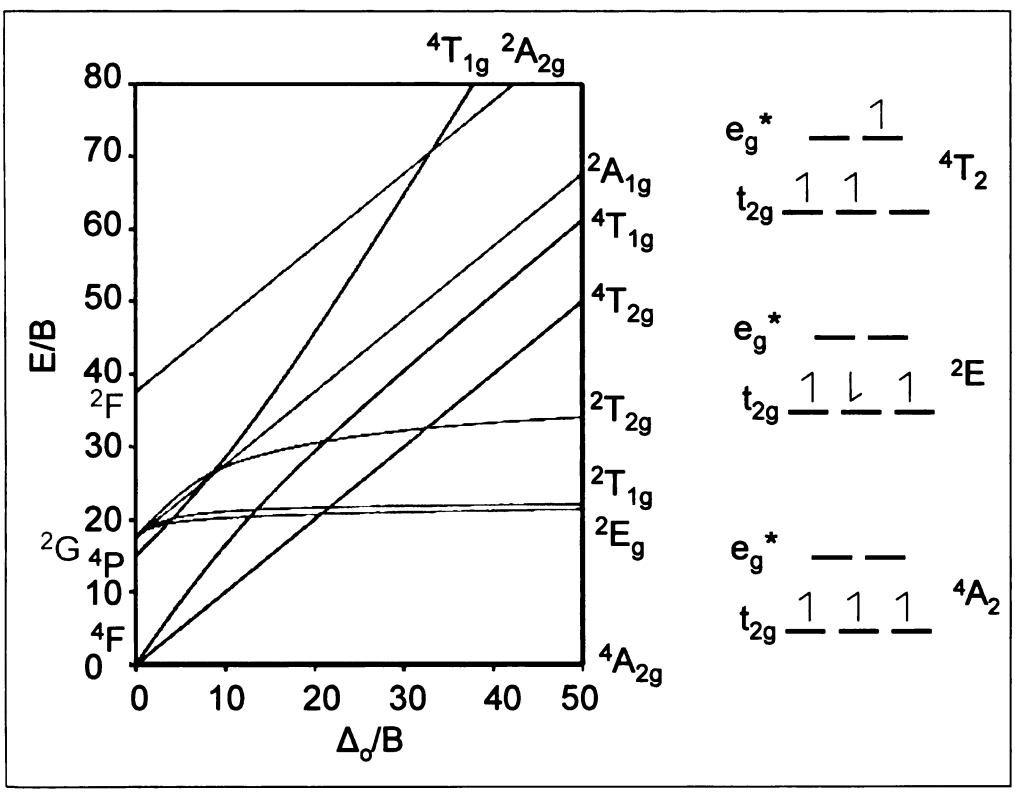

Figure 1-1: Tanabe-Sugano diagram for a d^3 ion in O symmetry.[47] One-electron representations of the relevant electronic levels in the ligand-field manifold of the chromium(III) ion in an O_h environment.

This representation is strictly not correct because the electronic states of any d > 1 species are in fact multielectronic wavefunctions, but this formalism remains useful for gaining a qualitative understanding of the relevant electronic states. Chromium(III) is a d^3 ion, with a $^4A_2$ ($(t_{2g})^3$ in an infinitely strong field) ground state. The free-ion (no imposed crystal or ligand field potentials) ground state term is ^4F, which splits into the aforementioned $^4A_2$ state as well as the first spin-allowed excited states, $^4T_2$ or $^4T_1$, under pseudo-octahedral symmetry. Transition from the ground state to the low-lying quartet excited states corresponds to the orbital ("one electron") transition $(t_{2g})^3 \rightarrow (t_{2g})^2(e_g^*)$. The final quartet ligand field state, the upper lying $^4T_1$, derives from the ^4P term. Repulsion, which can occur between states of the same irreducible representation, occurs between this state and the lower-lying $^4T_1$ (derived from ^4F), leading to the non-linear energy of these electronic states as a function of the ligand field strength.

As can be inferred from the Tanabe-Sugano diagram, in the majority of chromium(III) complexes the $^2T_1$ states lies about 500 cm^{-1} above the ^2E state, so that the states can be treated kinetically as a single state, which we will call ^2E.[46] In general, if the symmetry of the molecule is O (the pure rotational subgroup of O_h, so the subscripts g and u can be dropped) or can be approximated as such, two cases can be considered: 1) if the energy of the intraconfigurational spin flip is less than 10 Dq (the ligand field strength), then ^2E lies below $^4T_2$, or 2) the ligand

field strength is small enough so that the energy of the spin flip exceeds the ligand field strength, and ^2E lies above $^4T_2$.

Considering a chromium(III) ion under the influence of an octahedral ligand field, one can see that from simple molecular orbital considerations that formation of any quartet ligand field state must result in antibonding metal-ligand character to be introduced. In an excellent review, Kirk describes the effect of promotion of an electron to the e_g^* set (Figure 1-2), specifically $d_{xy} \rightarrow d_{x2-y2}$, $d_{xz} \rightarrow d_{z2-x2}$, and $d_{yz} \rightarrow d_{z2-y2}$ in the following manner: [the transition effectively] "constitutes a rotation of charge distribution by 45° in one or another of the three orthogonal planes containing the ligands. Because of the antibonding electron density on two of the the Cr-L bonding axes in the quartet excited state, relaxation will occur to a new geometry; a tetragonal distortion is suggested...some theories have allowed for trigonal distortions."[6] That said, it is assumed from this model that geometry distortions with respect to the ground state in the intraconfigurational ^2E state are negligible. The small geometrical change in this state with respect to the ground state is in fact manifested by the narrow emission spectrum from the ^2E state (discussed in Chapter 3).

In 1978, Wilson and Solomon's high-resolution polarized single-crystal spectroscopic study of hexaamminechromium(III), and their tour-de-force application of ligand field theory allowed for an estimation of the extent of the Jahn-Teller distortion in the $^4T_{2g}$ state of this complex.[48] They found, in

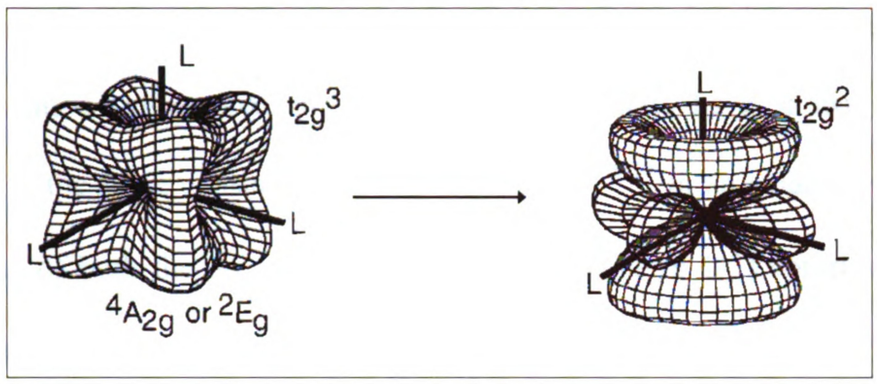

Figure 1-2: Charge redistribution in d^3 system as a result of promotion to an e_g* type orbital.[6]

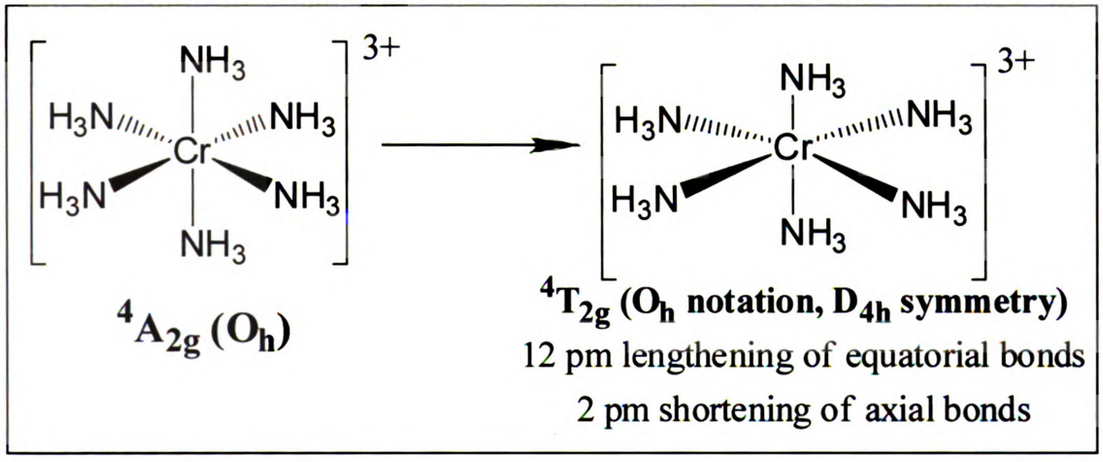

Figure 1-3: Excited state ($^4T_2$) distortions of hexaamminechromium(III), as determined by Wilson and Solomon.[48]

accordance with the simplified picture presented above, that the equatorial chromium-nitrogen bonds lengthened by 12 pm, while the axial bond lengths are shortened by 2 pm from the ground state (and presumably ^2E) geometry of 206 pm, representing a ~6 % change in the equatorial bond length. Furthermore, the authors point out that their study required a low temperature single crystal, and

that the magnitude of the excited state distortions may increase in a solution environment, as vibrational studies in the ground state have shown a 5-10% decrease in the force constant in the solution phase.[49,50] In an octahedral system, distortions of both the A_{1g} and E_g normal modes (Figure 1-3) contribute to the excited state geometry distortions.

Forster provides an excellent overview of various kinetic processes that can occur in chromium(III) systems.[5,46] Upon excitation into the Frank-Condon state, only a handful of kinetics processes can ensue to provide relaxation back to the ground $^4A_2$ state. A Jablonski diagram of the kinetic processes that can occur within a photochemically stable chromium(III) species wherein the energy of the ^2E state is below that of the $^4T_2$ is shown in Figure 1-4. Upon excitation into the $^4T_2$ state a variety of processes ensue which dissipate the absorbed energy. From the Frank-Condon state the lone radiative mechanism is fluorescence (FL), emission between states of the same spin multiplicity. The nonradiative mechanism of energy dissipation from this state include internal conversion (IC), which is a nonradiative decay mechanism between states of the same spin multiplicity, and intersystem crossing (ISC) an isoenergetic process between electronic states of different spin multiplicity. Fluorescence and internal conversion both lead to ground state formation, while intersystem crossing results in the formation of the ^2E state, which is generally long-lived. If enough thermal energy is present and the $^4T_2$ and ^2E states are close in energy, back intersystem

crossing (BISC) can occur. In a system where the $^4T_2$ lies lowest in energy the system will undergo internal conversion from this state to repopulate the quartet ground state.

The ^2E state can decay via phosphorescence (PH), a radiative emission between states of different spin multiplicities, or by ISC into the ground $^4A_2$ manifold. These are the various processes that occur *between* different electronic states. However, one must keep in mind that other nonradiative events (vibrational cooling (VC), redistribution of vibrational energy) are occurring within the electronic state before the formation of the thermalized, metastable state. These processes will be discussed at great length later.

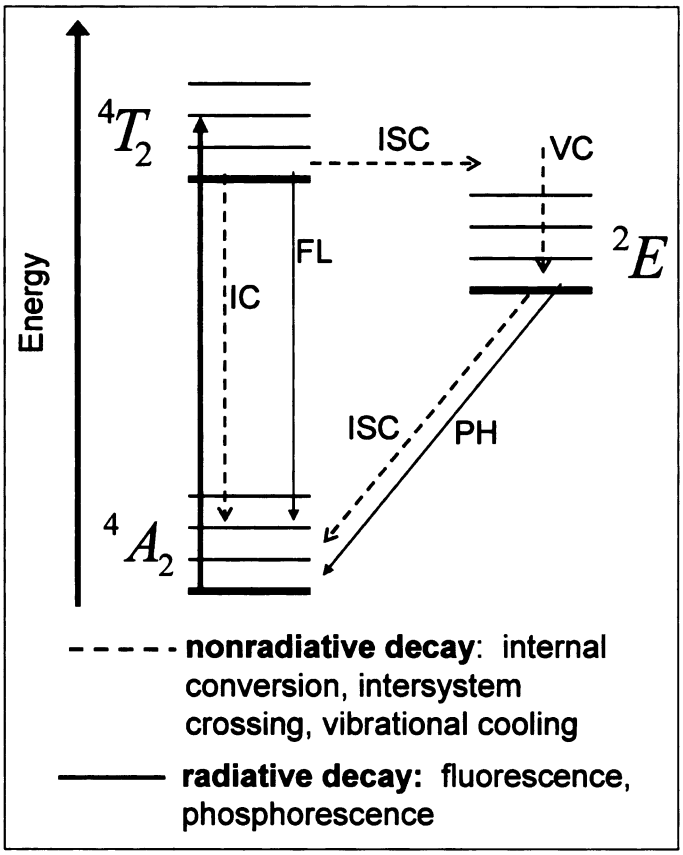

Figure 1-4: Jablonski diagram of photophysical processes that occur in a d^3 ion under O symmetry.

Finally, while various photochemical events can quench radiative (FL, PH) and nonradiative (IC, ISC, VC) processes from the excited electronic states, we will concern ourselves only with photophysical processes, i.e. those that cause no chemical change to the system. This is, in fact, a good approximation given the low photochemical quantum yields for the complexes employed in this study,[51] although the researcher must be vigilant not to discount these mechanisms even in

seemingly photostable complexes. The rates of excited state decay are intimately tied into the nuclear displacement (Q) and relative energies (E_0) of the potential energy surfaces of the two states in question. All of these factors are dealt with within the formalism of nonradiative decay theory.

1.3.2 Nonradiative Decay Theory. As described in the previous section, when a system absorbs a photon, the ensuing processes that relax the molecule back to the ground state can be classified as either radiative (fluorescence, phosphorescence) or nonradiative (vibrational cooling, internal conversion, intersystem crossing, quenching mechanisms). Nonradiative and radiative dynamics can be summarized by Fermi's "Golden rule" (equation 1.1).

$$k = \frac{2\pi}{\hbar}\left|H^{(1)}\right|^2 \rho(E) \qquad (1.1)$$

In this equation $\left|H^{(1)}\right|^2$ quantifies the coupling of the participating vibrational and electronic wavefunctions and $\rho(E)$ is a density-of-states term. Starting from Fermi's Golden rule, nonradiative decay theory was developed in the 1960's and 70's through the work of Jortner, Freed, El-Sayed, and others.[52,53] An eventual goal of this research program is ascertaining whether this theory is generally applicable to ultrafast processes of transition metal systems.

A general treatment of nonradiative decay theory is presented here, and several specific examples are presented later in the text. The Born-Oppenheimer

approximation allows one to decouple the electronic and nuclear components due to the relative timescales on which they operate (this approximation has been shown to breakdown for some ultrafast processes where strong vibronic coupling is implicated, as discussed later in this dissertation). The resulting total wavefunction for any electronic state is then the product of the electronic part, ψ, and all 3N-6 vibrational modes, χ. We consider two states, the initial (promoting) and final (accepting):

$$\psi_1 = \psi_1^0(r)\prod_{i=1}^{3N-6}\chi_i^{(1)}(Q) \tag{1.2}$$

$$\psi_2 = \psi_2^0(r)\prod_{i=1}^{3N-6}\chi_f^{(2)}(Q) \tag{1.3}$$

Applying the Golden Rule of Fermi, the nonradiative rate takes the form

$$k_{nr} = \frac{2\pi}{\hbar}\left|\int\psi_2^*\hat{H}\psi_1 d\tau\right|^2\rho(E) \tag{1.4}$$

Note that the coupling term now takes the form of a transition moment integral. As the Born-Oppenheimer approximation demands that the electronic and vibrational wavefunctions are distinct, the operator is expanded to include separate electronic and nuclear operators

$$\hat{H} = \hat{H}_{Elec} + \hat{H}_{Vib} \tag{1.5}$$

where $\hat{H}_{Elec}$ operates only on the electronic terms and $\hat{H}_{Vib}$ operates on the vibrational components. By putting the wavefunctions and operator in the full form and rearranging, one obtains a form that includes both electronic and vibrational transition moment integrals:

$$k_{nr} = \frac{2\pi}{\hbar}\left|\int \psi_2^*(r)\hat{H}_{Elec}\psi_1 d\tau \int \prod_{i=1}^{3N-6} \chi_f^{(2)}(Q)\hat{H}_{Vib}\prod_{i=1}^{3N-6}\chi_i^{(1)}(Q)d\tau\right|^2 \rho(E) \quad (1.6)$$

This equation can be simplified by eliminating non-participating terms, or by considering a single accepting mode, continuum of modes, etc. Manipulation and determination of this result is the work of all the theory on nonradiative decay (again, except for those cases where the Born-Oppenheimer approximation fails).

The driving force for nonradiative decay can be understood by examining equation 1.6, the basic equation governing this phenomenon. For nonradiative decay the vibrational overlap between the participating states, called Frank-Condon factors, which relate to the geometry of the system, is an important factor determining the rate. The rate is proportional to the matrix element of the vibrational Frank-Condon factors:

$$k_{nr} \propto \left\langle \chi_i \middle| \chi_f \right\rangle \quad (1.7)$$

Where χ_i corresponds to the vibrational mode (or modes) from which the transition is originating, the so-called promoting mode, and χ_f is the mode (or

modes) to which the energy is transferred, called the accepting mode. The vibrational overlap, in turn, depends on two different factors, the relative nuclear displacements of the electronic states (ΔQ) and the difference in the zero-point energies between the two states (ΔE). To understand this, we will employ some of the terminology from Marcus's theory of electron transfer and describe two limiting cases of ΔQ positions, the "normal" region and the "inverted" region, where changing ΔE while maintaining the same nuclear displacement results in two opposing trends in the rate of k_{nr}.

In the following discussion we will consider a single promoting mode and a single accepting mode, however theories have been developed which consider multiple promoting and accepting modes. The vibrational wavefunctions under consideration are the lowest vibrational component of the upper state (the promoting mode—assuming that this upper state is thermalized), and the isoenergetic vibrational wavefunction of the lower potential (accepting mode). Figure 1-5 shows two harmonic potentials corresponding to electronic potential wells with the vibrational component wavefunctions superimposed on the potentials. The upper potential is displaced with respect to the lower state along the nuclear coordinate, Q. As the energetic separation of the two potential wells decreases, the extent of vibrational overlap between the lowest component of the upper well and the isoenergetic level of the lower well decreases; a concomitant decrease in the rate of nonradiative decay between these two states results according to equation 1.7. This describes the situation of the "normal" region,

which arises due to the greater amplitude on the edges of the potential for higher-energy component vibrational wavefunctions.

Figure 1-6 again shows two harmonic potentials, but now with minimal relative displacement along the nuclear coordinate axis. In this case the dearth of amplitude of upper lying vibrational wavefunctions in the center of the potential leads to a poor overlap between the lowest-lying vibrational wavefunction of the upper state and isoenergetic levels of the lower state. As the energetic separation is reduced, vibrational overlap increases, and an associated increase in k_{nr} occurs according to equation 1.7. This situation is descriptive of the "inverted" region.

Finally, another general concept of nonradiative decay theory is the role of entropy. Entropy plays an important role in driving nonradiative decay: the term $\rho(E)$ of equation 1.1 quantifies the density of states in the system. A final state that has a greater density of vibrational levels will entropically drive the transition, while under similar conditions a final state with a more dilute manifold of vibrational states will have a correspondingly lower nonradiative rate. This concept was proposed early on in the development of the theory.[54,55]

The role of conformational changes (modifying ΔE and ΔQ) between the ground and excited states on the rate of nonradiative decay has been studied extensively. Some of the earliest studies on nonradiative dynamics involved monitoring the formation of the ground state via the lowest-energy excited state, a triplet state, in hydrocarbon systems. The majority of these systems operate in the

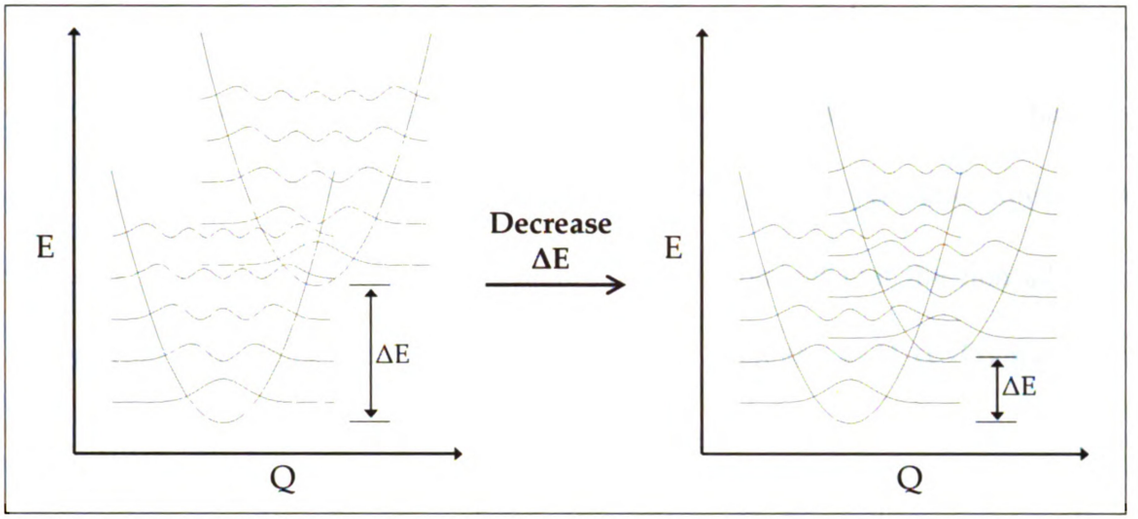

Figure 1-5: Normal region—as ΔE is decreased the rate of electron transfer decreases as a result of decreased vibrational overlap between component vibrational wavefunctions.

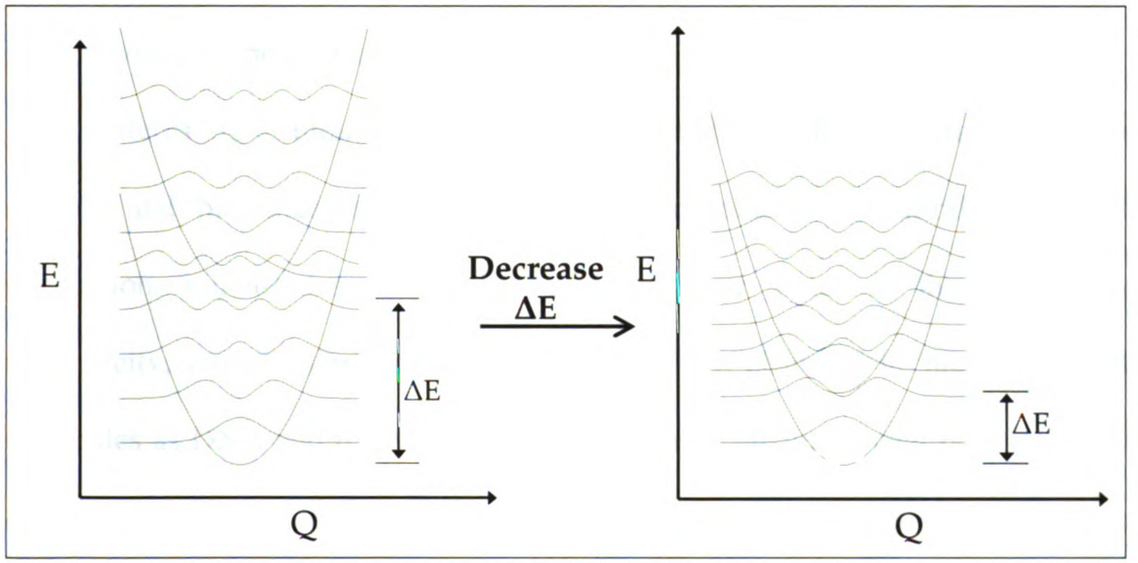

Figure 1-6: Inverted region—as ΔE is decreased the rate of electron transfer increases as a result of increased vibrational overlap between component vibrational wavefunctions.

inverted region; a paper published in 1966 by Siebrand[56] explains "a crude correlation between τ and the triplet energy E_T has been noted and traced back to the Franck-Condon factor $F(\propto 1/\tau)$ of the transition..." A year later, through a series of deuterated hydrocarbons, Siebrand et.al. showed that the nonradiative decay from the triplet state occurs efficiently through the C-H (C-D) modes.[57] Later studies expanded the theory for hydrocarbons[58,59] and there are also noteworthy examples of studies of aromatic systems.[60] Since these early studies, the general concepts outlined above been applied to a broad range of chemical systems for nonradiative transitions between the emissive, lowest-lying excited state and the ground state. Several examples relevant to transition metal photophysics are presented below.

Interesting examples of the role of conformational changes can be found in organic and biological systems, where the phenomenon of ultrafast internal conversion, radiationless decay between electronic states of the same spin multiplicity, is particularly relevant. This has been observed in such biological molecules as DNA and RNA nucleosides and the green-fluorescent protein (GFP) chromophore.[61] Kohler and coworkers[62] found excited state lifetimes under 1 ps for all nucleosides, and those nucleosides with faster internal conversion rates had a lower propensity toward photochemical damage. They suggest that this property likely played an essential role in the early evolution of life on earth. The GFP chromophore is composed of two halves, and semi-empirical quantum mechanical

calculations suggest that the two halves are planar in the ground S_0 state, while they are perpendicular in the S_1 state.[63] This large conformation change means the S_0 and S_1 potential wells are displaced along the coordinate corresponding to the axis of rotation, and correspond to the "normal region." This displacement of the wells results in a much larger Frank-Condon overlap (vibrational overlap) and thus a much more efficient internal conversion than if the wells were in the Marcus inverted region. This ultrafast decay is responsible for the stability and low quantum yields for photochemistry. This suggests a means to controlling photochemical and photophysical events by controlling the environment, and thus the relative displacements of the electronic states involved, and ultimately the Frank-Condon overlap. In fact, these large conformational changes in organic and biological systems, and the associated rapid nonradiative rates, may be the bridge between organic photophysics and transition metal photophysics, where large conformational changes are quite common.[64]

The theory is expanded by considering the so-called "weak coupling limit." In this limit the nonradiative decay rate is the product of the electronic (β_0) and vibrational overlap (F, Franck-Condon) factors (equation 1.8).

$$k_{nr} = \beta_0 F \tag{1.8}$$

$$\beta_0 = C_k^2 \omega_k \sqrt{\frac{\pi}{2}} \tag{1.9}$$

$$F = \sum \prod_n \left| \langle \chi_f | \chi_i \rangle \right|^2 \tag{1.10}$$

The electronic factors includes the promoting mode, ω_K, from which the transition originates, and a constant C_k, which includes contributions from vibronic coupling, which acts to make formally symmetry-forbidden (LaPorte forbidden) transitions allowed, and spin-orbit coupling, which increases the allowedness of formally spin-forbidden transitions. For an intersystem crossing (spin-forbidden) event a non-zero value of β_0 is obtained only if spin-orbit coupling contributions are considered. The vibrational factor, F, is accepting-mode dependent and will take on different forms depending on the approximation: is there a single accepting mode, a continuum of modes, or a ladder[53,65] of modes? Note that equations 1.8 through 1.10 effectively constitute the quantitative result of equation 1.7.

A popular model that has found success in describing nonradiative rates between lowest-energy excited states and ground states is the so-called polaron (also known as the spin-boson) model. In this model, many vibrational states are playing a role in the nonradiative transition and the following equation for the vibrational overlap factor, F, results:[46]

$$F = \left(\frac{1}{\hbar\omega_M E}\right)^{1/2} \exp\left(-S_M - \frac{\gamma E}{\hbar\omega_M} + \left(\frac{\gamma+1}{\hbar\omega_M}\right)^2 \frac{\left(\Delta\nu_{1/2}\right)^2}{16\ln 2}\right) \qquad (1.11)$$

$$\gamma = \ln\left(\frac{E}{S_M \hbar\omega_M}\right) - 1 \qquad (1.12)$$

In equations 1.11 and 1.12 E is the energy separation between the two states, S_M is the Huang-Rhys factor, which describes the displacement of the potential minima of the promoting and accepting electronic states along the accepting mode coordinate, ω_M is the dominant accepting mode, and $\Delta\upsilon_{1/2}$ is the full width at half-maximum of the emission spectrum. In the context of electron transfer one simply needs to replace E with the corresponding quantities familiar to the theory of electron transfer :[66,67]

$$E = \left|\Delta G^0\right| - \lambda_0 \tag{1.13}$$

$$\frac{\left(\Delta\nu_{1/2}\right)^2}{16\ln 2} = \lambda_0 k_B T \tag{1.14}$$

Equations 1.13 and 1.14 form of the "Energy Gap Law" a limiting case of nonradiative decay theory in the inverted region, which predicts a linear relationship between the energy gap (E) and $\ln k_{nr}$. Meyer et al. have confirmed the "Energy Gap Law" between the emissive state and the ground state in several series of substituted Os(II), Ru(II), and Re(I) complexes.[68,69] Employing the spin-boson model, and considering only one vibrational mode (ω) and an equilibrium displacement (ΔQ), the reorganizational energy for this mode is:

$$\lambda_i = \left(\frac{f}{2}\right)\left(\Delta q_e\right)^2 \tag{1.15}$$

Where $f = \mu\omega^2$ is the force constant. This is related to the Huang-Rhys factor, also called the electron vibrational coupling constant, a dimensionless quantity

that takes into account the equilibrium nuclear displacement (ΔQ) and the reorganization energy:

$$S = \frac{\lambda_i}{\hbar\omega} = \frac{f(\Delta q_e)^2}{2\hbar\omega} = \frac{\mu\omega(\Delta q_e)^2}{2\hbar} \qquad (1.16)$$

Meyer et. al. have used the concepts outlined above to fit emission spectra of Ru(II) and Os(II) polypyridyl complexes. From these fits, which utilize concepts of nonradiative decay theory, they were able to obtain kinetic information on these molecules.[70-74]

1.3.3 Applications of Nonradiative Decay Theory to Complexes of Chromium(III). The first theoretical application of nonradiative decay theory specifically to transition metal complexes was carried out by Robins and Thomson in 1973,[75] wherein they applied a qualitative, symmetry-based approach to nonradiative decay theory to describe the nonradiative $^2E \rightarrow {}^4A_2$ conversion in a series of chromium(III) complexes previously studied by Forster and coworkers. The majority of theoretical work in the field up to that point was concerned with organic systems, however this theory had been applied in several papers[76-78] to transition metal systems, with varying success. The approach adopted by Robins and Thomson was motivated by the inherent high symmetry of many metal complexes, such that symmetry-based selection rules likely play a large role in the coupling terms affecting the rates of nonradiative relaxation. This concept arose a

few years prior via the work of Gardner and Kasha,[79] who suggested that molecules that display slow radiationless decay are "vibrationally deficient," meaning that the molecules lack promoting and accepting modes of the same symmetry to facilitate rapid nonradiative decay. Using this symmetry based approached, they determined for octahedral and pseudo-octahedral complexes 1.) that metal-ligand modes are likely not active in $^2E \rightarrow {}^4A_2$ nonradiative conversion and 2.) that the rate of nonradiative decay was linearly dependent on the number of hydrogen atoms attached to the diketonate skeletal framework: the more hydrogen atoms bound directly to the π system of the ligand, the faster the rate of intersystem crossing. The authors also note that comparison with systems that have aliphatic ligands suggests that coupling to the π system leads to more efficient nonradiative decay. This result is likely not general for state changes in transition metal systems, and probably reflects the intraconfigurational nature of the state change that they were describing, where both states can be described in terms of orbitals of π symmetry. These symmetry-based selection rules were later applied to describe internal conversion (radiationless $^4T_2 \rightarrow {}^4A_2$ conversion) in various chromium(III) doped glasses.[80]

From the 1970s onwards many studies appeared which attempted to address the mechanism of decay of the lowest energy excited state in simple chromium(III) systems. In general, at low temperatures (< 100 K), the relaxation was insensitive to the matrix and temperature, however various studies showed

that the decay depended on high frequency vibrations of ligated atoms, spin-orbit coupling, as well as low-frequency modes.[81-83] A separate regime of dynamics was found at higher temperatures, where dynamics vary with temperature and solvent, such that the decay of the ^2E state is given by:

$$k = k_{LT} + k_{HT}(T) \tag{1.17}$$

Where $k_{LT} = k_r + k_{nr}$ and $k_{HT}(T)$ is the temperature dependent additional dynamics observed at higher temperatures.[84] At the time, researchers were attempting to determine a unified model for this so-called "thermally activated relaxation," and three mechanisms were put forth to account for the decay of the ^2E state: 1.) quenching of the excited doublet state by direct chemical reaction, 2.) back intersystem crossing to a low-lying quartet state, which can undergo internal conversion to form the ground state or 3.) crossing to the potential energy surface of a "ground state intermediate," facilitated by low-frequency solvent and/or normal modes of the molecule (Figure 1-7).[85] Many studies were interested in determining the dominant mechanism in various systems; most of the major studies of this time employed am(m)ine complexes of chromium(III). Early on, quenching of the ^2E state by direct reaction was the favored candidate for the major relaxation pathway for most complexes of this type. This arose from studies of *trans*-$Cr(NH_3)_4XY$ and *trans*-$(Cr[14]aneN_4)XY$ (where X and Y are simple ligands such as SCN, CN and NH_3 and $[14]aneN_4$ is 1,4,8,11-tetraazacyclotetradecane).[86-88] These studies showed high yields of

photosubstitution for the *trans*-$Cr(NH_3)_4XY$ type complexes but very low yields of photosubstitution for the *trans*-(Cr[14]aneN_4)XY complexes. This was attributed to the closed ring structure of the [14]aneN_4 ligand (i.e. cyclam, Figure 1-8), which ostensibly prevented photosubstitution at the equatorial coordination sites, bolstering support for the direct reaction quenching mechanism. Support for the mechanism wherein state crossing was facilitated by low frequency modes came mainly from variable temperature/solvent studies, which showed that freezing of the skeletal vibrations of the molecule, that apparently acted as promoting modes, hindered decay of the ^2E state.[89] This question was ultimately addressed by Ramasami *et al.* in a study where $[Cr(en)_3]^{3+}$ and $[Cr(sep)]^{3+}$ (sep = (S)-1,3,6,8,10,13,16,19-octaazabicyclo[6.6.6]eicosane, see Figure 1-8) were compared.[85] The sep ligand fully encapsulates the chromium(III) ion, so direct reaction is completely discounted. If the direct reaction mechanism was the dominant mechanism for ^2E decay then this complex would have a very long ^2E lifetime relative to the electronically similar $[Cr(en)_3]^{3+}$. Furthermore, the authors note that the back intersystem crossing mechanism is anticipated to be highly inefficient in this system because of the large energy gap. The authors found that the lifetime of the ^2E state of $[Cr(sep)]^{3+}$ was only slightly longer than that of $[Cr(en)_3]^{3+}$, making direct reaction an unlikely candidate and supporting intersystem crossing as a deactivation pathway. Endicott *et al.* later noted that the same mechanism, namely coupling of low-frequency modes, would account for

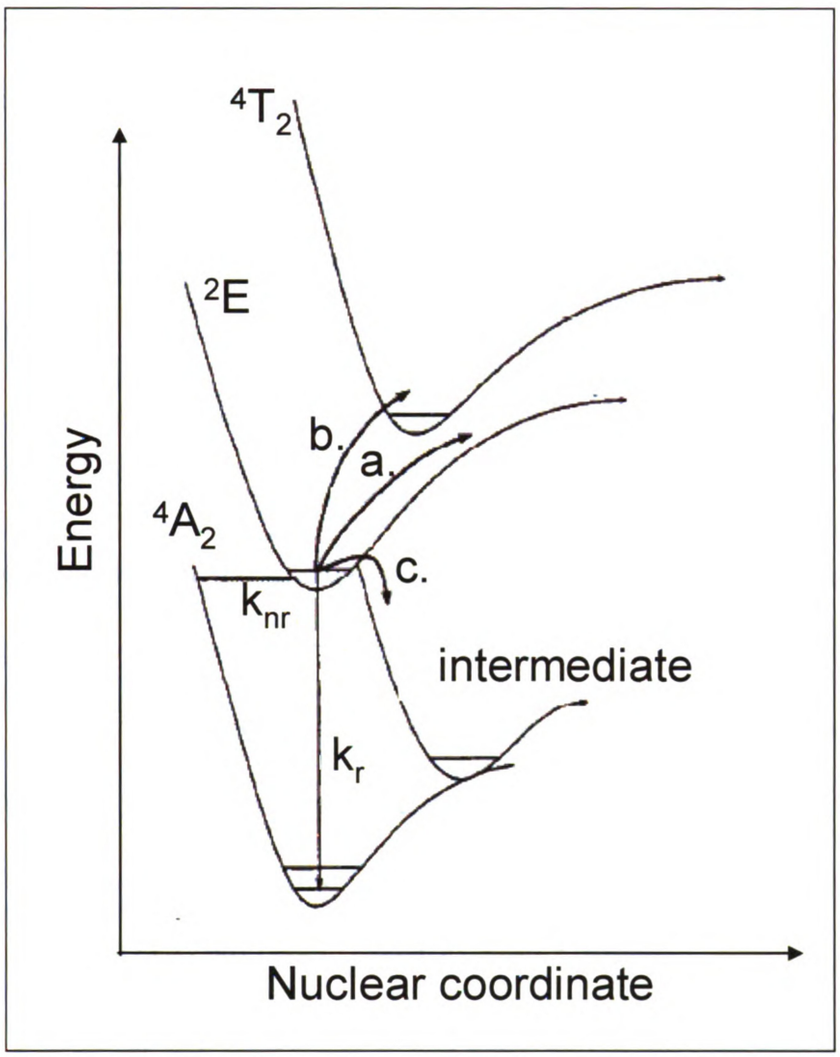

Figure 1-7: Proposed mechanisms for thermally activated ^2E state deactivation, reproduced from reference 84. (a. = direct reaction, b. = back intersystem crossing into the quartet manifold and c. = surface crossing to a ground state intermediate.)

both the direct reaction deactivation as well as intersystem crossing to the ground state intermediate, and relative contributions of each pathway are determined by nuclear configuration.[90] In this sense, they added that the direct reaction pathway

should be considered a limiting case of a mechanism involving deactivation promoted by low frequency normal modes or solvent modes.

The role of stereochemistry in these thermally activated relaxation events was first proposed by Kane-Maguire *et al.*[91,92] Theoretical aspects of this were studied by Vanquickenborne and coworkers.[93] They showed that trigonal distortions, which lower the symmetry of the system, mix d-orbitals creating microstates of doubly filled d-orbitals. These doubly filled d-orbitals decrease electronic repulsion in the excited state, thus providing a facile mechanism of achieving the ground state electronic configuration. Later, experimental evidence began to arise which implicated trigonal distortions as playing an important role in facilitating intersystem crossing: these studies compared amine complexes to analogous constrained amine ligands, mostly derivatives of 1,4,7-triazacyclononane (TACN) (see Figure 1.8). [82,84,94-96]

In the 1990s, as a forerunner to this dissertation, ultrafast spectroscopy was beginning to be applied to the study of chromium(III) photophysics.[36-38] These studies, which were carried out with ~ 100 fs optical pulses, are reviewed extensively in chapters 4 and 5. For the archetypal complex $Cr(acac)_3$ it was found that intersystem crossing between the first spin-allowed $^4T_2$ state and lowest-energy ^2E occurred with $k_{isc} > 10^{13}$, and an ~ 1 ps lifetime was observed which was assigned as vibrational cooling within the ^2E state. These dynamics represented a new observation in field of chromium(III) photophysics: one of the

rapidly evolving, non-thermalized state, explored in great detail in Chapter 3 of this dissertation.

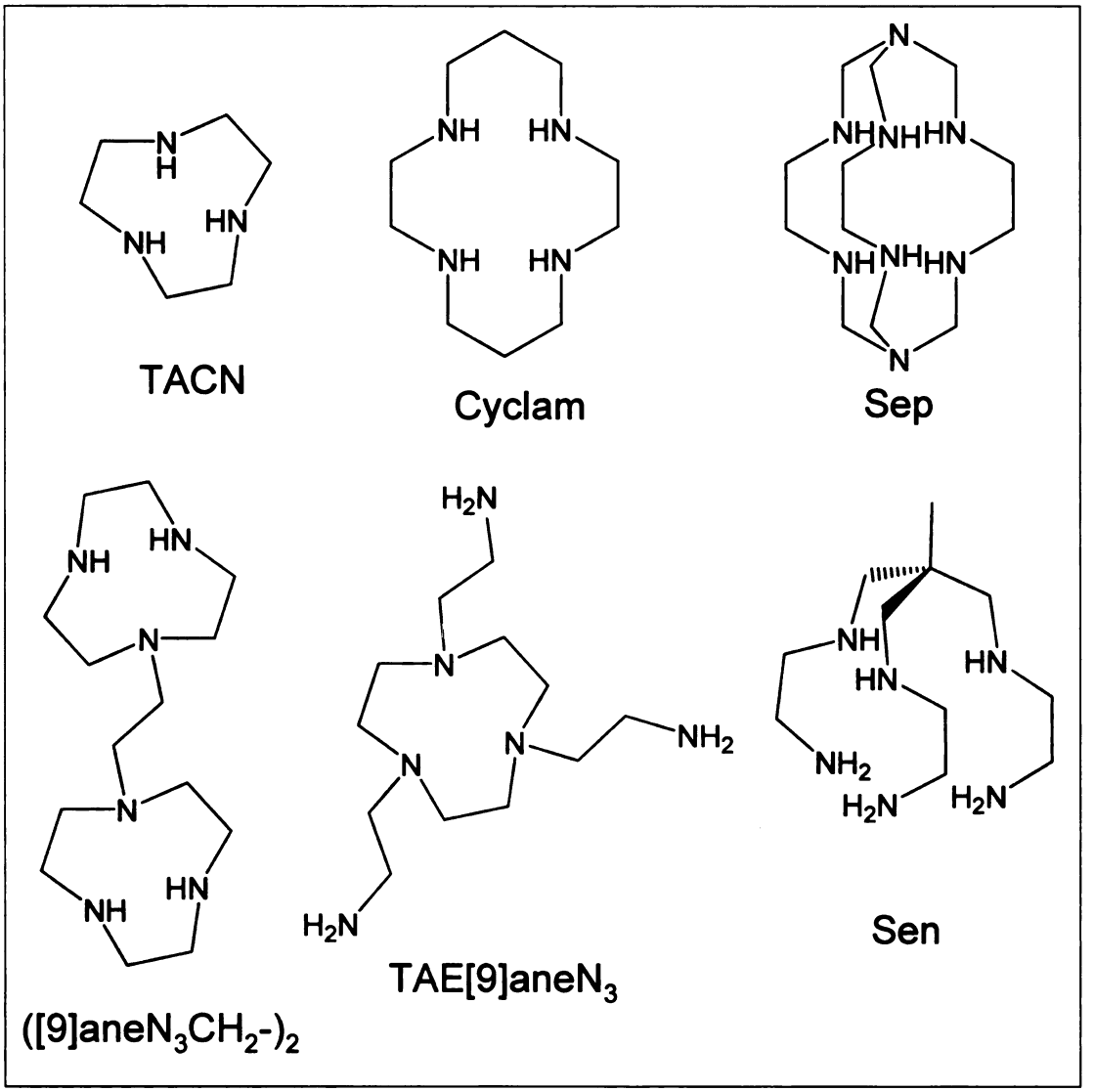

Figure 1-8: Sterically constraining ligands that helped to elucidate modes of ^2E deactivation.

1.4 Dissertation Outline

The work presented herein will include studies on a variety of chromium(III) complexes, including π-delocalized ligand systems, low-symmetry ligand fields, and spin exchange systems. The aim of this work is to fully characterize the electronic, magnetic, and geometrical structures of these complexes with the goal of correlating these structural changes to the observed excited state dynamics, which are nonradiative in nature. Studies on complexes of gallium(III), an effective analog of chromium(III) which provides useful information in the absence of unpaired spin, are also presented. Finally, Heisenberg spin exchange complexes of chromium(III) are explored. The outline of this dissertation is as follows:

· In **Chapter 2**, the electronic and magnetic structures of the ground states of various systems are explored via electron spin resonance techniques. Gallium semiquinones will be explored and issues relevant to understanding and controlling spin distribution in such systems will be discussed. The ground state magnetic structures of quartet complexes of chromium(III) will also be explored, and an extensive investigation of the effect of zero field splitting on the appearance of spin resonance spectra is presented.

· **Chapter 3** focuses on the electronic structure and excited state dynamics of high-symmetry complexes of chromium(III). Spectroscopic techniques, both static and time-resolved, are employed to characterize the excited electronic structure and dynamics therein. This work includes ultrafast transient absorption results on

high-symmetry chromium(III) complexes, which aims to address fundamental questions vis-à-vis mechanisms of nonradiative decay in these systems. These studies were carried out with various time resolutions, employing ultrafast optical pulses typically of 100 fs duration.

· **Chapter 4** explores the electronic structure and dynamics of spin exchange complexes of chromium(III), employing the same techniques as those of Chapters 3 and 4. The results of the previous chapters are employed to aid in the characterization of these systems.

· **Chapter 5** highlights future work.

1.5 References

(1) Hagfeldt, A.; Gratzel, M. *Accounts of Chemical Research* **2000**, *33*, 269-277.

(2) Meyer, T. J. *Accounts of Chemical Research* **1989**, *22*, 163-170.

(3) Becquerel, E. *La lumiere, ses causes et ses effects*; Gauthier-Villars: Paris, 1867.

(4) *Chromium in the natural and human environments*; Wiley: New York, 1988; Vol. 20.

(5) Forster, L. S. *Chemical Reviews* **1990**, *90*, 331-353.

(6) Kirk, A. D. *Chemical Reviews* **1999**, *99*, 1607-1640.

(7) Finkelstein, R.; Vleck, J. H. V. *Journal of Chemical Physics* **1940**, *8*, 790-797.

(8) Sugano, S.; Tanabe, Y. *Journal of the Physical Society of Japan* **1958**, *13*, 880-899.

(9) Forster, L. S.; DeArmond, K. *Journal of Chemical Physics* **1961**, *34*, 2193-94.

(10) Piper, T. S.; Carlin, R. L. *Journal of Chemical Physics* **1960**, *33*, 608-609.

(11) Piper, T. S.; Carlin, R. L. *The Journal of Chemical Physics* **1962**, *36*, 3330-3332.

(12) DeArmond, K.; Forster, L. S. *Spectrochimica Acta* **1963**, *19*, 1403-1406.

(13) DeArmond, K.; Forster, L. S. *Spectrochimica Acta* **1963**, *19*, 1687-1693.

(14) Maiman, T. H. *Nature* **1960**, *187*, 493-494.

(15) Bakker, H. J.; Planken, P. C. M.; Lagendijk, A. *Journal Of Chemical Physics* **1991**, *94*, 6007-6013.

(16) Akesson, E.; Walker, G. C.; Barbara, P. F. *Journal Of Chemical Physics* **1991**, *95*, 4188-4194.

(17) Elsaesser, T.; Kaiser, W. *Annual Review Of Physical Chemistry* **1991**, *42*, 83-107.

(18) Tominaga, K.; Walker, G. C.; Jarzeba, W.; Barbara, P. F. *Journal Of Physical Chemistry* **1991**, *95*, 10475-10485.

(19) Willberg, D. M.; Breen, J. J.; Gutmann, M.; Zewail, A. H. *Journal Of Physical Chemistry* **1991**, *95*, 7136-7138.

(20) Bowman, R. M.; Dantus, M.; Zewail, A. H. *Chemical Physics Letters* **1989**, *161*, 297-302.

(21) Gruebele, M.; Roberts, G.; Dantus, M.; Bowman, R. M.; Zewail, A. H. *Chemical Physics Letters* **1990**, *166*, 459-469.

(22) Breen, J. J.; Willberg, D. M.; Gutmann, M.; Zewail, A. H. *Journal Of Chemical Physics* **1990**, *93*, 9180-9184.

(23) Potter, E. D.; Herek, J. L.; Pedersen, S.; Liu, Q.; Zewail, A. H. *Nature* **1992**, *355*, 66-68.

(24) Dantus, M.; Bowman, R. M.; Zewail, A. H. *Nature* **1990**, *343*, 737-739.

(25) Dantus, M.; Bowman, R. M.; Gruebele, M.; Zewail, A. H. *Journal Of Chemical Physics* **1989**, *91*, 7437-7450.

(26) Dantus, M.; Rosker, M. J.; Zewail, A. H. *Journal Of Chemical Physics* **1988**, *89*, 6128-6140.

(27) O'Regan, B.; Gratzel, M. *Nature* **1991**, *353*, 737-740.

(28) Hagfeldt, A.; Gratzel, M. *Accounts Of Chemical Research* **2000**, *33*, 269-277.

(29) Tachibana, Y.; Moser, J. E.; Gratzel, M.; Klug, D. R.; Durrant, J. R. *Journal Of Physical Chemistry* **1996**, *100*, 20056-20062.

(30) Yeh, A. T.; Shank, C. V.; McCusker, J. K. *Science* **2000**, *289*, 935-938.

(31) Vlcek, A. *Coordination Chemistry Reviews* **2000**, *200*, 933-977.

(32) Saes, M.; Bressler, C.; Abela, R.; Grolimund, D.; Johnson, S. L.; Heimann, P. A.; Chergui, M. *Physical Review Letters* **2003**, *90*.

(33) Henry, W.; Coates, C. G.; Brady, C.; Ronayne, K. L.; Matousek, P.; Towrie, M.; Botchway, S. W.; Parker, A. W.; Vos, J. G.; Browne, W. R.; McGarvey, J. J. *Journal Of Physical Chemistry A* **2008**, *112*, 4537-4544.

(34) Yoon, S.; Kukura, P.; Stuart, C. M.; Mathies, R. A. *Molecular Physics* **2006**, *104*, 1275-1282.

(35) Damrauer, N. H.; Cerullo, G.; Yeh, A.; Boussie, T. R.; Shank, C. V.; McCusker, J. K. *Science* **1997**, *275*, 54-57.

(36) Juban, E.; McCusker, J. *Journal of the American Chemical Society* **2005**, *127*, 6857-6865.

(37) Juban, E. A.; Smeigh, A. L.; Monat, J. E.; McCusker, J. K. *Coordination Chemistry Reviews* **2006**, *250*, 1783-1791.

(38) Juban, E., Ph.D. Thesis, University of California, 2006.

(39) Macoas, E. M. S.; Kananavicius, R.; Myllyperkio, P.; Pettersson, M.; Kunttu, H. *Journal of the American Chemical Society* **2007**, *129*, 8934-8935.

(40) Inamo, M.; Okabe, C.; Nakabayashi, T.; Nishi, N.; Hoshino, M. *Chemical Physics Letters* **2007**, *445*, 167-172.

(41) To, T. T.; Heilweil, E. J.; Duke, C. B.; Burkey, T. J. *Journal Of Physical Chemistry A* **2007**, *111*, 6933-6937.

(42) Neuman, D.; Ostrowski, A. D.; Mikhailovsky, A. A.; Absalonson, R. O.; Strouse, G. F.; Ford, P. C. *Journal of the American Chemical Society* **2007**, *130*, 168.

(43) Kane-Maguire, N. A. P. In *Photochemistry And Photophysics Of Coordination Compounds I*; Springer-Verlag Berlin: Berlin, 2007; Vol. 280, p 37-67.

(44) Forster, L. S. *Coordination Chemistry Reviews* **2006**, *250*, 2023-2033.

(45) Juban, E. A., Ph.D. Thesis, University of California, Berkeley, 2006.

(46) Forster, L. S. *Coordination Chemistry Reviews* **2006**, *250*, 2023-2033.

(47) Bethune, A. http://www.albion.edu/chemistry/abbethune, **2009**.

(48) Wilson, R. B.; Solomon, E. I. *Inorganic Chemistry* **1978**, *17*, 1729-1736.

(49) Schmidt, K. H.; Mueller, A. *Inorganic Chemistry* **1975**, *14*, 2183-2187.

(50) Nakamoto, K. *"Infrared Spectra of Inorganic and Coordination Compounds"*; 2 ed.; Wiley: New York, 1971.

(51) Fleming, C. A.; Thornton, D. A. *Journal of Molecular Structure* **1975**, *25*, 271-279.

(52) Freed, K.; Jortner, J. *Journal of Chemical Physics* **1970**, *52*, 6272-6291.

(53) Avouris, P.; Gelbart, W.; El-Sayed, M. A. *Chemical Reviews* **1977**, *77*, 794-833.

(54) Douglas, A. E. *Journal Of Chemical Physics* **1966**, *45*, 1007.

(55) Chock, D. P.; Jortner, J.; Rice, S. A. *Journal Of Chemical Physics* **1968**, *49*, 610.

(56) Siebrand, W. *Journal of Chemical Physics* **1966**, *44*, 4055-4056.

(57) Siebrand, W.; Williams, D. F. *Journal of Chemical Physics* **1967**, *46*, 403-404.

(58) Siebrand, W. *Journal of Chemical Physics* **1967**, *47*, 2411-2424.

(59) Siebrand, W.; Williams, D. F. *Journal of Chemical Physics* **1968**, *49*, 1860-1871.

(60) Kistiakowsy, G.; Parmenter, C. *Journal Of Chemical Physics* **1965**, *42*, 2942.

(61) Zimmer, M. *Chemical Reviews* **2002**, *102*, 759-781.

(62) Pecourt, J.-M. L.; Peon, J.; Kohler, B. *Journal of the American Chemical Society* **2001**, *123*, 10370-10378.

(63) Voityuk, A. A.; Michel-Beyerle, M.-E.; Rosch, N. *Chemical Physics Letters* **1998**, *296*, 269-276.

(64) Fidder, H.; Rini, M.; Nibbering, E. T. J. *Journal Of The American Chemical Society* **2004**, *126*, 3789-3794.

(65) Bixon, M.; Jortner, J. *Journal of Chemical Physics* **1968**, *48*, 715-726.

(66) Chen, P.; Meyer, T. J. *Chemical Reviews* **1998**, *98*, 1439-1477.

(67) Barbara, P. F.; Meyer, T. J.; Ratner, M. A. *Journal of Physical Chemistry* **1996**, *100*, 13148-13168.

(68) Caspar, J. V.; Kober, E. M.; Sullivan, B. P.; Meyer, T. J. *Journal of the American Chemical Society* **1982**, *104*, 630-632.

(69) Caspar, J. V.; Meyer, T. J. *Journal of the American Chemical Society* **1983**, *87*, 952-957.

(70) Murtaza, Z.; Zipp, A. P.; Worl, L. A.; Graff, D.; Jr, W. E. J.; Bates, W. D.; Meyer, T. J. *Journal of the American Chemical Society* **1991**, *113*, 5113-5114.

(71) Murtaza, Z.; Graff, D. K.; Zipp, A. P.; Worl, L. A.; Jr, W. E. J.; Bates, W. D.; Meyer, T. J. *Journal of Physical Chemistry* **1994**, *98*, 10504-10513.

(72) Liang, Y. Y.; Baba, A. I.; Kim, W. Y.; Atherton, S. J.; Schmehl, R. H. *Journal of Physical Chemistry* **1996**, *100*, 18408-18414.

(73) Kober, E. M.; Caspar, J. V.; Lumpkin, R. S.; Meyer, T. J. *Journal of Physical Chemistry* **1986**, *90*, 3722-3734.

(74) Caspar, J. V.; Meyer, T. J. *Inorganic Chemistry* **1983**, *22*, 2444-2453.

(75) Robbins, D. J.; Thomson, A. J. *Molecular Physics* **1973**, *25*, 1103-1119.

(76) DeArmond, M. K.; Hllis, J. E. *Journal of Chemical Physics* **1971**, *54*, 2247.

(77) Mitchell, W. J.; DeArmond, M. K. *Journal of Luminescence* **1971**, *4*, 137.

(78) Watts, R. J.; Crosby, G. A. *Journal of the American Chemical Society* **1972**, *94*, 2606.

(79) Gardner, P. J.; Kasha, M. *Journal of Chemical Physics* **1969**, *50*, 1543.

(80) Andrews, L. J.; Lempicki, A.; McCollum, B. C. *Chemical Physics Letters* **1980**, *74*, 404-408.

(81) Kuhn, K.; Wasgestian, F.; Kupka, H. *Journal Of Physical Chemistry* **1981**, *85*, 665-670.

(82) Endicott, J. F.; Lessard, R. B.; Lynch, D.; Perkovic, M. W.; Ryu, C. K. *Coordination Chemistry Reviews* **1990**, *97*, 65-79.

(83) Forster, L. S. *Chemical Reviews* **1990**, *90*, 331-353.

(84) Perkovic, M. W.; Heeg, M. J.; Endicott, J. F. *Inorganic Chemistry* **1991**, *30*, 3140-3147.

(85) Ramasami, T.; Endicott, J. F.; Brubaker, G. R. *Journal Of Physical Chemistry* **1983**, *87*, 5057-5059.

(86) Gutierrez, A. R.; Adamson, A. W. *The Journal of Physical Chemistry* **1978**, *82*, 902.

(87) Kirk, A. D. *The Journal of Physical Chemistry* **1981**, *85*, 3205.

(88) Kutal, C.; Adamson, A. W. *Journal of the American Chemical Society* **1971**, *93*, 5581.

(89) Pyke, S. C.; Ogasawara, M.; Kevan, L.; Endicott, J. F. *Journal Of Physical Chemistry* **1978**, *82*, 302-307.

(90) Endicott, J. F.; Tamilarasan, R.; Lessard, R. B. *Chemical Physics Letters* **1984**, *112*, 381-386.

(91) Kane-Maguire, N. A. P.; Crippen, W. S.; Miller, P. K. *Inorganic Chemistry* **1983**, *22*, 696.

(92) Kane-Maguire, N. A. P.; Wallace, K. C.; Miller, D. B. *Inorganic Chemistry* **1985**, *24*, 597.

(93) Ceulemans, A.; Bongaerts, N.; Vanquickenborne, L. G. *Inorganic Chemistry* **1987**, *26*, 1566.

(94) Ramasami, T.; Endicott, J. F.; Brubaker, G. R. *The Journal of Physical Chemistry* **1983**, *87*, 5057.

(95) Perkovic, M. W.; Endicott, J. F. *The Journal of Physical Chemistry* **1990**, *94*,1217.

(96) Lessard, R. B.; Heeg, M. J.; Buranda, T.; Perkovic, M. W.; Schwarz, C. L.; Yang, R. D.; Endicott, J. F. *Inorganic Chemistry* **1992**, *31*, 3091-3103.

Chapter 2: Ground State Electronic and Magnetic Structure of Gallium(III)-Semiquinone Complexes and Quartet Complexes of Chromium(III)

2.1 Introduction

Rational design of molecular magnetic materials requires a thorough understanding of all factors contributing to the electronic and magnetic structures of the system. To this end, Guo et. al. have reported the synthesis and spectroscopic properties of the $[M_1M_2(tren)_2(CA^{n-})]^{m+}$ series, where M is gallium(III) or chromium(III), tren = tris(2-aminoethyl)amine and CA^{n-} is the chloranilate anion, the bridging chelate between the two metal ions, which takes on a tetraanionic dicatecholate ($CA^{cat,cat}$) or trianionic semiquinone-catecholate radical ($CA^{sq,cat}$) form in this series (Figure 2-1).[1] Systematic incorporation of chromium(III), (d^3, $S = 3/2$ ground state) and/or gallium(III) (d^{10}, diamagnetic) coupled with either bridging form yielded six complexes (Figure 2-2). The initial study of these complexes characterized this series via magnetic susceptibility, cyclic voltammetry, steady-state emission, and static absorption. The magnetic susceptibility data revealed a variety of magnetic ground states, ranging from the singlet (S = 0) ground state of **1** to the sextet ($S = 5/2$) ground state of **6**. This chapter will present ground state characterization of the magnetically dilute, non-spin-exchange complexes of this series utilizing electron spin resonance techniques. These experiments use magnetic fields to break the degeneracy of

electronic states with unpaired spin. Once these states are split by the applied magnetic field, a probe is employed—either continuous-wave or pulsed microwave radiation—to characterize the interaction of the unpaired spin with the applied magnetic field. Using this general picture many different electron spin resonance techniques have been developed which allow one to characterize not only the spin of interest but also interactions with magnetic nuclei. Further additional spin resonance spectra are presented which are relevant to the high-symmetry systems explored in chapter 3. Chapter 4 will explore the properties of the spin-exchange members of this series.

This research is focused on gaining an understanding of the effects of Heisenberg spin exchange interactions on the photophysical properties of a molecule. Metal-quinone complexes are ideal for the study of physicochemical properties of exchange-coupled molecules because the redox activity of the quinone ligand effectively provides a mechanism for turning the exchange interaction on or off: in this series one is able to selectively turn on spin exchange with incorporation of the paramagnetic species chromium(III), and $CA^{sq,cat}$, or turn off exchange interactions by substituting in the diamagnetic analogs gallium(III) and $CA^{cat,cat}$. In this manner the series of molecules provides the ability to differentiate properties inherent to the constituents of the molecule from those which arise due to exchange interactions between the constituents.

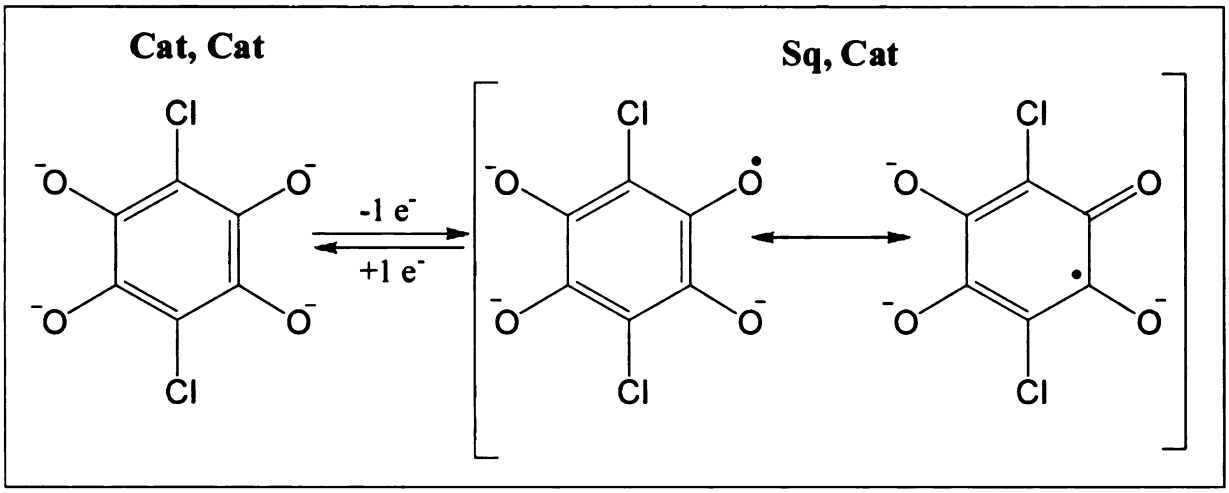

Figure 2-1: Bridging forms of chloranilic acid. $CA^{cat,cat}$ refers to the diamagnetic dicatecholate form, while $CA^{sq,cat}$ is the semiquinone-catecholate form, and is paramagnetic (S = ½). The resonance forms show that SOMO (singly-occupied molecular orbital) density should be distributed among the ketone-like C-O moieties.[2-4]

A logical starting point for the characterization of the magnetic ground states of the molecules in this series is complex **2**. This molecule is the most magnetically simple paramagnetic member of the series, consisting of two diamagnetic metal centers bridged by the semiquinone ligand radical $CA^{sq,cat}$, resulting in a total S = ½ for the system. The goal of the work presented in the first section of this chapter is the characterization of the magnetic ground state of this complex via electron paramagnetic resonance (EPR) spectroscopy.

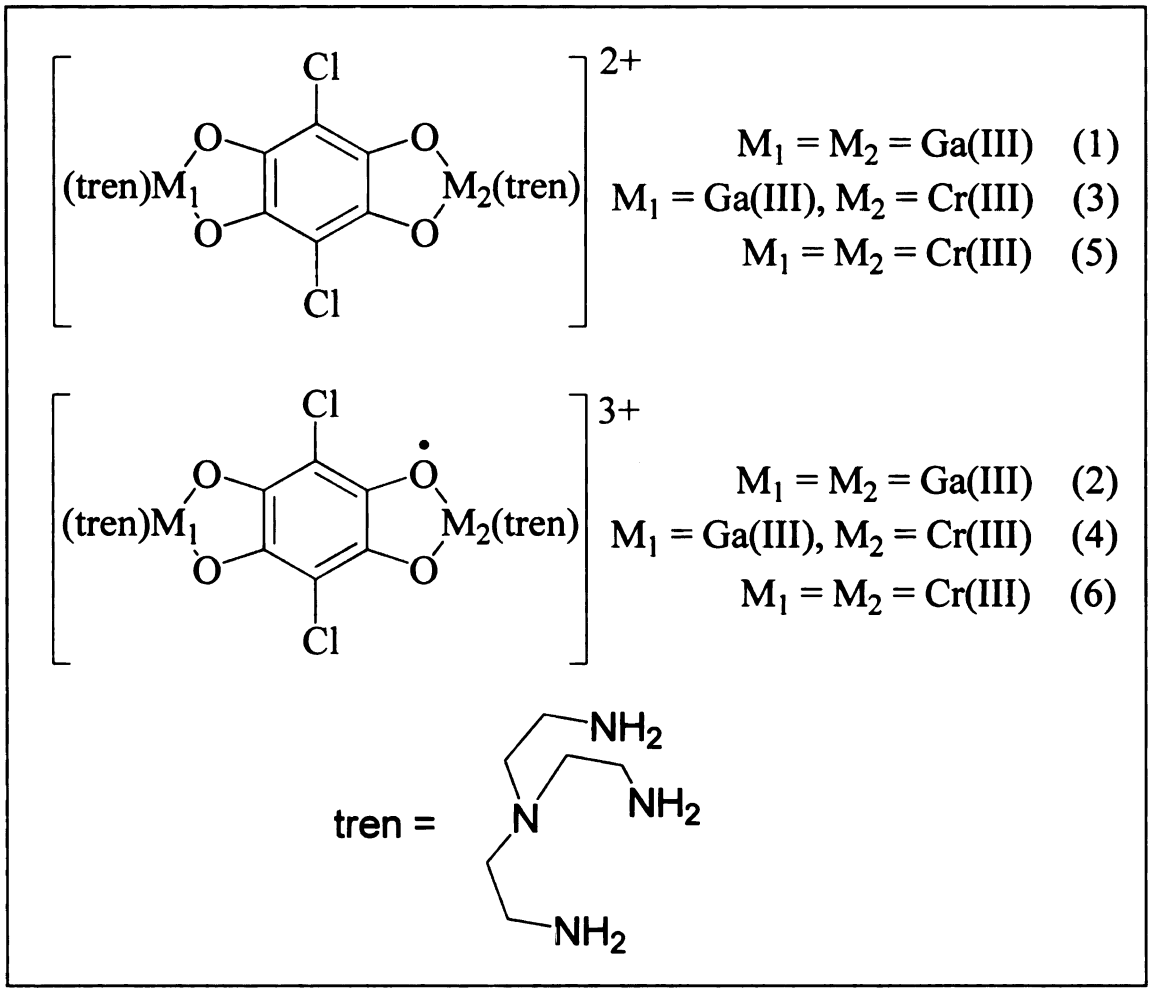

Figure 2-2: Members of the bimetallic $[M_1M_2(tren)_2(CA^{n-})]^{m+}$ series.

Additionally, the ground state of a model complex, $[Ga_2(tren)_2(DHBQ)](BPh_4)_2(BF_4)$ (where DHBQ = 2,5-dihydroxy-1,4-benzosemiquinone and BPh_4 = tetraphenylborate anion), which was employed to aid in the assignment of EPR spectral features of **2**, was also explored. Furthermore, several additional complexes of the form $[(tren)Ga(III)PSQ]^{2+}$ (where PSQ is a substituted phenanthrenesemiquinone ligand) will be discussed. These simple systems, which were also explored by our group[4] reveal various

mechanisms by which control of spin distribution can be achieved. EPR has been implemented to characterize the ground states of other metal-semiquinone complexes with diamagnetic metals, like **2**. Most significantly, gallium(III) complexes of the 3, 5-di-*tert*-butyl-1,2-benzosemiquinonate anion species have been prepared and studied via X-band EPR by the Tuck group,[5] and Wieghardt and coworkers have synthesized and studied the magnetic properties of a series of metal complexes, including gallium(III), with a phenoxy radical ligand.[6] More recently, Baker *et al.* have carried out synthetic, EPR and electron nuclear double resonance (ENDOR) studies on a series of gallium(III), indium(III), and aluminum(III) complexes of the radical anion of diazabutadiene.[7-9] In all cases hyperfine coupling from the metal nuclear spin (either ^{27}Al, $^{69, 71}Ga$ or ^{115}In) was observed, and room temperature X-band spectra of the gallium(III) complexes were simulated with different isotropic hyperfine couplings from the different Gallium isotopes. Other semiquinone species have been prepared with diamagnetic metal cations such as closed-shell alkali and alkaline earth cations.[10, 11] A common theme in all studies mentioned above is that spin is delocalized to some extent (generally much less than 1%) onto the metal center from the primarily organic based (π-based) radical. This is manifested by the weak hyperfine couplings (HFC) stemming from the interaction of the electronic spin with the nuclear spin.

Different challenges arise in systems with $S > \frac{1}{2}$. In non-doublet spin

systems zero-field splitting, i.e. loss of degeneracy of m_s spin sublevels, arises, and small changes in zero field splitting can drastically affect the appearance of an EPR spectrum. After exploring the (magnetically) simple gallium(III)-semiquinone complexes, this chapter continues on by characterizing the paramagnetic ground state of the quartet complexes of chromium(III), starting with high-symmetry $Cr(acac)_3$-type (where $Cr(acac)_3$ is tris(acetylacetonato)chromium(III)) complexes, then exploring low-symmetry complexes such as the bimetallic complex $[GaCr(tren)_2(CA^{cat,cat})](BPh_4)_2$ (**3**) (Figure 2-3). Electron paramagnetic resonance is employed to characterize the ground state. A mononuclear Cr^{III} complex, $[Cr(tren)(DTBCat)](PF_6)$ (where DTBCat = 3,5-di-*tert*-butylorthocatechol), was employed to aid in the characterization of **3**.

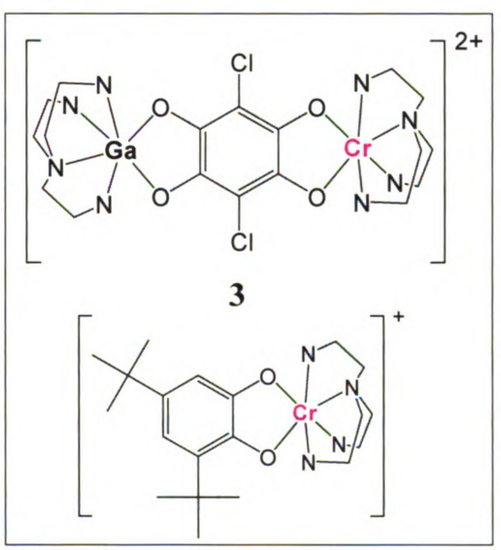

Figure 2-3: The complex $[GaCr(tren)_2(CA^{cat,cat})](BPh_4)_2$ (**3**) and its model complex $[Cr(tren)(DTBCat)](PF_6)$.

EPR has been implemented to characterize mononuclear chromium(III) complexes in a variety of ligand environments, including bis-bipyridine and bis-phenanthroline complexes,[12, 13] corroles,[14] and Cr^{III}-alkyl species.[15] $Cr(acac)_3$ doped in $Al(acac)_3$ has been probed by EPR at 110 K,[16] which revealed slightly different zero field splitting values, all around 1.2 cm^{-1}, for the three different crystal sites. These values were recently confirmed using luminescence and excitation line narrowing spectroscopy.[17] Wang and Pillbrow[18] have carried out an extensive study of the symmetry relationships between the different eigenstates within the quartet manifold, and Mabbs has presented a similar study.[19]

To lead to a greater understanding of the ground state electronic structure of quartet systems and the origin of perpendicular-mode transitions within quartet systems, the effect of the axial (D) and rhombic (E) zero field splitting parameters on the energy profile of the ground state, and thus the appearance of the low temperature EPR spectrum, is explored in the final sections of this chapter. Furthermore, a more extensive and systematic study of the effect of zero field splitting on the appearance of the EPR spectra of powder axial and rhombic quartet systems at low temperatures (4 K) was carried out.

Beyond the realm of simple metal-centered paramagnetic systems, we also expand on previous reports and our results by providing simulated spectra and energy level diagrams with different D and E/D values relevant to other quartet spin systems, such as quartet ground state organic compounds such as 2,3,5,6-

tetrafluorophenylnitren-4-yl[20, 21] and high spin clusters of C_{60}.[22] This report would also serve to aid in the characterization of exchange coupled metal compounds with isolated quartet ground states ($|J| >> kT$), such as trinuclear copper(II) complexes,[23] and metal-semiquinone complexes.[24] It is the hope of the author that this subsection can serve as a general tool to aid in simple and quick characterization of quartet magnetic systems via X-band EPR spectroscopy.

2.2 Experimental Section

2.2.1 Synthetic Methods. All reagents and materials were used as received unless otherwise noted. Solvents were purchased from Aldrich Chemical Co. and distilled and degassed by the freeze-pump-thaw method. The ligand tris(2-aminoethyl)amine (tren) was purchased from Aldrich and vacuum-distilled prior to use. All synthetic procedures involving hydrochloranilic acid and 1, 2, 4, 5-tetrahydroxybenzene were performed under an inert atmosphere. $[FeCp^*_2](BF_4)$ was prepared according to literature methods.[25] Hydrochloranilic acid and 1, 2, 4, 5-tetrahydroxybenzene was synthesized by a modification of a previously reported method.[26, 27] $Ga(tren)(NO_3)_3$ was prepared according to our previous paper.[28]

$[Ga_2(tren)_2(CA^{sq,cat})](BPh_4)_2(BF_4)$ (2). Complex **2** was achieved by Dr. Dong Guo, and synthesized according to previously published procedures.[28, 29]

$[Ga_2(tren)_2(DHBQ)](BPh_4)_2$. Preparation of this complex was carried out by Dr. Dong Guo. Under N_2, 1, 2, 4, 5-tetrahydroxybenzene (1.00 mmol, 0.142 g) and triethylamine (4.00 mmol, 0.404 g) were dissolved in 100 mL of degassed methanol. This solution was added dropwise into a solution of $Ga(tren)(NO_3)_3$ (1.80 mmol, 0.724 g) in 80 mL of methanol. Following filtration of a green precipitate, excess sodium tetraphenylborate (4.00 mmol, 1.37 g) in 20 mL methanol solution was added to the filtrate. After standing overnight, white microcrystals were obtained. Yield: 0.53 g (45%).

$[Ga_2(tren)_2(DHBQ)](BPh_4)_2(BF_4)$. Preparation of this complex was carried out by Dr. Dong Guo. Under N_2, $[Ga_2(tren)_2(DHBQ)](BPh_4)_2$ (0.141 mmol, 0.171 g) and $[FeCp^*_2](BF_4)$ (0.15 mmol, 0.062 g) were dissolved in 2 mL of acetonitrile and stirred for 30 min, resulting in a green solution. After filtration, 5 mL of dichloromethane and 5 mL of ether was added to the filtrate yielding a yellow solid. The product was filtered and washed with ether (3 X 20 mL) and dichloromethane (3 X 20 mL) and dried. Yield: 0.100 g (59%). Anal. Calcd $Ga_2B_3F_4N_8C_{66}H_{78}O_4$: C, 61.2; H, 6.1; N: 8.7. Found: C, 61.4; H, 6.0; N, 9.0.

Synthesis of Chromium complexes. Complex **3** and the model complex $[Cr(tren)(DTBCat)](PF_6)$ were synthesized according to previously published procedures.[28, 29]

2.2.2 Physical Measurements on Gallium-Semiquinone Complexes. Unless otherwise noted, X-band EPR samples were prepared in a dry, inert atmosphere (N_2) by dilution in a mixture of butyronitrile and propionitrile (9:2), both of which had been distilled from CaH_2, degassed, and stored under an inert atmosphere. The resulting sample concentrations were approximately of millimolar concentration. The sample holder was a typical quartz tube of an appropriate inner diameter (~0.6 mm) for X-band experiments. Low temperature continuous-wave (cw) X-band EPR spectra were obtained with a Bruker ESP300E spectrometer using two different resonant cavities: a perpendicular-mode cavity (Bruker ST4102/8943) with resonances around 9.46 GHz and a duel-mode cavity (Bruker DM1466) with perpendicular-mode resonances at 9.6 GHz and parallel-mode resonances around 9.4 GHz. For each compound an appropriate power was chosen to avoid saturation of the signal. An Oxford ESR A900 helium cryostat was employed to maintain the temperature at 4 K. X-Band spectra were also acquired at room temperature for several complexes. Samples were prepared as described above, but acquisition was carried out using a flat cell and a room temperature cavity (Bruker 4103TM).

Electron nuclear double resonance (ENDOR) of the model complex of **2** was carried out at 10 K using a typical Davies-type ENDOR pulse sequence.[30] Radio frequencies were scanned from 2 – 28 MHz and samples were prepared as described above. W-band measurements of **2** were carried out at 4 K on a Bruker

e680 W-band instrument with a typical two-pulse sequence of a $\pi/2$ pulse (68 ns) followed by a π pulse (136 ns). The frequency was 94.158 GHz and a pseudo-modulation of 10 KHz was applied to the signal prior to simulation to obtain the characteristic first derivative shape.

2.2.3 Physical Measurements of Chromium complexes. X-band samples were prepared in a dry, inert atmosphere (N_2) by dilution in a mixture of butyronitrile and propionitrile (9:2), both of which had been distilled from CaH_2, degassed, and stored under an inert atmosphere. The resulting sample concentration was approximately millimolar. Continuous-wave X-band EPR spectra were obtained with a Bruker ESP300E spectrometer using a perpendicular-mode cavity (Bruker 4102ST/9516) with resonances around 9.458 GHz. For each compound an appropriate power was chosen to avoid saturation of the signal. An Oxford ESR A900 helium cryostat was employed to maintain the temperature at 4 K.

2.2.4 Calculations: Gallium-Semiquinone Complexes. All simulations of X-band perpendicular mode EPR spectra of were performed using Bruker XSophe [31-33] in order to obtain spin Hamiltonian parameters. Resonant magnetic fields were calculated assuming that $\tilde{g}$ and $\tilde{A}$ have coincident principal axes,[34, 35] which is true for spin centers of D_{2h} symmetry. Once a reasonable fit for the EPR spectrum was obtained, the parameters from the EPR simulations were applied to calculate energy-level diagrams using programs of local origin.

In order to simulate the room temperature data, which prominently displays ^{69,71}Ga hyperfine coupling, both isotopes must be taken into account. The natural abundances for the two isotopes are 60.2% for ^{69}Ga and 39.8% for ^{71}Ga. An accurate simulation of the spectrum must take into account the three possible combinations of isotopes, which are ^{69}Ga-^{69}Ga (with a probability of 36.24%), ^{71}Ga-^{71}Ga (15.84 %), and ^{69}Ga-^{71}Ga (47.90%), and weigh the spectrum of each combination by its probability prior to summing them. XSophe is capable of doing this, and presents a weighted average of the HFC values to the user. In order to extract the different HFC values for each isotope, one simply has to work backward from the weighted average. The isotropic HFC is proportional to the nuclear g-value (g_n) and the spin density at the nucleus (ρ):

$$A_{iso} \propto g_n \rho \tag{2.1}$$

For complex **2**, the symmetry of the molecule dictates that the same amount of spin will be delocalized onto both Ga nuclei, whether it happens to be ^{69}Ga or ^{71}Ga. Because of this we can write:

$$\frac{A(^{69}Ga)}{A(^{71}Ga)} = \frac{g_n(^{69}Ga)}{g_n(^{71}Ga)} = \frac{1.344393}{1.708180} = 0.787 \tag{2.2}$$

The weighted average is:

$$\bar{A} = A(^{69}Ga)\, w(^{69}Ga) + A(^{71}Ga)\, w(^{71}Ga) \tag{2.3}$$

where $\overline{A}$ is the average, and $w(^{69}Ga)$ and $w(^{71}Ga)$ are the weights (natural abundances) of ^{69}Ga and ^{71}Ga. Using equations 2.2 and 2.3 one can work backward and determine the HFC for each isotope, assuming that the same amount of spin is delocalized onto both metal centers.

Time-independent calculations of the electronic structures of complex **2**, the model complex $[Ga_2(tren)_2(DHBQ)](BPh_4)_2(BF_4)$, and the two free bridging ligands in the trianionic semiquinone form were carried out using density functional theory as implemented in Gaussian 98[36] using the UB3LYP/6-311G** level of theory. The initial geometry of the molecule was generated using GaussView[37] and optimized using the UB3LYP functional and a 6-311G** basis set with imposed symmetries of C_{2v} and D_{2h}. Single-point calculations were carried out using the unrestricted UB3LYP functional and a 6-311G** basis, assuming a doublet ground state and a molecular charge of 3+ for the Ga^{III} dimers and 3- for the free ligands.

2.2.5 Calculations: Chromium Complexes. The X-band perpendicular mode EPR spectra were simulated using Bruker XSophe [31-33] in order to obtain spin Hamiltonian parameters. A partition number greater than 100 was used for all simulations to reduce the "noise" associated with the numerical integration. For XSophe, it should be noted that although a segment number of 2 is suitable for doublet systems,[32] more complex systems ($S > {}^1/_2$) require a segment number of 4

or 8. Once a reasonable fit for the EPR spectrum was obtained, the parameters from the EPR simulations were applied to calculate energy-level diagrams and the angular dependence of EPR transitions for the compounds using either XSophe or homemade programs.

The effect of zero-field splitting on the appearance of the X-Band EPR spectra of a mononuclear Chromium(III) complex was explored. Simulations were carried out in Bruker XSophe, with line widths equal to those determined from the simulation of the experimental data. For the general study of the effects of zero field splitting, the linewidths were arbitrarily set at 10 G. Transition roadmaps, which illustrate how the field position of transitions changes as the spin system is rotated with respect to the applied magnetic field, were also calculated using XSophe. Calculations of energy level diagrams and transition diagrams were carried out in Mathematica (*vide infra*).[38] Transition diagrams, which map out the field of transition as a function of the zero field splitting parameters, were calculated by taking the difference between two eigenvalues of a given orientation as the energy of transition (about 0.3 cm^{-1} at X-Band frequency and 3.3 cm^{-1} at W-Band frequency) and solving for D or E. At X-band frequency solutions were discarded which did not have transition probably within the window $|D| < 1$ cm^{-1} and $0 < B < 10000$ G (1 T) for the axial system and $0 < E/D < 1/3$ and $0 < B <$ 10000 G for the rhombic case.

2.3 Results and Discussion. Gallium(III)-Semiquinone Complexes.

2.3.1 $[Ga_2(tren)_2(CA^{sq,cat})](BPh_4)_2(BF_4)$ (2). The X-band EPR spectrum of $[Ga_2(tren)_2(CA^{sq,cat})](BPh_4)_2(BF_4)$ (**2**) at 4 K is shown in Figure 2-4(A). The spectrum shows a main peak around g' = 2 (where $g' = h\upsilon/\beta B$) with multiple lines due to hyperfine splitting. The rhombic nature of the g-tensor and hyperfine tensor are clearly apparent from the dissymmetry of this main peak. All of the complexes reported herein have either D_{2h} or C_{2v} local symmetry at the magnetic centers, and therefore possess "rhombic" EPR symmetry,[19] meaning that, in general the principal axes (the diagonal components of the g-tensor) are nonequivalent, i.e. $g_{xx} \neq g_{yy} \neq g_{zz}$ as a result of different magnetic field projections along the principal axes. Two sidebands of much lower intensity are also observed, and no half-field transition ($\Delta m_s = 2$) is observed, as seen for other Ga^{III}-semiquinone complexes, as will be discussed later.[5, 10]

This molecule is the most magnetically simple of the series, consisting of two diamagnetic metal centers bridged by a semiquinone ligand radical, resulting in a total S = ½ for the system. Magnetic susceptibility data for this complex from 2 - 350 K, which reveal a temperature-independent magnetic moment of $\mu_{eff} = 1.64 \pm 0.04\ \mu_B$, ($\mu_{spin\text{-}only}$ for S = ½ is 1.73 μ_B) confirm this formulation. From the magnetic susceptibility data and previous investigations of the isolated $CA^{sq,cat}$ bridge,[39] one would expect the EPR spectrum to exhibit a simple doublet

spectrum, with possible HFC contributions from the bridging atoms (^{13}C, $^{35,37}Cl$) and the gallium ($^{69,71}Ga$) nuclei.

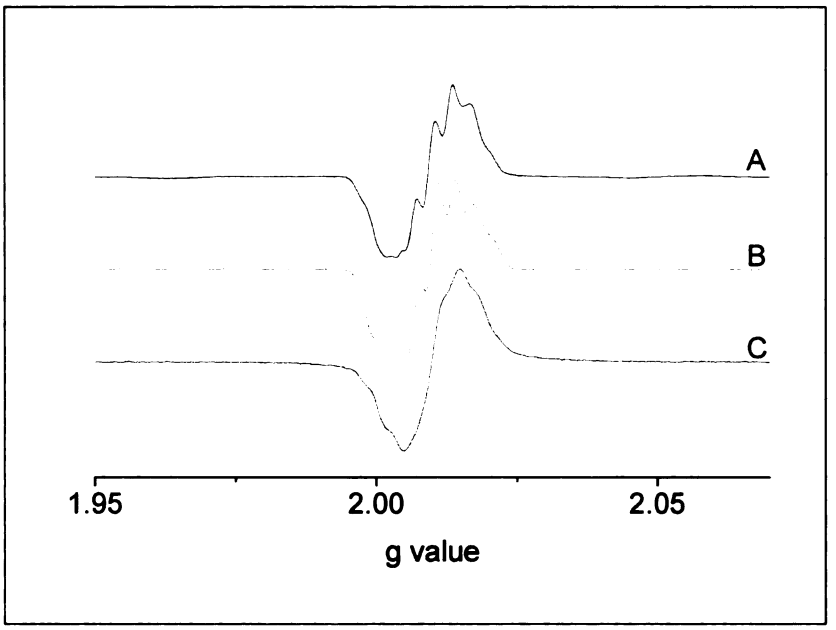

Figure 2-4: (A) Experimental X-band spectrum of complex 2 acquired in a butyronitrile/propionitrile (9:2) glass at 4 K (0.63 μW, 9.458 GHz). This spectrum was simulated (B) using the following parameters: g_{xx} = 2.0100, g_{yy} = 2.0097, g_{zz} = 2.0060, a_{xx}(Ga) = 4.902 G, a_{yy}(Ga) = 4.124 G, a_{zz}(Ga) = 3.167 G. (C) is the experimental X-band spectrum of $[Ga_2(tren)_2(DHSQ)](BPh_4)_2(BF_4)$, acquired at 4.4 K, 63 nW, 9.624 GHz.

A DFT calculation of the SOMO (Singly Occupied Molecular Orbital) of complex **2** (α-SOMO, Figure 2-5a) and the corresponding spin density distribution

(2.5b) is useful in the interpretation of this spectrum. The β-SOMO is at a much greater energy than the α-SOMO (molecular orbital 1068 for the β-SOMO versus 163 for the α-SOMO), so that the spin density can be described entirely in terms of the α-SOMO. Figure 2-5 reveals that although the SOMO density is greatest at the four equivalent carbon atoms and four equivalent oxygen atoms, with a node along the central C_2 axis that runs through the two chlorine atoms, the spin density is present at every position on the CA bridge as a result of spin polarization: the α-spin populated SOMO orbitals induce β-spin at adjacent positions as a result of the spin-polarization mechanism.[40, 41] The bridging ligand has B_{1g} symmetry in D_{2h}, which can not support degeneracy, so that a rhombic g-tensor and hyperfine tensor are expected. In terms of hyperfine coupling (HFC), which gauges the interaction between the unpaired electron spin and nuclear spins, weak and perhaps unobservable peaks are expected from the four equivalent carbon atoms because ^{13}C (I = ½) only has a natural abundance of 1.1%. For the four equivalent oxygen atoms which display SOMO density in Figure 2-5, there is no expected observable contribution to the hyperfine splitting because ^{17}O ($I = 5/2$) has a natural abundance of only 0.037%. For S = ½ systems, isotropic hyperfine splitting results in $(2n_jI_j+1)$ peaks for n_j nuclei of spin I_j, so that, if indeed the peaks are observable, five peaks are expected for the four equivalent central carbon atoms (with a positive HFC because α-spin resides about these atoms) and three peaks for the other two carbon atoms (with a negative HFC as a result of β-spin). Hyperfine

interactions with Gallium (^{69}Ga and ^{71}Ga, both of which have $I = 3/2$ and account for 100% natural abundance) or Chlorine nuclei (^{35}Cl and ^{37}Cl, with $I = 3/2$ account for 100% natural abundance) are potentially important. Previous investigations of Ga-semiquinones, as noted in the introduction to this report, corroborate the assignment of HFC as due to Gallium nuclei.

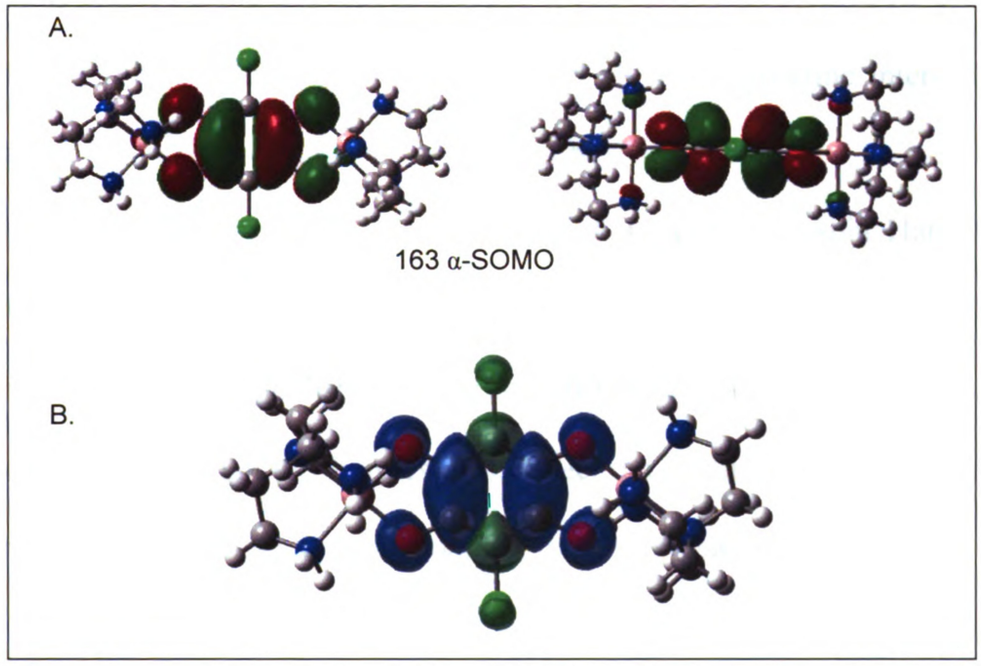

Figure 2-5: Calculated SOMO (a.) and spin density (b.) of complex 2 at the UB3LYP/6-311G** level.

The sidebands are of the correct number—assuming splitting from four equivalent ^{13}C nuclei, as the SOMO calculation suggests—and intensity to result from ^{13}C splitting. While this explanation is justified by the position of the calculated SOMO density, a previous EPR investigation of the $CA^{sq,cat}$ bridge,[39]

in addition to our own investigation (*vide infra*) revealed HFC values that are much to small to account for the sidebands, separated from the main peak by approximately 70 G. Furthermore, this description does not take into account the carbon atoms adjacent to the chlorine atoms, which have an excess of β-spin. The isolated chloranilic trianion species in alkaline solution (6 N NaOH) has been previously studied using EPR spectroscopy.[39] The spectrum revealed HFC of 2.71 and -8.17 gauss, resulting in 4 sidebands, and chlorine hyperfine interaction of 0.18 gauss. The origin of these sidebands will be discussed later.

Given the DFT picture, consideration of the dominant spin Hamiltonian parameters, natural abundances of magnetic nuclei, the splitting rules for a S = ½ system, and previously published hyperfine constants for similar compounds,[42] we can now begin to assign the features of the spectrum of this compound. The EPR spectrum of the main peak, corresponding to **2,** was calculated according to the spin Hamiltonian

$$\hat{H} = \beta_e \vec{B} \cdot \tilde{g} \cdot \vec{S} + \vec{I} \cdot \tilde{A} \cdot \vec{S} \qquad (2.4)$$

The first term on the right side is the Zeeman splitting of the spin states upon application of a magnetic field **B**, where $\tilde{g}$ is the g-tensor. In general, if the g-value corresponds to that of an organic-based radical, a small deviation from the free-electron g-value (g_e = 2.0023), on the order of 10^{-3}, is expected.[43] The second term on the right side is the hyperfine coupling term, with $\tilde{A}$ being the hyperfine tensor, which gauges the magnitude of the interaction between the

nuclear and electronic spins. $\vec{I}$ is a vector describing the nuclear spin, and $\vec{S}$ is the electronic spin vector. The nuclear Zeeman term ($\beta_e \vec{B} \cdot \tilde{g}_n \cdot \vec{I}$) is excluded as an approximation, because the interaction is only about 1/2000 of the electronic Zeeman interaction, as a result of the smaller magnetic moment of nuclei as compared to that of the electron.

The simulation, Figure 2-4(B), confirms the expected spin Hamiltonian parameters. The g-tensors and hyperfine tensors are rhombic. The spectrum was simulated assuming that hyperfine splitting from ^{69,71}Ga nuclei are responsible for the splitting pattern observed on the central-field feature, although we were unable to fit this peak with different HFC values for both Ga isotopes because of the lack of structure on the peak, due to the expression of the anisotropy in the HFC tensor in frozen solutions. Although this simulation may not provide accurate numbers for the diagonal components of the HFC tensor for both ^{69}Ga and ^{71}Ga it does allow us to put limits on the anisotropy present in the g-tensor. The value of Δg ($= g_{xx} - g_{zz}$) of 0.004 is a reasonable value for a organic-based radical, and any larger value of Δg would likely result in a much broader spectrum than that of Figure 2-4(A). The room temperature EPR spectrum of **2**, presented in Figure 2-6, shows a dynamically averaged (isotropic) HFC as a result of tumbling in solution, and the isotropic HFC for both gallium isotopes can be extracted. This spectrum was simulated with the isotropic HFCs A(^{69}Ga) = 3.136 G, A(^{71}Ga) = 3.980 G.

As mentioned previously, the splitting of the main peak to produce seven peaks is likely the result of HFC to the gallium nuclei or the chlorine nuclei, both of which have I = $^3/_2$. To aid in the assignment of these peaks as due to gallium or chlorine HFC, the compound $[Ga_2(tren)_2(DHBQ)](BPh_4)_2(BF_4)$ was synthesized. This compound is a useful control because it has no chlorine atoms, so a pattern of hyperfine splitting for this complex similar to that of compound **2** would indicate splitting due to interaction of the unpaired electron with the gallium nuclei. The X-band spectrum of $[Ga_2(tren)_2(DHBQ)](BPh_4)_2(BF_4)$ is presented in Figure 2-4(C). The spectrum, when acquired at low microwave powers, reveals hyperfine splitting at the main peak, which manifests itself only as slight shoulders on this peak. To confirm that broadening of the spectrum relative to that of **2** and apparent lack of sidebands was not the result of concentration effects due intermolecular spin exchange, further spectra were collected at a lower sample concentration, yielding the same results. Although the spectrum at 4 K leaves some doubt as to the nature of the HFC in this complex, the room temperature isotropic spectrum, Figure 2-6, clearly confirms the origin of the splitting on the main peak as due to HFC with Gallium nuclei, and was simulated with A(^{69}Ga) = 3.337 G, A(^{71}Ga) = 4.240 G.

For both complexes at 4 K we were unable to fit the spectra with different ^{69}Ga and ^{71}Ga HFC values because of the anisotropy inherent to powder spectra, which can often result in one broadened line, as is observed for the model complex

at high microwave powers. As aforementioned, when the power is low some fine structure, which reveals itself as shoulders on the main peak, can be resolved. ^{69,71}Ga HFC values of about 4 G fit this peak relatively well, revealing that about 0.08% of the spin is delocalized onto the Ga centers (a_0 = 4356 G for ^{69}Ga and 5535 G for ^{71}Ga), and that > 99% of the spin density is ligand centered. This is similar to other Ga^{III}-semiquinone complexes, where in general less than 0.1 % of the total spin density is delocalized onto the metal.[9] Proton HFC is also likely buried under this peak. The X-band EPR spectrum of the trianionic semiquinone species DHBQ, acquired at 298 K, has been studied previously, both times in basic aqueous solution, revealing isotropic hyperfine couplings of A_H = 0.79 G, $A_{C(1)}$ = 2.82 G and $A_{C(2)}$ = 6.62 G (where $A_{C(1)}$ corresponds to the hyperfine coupling of the ^{13}C nuclei adjacent to the oxygen atoms, and $A_{C(2)}$ corresponds to the hyperfine coupling of the ^{13}C nuclei adjacent to the hydrogen atoms).[44] A later report by Das and Fraenkel confirms and refines these values, and the authors apply the appropriate sign to the hyperfine constant depending on the assumed spin density.[45] We also carried out this experiment, and in this case only the isotropic ^{1}H HFC, which will be useful for assigning the features of the ENDOR spectrum of the model complex, were fit with g = 2.00923, a_H = 0.801 G, again indicating the expected organic radical nature of the species. This topic will be further explored when the ENDOR spectra are examined.

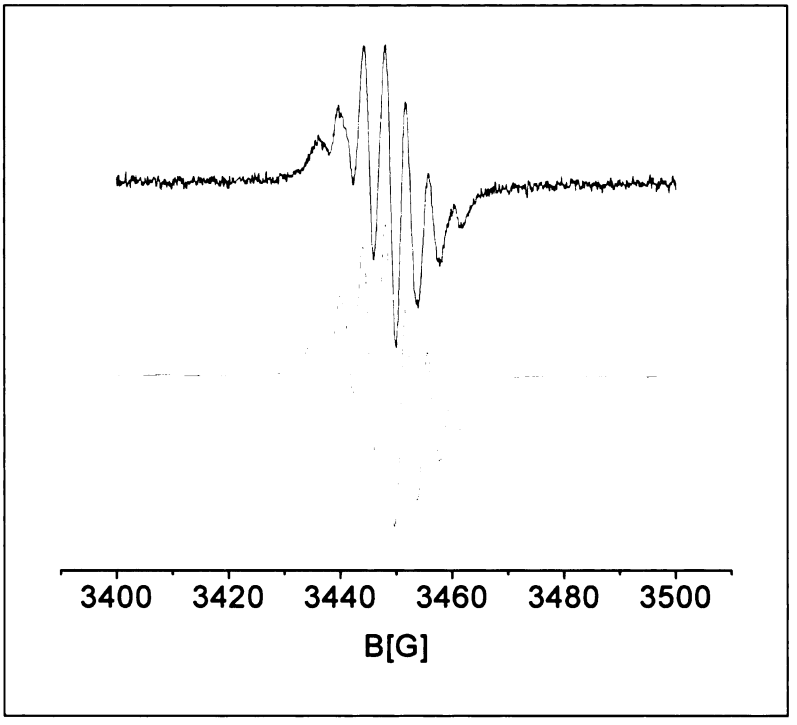

Figure 2-6: Room temperature X-band spectrum of **2** (black), acquired at 9.696 GHz. The spectrum was simulated (red) with g = 2.00858, $\overline{A}$ = 3.474 G ($A(^{69}Ga)$ = 3.136 G and $A(^{71}Ga)$ = 3.980 G).

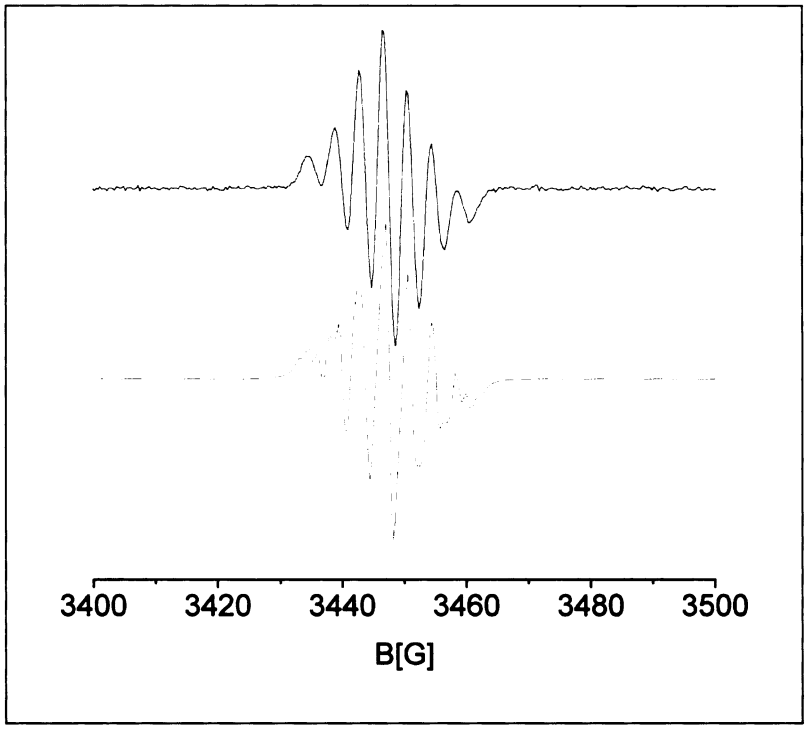

Figure 2-7: Room temperature X-band spectrum of the model complex (black), acquired at 9.695 GHz. The spectrum was simulated (red) with g = 2.00906, $\overline{A}$ = 3.697 G (A(^{69}Ga) = 3.337 G and A(^{71}Ga) = 4.240 G).

2.3.2 Observation of a Triplet State. It was mentioned previously that the sidebands are of the correct number to correspond to HFC of four equivalent ^{13}C nuclei, which are present in the bridging CA^{sq,cat} unit of **2**. This idea was discarded, however, because the observed HFC to ^{13}C nuclei in a previous report of the CA^{sq,cat} ligand revealed HFC values much too small to account for the observed splitting in the low-temperature X-band spectrum of **2**. A more likely possibility, given the ^{13}C HFC revealed by the isolated semiquinones are much

smaller than the splitting observed for **2** (2.4 and 8.2 G vs. ~140 G), is that another electronic state is contributing to this spectrum. This has been observed before in other metal-semiquinone complexes, including Ga^{III}, In^{III} and Tl^{III} complexes of the 3, 5-di-*tert*-butyl-1,2-benzosemiquinonate anion,[5] Mg^{II}, Zn^{II}, Cd^{II} and Ba^{II} complexes of the same anion,[10] and others,[46] where the side bands are different resonances within a triplet state, due to the formation of a biradical (S = 1) complex. An unequivocal test for the presence of a triplet electronic state would be the presence of a half-field ($\Delta m_s = 2$) resonance, although we were unable to observe this resonance in either our cw-EPR experiments at 4 K or room temperature.

Although the furthest sidebands can not be observed in the spectrum presented in Figure 2.4, increasing the power reveals that these side bands are present (Figure 2-8). The sidebands were simulated assuming a triplet (S = 1) state, using the following spin Hamiltonian:

$$\hat{H} = \beta_e \vec{B} \cdot g \cdot \vec{S} + \vec{S} \cdot D \cdot \vec{S} \qquad (2.5)$$

with definitions for the first term as described previously. The right-hand term accounts for zero-field splitting effects, where **D** is a matrix describing the zero-field splitting in three dimensions and **S** is a spin vector. The triplet state was simulated with g = 2.009 and D = 150 G (422 MHz or 0.012 cm^{-1}), and the simulation parameters were applied to calculate energy level diagrams for this state for the orientations of the magnetic field perpendicular and parallel to the z

axis (Figure 2-9, utilizing the secular determinant shown in Appendix B). Resonances are shown at X-band frequency (~ 0.3 cm^{-1}).

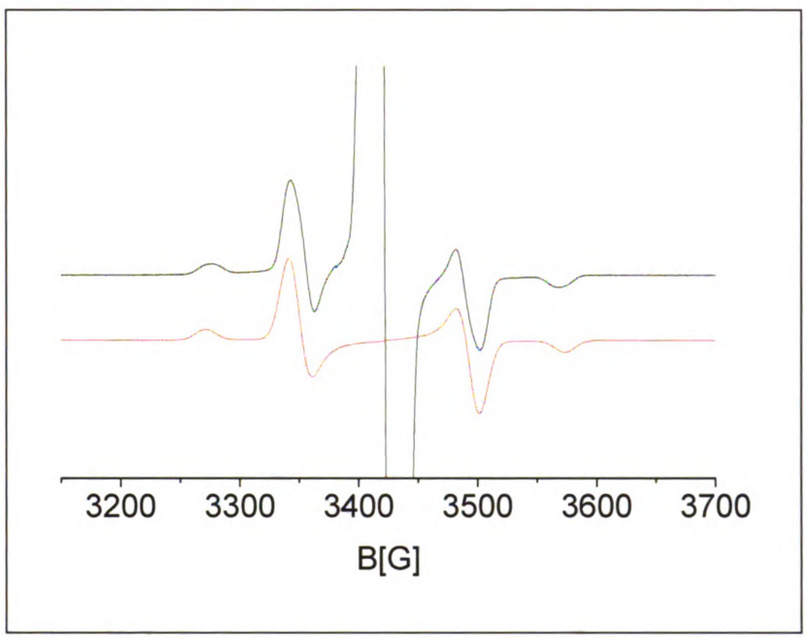

Figure 2-8: EPR resonances produced by the triplet state of a biradical complex. The spectrum of 2 (black) was acquired at 4 K (9.624 GHz, 0.63 mW), and simulation of the sidebands (red) was carried out assuming a triplet state, and with the spin Hamiltonian parameters g = 2.009 and D = 150 G.

The intensity of the bands can be understood by the population distribution of different orientations of the molecules with respect to the direction of the magnetic field. In general, there are many more orientations with the molecular z-axis perpendicular to the direction of the magnetic field, while there is only one orientation that is perfectly parallel to the field. The greater population of a given orientation results in a greater signal. The energy level diagrams reveal that

molecules with an orientation where z is perpendicular to the magnetic field direction have resonances closer to g' = 2 than those with parallel orientation, resulting in the observed pattern of sidebands.

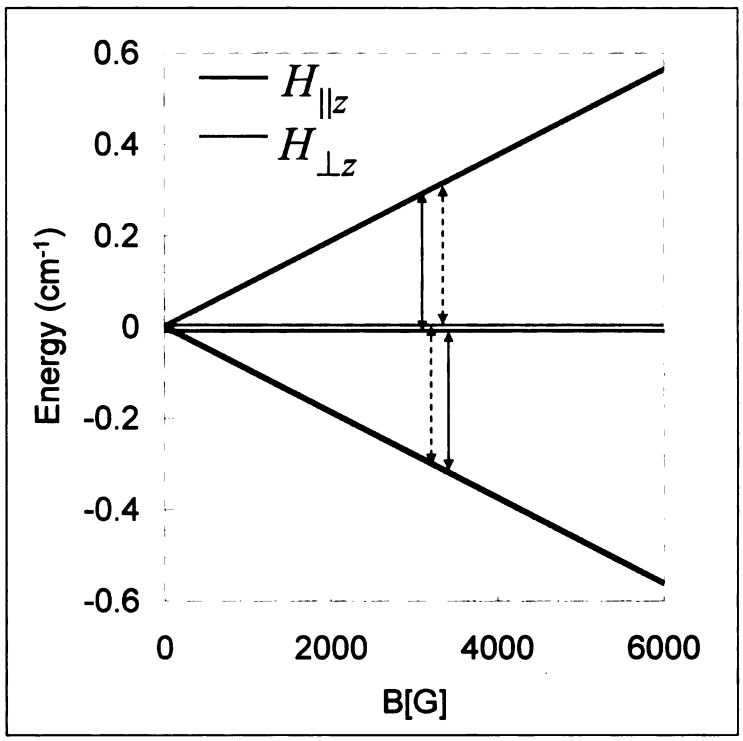

Figure 2-9: Energy level diagram of the Zeeman splitting of the triplet state formed by ferromagnetic exchange between two molecules of **2**. The diagrams were produced from the simulation parameters g = 2.009 and D = 150 G, and resonances are shown at X-band frequency (~ 0.3 cm^{-1}).

As further confirmation of the spin Hamiltonian parameters, a W-band (~ 95 GHz) spectrum of **2** was acquired, and is presented in Figure 2-10(A). In these spectra g-values may not be accurate, as the magnetic field could be incorrect by

as much as 50 G, due mainly to the large magnetic fields required to achieve resonance at W-Band frequency. The main peak, which is lacking HFC from gallium nuclei, again reveals the rhombic nature of the ground state of **2**, with g = (2.0077, 2.0062, 2.0053). The simulation is shown in Figure 2-10(C). The W-band spectra confirm that the sidebands are indeed the result of a biradical (S = 1) complex, as the intensities are much too great to fit the sidebands with ^{13}C HFC, given the natural abundance of this isotope. These sidebands were simulated with g = 2.006 and D = 150 G, indicating the detection of the same triplet state.

To investigate whether the observed triplet electronic state is the result of intramolecular or intermolecular Heisenberg spin exchange coupling between two unpaired electrons a sample was prepared and saturated with tetrabutylammonium tetraphenylborate. If intermolecular exchange is the mechanism, the salt should act to inhibit any aggregation of the molecules, and thus eliminate the observed triplet signal, or at least decrease the intensity of the signal. This was in fact observed (Figure 2-11). This result is as expected, given that cyclic voltammetry presented in the previous report revealed a quasi-reversibility in the sq,cat/sq,sq couple, suggesting degradation upon oxidation of $CA^{sq,cat}$ to the dianionic $CA^{sq,sq}$ form. The inability of this form to chelate is also evidenced by the many unsuccessful syntheses of bimetallic complexes employing the $CA^{sq,sq}$ species as the bridging ligand. Furthermore, stabilization of a biradical within the fully aromatic $CA^{cat,cat}$ form seems unlikely as well. This result allows us to

conclusively ascribe the origin of this state as due to intermolecular exchange coupling.

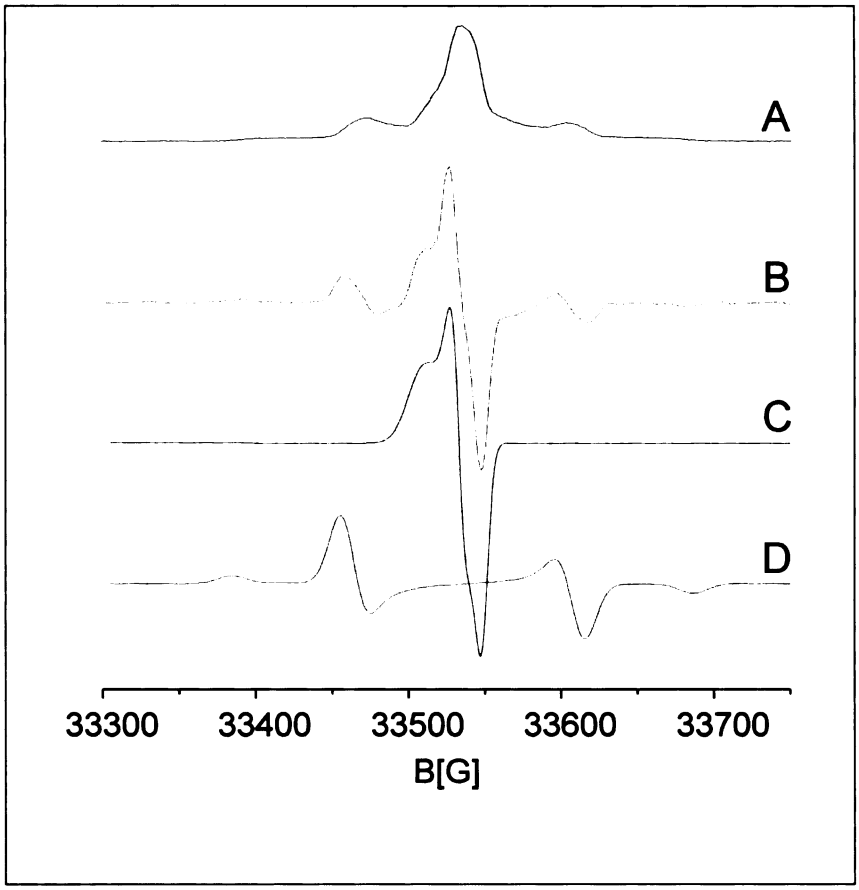

Figure 2-10: (A) W-band data of 2 acquired at 94.158 GHz, 5 nW, 10 K. The first derivative was taken by applying a pseudo-modulation of 10 kHz (B). The main peak belongs to the monoradical 2, and was simulated with an anisotropic g tensor (2.0077, 2.0062, 2.0053) with widths (11, 5, 4) G (C). The sidebands were simulated assuming a triplet electronic state formed by interaction of two monoradical species (D). Simulated with g = 2.006 and D = 150 G.

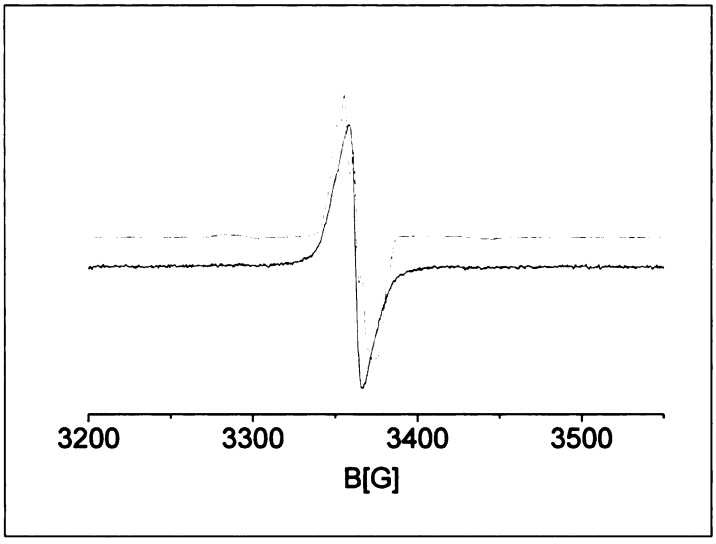

Figure 2-11: Comparison of the experimental X-band spectrum of complex 2 (red) acquired in a butyronitrile/propionitrile (9:2) glass at 4 K (0.63 μW, 9.458 GHz) with another sample saturated with tetrabutylammonium tetraphenylborate salt (black), collected under the same conditions. The diminished intensity of the sidebands for the spectrum of solution containing the TBA salt reveals that these peaks are likely due to an electronic state formed by aggregation of complex **2** in solution.

2.3.3 ENDOR of the Model Complex. To confirm the values of the hyperfine constants for both **2** and its model complex, ENDOR was carried out. ENDOR of **2** yielded no peaks but ENDOR of the model complex at 10 K (Figure 2-12) revealed a series of peaks centered around 14 MHz and a broad featureless peak near 8 MHz. ENDOR is implemented to provide information on the weaker interactions between the unpaired electron and the remote magnetic nuclei which

EPR cannot at times provide. This is especially true of unpaired electrons in π-based organic systems, where hyperfine interactions can be unresolved due to small anisotropy in the g- and A-tensors and delocalization over many nuclei.[9] ENDOR also offers a significant enhancement in resolution as compared to standard cw-EPR techniques. ENDOR has been employed successfully to elucidate the HFC of ^{1}H on the peripheral *tert*-Butyl and aryl groups of several Ga^{III} radical complexes, including $[(Bu^{t}\text{-DAB})Ga\{E(SiMe_3)_2\}I]$ (E = N, P, As and DAB is the radical anion of diazabutadiene),[7] $[(R\text{-DAB})MX_2]$ (R = Aryl or t-Butyl, M = Al^{III}, Ga^{III} or In^{III} and X = I or Br).[9] In all cases the HFC from the peripheral *tert*-butyl and aryl groups in the RT isotropic fluid spectra were not observable, but cw-ENDOR revealed the HFC from the protons on these moieties. For the case of $[(Ar\text{-DAB})GaI_2]$ the EPR signal was too broad to resolve any HFC, but cw-ENDOR at X-band frequency and 10 K revealed HFC from not only the aryl groups, but also from the nuclei of the Ga^{III} center of the complex in the 20-55 MHz region. While the spectroscopic features assigned as Ga HFC were difficult to assign due to many complicating factors, including overlapping features due to anisotropy in **A** and **Q** tensors, different isotopic abundances, magnetic moments, quadrupole moments and isotropic HFC constants for the two Gallium isotopes, the preliminary results of simulation of the spectrum suggests **A** = (67, 74, 86) MHz and a value for Q, the isotropic quadrupolar moment, of ~ 0.1 MHz. These values are over an order of magnitude greater than the HFC values

we obtained via cw X-band EPR spectroscopy, indicating a greater degree of spin delocalization onto the gallium atom (per gallium) for [(Ar-DAB)GaI_2] as compared to **2**.

In general, for a doublet ground state system in an isotropic fluid interacting with a nucleus with I = 1/2, two ENDOR lines are expected at the resonance frequencies

$$\nu_{ENDOR} = \left|\nu_n \pm \tfrac{1}{2} a_{iso}\right| \tag{2.6}$$

where υ_n is the Larmor frequency of the nucleus (for ^1H the Larmor frequency is 14.689 MHz at 3500 G) and a_{iso} is the isotropic hyperfine coupling constant. If the Larmor frequency of the nucleus is less than ½ a_{iso}, resonances will be separated by $2\upsilon_n$ and centered at $a_{iso}/2$

$$\nu_{ENDOR} = \left|\tfrac{1}{2} a_{iso} \pm \nu_n\right| \tag{2.7}$$

If the symmetry of the system is lowered, by having a system that inherently possesses lower than cubic symmetry and sampling a powder or frozen matrix rather than an isotropic fluid, a_{iso} can be replaced with A_i, one of the principal components of the hyperfine tensor. All different orientations must then be taken into account, vastly complicating the interpretation of the spectrum.

The most prominent feature of the ENDOR spectrum of the model complex is the broad quartet of peaks centered on 14.5 MHz, which can unequivocally be assigned as ^1H HFC given the proton Larmor frequency and isotropic HFC value

determined by exploration of the free ligand (2.25 MHz, where 1 G = 2.81 MHz), so that the peaks fall into the regime governed by equation 2.6. The quartet reveals an axial symmetry, with $A_{\perp} \approx 0.7$ MHz and $A_{\parallel} \approx 3.4$ MHz. The dynamically average isotropic HFC of the free ligand falls into this range, indicating a negligible perturbation to the organic-based spin system upon bonding to the Ga^{III} metal centers.

As discussed above, the ENDOR spectra corresponding to gallium nuclei can be extremely difficult to interpret. For nuclei that possess a quadrupole, i.e. those with I > 1, ENDOR peaks are found at the resonant frequencies

$$\nu_{ENDOR} = \left| \tfrac{1}{2} A_i \pm \nu_n \pm \tfrac{3}{2} Q_i (2m_I + 1) \right| \qquad (2.8)$$

where Q_i is one of the principal components of the quadrupole tensor and m_I can take the values I, I-1, ...-I. The Larmor frequency for ^{69}Ga and ^{71}Ga are 3.5867 MHz and 4.6913 MHz (at 3500 G), respectively. Given this, and the $^{69,71}Ga$ HFC values determined from the X-band EPR spectrum of the model complex (~ 4 G or 11.2 MHz), and considering the quadrupole contribution to be negligible, the peaks corresponding to Ga HFC should be found in the region governed by equation 2.7: if the Larmor frequencies of the Gallium nuclei are less than $\frac{1}{2}\, a_{iso}$, which appears to be the case, the peaks will be centered around 5.6 MHz and separated by υ_n, so that, considering anisotropy as well, a broad peak will be present from about 7 – 10 MHz, as an estimate, with its partner peak in the range 1

– 4 MHz. However, if the nuclear quadrupole interactions are not negligible, which may be the case in this system, the ENDOR spectrum will be vastly affected, and much more difficult to interpret.

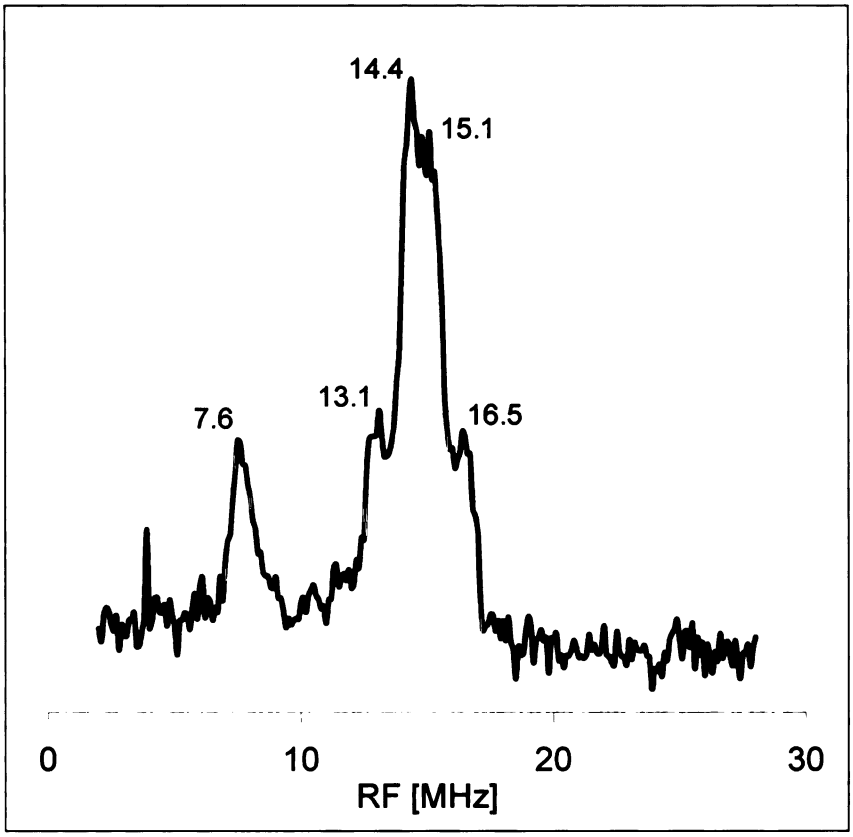

Figure 2-12: ENDOR spectrum of the model complex $[Ga_2(tren)_2(DHSQ)](BPh_4)_2(BF_4)$ acquired at X-band frequency and 10 K in a 9:2 butryonitrile/propionitrile glass.

Despite the problematic assignment of the peak at 7.6 MHz via the formalism presented above, we can rule out every other atom in this molecule as being the source of the HFC given the Larmor frequencies and experimentally

determined HFC values. At this time a tentative assignment of the peak at 7.6 MHz as resulting from ^{69,71}Ga HFC is made, and as to the best of our knowledge is only the second incidence of a ENDOR signal corresponding to Gallium nuclei in a discrete molecular metal complex system.[9]

2.3.4 Further Studies. EPR and ESEEM investigations of the nitro-substituted gallium(III)-semiquinones [Ga(tren)(2,7-di-NO_2-PSQ)](Cl)(BF_4) and [Ga(tren)(3,6-di-NO_2-PSQ)](BF_4)$_2$ (where PSQ = phenanthrenesemiquinone) were carried out. This work has been presented elsewhere,[47, 48] and the reader is directed to the references. The results add a great deal to the work presented above by providing a more detailed look at the spin distribution in these complexes, as well as elucidating the mechanisms of spin distribution. Perhaps most importantly, it was shown that spin density at the gallium(III) metal center could be modified by varying the substituent position on the ligand. This observation opens up exciting avenues toward control of spin distribution and magnetic properties of single molecules, which is discussed more fully in the final chapter of this dissertation.

2.3.5 DFT Calculations of Ga-SQ complexes. The application of DFT in determining HFC parameters, in particular the B3LYP functional,[49] has enjoyed reasonable success recently, as evidenced by the Larsen group's work on VO^{2+}

complexes[50, 51] as well as our own group's work.[47, 48, 52] It has also been reported that in the study of organic radicals, DFT is far superior to unrestricted Hartree-Fock calculations in terms of accurately predicting spin densities.[49, 53, 54] Of note and significance to this study are recent studies by Tuononen *et. al.* wherein different non-relativistic, quasi-relativistic fully relativistic functionals were implemented to calculate HFC parameters for a series of Gallium-dipnictogen diazabutadiene racials.[55, 56] These values were then used as initial guesses for simulations, which employed iterative least-squares fitting routines, of the EPR spectra of the molecules in this series. This approach proved to be useful in these instances, and in general is especially useful for compounds containing atoms beyond the second period, which can often have $I > \frac{1}{2}$ and/or possess different isotopes with different nuclear magnetic moments.

Herein we wish to test the ability of DFT, and specifically the UB3LYP/6-311G** level of theory, to accurately predict the spin density about a given atom within this system. To do this, we relate the calculated spin densities from the natural population analysis (NPA), as given by DFT, to the experimental spin densities, which are calculated from the isotropic HFC constants. The isotropic HFC values only give information on the spin at the nucleus, i.e. Fermi contact, due to the fact that in room temperature isotropic media, which produces a dynamically averaged value for the HFC, the dipolar (i.e. anisotropic) component collapses to zero.[57] As described earlier, Fermi contact coupling is the result of

unpaired electron spin density residing in an orbital (atomic or molecular) that has a non-zero amplitude at a nucleus where $I \neq 0$. The isotropic HFC for nucleus N is calculated from equation 2.9:

$$a_{iso}(N) = \frac{4\pi}{3} g_e g_n \beta_e \beta_n \langle S_z \rangle^{-1} \rho(N) \tag{2.9}$$

where g_e and g_n are the electronic and nuclear g-factors, β_e and β_n are the electronic and nuclear Bohr magneton. $\rho(N)$ is the Fermi contact integral, which corresponds to the spin density at N. By replacing all the constants in equation 2.9 Nguyen *et. al.*[58] produced the following conversion factors, where $a_{iso}(N)$ is given in Gauss:

$$a_{iso}(^1H) = 1594.9\rho(^1H) \tag{2.10a}$$

$$a_{iso}(^{13}C) = 401.1\rho(^{13}C) \tag{2.10b}$$

$$a_{iso}(^{35}Cl) = 52.1\rho(^{35}Cl) \tag{2.10c}$$

Using these conversion factors, we were easily able to calculate the spin density at these nuclei (i.e. the Fermi contact) by using the experimentally determined isotropic HFC values. In the case of the ^{1}H HFC in the model complex, which was only observed in the low-temperature ENDOR spectrum, the isotropic HFC value must be extracted from the hyperfine tensor. From this experiment it was determined that $A_\perp \approx 0.7$ MHz and $A_\parallel \approx 3.4$ MHz, leading to the following A-tensor:

$$\begin{bmatrix} 0.7 & 0 & 0 \\ 0 & 0.7 & 0 \\ 0 & 0 & 3.4 \end{bmatrix}$$

The isotropic HFC value is simply one-third the trace of this tensor, or ± 1.6 MHz (0.57 G). Naturally, there is some error in this measurement due to the noise level of the ENDOR spectrum; this is to be compared to the value of ± 0.79 G found for the trianionic semiquinone DHBQ species. To determine the spin density at the Gallium nuclei a weighted average of the HFC for the two different isotopes must be carried out, assuming the following relation, as reported by Weltner,[35] holds true:

$$a_{iso} = a_0 \rho(N) \tag{3.11}$$

Here a_0 is the HFC if the spin density at N is unity, and equals 4356 G for ^{69}Ga and 5535 G for ^{71}Ga.

The lower half of Table 2.1 gives the comparison between the experimental and calculated spin densities about the gallium nuclei in both **2** and the model complex. For both systems the calculation overestimates the magnitude of the Fermi contact by less than a factor of two. The negative value of the Fermi coupling is explained as follows. Unpaired spin density at the nucleus may arise via s-orbital admixture into the molecular orbital containing the unpaired spin or by spin polarization of filled inner orbitals by outer orbitals which contain an unpaired spin. The calculated magnitude of the spin density for Gallium in **2** was

found to be 0.00072, corresponding to the s-orbital spin density. By summing up the contributions of the s-orbitals, the calculation gives a value of -0.0012 for **2** and -0.0013 for the model complex. The calculated Fermi contact coupling of -6.74 G for ^{69}Ga in complex **2** and -6.87 G for the model complex indicates β-spin density of the core s-orbitals, as indicated by the sum of the spin density in the s-orbital contribution to the molecular orbital. The β-spin density of the s-orbital contribution is a result of spin polarization by the α-spin populated p and d orbitals.

The upper half of Table 2.1 explores the relationship between spin density, Fermi contact coupling, and HFC for the six carbon atoms in the trianionic semiquinone forms of the bridging ligands CA and DHBQ. The values for the HFC were obtained from previously published results.[39, 45] The calculated Fermi contact couplings compare well with the experimental HFC results, and provides a good example of the anisotropic components (p- and d-orbital contributions) collapsing to zero in a dynamically averaged system: although the main contributions to the spin density arise from the p-orbitals, these cancel out in solution. The experimental spin density and the sum of the total s-orbital spin densities differ by no more than a factor of 3.1 and no less than a factor of 1.5 for all carbon atoms in both molecules.

The upper half of Table 2.1 also explores the spin density about the chlorine atoms in **2** and CA^{3-} and the protons in the model complex and $DHBQ^{3-}$.

In both cases the atoms are in the same position with respect to the oxygen atoms and lie along a C_2 axis. In general, for the three systems for which experimental HFC values were available, the magnitudes of the calculated and experimental spin densities are remarkably similar. Perhaps the most interesting aspect of the data presented in this section of Table 2.1 is that the calculation indicates β-spin density on the chlorine atom in CA^{3-} while α-spin density is indicated on the proton for both the model complex and $DHBQ^{3-}$. Figure 2.5 indicates that for complex **2** polarization of the spin density by the α-SOMO leaves residual β-spin density on the carbon atom adjacent to the chlorines (or protons in the case of the model complex). This indicates that chlorine atoms of **2** induce spin delocalization, while in the model complex a spin polarization mechanism is occurring.

Table 2.1: Experimental and calculated spin densities for $[Ga_2(tren)_2(CA^{sq,cat})]^{3+}$ (2), $[Ga_2(tren)_2(DHBQ)]^{3+}$ (2a), and the free ligands $[CA^{sq,cat}]^{3-}$ and $[DHBQ]^{3-}$. (Key: a. calculated using equations 3.9 and 3.10 based on exp. values; b. summed contributions for s, p, and d orbitals. Only s contributions are relevant for Fermi contact; c. ref 39; d. applies to ^{35}Cl only (see text for details); e. ref 45; f. ref 44; g. applies to ^{69}Ga only (see text for details)).

	Experimental		Calculated			
	A_{iso} (G)	ρ(N)[a]	s[b]	p[b]	d[b]	Fermi (G)
$[CA^{sq,cat}]^{3-}$						
C1	2.71[c]	0.00656	0.00441	0.13085	0.00044	0.59
C2	-8.17[c]	-0.0204	-0.00660	-0.06705	0.00034	-9.39
$^{35,37}Cl$	0.18[c]	0.00345	-0.00023	-0.00310	-0.00020	-0.51241[d]
$[DHBQ]^{3-}$						
C1	2.63[e]	0.00656	0.00469	0.13831	0.00034	0.82
C2	-6.66[e]	-0.0166	-0.0053	-0.07359	0.00024	-7.01
^{1}H	0.79[f]	0.00050	0.00070			1.13674
2						
^{69}Ga	3.136	0.00072	-0.00120	0.00176	0.00031	-6.74169[g]
^{71}Ga	3.980					
$^{35,37}Cl$			-0.00017	-0.00614	-0.00008	-0.31707
2a						
^{69}Ga	3.337	0.00077	-0.00130	0.00205	0.00029	-6.86987[g]
^{71}Ga	4.240					
^{1}H	0.570	0.00036	-0.000130			0.03196

2.3.6 Conclusions for Ga-SQ complexes. The doublet ground state of $[Ga_2(tren)_2(CA^{sq,cat})](BPh_4)_2(BF_4)$ (**2**) has been characterized by several techniques, including EPR, ENDOR, and application of density functional theory. A triplet electronic state was observed and characterized as arising due to the interaction of a pair of molecules in solution. Comparison of experimental Fermi contact couplings with those calculated by DFT has proven this method to be an effective tool for predicting spin densities in both the gallium dimer systems and CA and DHBQ semiquinones. This molecule is the simplest paramagnetic species within the bimetallic $[M_1M_2(tren)_2(CA^{n-})]^{m+}$ series, and therefore the work presented herein, in addition to the results of the previous report, form the foundation for understanding the paramagnetic ground states of the molecules in this series. The remainder of this chapter will focus on the more complex paramagnetic species within this series: first the mononuclear Cr^{III} species will be explored, and from there the next topic of interest will be the introduction of exchange coupling by turning "on" or "off" the semiquinone nature of the bridging ligand.

2.4 Results and Discussion. Quartet Complexes of Chromium(III).

2.4.1 Theory. Electronic Structure. A quartet ($S = {}^3/_2$) state has $2S + 1 = 4$ degeneracy, which is manifested in any system of cubic or lower symmetry as two Kramer's doublets, $m_s = \pm {}^1/_2$ and $m_s = \pm {}^3/_2$ (Figure 2-13). This is a result of

Kramer's rule, which states that if an ion has an odd number of unpaired electrons the degeneracy of every level must remain at least twofold in the absence of a magnetic field. The splitting of these doublets is called zero field splitting (zfs), which arises from the point group being unable to support the four-fold degeneracy of the state, and originates from magnetic dipole-dipole interactions between the unpaired electrons. In our target molecules the spin density resides on the Cr^{III} center, which has local *cis*-N_4O_2 (C_{2v}) symmetry, and as a result should have rhombic spin Hamiltonian parameters (*vide infra*), meaning in general that the tensors describing the interactions in these systems will be anisotropic. In the presence of applied magnetic field, the most general spin Hamiltonian for a $S = {}^3/_2$ system in the absence of hyperfine coupling is

$$\hat{H} = \beta_e \vec{B} \cdot \tilde{g} \cdot \vec{S} + \vec{S} \cdot \tilde{D} \cdot \vec{S} \qquad (2.12)$$

The leftmost term on the right describes the familiar Zeeman interaction (Figure 2.13d), which breaks the degeneracy of $\pm {}^1/_2$ and $\pm {}^3/_2$ Kramer's doublets, resulting in a linear stabilization or destabilization (depending on the sign of the m_s level) as a function of the magnetic field, B. The right-hand term accounts for zero field splitting effects, and is represented here in matrix form, where $\tilde{D}$ is the zero field splitting tensor, a 3x3 matrix which quantifies the interaction between the spin vectors $\vec{S}$. Because the zero-field splitting matrix has a zero trace ($X + Y + Z = 0$, where X, Y, and Z are the diagonal components of the zero field splitting tensor), the zero field splitting can be given by two values,

$D = \frac{1}{2}(X+Y) - Z$ and $E = -\frac{1}{2}(X-Y)$, resulting in the spin Hamiltonian of equation 2.13.

$$\hat{H} = \beta_e \vec{B} \cdot \tilde{g} \cdot \vec{S} + D[S_z^2 - \tfrac{1}{3}S(S+1)] + E(S_x^2 - S_y^2) \qquad (2.13)$$

where the parameter D describes axial splitting ($g_{xx} = g_{yy} \neq g_{zz}$) of the zero-field states, while the parameter E is required to account for rhombic zero-field effects ($g_{xx} \neq g_{yy} \neq g_{zz}$) (Figure 2-13c).[18] While the presence of the parameter E indicates a lower than axial symmetry, the magnitude of E does not in itself reflect a given symmetry. The complexes reported herein have either D_{2h} or C_{2v} local symmetry at the magnetic centers, and therefore possess a "rhombic" EPR symmetry,[19] that is, in general the principal axes (the diagonal components of the g-tensor) are nonequivalent, i.e $g_{xx} \neq g_{yy} \neq g_{zz}$ as a result of different magnetic field projections along the principal axes. With different g-values for the principal axes EPR transitions will occur at different positions in the spectrum, and can have a dramatic impact on the appearance of the EPR spectrum, especially when zero field splitting is present.

Both **3** and its model complex have a d^3 paramagnetic center, which has a $^4A_2$ ground state in C_{2v} symmetry. This ground state in isolation should exhibit no zero-field effects due to quenching of the orbital angular momentum, though second-order spin-orbit effects, which result from admixture of excited electronic states into the ground state, account for a small zero-field splitting, even in O_h

symmetry. Macfarlane[59] has carried out calculations in trigonal symmetry and concluded that the major contributions to the zero-field splitting come from the a^4T_1, a^2T_2, and b^2T_2, with $^4T_2$ contributing very little.

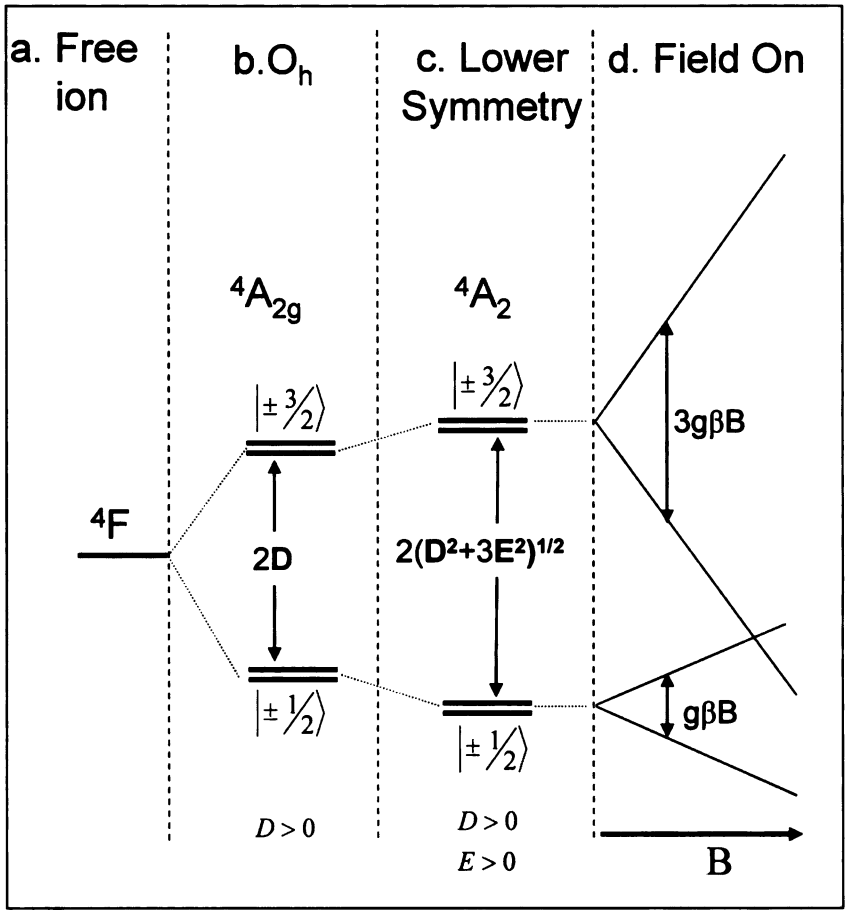

Figure 2-13: The ground quartet state of a Cr(III) ion under O_h symmetry ($^4A_{2g}$) consists of two Kramer's doublets split by $2|D|$. As the symmetry is lowered the rhombic zero field splitting parameter E affects the splitting, and as the system is introduced to an external magnetic field (B) the Kramer's doublets split further according to the Zeeman interaction.

Basis functions for the quartet spin system can be represented with respect to the one electron spin functions α and β as:

$$\left|+\tfrac{3}{2}\right\rangle = |\alpha\alpha\alpha\rangle \tag{2.14a}$$

$$\left|+\tfrac{1}{2}\right\rangle = \frac{1}{\sqrt{3}}|\alpha\alpha\beta + \alpha\beta\alpha + \beta\alpha\alpha\rangle \tag{2.14b}$$

$$\left|-\tfrac{1}{2}\right\rangle = \frac{1}{\sqrt{3}}|\alpha\beta\beta + \beta\alpha\beta + \beta\beta\alpha\rangle \tag{2.14c}$$

$$\left|-\tfrac{3}{2}\right\rangle = |\beta\beta\beta\rangle \tag{2.14d}$$

For the spin Hamiltonian of equation 2.13 and the symmetrical quartet spin basis set the secular determinant is:[19, 60]

$$\begin{vmatrix} +\frac{3}{2}g_{zz}\beta_e Bn + D - \varepsilon & \frac{\sqrt{3}}{2}\beta_e Bg_- & \sqrt{3}E & 0 \\ \frac{\sqrt{3}}{2}\beta_e Bg_+ & \frac{1}{2}g_{zz}\beta_e Bn - D - \varepsilon & \beta_e Bg_- & \sqrt{3}E \\ \sqrt{3}E & \beta_e Bg_+ & -\frac{1}{2}g_{zz}\beta_e Bn - D - \varepsilon & \frac{\sqrt{3}}{2}\beta_e Bg_- \\ 0 & \sqrt{3}E & \frac{\sqrt{3}}{2}\beta_e Bg_+ & -\frac{3}{2}g_{zz}\beta_e Bn + D - \varepsilon \end{vmatrix} = 0$$

(2.15)

where $l = \sin\theta\cos\phi$, $m = \sin\theta\sin\phi$, $n = \cos\theta$ and $g_{\pm} = (g_{xx}l \pm ig_{yy}m)$. l, m, and n are the direction cosines. This secular determinant is derived in Appendix B. In all calculations presented below, the principal g-values are replaced by the isotropic g value (1.98 for Cr^{III}). β_e is the electronic Bohr magneton (4.65334 x

10^{-5} cm^{-1} G^{-1}), and B is the magnetic induction (in Gauss). D and E are scalar quantities and are the axial and rhombic zero field splitting parameters, respectively. Applying the appropriate angles and solving for ε yields solutions for the magnetic field along the z-axis ($\theta = 0$; $\varphi = 0$), x-axis ($\theta = \pi/2$; $\varphi = 0$), or y-axis ($\theta = \pi/2$; $\varphi = \pi/2$). Of course, one can solve for the eigenvalues of any other orientation with respect to the magnetic field by plugging in the correct angles.

For the axial case we need to only consider solutions along the z axis and either the x or y axis, due to the degeneracy of these axes in axial symmetry. Transitions that are not expected given the usual selection rule (i.e. $\Delta m_s = \pm 1$) arise due to the lowered symmetry of the system. To understand the origin of formally forbidden EPR transitions occurring in this system we look to the secular determinant, equation 2.15. A corresponding axial secular determinant is obtained by setting g_{xx} and g_{yy} to the same value (called $g_\perp$, called g-perpendicular and g_{zz} takes the name $g_\parallel$, g-parallel) and by simply setting the rhombic splitting parameter, E, to zero. The diagonal terms contain $g_\parallel$ and the off-diagonal terms contain $g_\perp$. For B parallel to the z-axis the eigenvalues are

$$W_{\pm 3/2} = D \pm \tfrac{3}{2}(g\beta_e B) \qquad (2.16a)$$

$$W_{\pm 1/2} = -D \pm \tfrac{1}{2}(g\beta_e B) \qquad (2.16b)$$

and the resulting zero-field splitting is $2|D|$. Off-diagonal terms all contain $g_\perp$, so that the different eigenvalues comprising the quartet state in a magnetic field along the x and y axes involve mixing of different pure spin states.[35]

In the case of a quartet spin system in rhombic symmetry, the same procedure used for axial symmetry is carried out. Namely, that the secular determinant is solved for orientations corresponding to the x, y, and z axes. The difference for rhombic systems is all three axes are non-degenerate and must be considered individually. Again looking to the secular determinant, equation 2.15, it is seen that further off-diagonal terms arise when $E \neq 0$. This additional state mixing in rhombic system is important for describing the origin of perpendicular-mode transitions given the typical EPR selection rule.

As described above, the magnitude of the zero field splitting in axially symmetric quartet systems between the $m_s = \pm {}^3/_2$ and $m_s = \pm {}^1/_2$ Kramer's doublets is $2|D|$ (*vide infra*). D can be positive, resulting in the $m_s = \pm {}^1/_2$ Kramer's doublet being stabilized, or negative so that the $m_s = \pm {}^3/_2$ states are stabilized. For rhombic quartet systems, the ratio E/D influences the magnitude of the zero field splitting, giving rise to Kramer's doublets separated by[61]

$$\Delta E = 2|D|\sqrt{1+3({}^E/_D)^2} \qquad (2.17)$$

as shown above in Figure 2-13. Finally, it should be noted that the validity of m_s as a good quantum number depends on the magnitude of the zero field splitting.

In general, for small zero field splitting ($|zfs| << h\nu$) extensive mixing between the various m_s levels occurs, and m_s is no longer valid. For large magnitudes of zero field splitting m_s becomes a good quantum number. Because of this state mixing, the magnetic sublevels of quartet electronic states will be called $|1\rangle$, $|2\rangle$, $|3\rangle$, and $|4\rangle$ rather than by their pure spin kets $|\pm 1/2\rangle$ and $|\pm 3/2\rangle$.

2.4.2 Theory. Selection Rules and State Mixing. In a perpendicular-mode EPR experiment, microwave radiation is applied perpendicular to the magnetic force lines. The magnetic component of the microwaves (B_{hv}) couples with the magnetic moment of the spin system, resulting in the transition. The probability of a transition from a state m_s to another m_s' is given by the modulus squared of the element of the secular determinant, $P = \left|\langle m_s | \mu B_1 | m_s' \rangle\right|^2$. Here μ is the magnetic moment, which along the x-axis is $\mu = -g\beta\hat{S}_x$, assuming an isotropic g value. When $\hat{S}_x$ operates on an m_s function the value is

$$\hat{S}_x |m_s\rangle = \frac{|m_s + 1\rangle |m_s - 1\rangle}{2} \qquad (2.18)$$

and such that the modulus squared of the transition element is zero unless $m_s' = m_s \pm 1$, that is, the final state must differ by one in m_s for the transition to be allowed. This is the commonly known selection rule for EPR.

For parallel mode the microwave radiation is applied along the same axis as the magnetic field, and the magnetic moment is given by $\mu = -g\beta\hat{S}_z$, and operates on the m_s states as:

$$\hat{S}_z|m_s\rangle = m_s|m_s\rangle \qquad (2.19)$$

The result is that the probability is non-vanishing only is $m_s = m_s'$, that is, the states must "look" the same, whether by having the same m_s values or taking on similar m_s values as a result of state mixing. In the case of small zero field splitting, state mixing occurs. In this case m_s would cease to be a good quantum number, as described above, with the result that formally forbidden EPR transitions arise. This is a concept important to the accurate simulation of EPR spectra.

2.4.3 High-Symmetry complexes of Chromium(III). The electron paramagnetic resonance spectra of chromium(III) ions have been recorded in many different high symmetry environments. In single crystals, the ion must be doped in at ~ 1 % concentration in order to avoid spin exchange interactions between the paramagnetic ions. While in most EPR studies chromium(III) has been doped into many different ionic solids, most notably ruby,[62] this section will focus on coordination complexes of chromium(III). Tris(acetylacetonato)chromium(III), $Cr(acac)_3$, forms an isomorphous series with both $Al(acac)_3$ and $Ga(acac)_3$ and can

be doped into these materials in order to carry out single-crystal EPR studies.[16, 63, 64] In general, in all of these studies the EPR spectra can be accounted for with the spin Hamiltonian of equation 2.13, with g values around 1.98, $|D|$ = 0.6 cm^{-1}, and $|E|$ = 0.015 cm^{-1} at low temperature. The axial splitting parameter, D, has been reported as 0.7 cm^{-1} for $Cr(hfac)_3$ (hfac = monoanion of 1,1,1,5,5,5-hexafluoro-2,4-pentandione).[65] At room temperature the magnitude of the rhombic zero field splitting parameter E for $Cr(acac)_3$ decreases to ~ 0.008 cm^{-1}, about half the low-temperature value. One interesting application of this temperature-dependence of the E parameter was carried out by Andriessen, who used $Cr(acac)_3$ doped into $Al(acac)_3$ or $Co(acac)_3$ to monitor phase transitions in these materials.[16] Finally, electron-nuclear hyperfine interactions of $Cr(acac)_3$ have been explored by McGarvey on isotopically enriched samples of $Cr^{53}(acac)_3$, revealing hyperfine interactions on the order of 10^{-4} cm^{-1}.[66] Given these spin Hamiltonian values, the high symmetry systems can be treated with the same formalization outlined below for lower symmetry (N_4O_2 coordination) systems.

Several reports on single crystal doped samples of $Cr(acac)_3$ have employed high resolution spectroscopic techniques (polarized emission, optically detected magnetic resonance, excitation line narrowing spectroscopy), to obtain state splittings and g-values of the lowest-energy, luminescent excited state and the ground state. In all cases a value of ~ 1.2 cm^{-1} was obtained for the ground state

splitting (consistent with $|D| = 0.6$ cm^{-1}; in one such study Möbius and coworkers have assigned D as negative for $Cr(acac)_3$).[17, 67, 68] Over the years these studies have led to some disagreement in the literature as to the nature and the degree of splitting of the emissive state. As this topic pertains to the excited electronic structure, it will be explored fully in Chapter 3.

Chapter 3 of this dissertation employs substituted complexes of $Cr(acac)_3$ in order to address fundamental issues of nonradiative decay in transition metal complexes. X-band EPR spectra of several of these high symmetry complexes were obtained to address the ground state splittings. The spectra were collected in a 9:2 butyronitrile:propopnitrile glass at 4 K, and a representative spectrum is shown in Figure 2-14. This spectrum was simulated using the spin Hamiltonian of equation 2.12. The values obtained for $Cr(acac)_3$ and $Cr(3\text{-}Brac)_3$ correspond to the values observed in doped single crystals (described above), revealing very little impact by the molecular environment on the spin Hamiltonian values. For all complexes studied the axial zero field splitting parameter was between 0.5 and 1.0 cm^{-1}, leading to a less than 2 cm^{-1} splitting in the ground state. The similarity of the spin Hamiltonian parameters reflects the similarity of the coordination environment and electronic structure across this series.

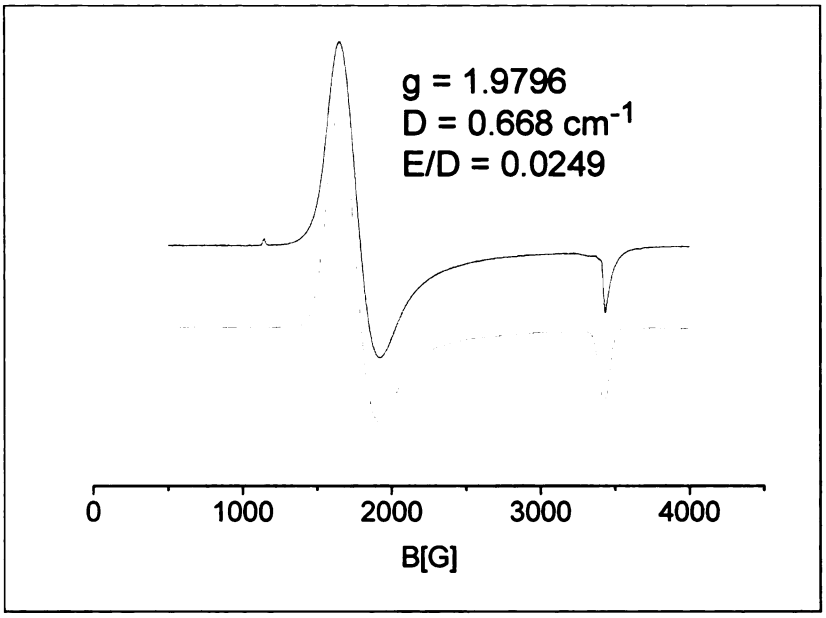

Figure 2-14: Experimental (black) and simulated (red) continuous-wave EPR spectra of tris(3-phenyl-2,4-pentanedionato)chromium(III) ($Cr(3\text{-}Phac)_3$) obtained in a 4 K glass of 9:2 butyronitrile:propionitrile. Experimental conditions: ν = 9.4775 GHz, modulation amplitude = 20 G, conversion time = 80 ms, power = 63 μW. Simulation parameters are indicated in the figure.

Table 2.2: Spin Hamiltonian parameters for several substituted complexes of $Cr(acac)_3$ obtained in a 4 K glass of butyronitrile:propionitrile.

	g_{iso}	D (cm^{-1})	E (cm^{-1})
Cr(acac)	1.9792	0.576	0.0080
$Cr(3\text{-}Brac)_3$	1.9796	0.664	0.0043
$Cr(3\text{-}Phac)_3$	1.9796	0.668	0.0166

Finally, of additional interest is a time-resolved EPR (TR-EPR) study of ruby and $Cr(acac)_3/Al(acac)_3$.[62] The samples were excited into the first spin-allowed ligand field state using a frequency doubled Nd:YAG source (532 nm). The experiment had a time resolution of about 0.5 μs. In ruby, which has a 3 ms lifetime for the lowest-energy excited state, ^2E, the authors noted no signal attributable to this state. The dynamics they observed, which were assigned entirely to dynamics between spin sub-levels of the $^4A_2$ ground state, where initially emissive and then switched to absorptive after about 700 μs, indicating changing populations of spin sublevels within the $^4A_2$ ground state. This essentially relates to changing spin distribution in the ground state in a time-resolve sense. The $Cr(acac)_3/Al(acac)_3$ system showed only an emissive signal, but this result may be due to the much lower S/N recorded for this measurement.

2.4.4 Low-Symmetry complexes of Chromium(III): X-band EPR spectra and simulations of $[GaCr(tren)_2(CA^{cat,cat})](BPh_4)_2$ (3) and $[Cr(tren)(DTBCat)](PF_6)$. Magnetic susceptibility data published in our previous report for complex **3** from 2 – 350 K reveal a temperature-independent magnetic moment of $\mu_{eff} = 3.44 \pm 0.09\ \mu_B$ ($\mu_{spin\text{-}only}$ for $S = {}^3/_2$ is 3.87 μ_B), indicating the expected $S = {}^3/_2$ ground state of Cr^{III}. In general, Cr^{III} centers with a *cis*-N_4O_2 local symmetry have g values around 1.98 and zero-field splitting parameters of $|D| \leq 0.5\ cm^{-1}$ and E/D of about 0.3, as revealed by an investigation of a series of Cr^{III} complexes including $[Cr(NH_3)_4XY]Z$, cis-$[Cr(2,2'\text{-bpy})_2XY]Z$ and cis-$[Cr(1,10\text{-phen})_2XY]Z$ (XY = H_2O-H_2O, H_2O-OH^-, oxalate or acetylacetonate, and Z is the counter-anion).[13, 69] These values provided useful initial guesses for our simulations. The X-band spectra of $[Cr(tren)(DTBCat)](PF_6)$ and **3** were simulated according to the spin Hamiltonian of equation 2.13.

The X-band EPR spectra and simulations of $[GaCr(tren)_2(CA^{cat,cat})](BPh_4)_2$ (**3**) and its model complex, $[Cr(tren)(DTBCat)](PF_6)$ are shown in Figure 2-15. The spin Hamiltonian parameters for both species are presented in Table 2-3. The spectra of the complex and its model are similar in almost all regards, and the differences are almost certainly due to impurities in **3**, of which one could be the S = ½ complex **2** and another the $S = {}^5/_2$ complex **6** (Figure 2-16).[28, 70] The spin Hamiltonian parameters for the two systems fall within the range of values reported for Cr^{III} complexes with a local *cis*-N_4O_2 ligand environment.

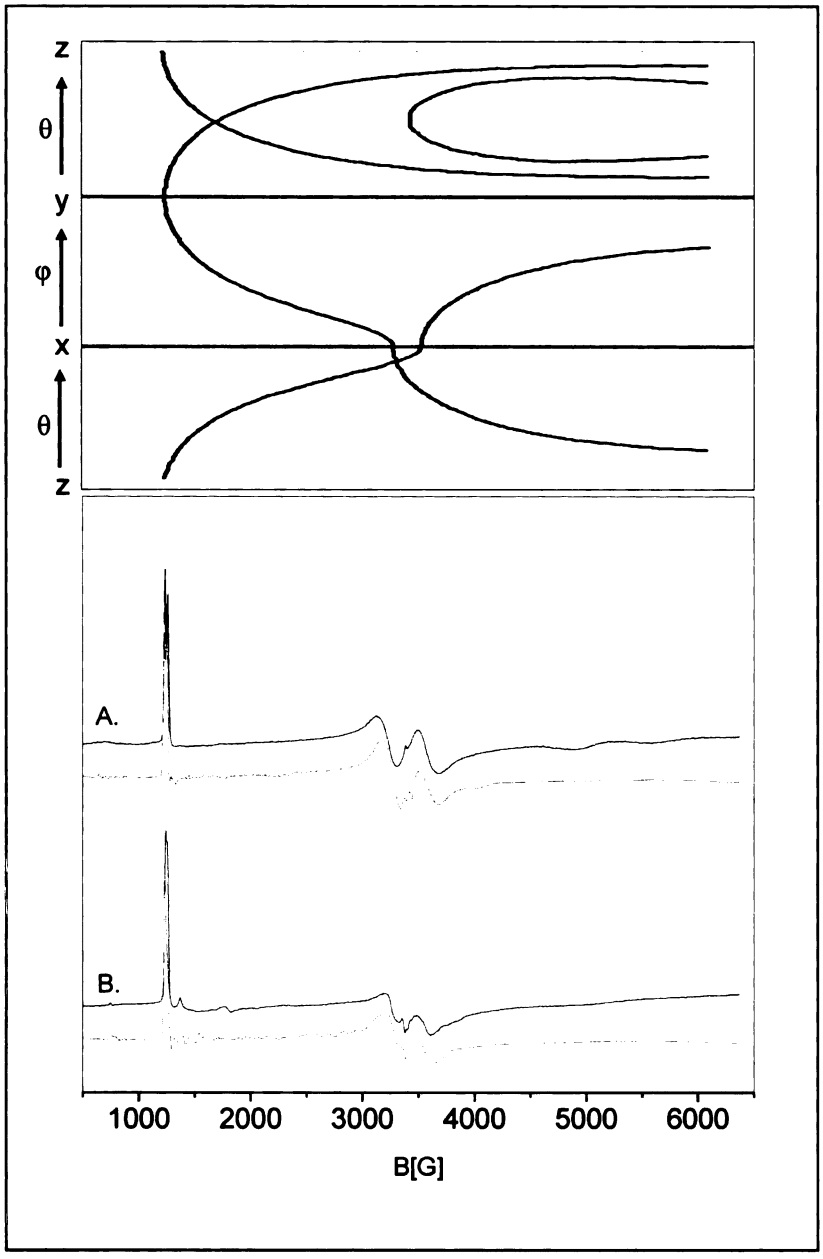

Figure 2-15: Experimental (black) and simulated spectra (red) for (a) [Cr(tren)(DTBCat)](PF6) and (b) Complex 3. The spectra were acquired at 4 K, with a power of 0.32 mW at 9.4595 GHz. The transition roadmap of 3 is shown above.

The spectra show no temperature dependence up to 60 K. Application of equation 2-17 results in a splitting of 0.894 cm^{-1} for $|D|$ = 0.392 cm^{-1} and $|E|$ = 0.124 cm^{-1}, the experimentally determined values for complex **3**. Here, in our simulations and calculations, it is assumed that D > 0, although we have not been able to prove this experimentally because the small magnitude of D allows for a nearly equal Boltzmann distribution of both quartet and doublet Zeeman states, even at 4 K.

The parameters were also applied to calculate energy-level diagrams for these two molecules by solving the secular determinant along the magnetic x, y, and z axes (*vide infra*).[18] The energy level diagrams reveal significant mixing between the $|\pm 1/2\rangle$ and $|\pm 3/2\rangle$ manifolds, so that formally forbidden transitions are allowed. The field positions of the transitions, indicated by a red arrow, are consistent with the observed spectrum.

Table 2-3: Spin Hamiltonian parameters, as obtained through simulation, for **3** and its model complex, [Cr(tren)(DTBCat)](PF_6).

	g_{xx}, g_{yy}, g_{zz}	D(cm^{-1})	E (cm^{-1})
model	1.985, 1.982, 1.970	0.396	0.122
3	1.980, 1.975, 1.970	0.392	0.124

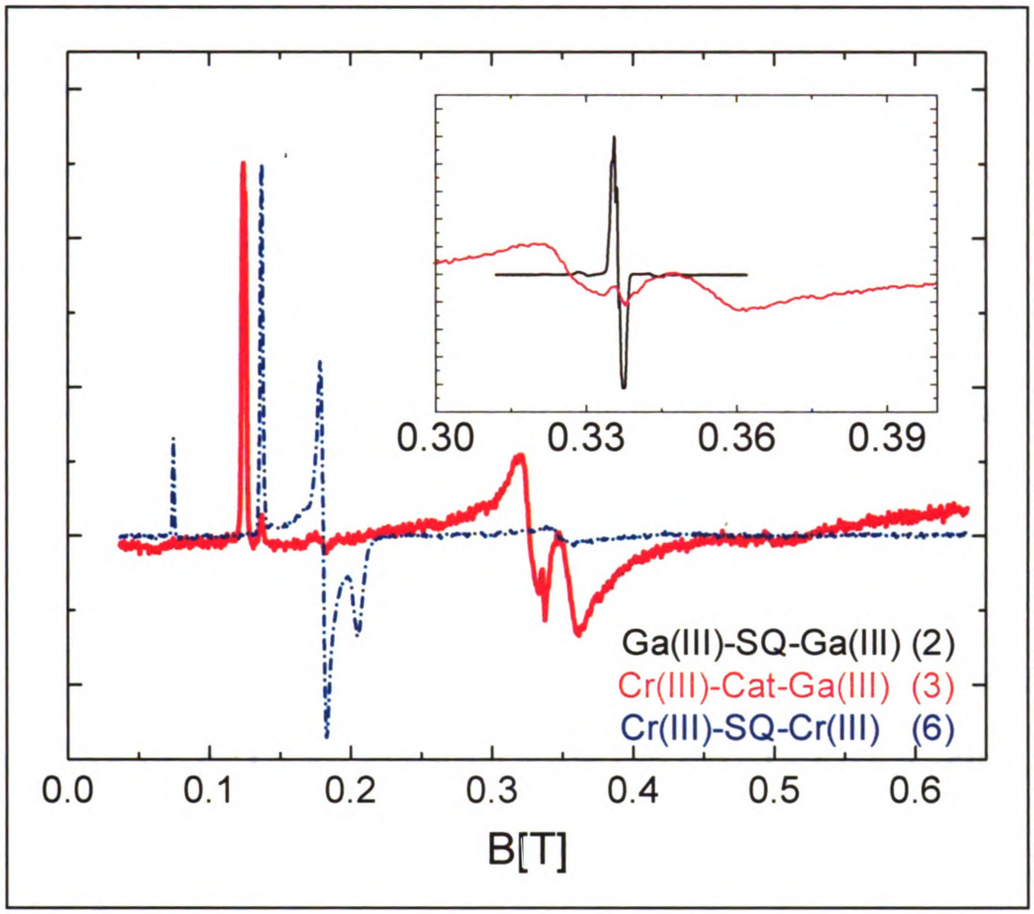

Figure 2-16: Impurity signals in the experimental X-band spectrum of complex **3** due to the homometallic species **6** and **2** (inset). All spectra were acquired at 4 K and 9.45 GHz.

The transition roadmap, the angular variation of the resonance position plot, which is presented above the EPR spectrum (Figure 2-15), shows the field of transition (abscissa, in Gauss) with respect to orientation (ordinate). Lines on the diagram plot the field of resonance for a particular transition as a function of the orientation of the spin system (the polar and azimuthal angles) with respect to the

direction of the magnetic field. The transition which each line corresponds to is shown with reference to the energy level diagram. The path follows the edges of an octet of a sphere, and is as follows: starting at the z-axis the angle θ is varied so that orientations in the xz plane are sampled until the x-axis is reached, then φ is varied so that orientations in the xy plane are sampled until the y-axis is reached, and finally rotating in the yz plane to return to the z axis. To gain an understanding of the angular variation of the position of resonance, this concept is shown schematically in Figure 2-17 for a simple S = ½ system under rhombic symmetry, where the position of the $|-½\rangle \rightarrow |+½\rangle$ transition with respect to the applied magnetic field varies with angular orientation. In the diagram of Figure 2-17 the variation with orientation is due to the anisotropy in the g-tensor. However, our Cr(III) systems are essentially isotropic with respect to the g-tensor, and are treated as such in the calculations, with an isotropic g value of 1.98. The orientation dependence in these systems arises from mixing of the pure m_s states due to the relatively small magnitude of the zero field splitting. The diagram of Figure 2-15 reveals extremely wide resonances, which are common for transition metal systems.

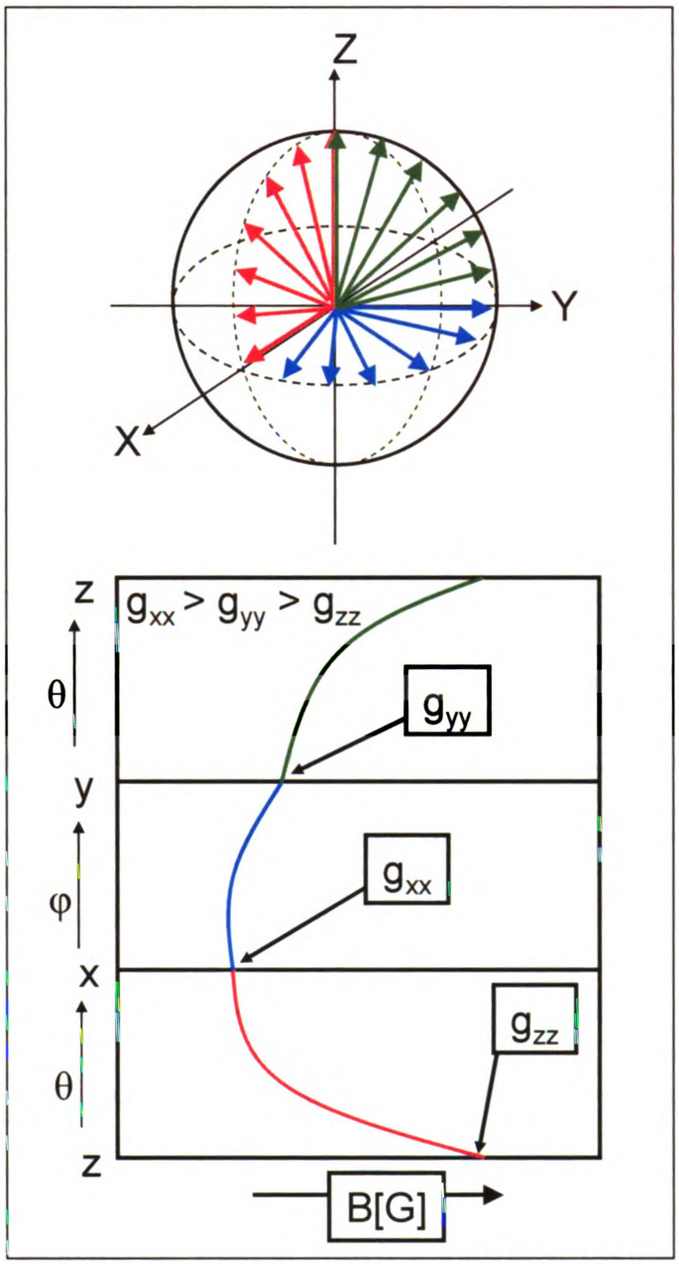

Figure 2-17: Schematic representation of an angular dependence diagram for a simple S = ½ system under rhombic symmetry.

2.4.5 Effect of Zero-Field Splitting Parameters on the Energy Profile of a Quartet Spin System. To best understand the origin of the transitions observed

for both **3** and the model complex, it is paramount to build up the spectra piece by piece using the Hamiltonian of equation 2.13. The simplest quartet spin system is isotropically symmetric, meaning that the scalar quantities D and E are zero, and only the electronic Zeeman term is operative (we are also considering an isotropic g tensor, with g = 1.98). The zero field splitting is zero because the symmetry of the system does not allow for any zero field splitting, as the zero field splitting tensor ($\tilde{D}$) is traceless. The result is the energy level diagram on the far left of Figure 2-18, where all allowed ($\Delta m_S = \pm 1$) transitions are at the same field and the energy profile is the same for all possible orientation of the molecule with respect to the applied magnetic field. Figure 2-19, left, shows the transition diagram for an axially symmetric quartet spin system. When D = 0, the system is isotropic, and one can see that all allowed transitions for the plotted orientations are occurring at the same field, with the exception being the g' = 4 ($\Delta m_S = \pm 2$) transition). All possible transitions in an isotropically symmetric quartet spin system are shown in the transition roadmap, Figure 2-20. As expected from the symmetry of the system, the field at which a transition occurs does not change with the orientation of the spin system with respect to the direction of the applied magnetic field. The transitions listed on the transition roadmap correspond to the states of the energy level diagram to the right of the roadmap. The simulated spectrum (Figure 2-21, top, D = 0) does not show the forbidden transitions revealed by the roadmap as their transition probabilities are extremely small.

Figure 2-18: (Facing page) Energy level diagrams showing how the experimental axial (D) and rhombic (E) zero field splitting parameters affect the energy profile of the ground ^4A state for the magnetic field parallel to the principal axes of the system. In an isotropic system the two Kramer's doublets of the ground state are degenerate, and the energy profiles are the same for every orientation with respect to the magnetic field. For an axial system the Kramer's doublets are split by 2D, and the x and y axes are degenerate. For rhombic systems an additional zero field splitting parameter is needed to describe the splitting between the Kramer's doublets, and the energy profiles for the magnetic field along the x, y, and z axes are different.

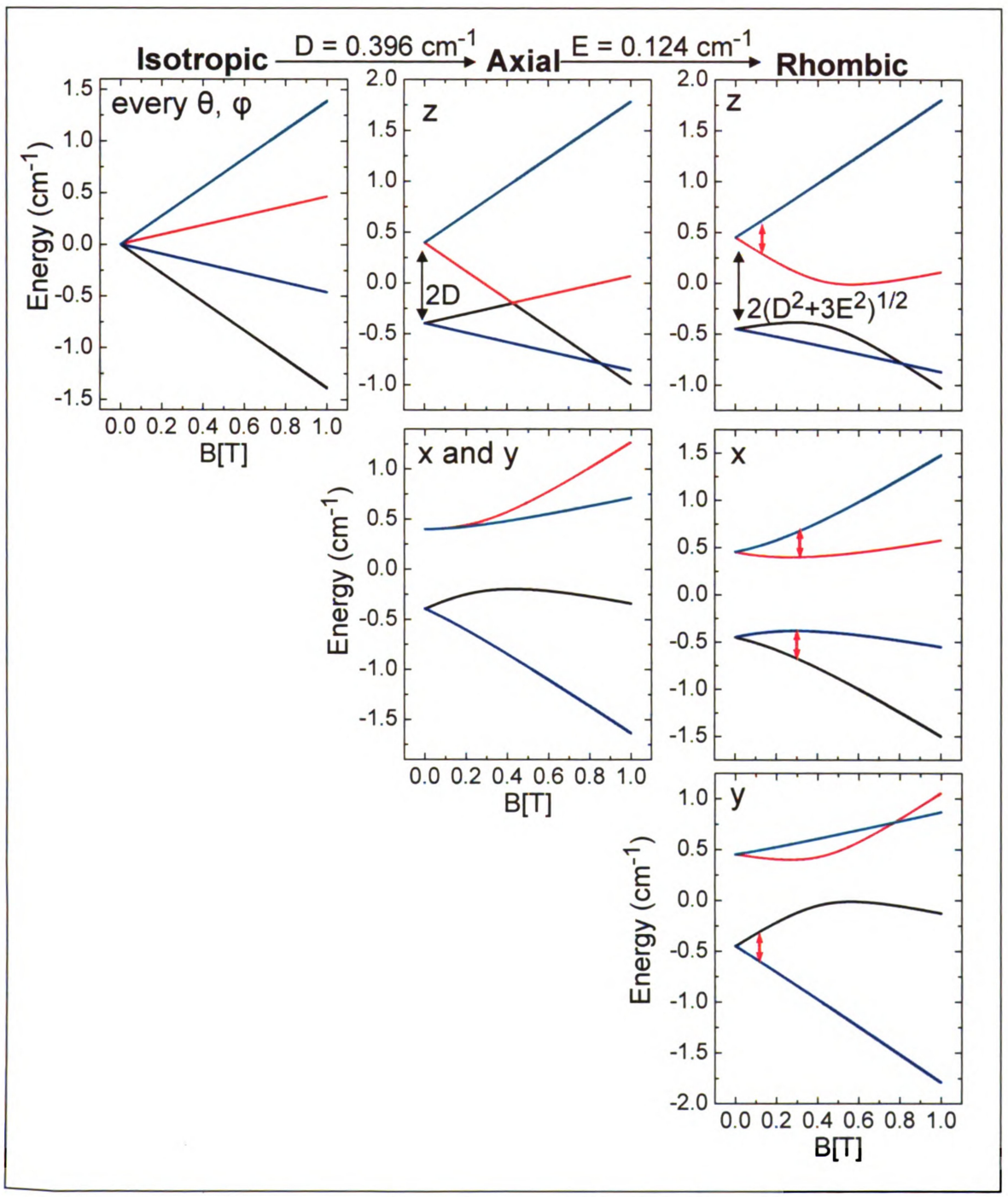
Isotropic
D = 0.396 cm-1
Axial
E = 0.124 cm-1
Rhombic
every θ, φ
z
2D
z
2(D2+3E2)1/2
x and y
x
y
Energy (cm-1)
B[T]

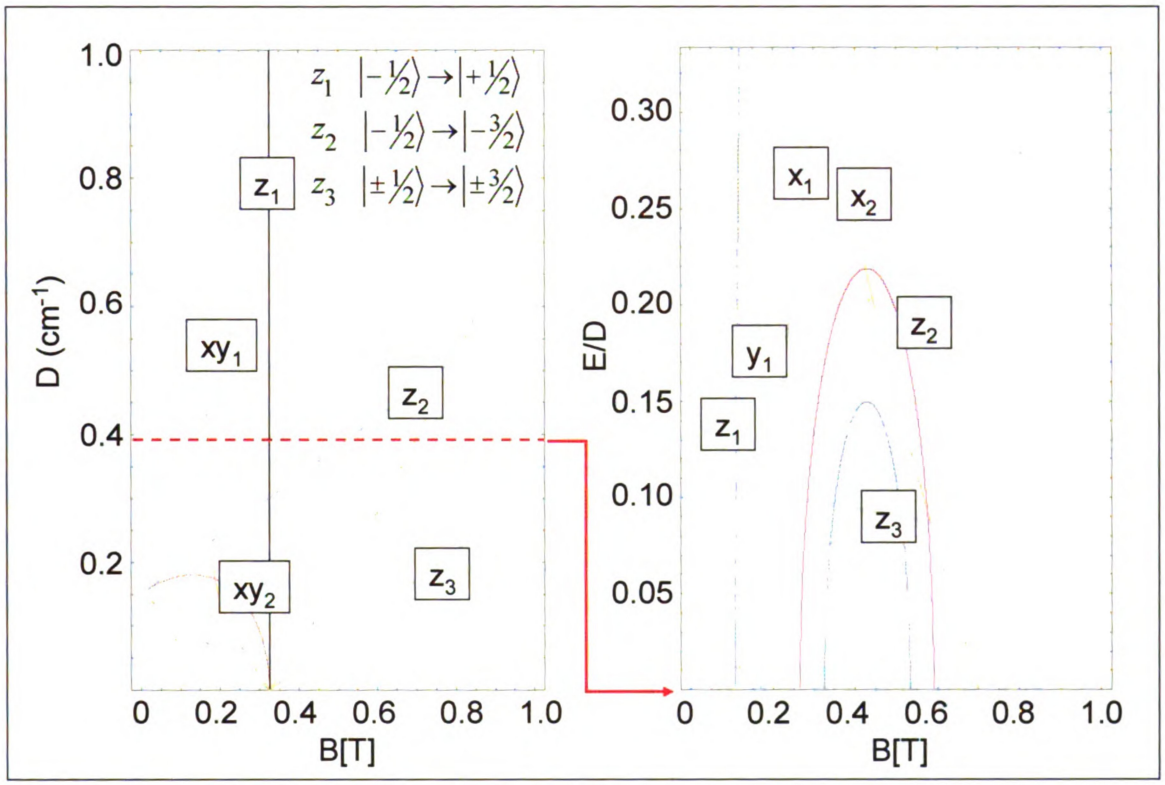

Figure 2-19: Transition diagrams for quartet systems. Left: Resonant field of transition at X- Band frequency for an axial quartet spin system with variable D. The labels indicate the origin of the particular transition as either the magnetic field parallel to the molecular z or xy axes, which are degenerate under axial symmetry. The line drawn across corresponds to the experimental value of D for the model complex, 0.396 cm^{-1}. Right: Resonant field of transition for a quartet system under rhombic symmetry for D = 0.396 cm^{-1} and variable E/D. The line drawn across the plot corresponds to the experimental value of E/D for the model complex, 0.308.

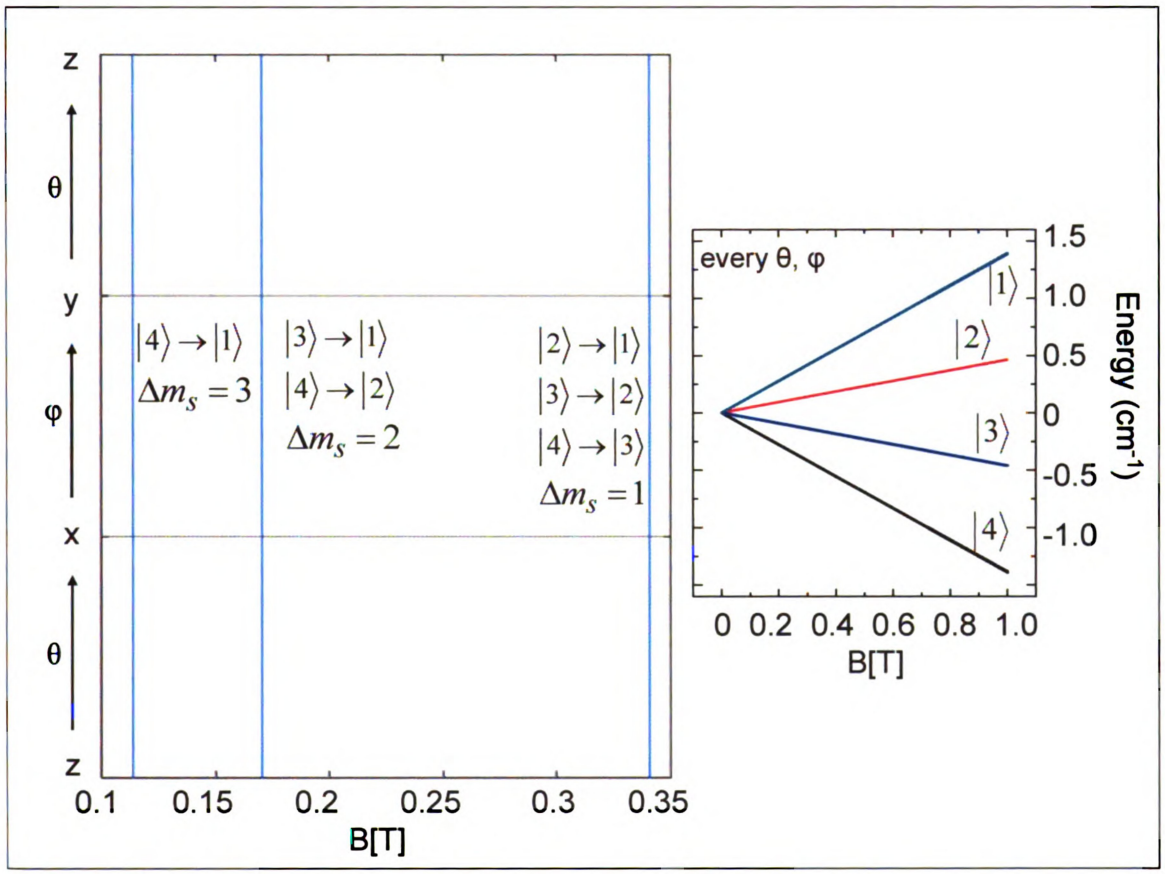

Figure 2-20: "Transition roadmap" of an isotropic quartet spin system. The diagram shows the position of transitions as a function of orientation with respect to the magnetic field. There are only three possible transitions in an isotropic system, and only the transition at g' = 2 (around 3300 G) is formally allowed.

Figure 2-21: (Facing page) Simulated spectra of quartet spin systems showing the effect of the axial and rhombic zero field splitting parameters. Top: Simulated spectra for variable D, from 0 to 0.5 cm^{-1}. The spectrum in red corresponds most closely to the experimental value of D for the model complex. Bottom: Variable E/D for D = 0.396 cm^{-1}, the experimental value of the model complex. The spectrum in red corresponds closely to the experimental E/D value for the model complex (0.308).

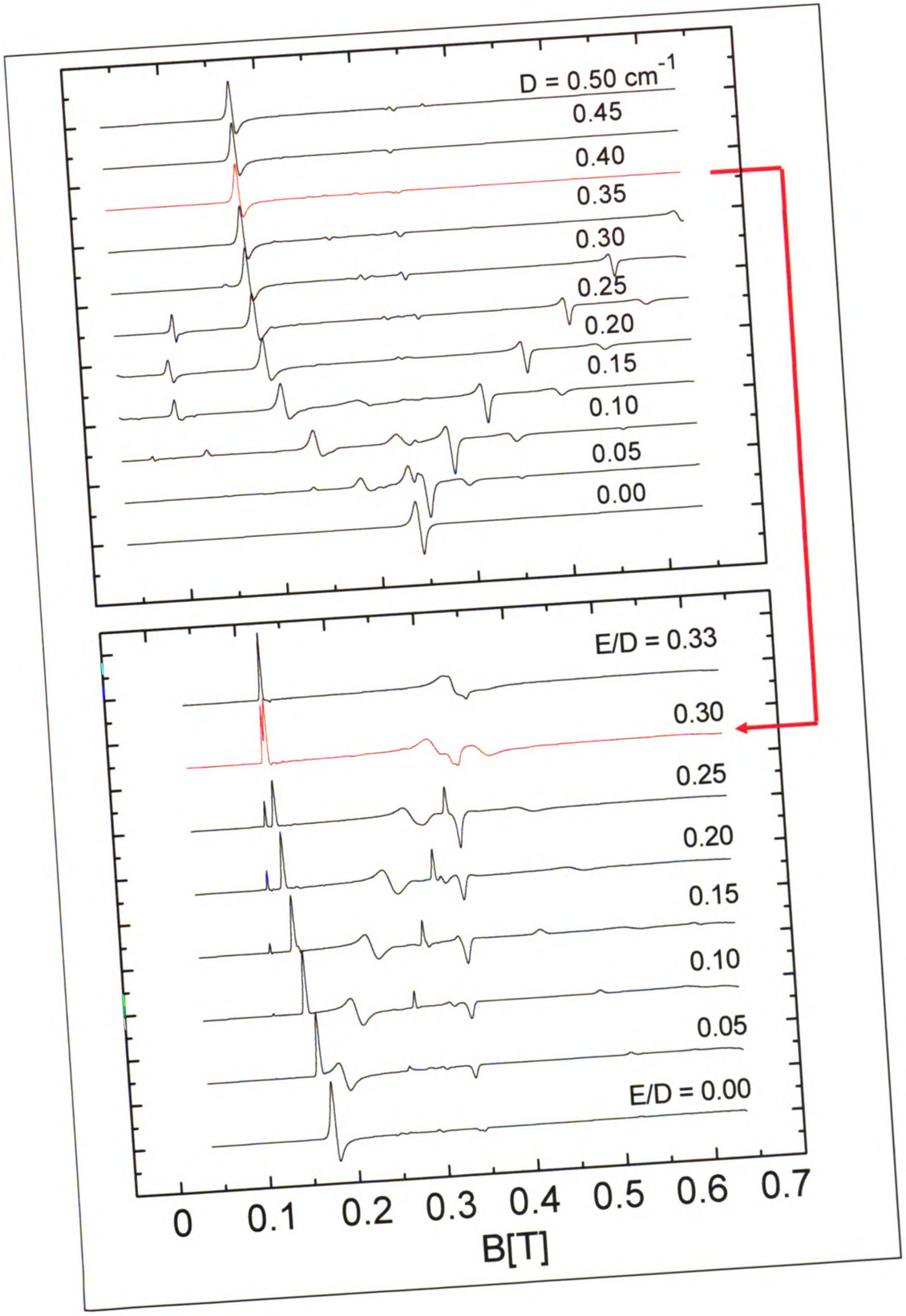
D = 0.50 cm-1
0.45
0.40
0.35
0.30
0.25
0.20
0.15
0.10
0.05
0.00
E/D = 0.33
0.30
0.25
0.20
0.15
0.10
0.05
E/D = 0.00
0
0.1
0.2
0.3
0.4
0.5
0.6
0.7
B[T]

A. Introduction of Axial Zero Field Splitting:

i. D = 0.396 cm^{-1}, the experimental value: Introducing the experimentally determined axial zero field splitting parameter (D = 0.396 cm^{-1}) drastically changes the spectrum. This is shown in the energy level diagrams of Figure 2-18 (middle column). Now the energy profile is dependent on the azimuthal angle (θ), but all orientations in the xy plane are degenerate. The effect of this particular symmetry on the field at which EPR transitions occur is seem most clearly in the transition roadmap of this system, Figure 2-22, where the field of transition for the two observed transitions in the xy plane does not change as orientations in the xy plane (changing ϕ) are sampled. To gain an insight into the effect of increasing D, one can look to the transition diagram for an axial quartet system (Figure 2-19, left) or the simulated spectra (Figure 2-21, top). As described above, for D = 0 (isotropic system), all allowed transitions occur at the same applied magnetic field. As D is increased these transitions diverge from g' = 2. The principal axes from which these transitions originate (either z or xy) are labeled. In Figure 2-19 (left) a line is drawn across the diagram which corresponds to the experimentally determined value of D for these Cr(III) systems. The spectrum that most closely matches this value is shown in red in Figure 2-21 (top). The transition roadmap (Figure 2-22) reveals wide resonances, and the energy profile changes dramatically with orientation as pure spin states mix. It should be noted that while the transition diagrams and transition roadmaps provide

information on the positions of transitions, it must be kept in mind that all transitions shown will not have the same transition probabilities. The simulations take this probability into account in order to construct the spectrum. Due to this, it is important to consider first the various simulations, which take into account the probability of a transition over all angles.

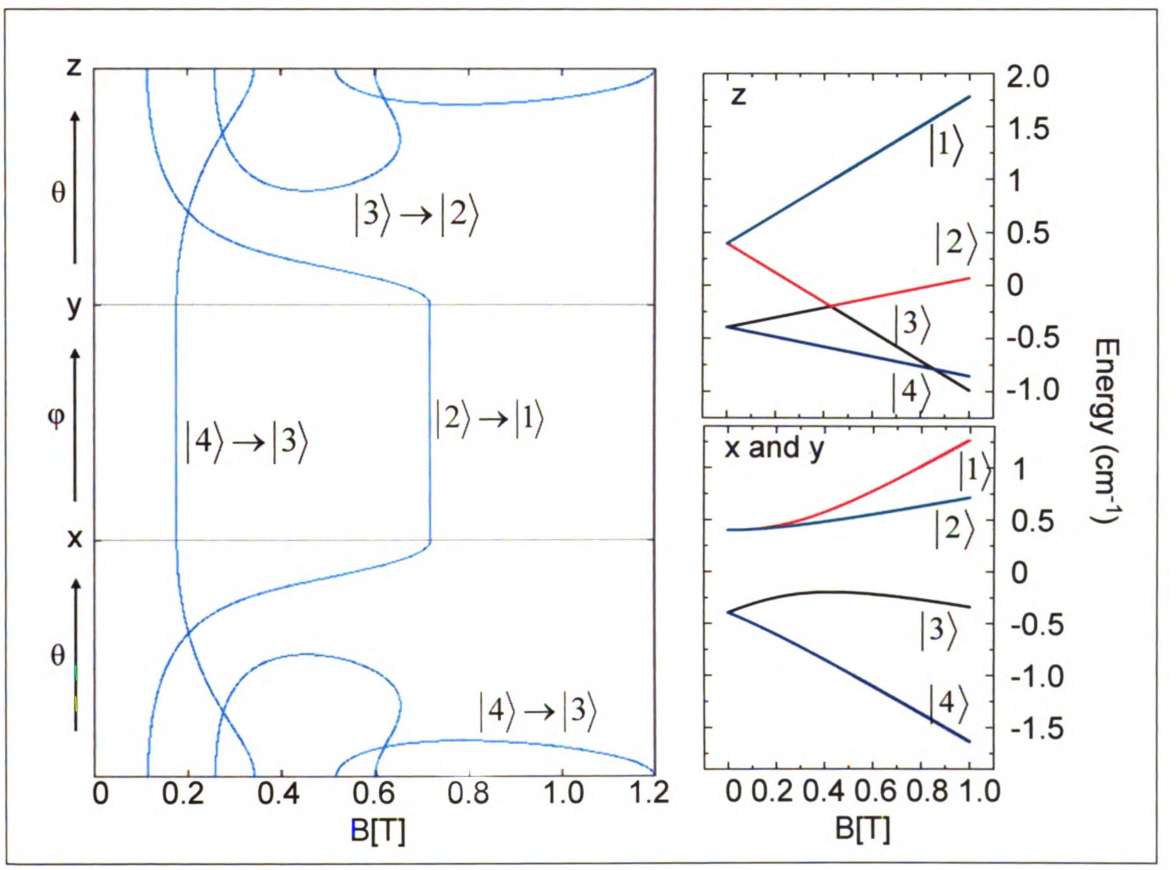

Figure 2-22: "Transition roadmap" of an axially symmetric quartet spin system, where D = 0.396 cm^{-1}, the experimentally observed value of the model system. The transitions are labeled according to the energy-level diagram on the right.

ii. General study, $0 \leq D \leq 0.5$ cm^{-1}. Simulations of axial quartet systems ($E = 0$) were carried out over the range $0 \leq D \leq 0.5$ cm^{-1}, and are plotted in Figure 2-23. In the limit of no zero field splitting ($D = 0$ cm^{-1}) only one peak can be observed, the $g' = 2$ resonance, which in this case is actually three different resonances occurring at the same field: $|-3/2\rangle \rightarrow |-1/2\rangle$, $|-1/2\rangle \rightarrow |+1/2\rangle$, and $|+1/2\rangle \rightarrow |+3/2\rangle$. In the limit of an isotropic g-tensor these transitions are completely orientation independent. Any introduction of zero field splitting then significantly complicates the spectrum. For example, multiple resonances which are nearly equally spaced are observed at $D = 0.05$ cm^{-1}, and as D increases these lines begin to move apart. The spectrum then simplifies again for larger values of D. This can be understood most simply by monitoring the transitions across a series of energy-level diagrams of the quartet ground state (Figure 2-24). At the limit of no zero field splitting the x, y, and z axes are equivalent, that is, the system is isotropic, and there are three different transitions occurring at the same magnetic field. Along the magnetic z axis, as D increases these transitions diverge, producing transitions both upfield and downfield of the transition around 3300 G (black arrow), which remains constant, and is best described as $\left|-\frac{1}{2}\right\rangle \rightarrow \left|+\frac{1}{2}\right\rangle$, although, as discussed above (*vide supra*) when $h\upsilon_{res} \approx D$ this description may not be the most accurate due to mixing of the pure spin states. Eventually the transitions present at low zero field splitting, which are best described as $\left|-\frac{1}{2}\right\rangle \rightarrow$

$\left|-\frac{3}{2}\right\rangle$ and $\left|+\frac{1}{2}\right\rangle \rightarrow \left|+\frac{3}{2}\right\rangle$ (green arrows) fall out of resonance, and the $\left|-\frac{1}{2}\right\rangle \rightarrow \left|-\frac{3}{2}\right\rangle$ transition (again, this may not be the best description) is reintroduced at higher values of D (turquoise arrow). The situation is similar along the x and y axes, although this time the states can not be expressed as having pure ½ or $^3/_2$ spin (*vide supra*). The transitions for the axial case are summarized in a transition diagram (Figure 2-25). In this diagram the transitions are labeled according to their origin, for B either parallel to the z axis (labels z_1, z_2, and z_3) or the x or y axes, which are degenerate in the case of an axially symmetric system (labels xy_1 and xy_2). The diagram clearly shows only one transition in the limit of no zero field splitting (with the exception of the spin-disallowed $\left|-\frac{1}{2}\right\rangle \rightarrow \left|+\frac{3}{2}\right\rangle$ $(\Delta m_s = 2)$ transition, which is plotted but not observed experimentally) and a further simplification of the spectral appearance occurs for D > 0.50 cm^{-1}, where only resonances at g'≈ 2 and g' ≈ 4 (where $g' = h\nu/\beta_e B$) remain within the range 0 ≤ B ≤ 7000 G.

Figures 2-26 and 2-27 shows the energy level diagram and transition diagram for an axially symmetric system at W-band frequency (resonances at about 3.3 cm^{-1}). Although the pattern shown in the transition diagram is the same as that for the transitions at X-band frequency, the important point is that the range of the plot is up to 8 cm^{-1}, meaning that one's ability to assign the proper sign and magnitude of the zero field splitting is greatly enhanced at this frequency.

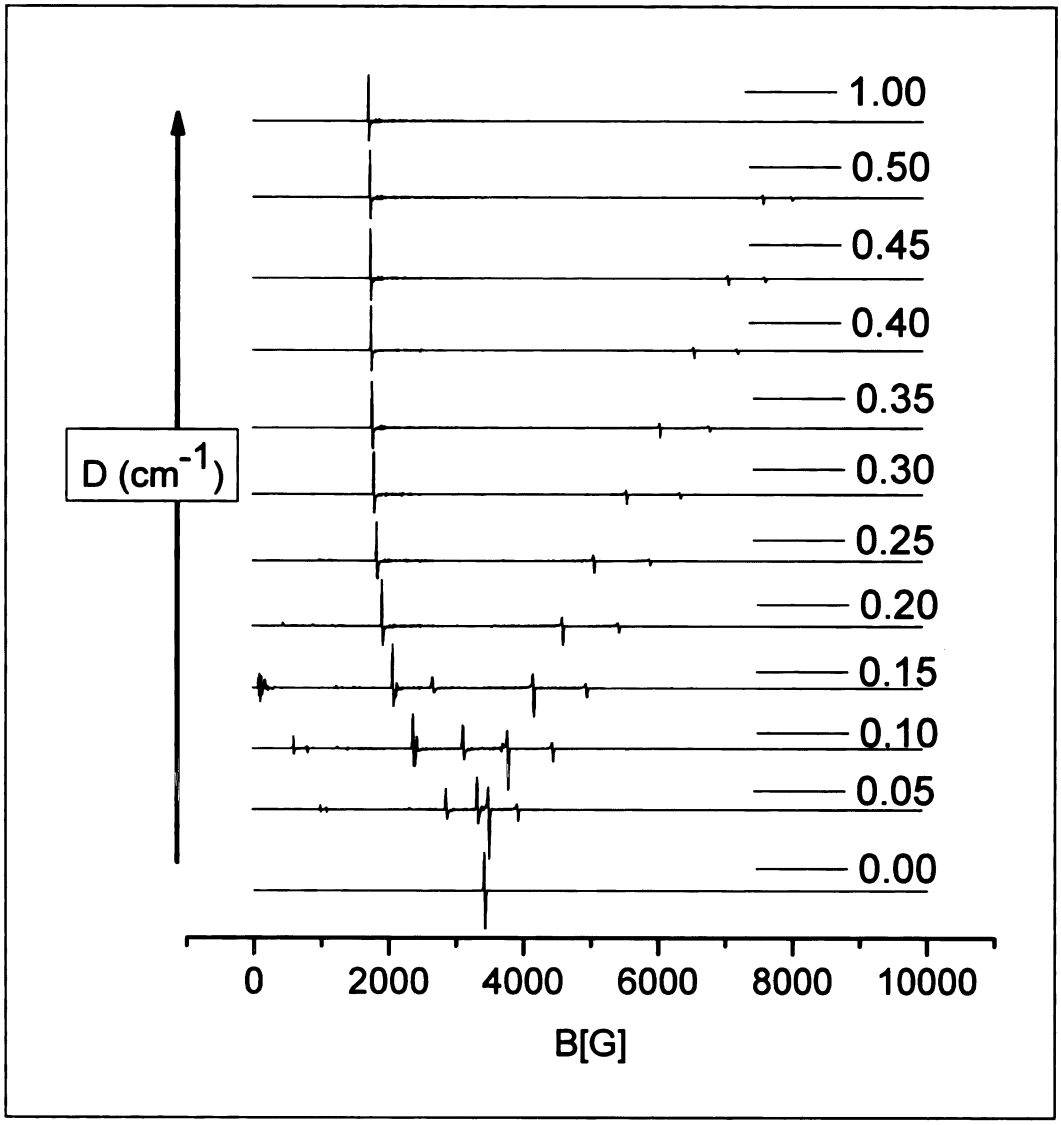

Figure 2-23: Calculated X-band EPR spectra for an axial quartet spin system with variable D (in cm^{-1}).

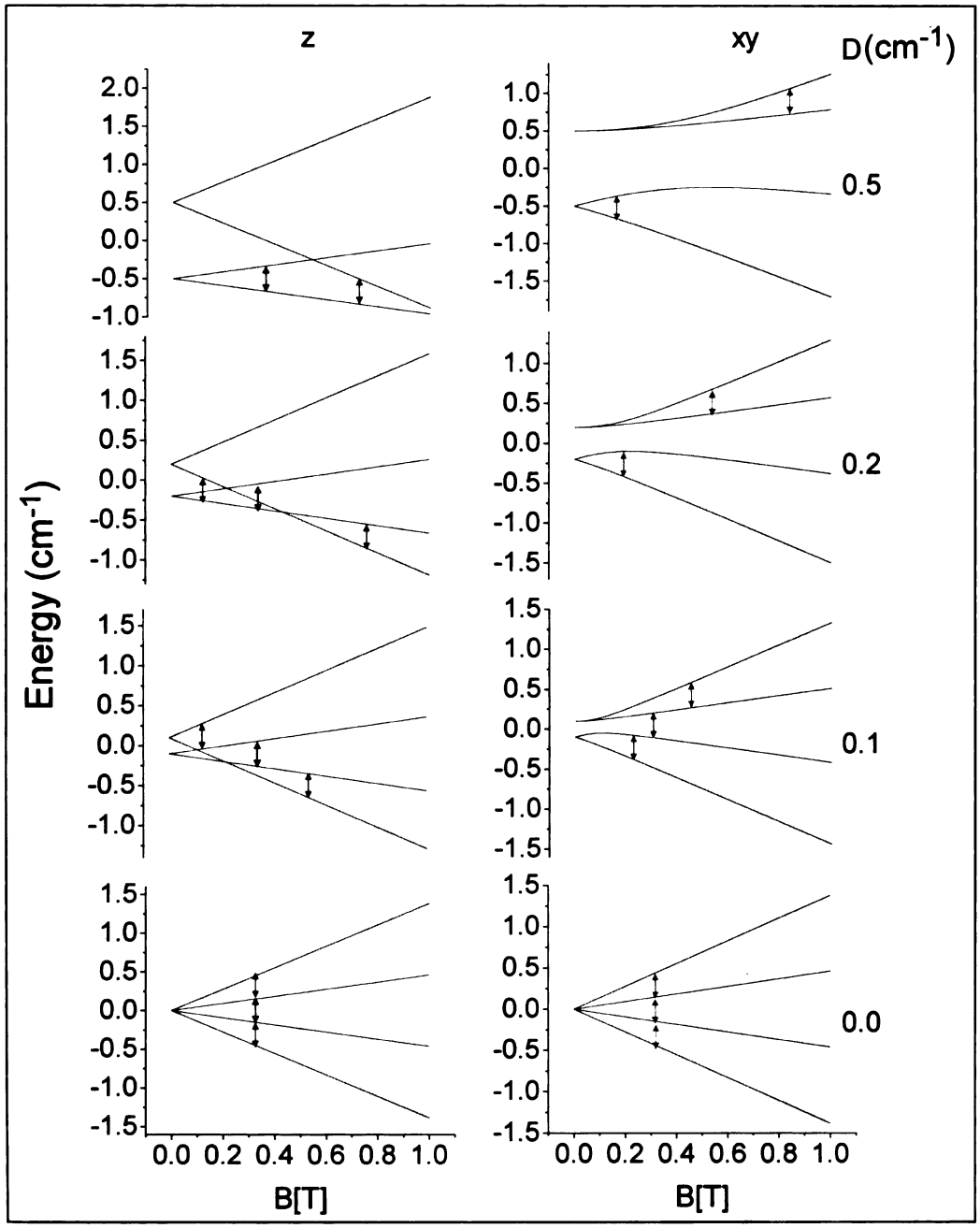

Figure 2-24: Energy level diagrams for B parallel to the x (or y), and z magnetic axes for an axial quartet spin system with variable D (in cm^{-1}).

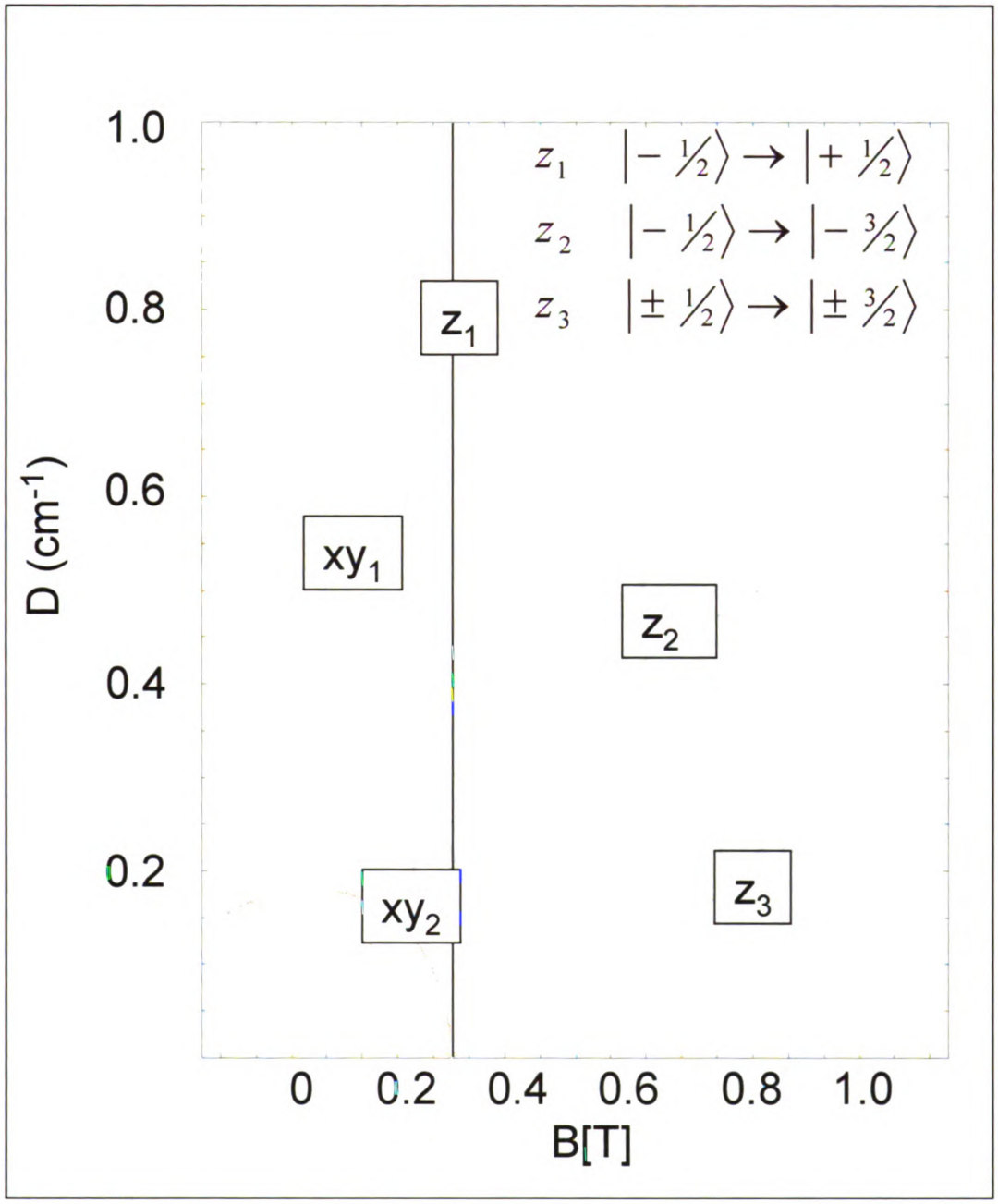

Figure 2-25: Resonant field of transition at X-Band frequency for an axial quartet spin system with variable D. These transitions are color-coded to those of Figure 2.24.

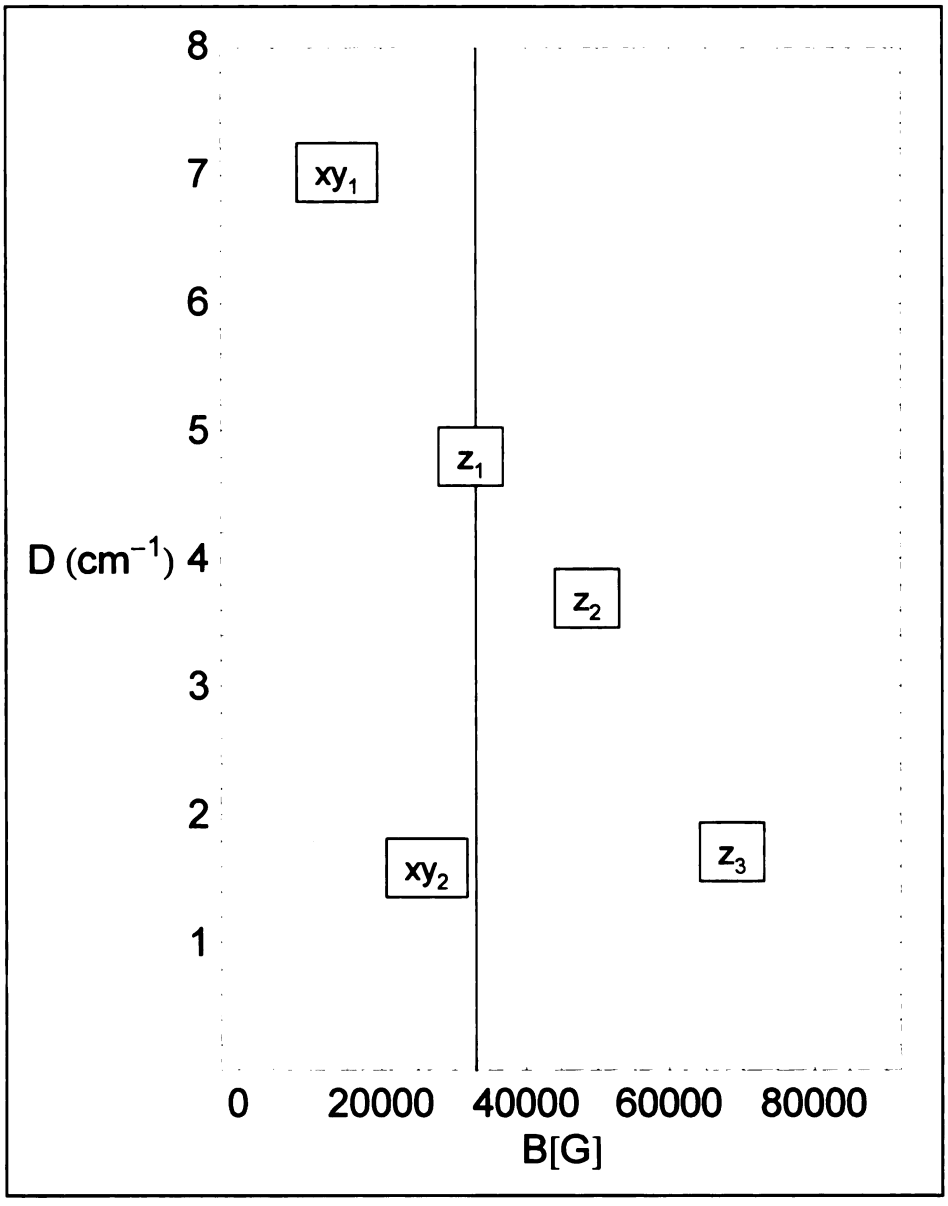

Figure 2-26: Resonant field of transition diagram along the X, Y, and Z magnetic axes for an axial quartet spin system with variable D (in cm^{-1}). The resonances are at W-Band frequency, and are color-coded to the energy-level diagram (Figure 2-27).

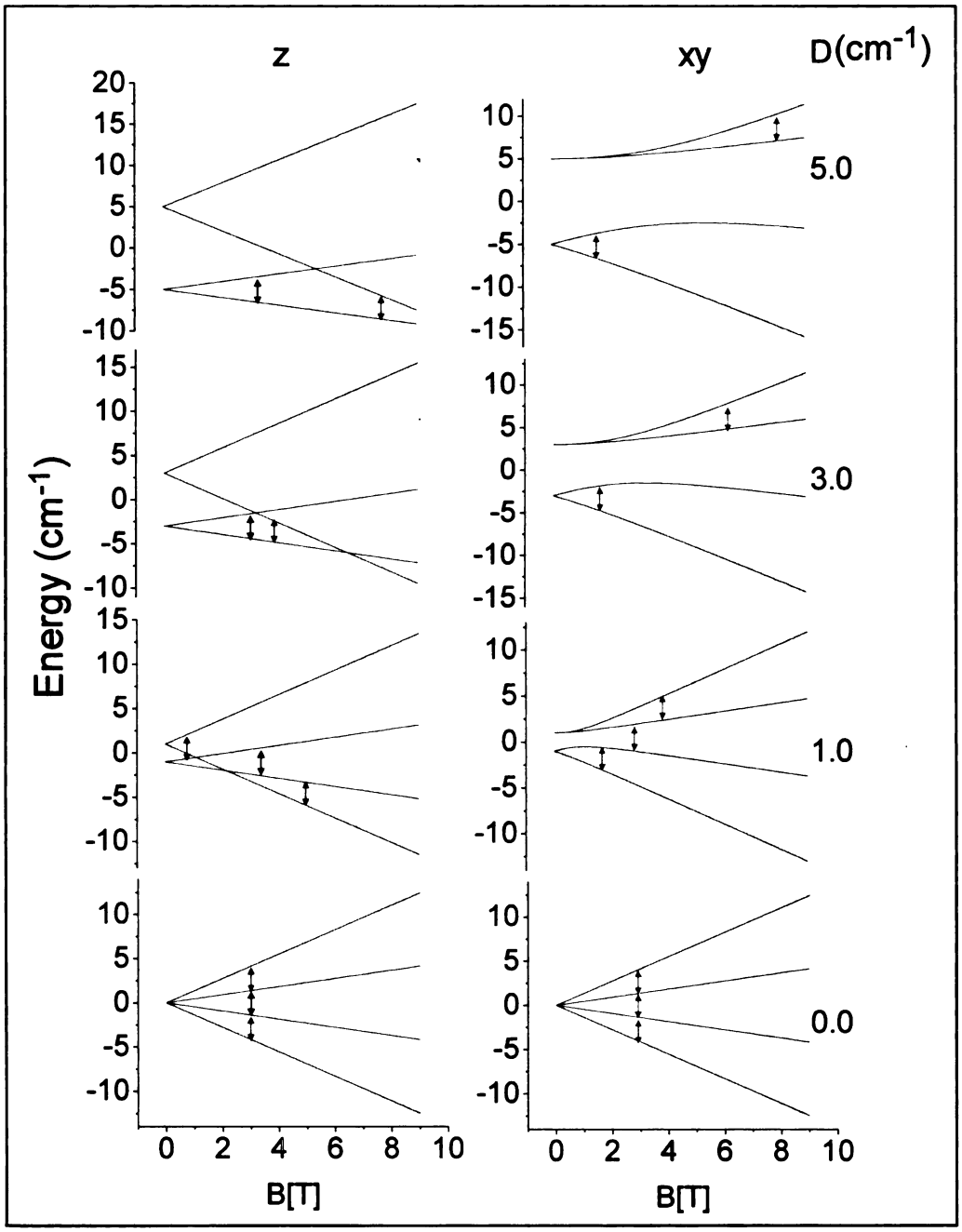

Figure 2-27: Energy level diagrams along the X, Y, and Z magnetic axes for an axial quartet spin system with variable D (in cm^{-1}). Resonances are shown at W-band frequency.

B. Rhombic model:

i. D = 0.396 cm^{-1} and E = 0.124 cm^{-1}, the experimental values: Introduction of the rhombic zero field splitting parameter, E, results in subtle changes to the energy profile, as modifying the polar angle (ϕ) now results in different energy profiles, and the principal x and y axes are now nondegenerate. The outcome of these two factors can be seen by comparing Figure 2-28, the transition roadmap for the experimentally determined values of D and E, to Figure 2-22, the corresponding diagram for the axial system. In the rhombic case, while the two separate $|4\rangle \rightarrow |3\rangle$ transitions blend into one, the $|3\rangle \rightarrow |2\rangle$ transition, which had resonances along the principal z-axis in the axial case, is now a closed loop, with transitions only for $0 < \theta < \pi/2$. Additionally, while changes in the $|2\rangle \rightarrow |1\rangle$ and $|4\rangle \rightarrow |3\rangle$ transitions may appear subtle, the result is a drastically different EPR spectrum (Figure 2-21, lower, in red). This is due primarily to variation with the polar angle, creating extremely wide resonances.

The right side of Figure 2-19 coupled with the series of spectra of Figure 2-20 demonstrate the effect of changing the ratio E/D while keeping the value of D fixed (in this instance, for the experimentally determined value of D = 0.396 cm^{-1}). For the transition diagrams (Figure 2-19) it must be kept in mind that only the orientations along the principal axes for which the magnetic field is applied are plotted. Therefore, the looping $|3\rangle \rightarrow |2\rangle$ transition observed between the principal z and y axes in Figure 2-28 will not appear on this diagram. However, the

transition diagram still has some utility: the red dashed line drawn across the top of Figure 2-19 corresponds to the experimental E/D value for our systems, and predicts very well the positions and origins of the observed EPR transitions.

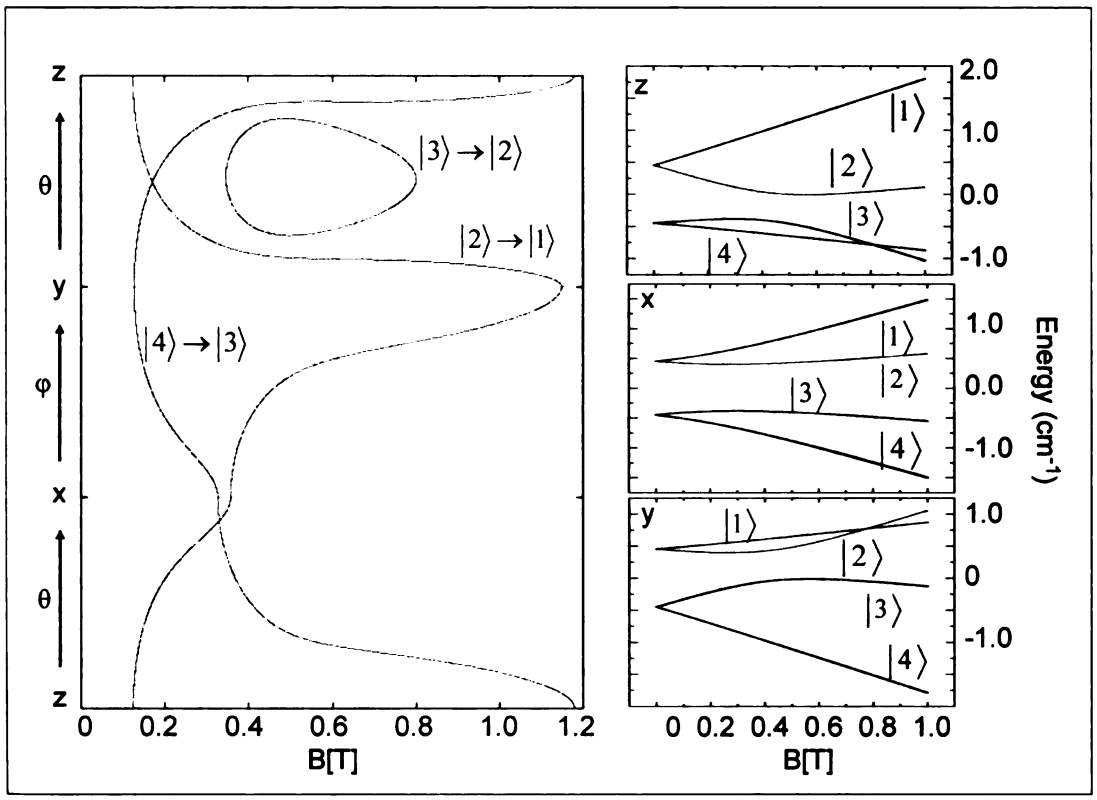

Figure 2-28: "Transition roadmap" of a rhombic quartet spin system, where D = 0.396 $cm^{-1}$and E = 0.124 cm^{-1}, the experimentally observed values of the model system. The transitions are labeled according to the energy-level diagram on the right.

ii. General study of rhombic quartet systems. For the case of a rhombic quartet spin system a series of spectra were obtained by selecting a value of D, ranging from 0.05 cm^{-1} to 0.50 cm^{-1}, and the ratio E/D was changed until the

theoretical maximum of 1/3 was reached, producing the series of spectra and transition diagrams presented in Figures 2-29 through 2-40. This maximum value is the result of a convention which places the x-axis at the highest energy.[18] For the transition diagram the eigenvalues are solved for a certain value of D ($0 < D < 1$ cm^{-1}) and viable solutions are simply divided by D so that the ratio E/D can be plotted. In the case of rhombic systems the spectra are much more difficult to describe than in the axial case. Three separate cases will be examined to gain an understanding of the origin of transitions across this series: 1.) spectra up to D = 0.15 cm^{-1}, with a detailed look at energy-level and transitions diagrams at D = 0.10 cm^{-1}, 2.) evolution of the spectra from D = 0.20 cm^{-1} to D = 0.30 cm^{-1}, with a detailed examination of the spectra for D = 0.30 cm^{-1}, and 3.) evolution from D = 0.35 to 0.50 cm^{-1}.

The most striking feature of the spectra for $D \leq 0.15$ cm^{-1} (Figures 2-29 and 2-30) is the high density of transitions between 1000 and 6000 G, with relatively few or no transitions at higher magnetic fields. This is due to the fact that for $D \leq 0.15$ cm^{-1}, the zero field splitting of $2|D|$ is less than or equal to the energy of resonance, ~0.30 cm^{-1}, with the result that certain transitions are accessible which are not accessible at higher zero field splitting. At D = 0.05 cm^{-1}, all of the transitions are contained within the window $1000 < B < 5000$ G, and there is very little change in the spectra as E/D is varied from 0.00 to 0.33, reflecting very small changes in the energy profile. In general, characteristic spectra at this value of D

will display a number of transitions in the g = 2 region, with several transitions at lower magnetic fields.

As D is increased to 0.10 cm^{-1} a pronounced spreading out of the peaks away from the g = 2 region is observed, although the transitions are still contained within the window 0 < B < 6000 G. A characteristic peak is observed around 600 G. The energy level diagram, Figure 2-31, which is summarized by the transition diagram, Figure 2-32, reveals that a large number of transitions, representing every possible combination of initial and final spin states, are capable of being probed at this value of D. As D is increased to 0.15 cm^{-1} certain transitions with large oscillator strengths are pushed to lower fields, as the splitting of the Kramer's doublets now equals the microwave quantum at which spin resonance occurs. The observed spreading of the spectrum continues.

For $D \geq 0.15$ cm^{-1} the spectra begin to simplify, to some extent, as certain transitions fall out of resonance due to the magnitude of the zero field splitting. Another pattern emerges which is most easily observable in a transition diagram—the solutions for B parallel to the z-axis have a parabolic shape, and solutions for B parallel to the x-axis converge at E/D = 0.33. This means that for E/D = 0 two resonances exist which begin to converge around g' = 2 as E/D is increased. This is observed in the series of spectra for D = 0.20 cm^{-1}, where resonances at 2000 and 4700 G for E/D = 0 converge around g' = 2 at the maximum value of E/D. The same pattern is observed for larger values of D, but as D increases the initial

position of the higher field transition moves to ever higher fields. In the energy-level diagram and transition diagram for D = 0.30 cm^{-1} (Figure 2-34 and 2-35, respectively) one can observe the parabolic transition along the z-axis (red arrows), which falls out of resonance around E/D = 0.29, and the convergence of the solutions along the x-axis as E/D is increased (green and orange arrows).

As D increases beyond 0.30 cm^{-1} the transitions attributed to the z-axis move to higher magnetic fields, and a second parabolic transition emerges. Again, the most conspicuous feature of this series of spectra (Figures 2-36 through 2-38) is that as E/D approaches the limit of 1/3, several transitions converge around g'= 2, while two others converge around g' = 4. The energy level diagram for D = 0.50 cm^{-1}, Figure 2-39, reveals that this is indeed the case: the transitions converging at g' = 2 can be attributed to transitions along the x-axis and those converging at g' = 4 correspond to transitions along the z and y axes. The transitions that converge around g' = 4 vary little with changing E/D, as they are contained within a single split Kramer's doublet. The parabolic transitions of the z-axis fall out of resonance at E/D = 0.17 and 0.27. The transition diagram of Figure 2-40 summarizes the allowed perpendicular-mode transitions within this system.

The series of spectra for D = 1.00 cm^{-1}, Figure 2-38, reveals that the trends continue even with very large values of D. Again transitions converge around g' = 4, attesting to the fact that these transitions occur within a single split Kramer's

doublet, and their field of resonance should therefore, to a first approximation, be independent of the zero field splitting.

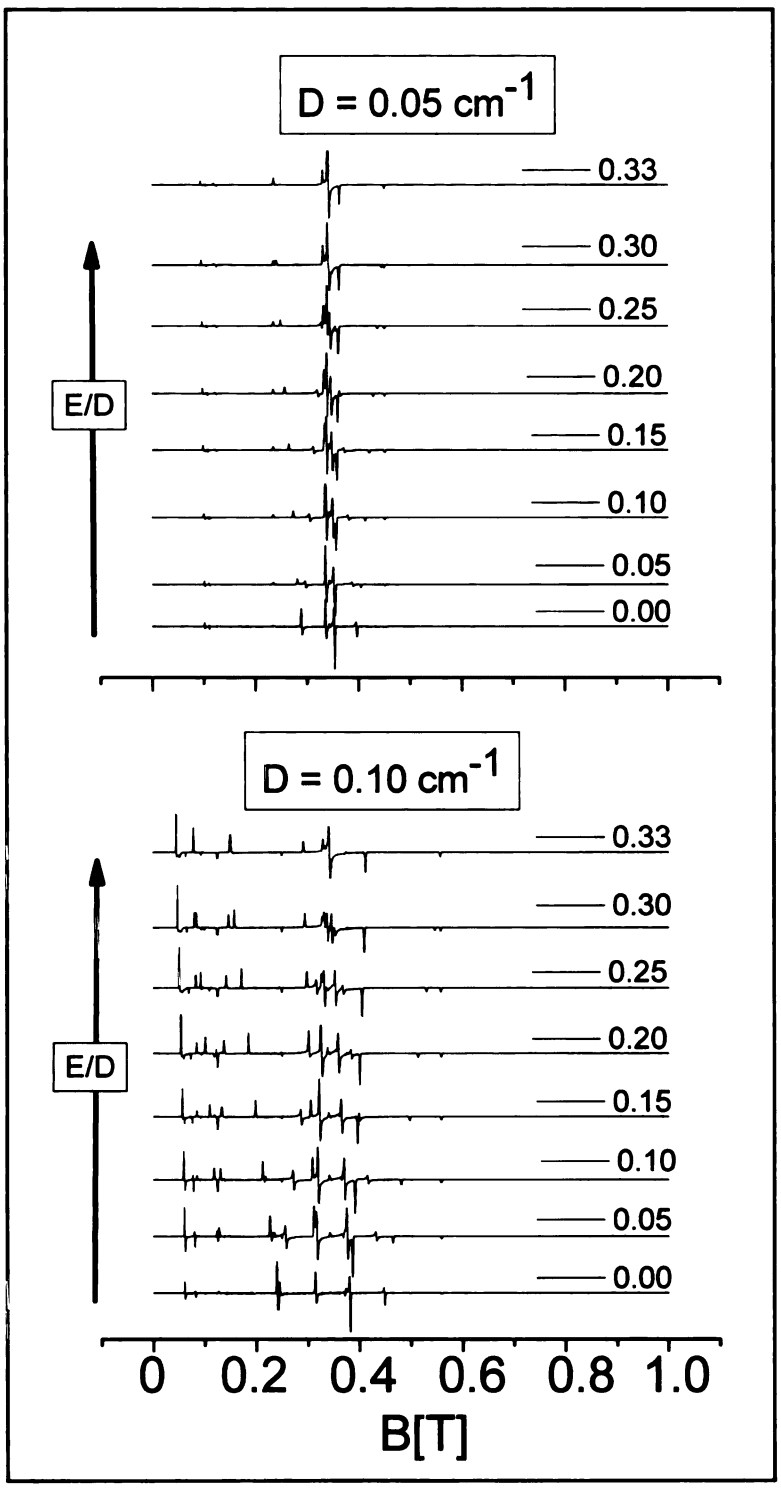

Figure 2-29: Calculated X-band EPR spectra for quartet spin system with D = 0.05 and 0.10 cm^{-1} and variable E/D.

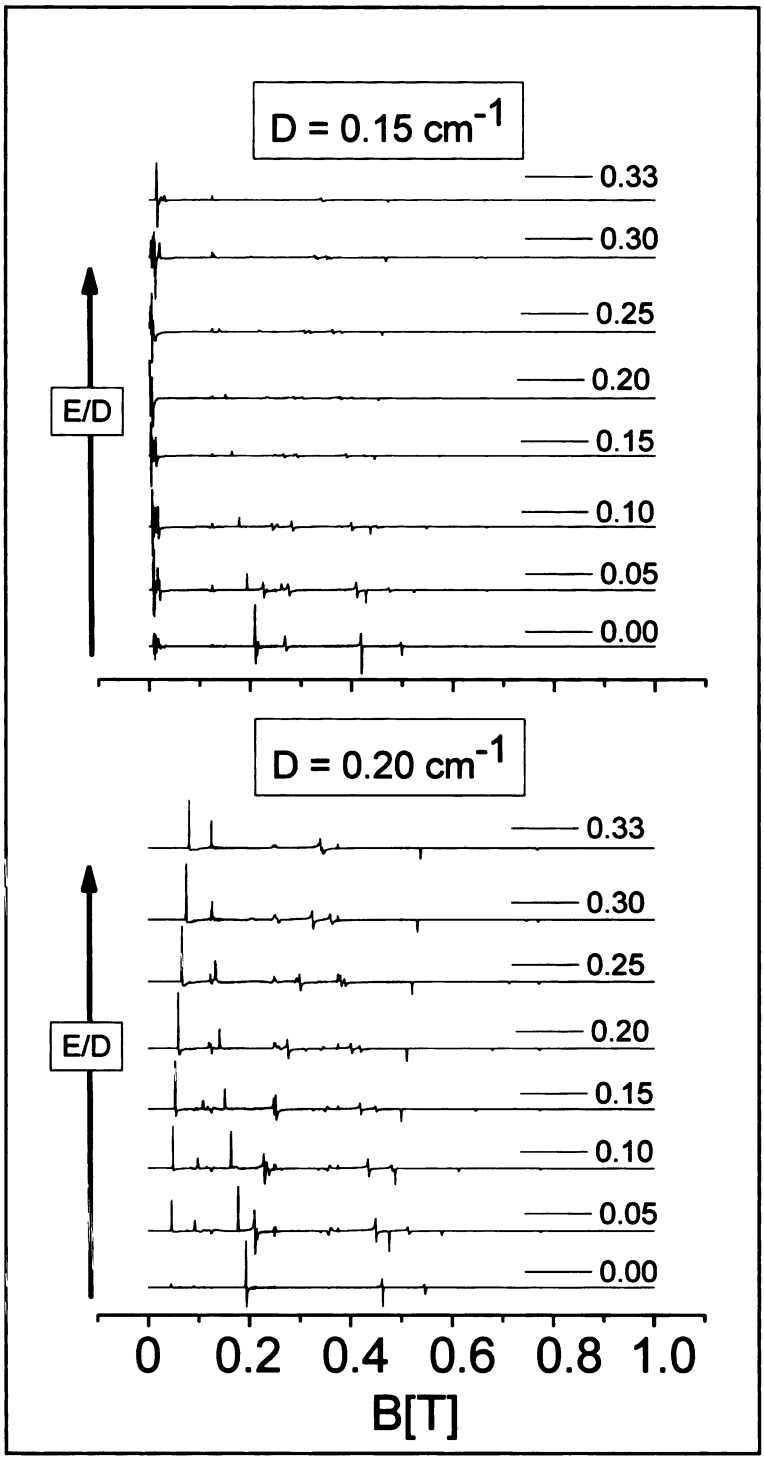

Figure 2-30: Calculated X-band EPR spectra for quartet spin system with D = 0.15 and 0.20 cm^{-1} and variable E/D.

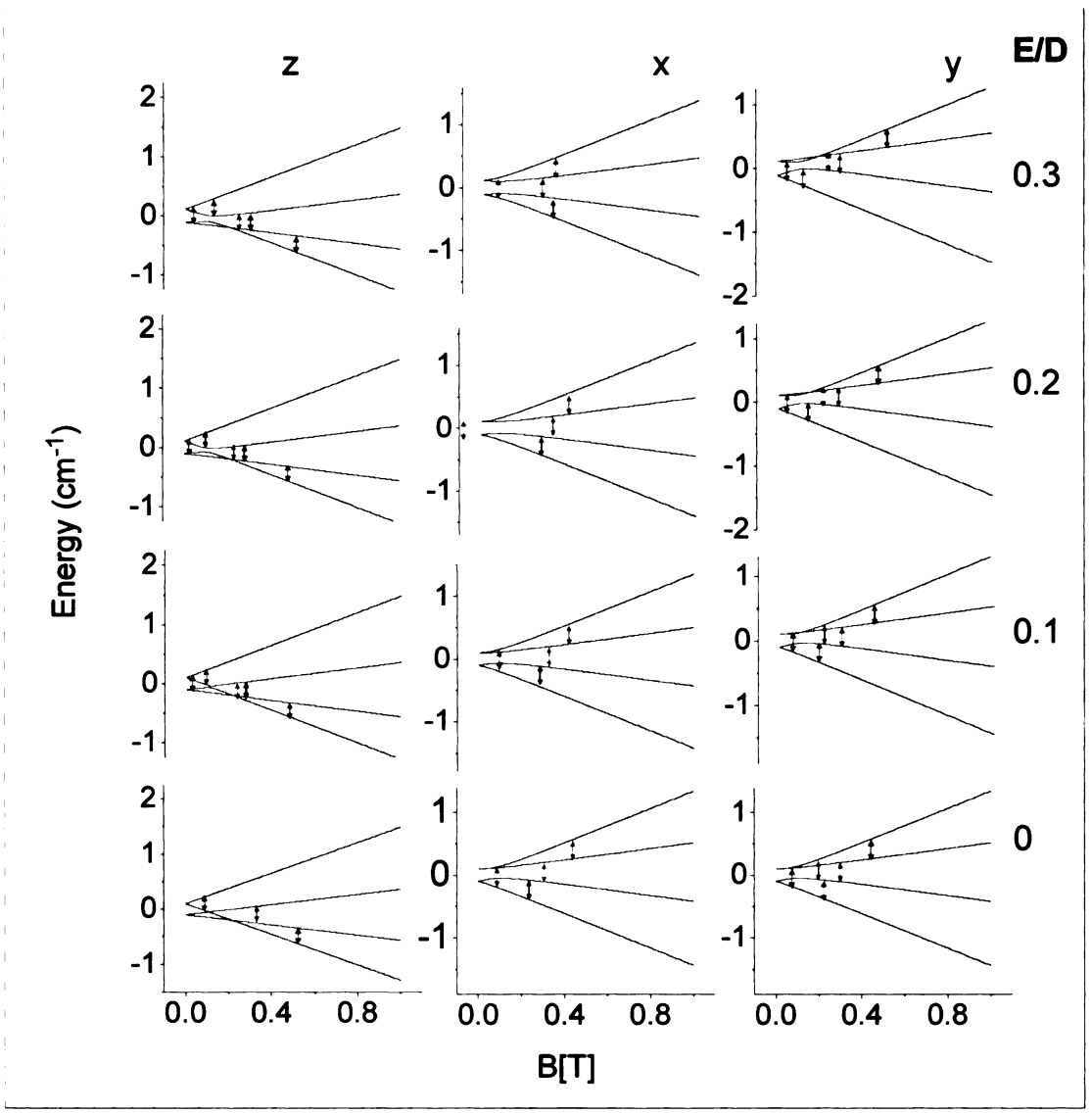

Figure 2-31: Energy level diagrams along the X, Y, and Z magnetic axes for a quartet spin system with D = 0.10 cm^{-1} and variable E/D. The resonances are at X-band frequency, and are color-coded to Figure 2-32.

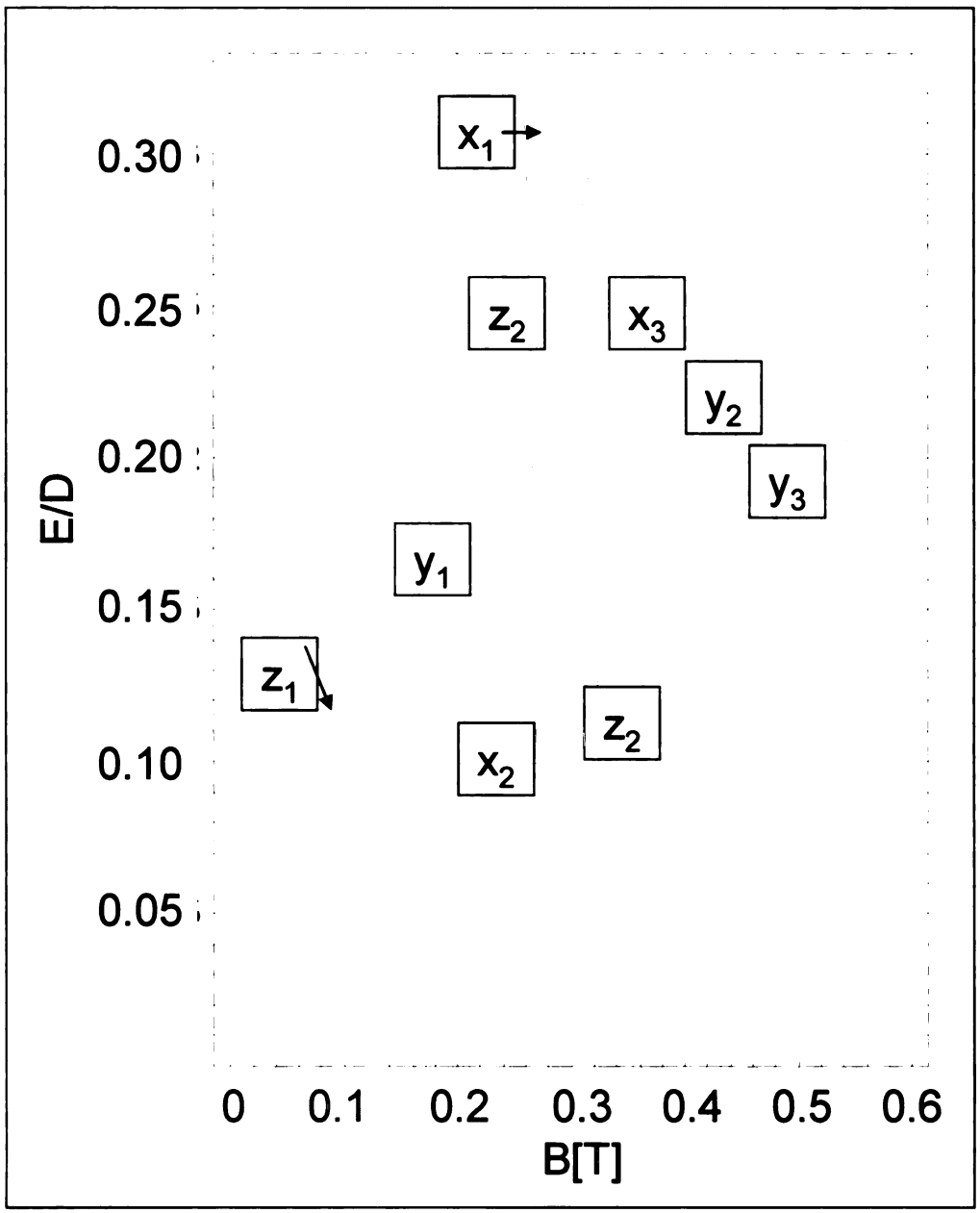

Figure 2-32: Resonant field of transition at X- Band frequency for a quartet spin system with D = 0.10 cm^{-1} and variable E/D.

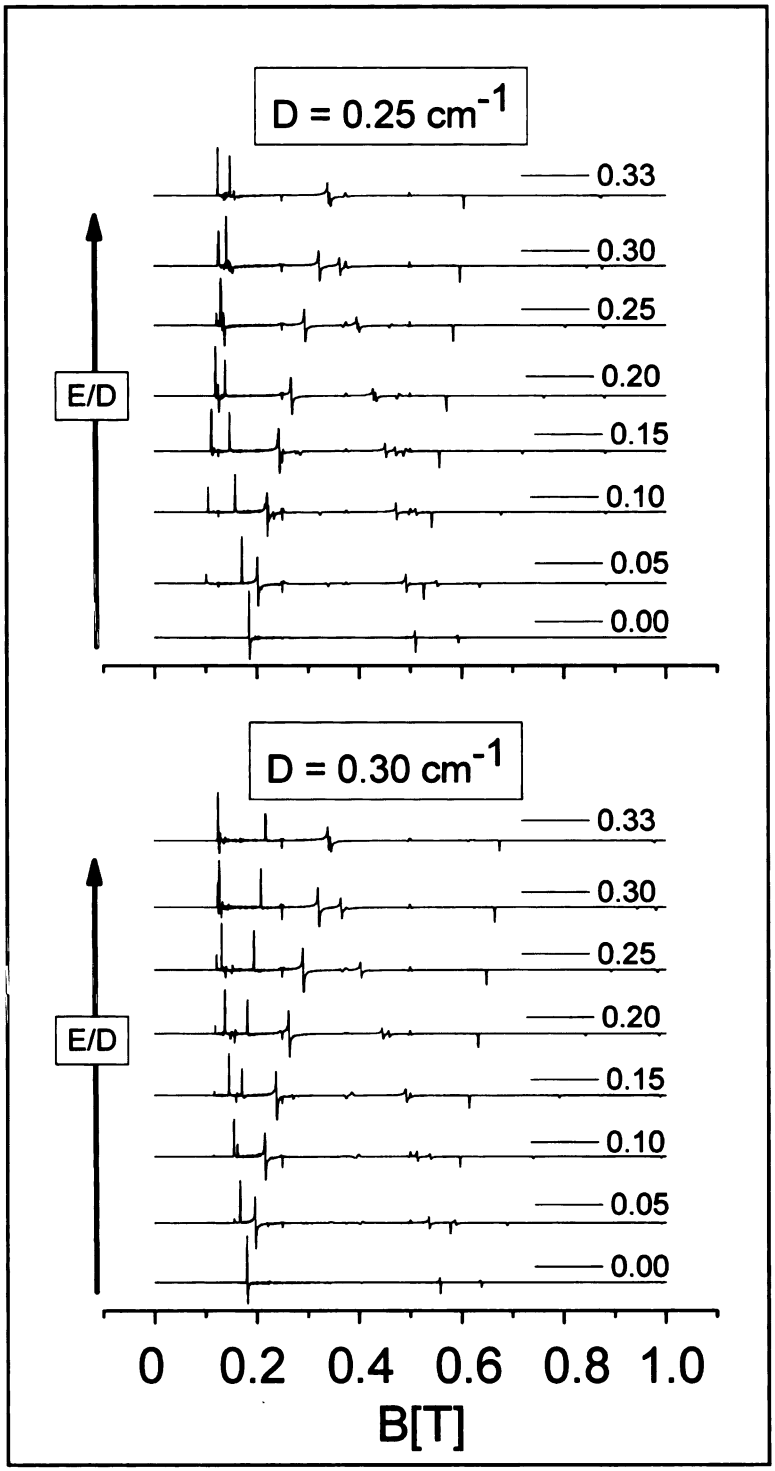

Figure 2-33: Calculated X-band EPR spectra for quartet spin system with D = 0.25 and 0.30 cm^{-1} and variable E/D.

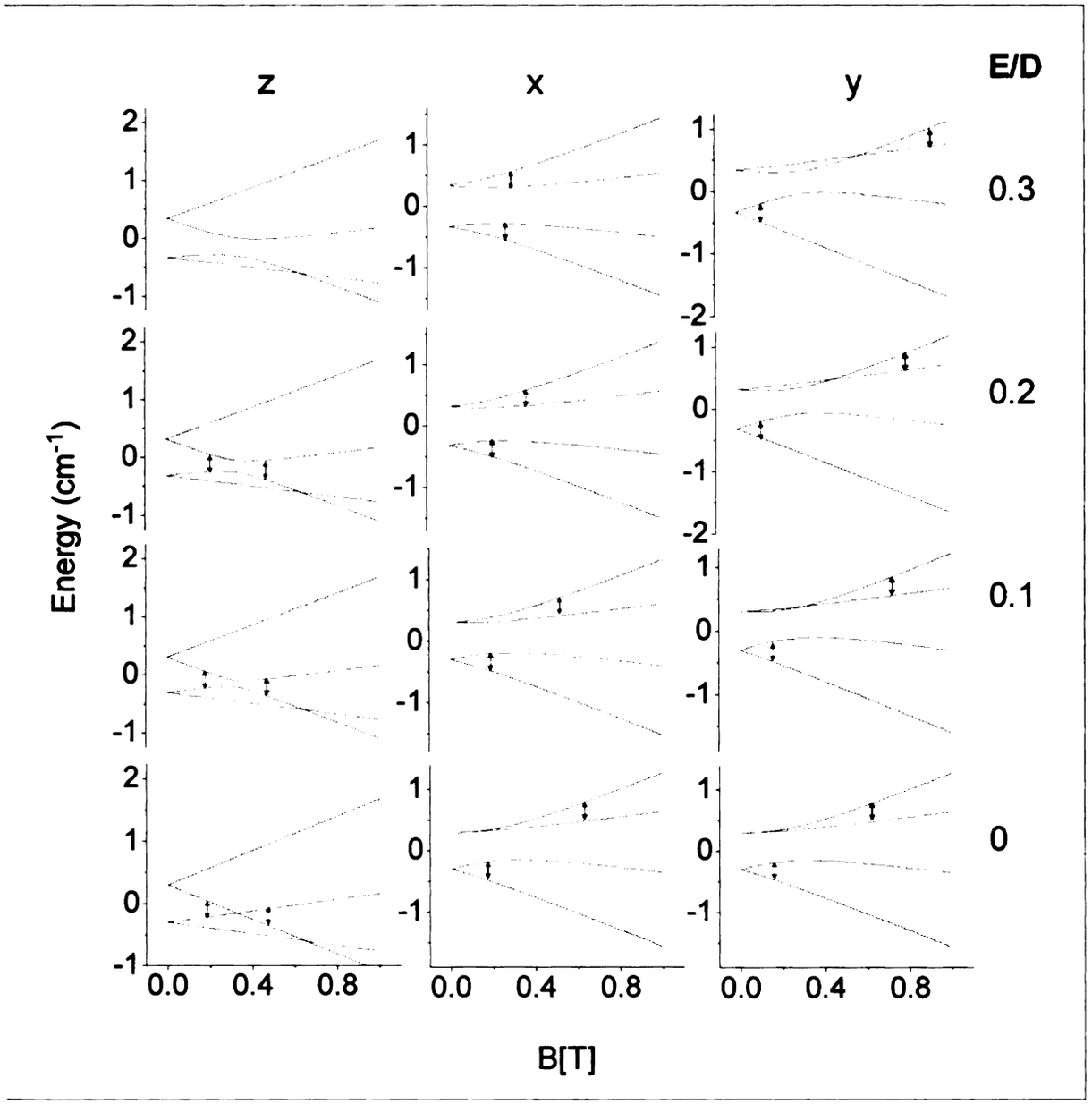

Figure 2-34: Energy level diagrams along the X, Y, and Z magnetic axes for a quartet spin system with D = 0.30 cm^{-1} and variable E/D. The resonances are at X-band frequency, and are color-coded to Figure 2-35.

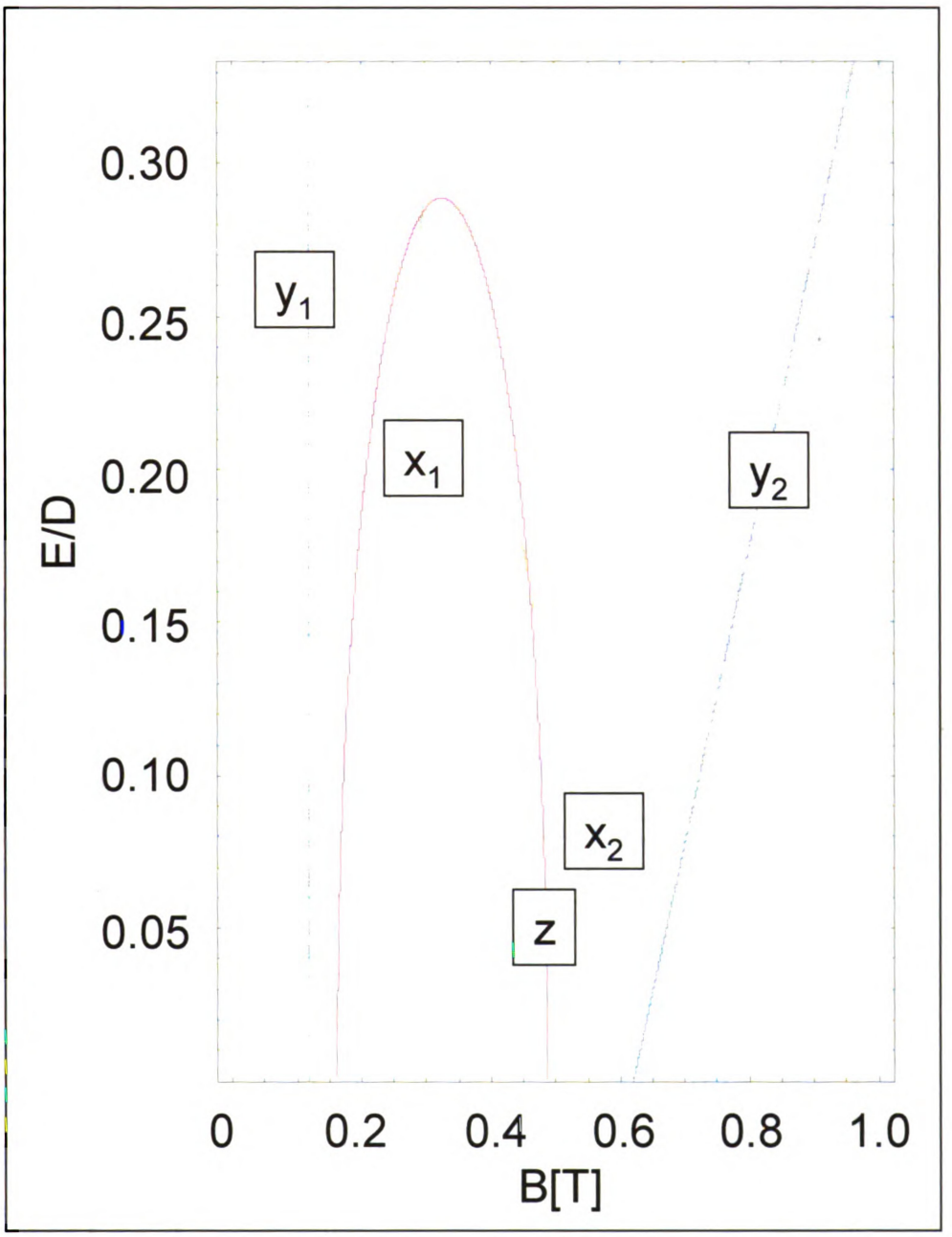

Figure 2-35: Resonant field of transition at X- Band frequency for a quartet spin system with D = 0.30 cm^{-1} and variable E/D.

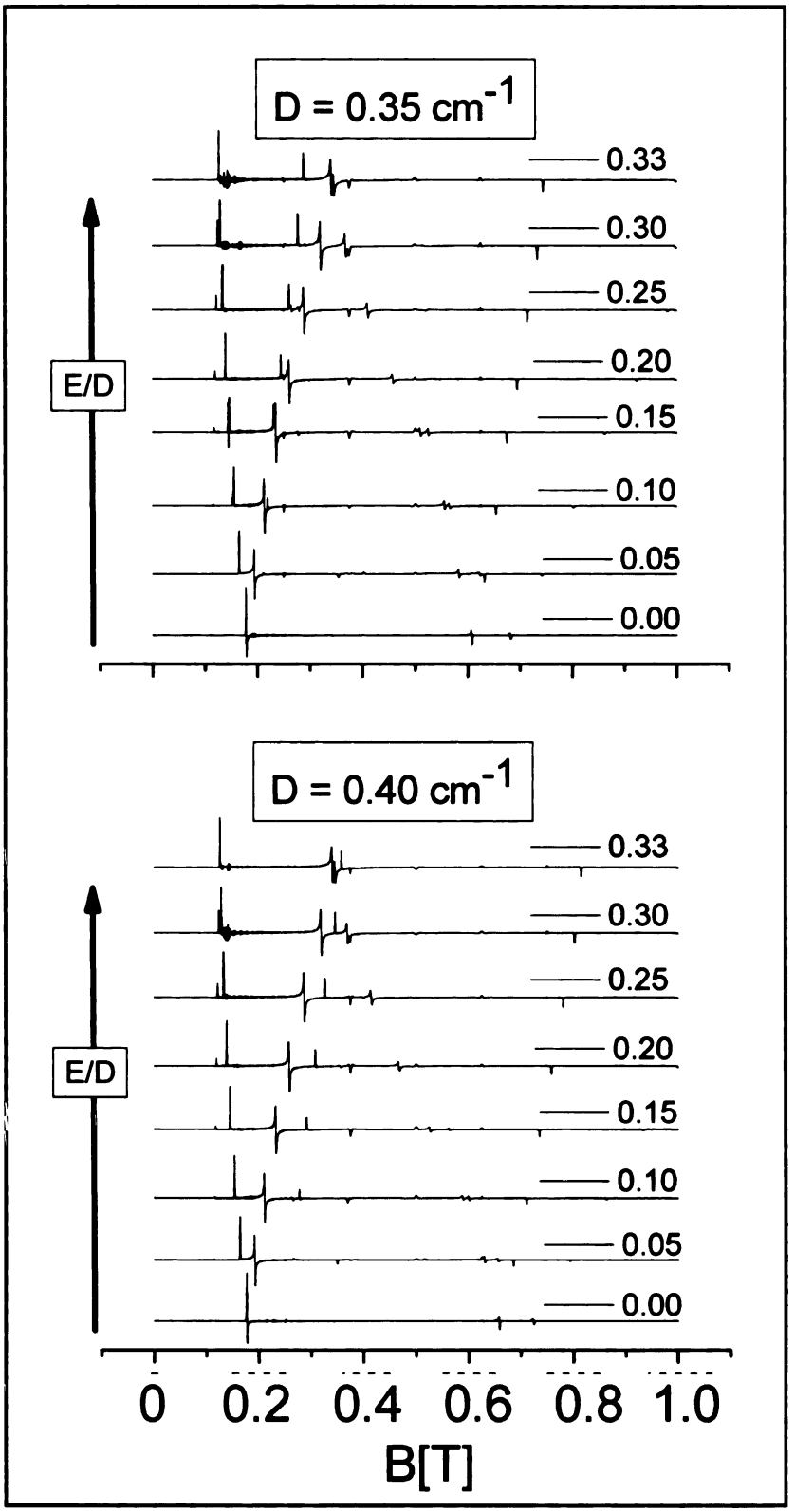

Figure 2-36: Calculated X-band EPR spectra for quartet spin system with D = 0.35 and 0.40 cm^{-1} and variable E/D.

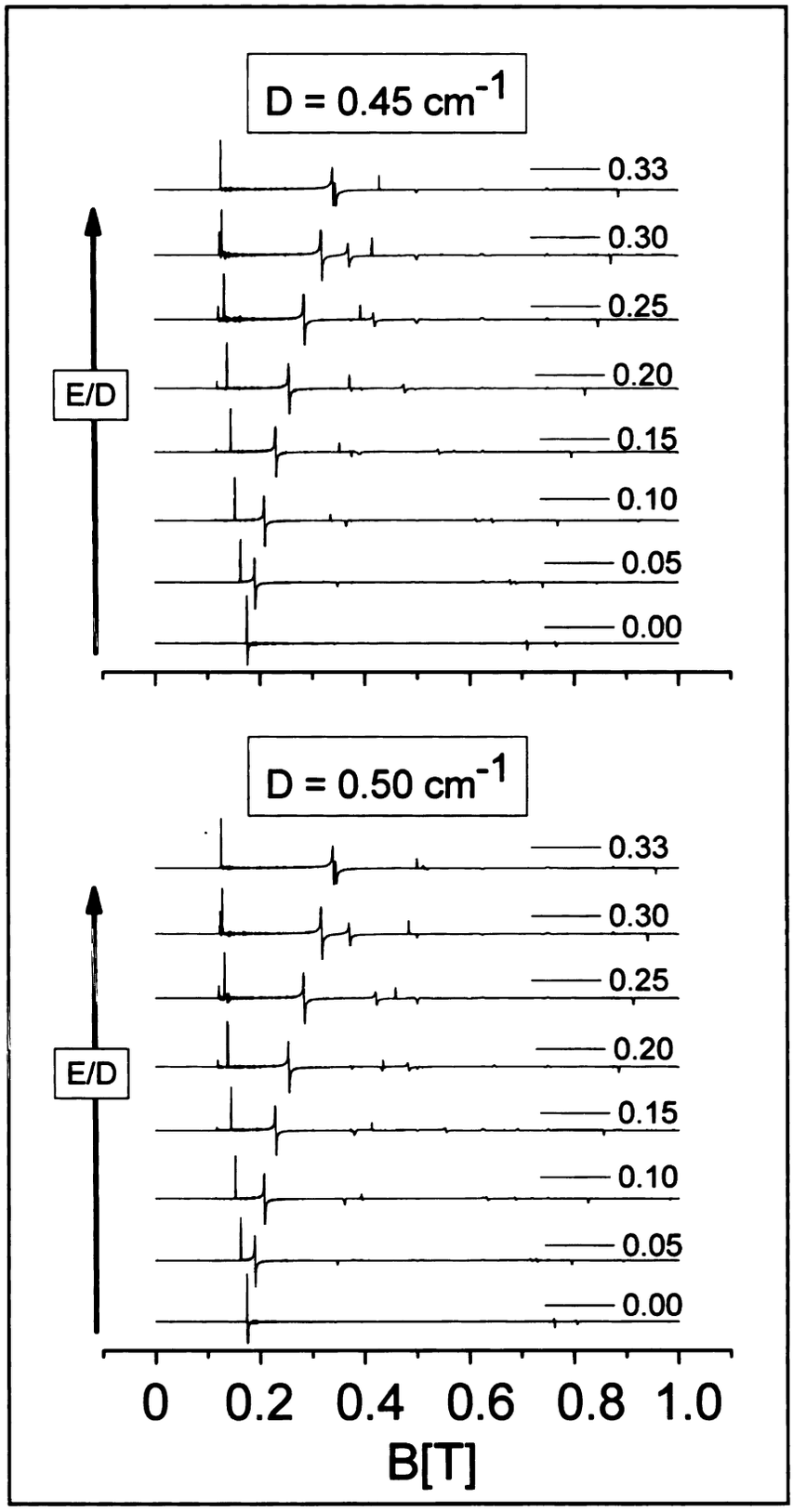

Figure 2-37: Calculated X-band EPR spectra for quartet spin system with D = 0.45 and 0.50 cm^{-1} and variable E/D.

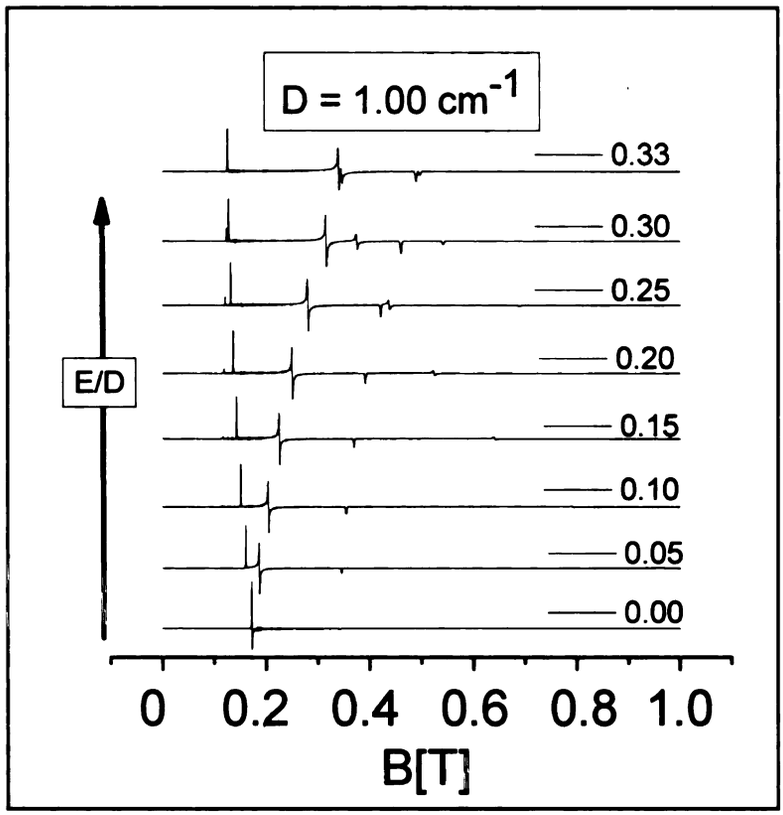

Figure 2-38: Calculated X-band EPR spectra for quartet spin system with D = 1.00 cm^{-1} and variable E/D.

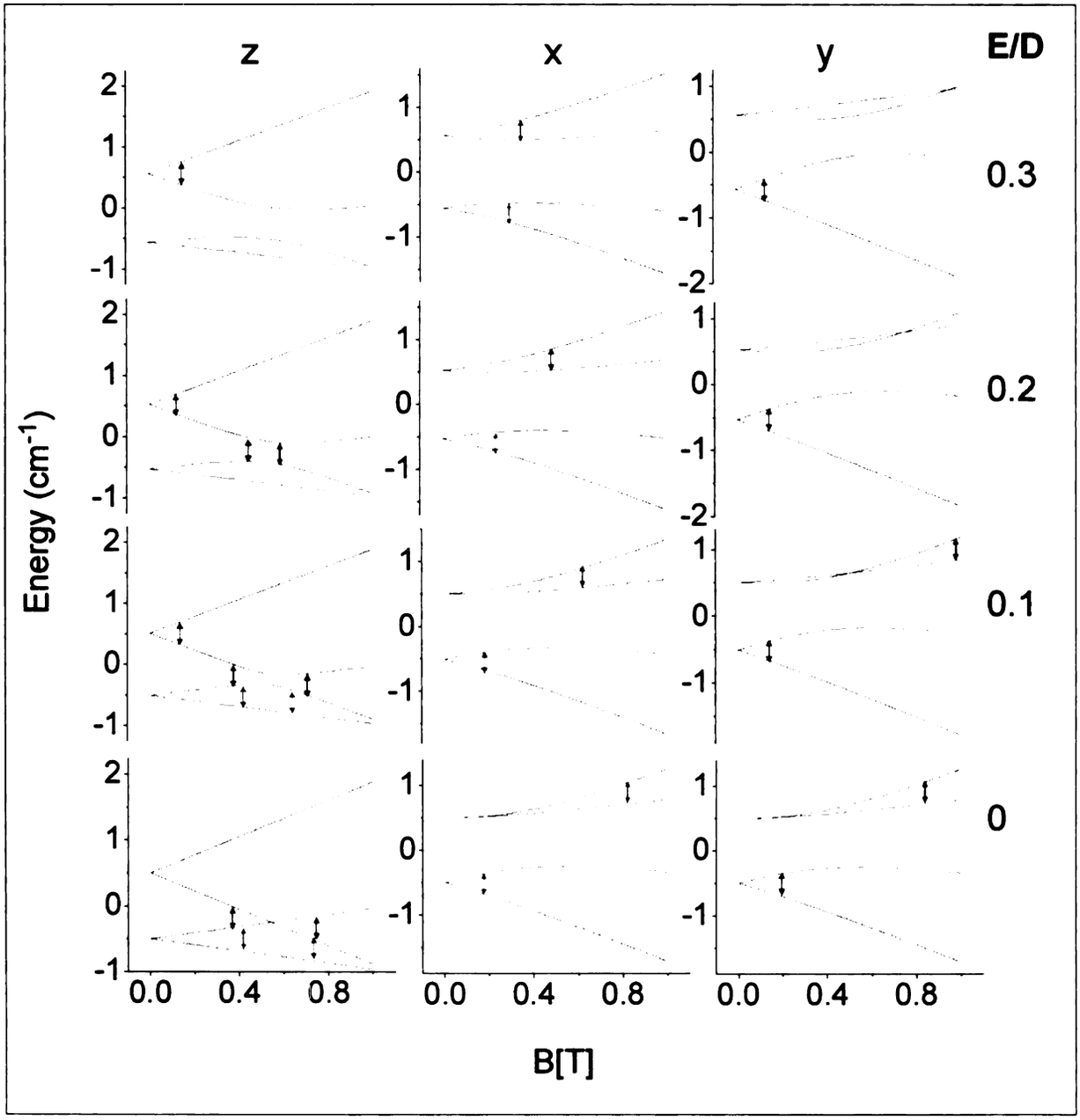

Figure 2-39: Energy level diagrams for B parallel to the X, Y, and Z magnetic axes for a quartet spin system with D = 0.50 cm^{-1} and variable E/D. The resonances are at X-band frequency, and are color-coded to Figure 2-40.

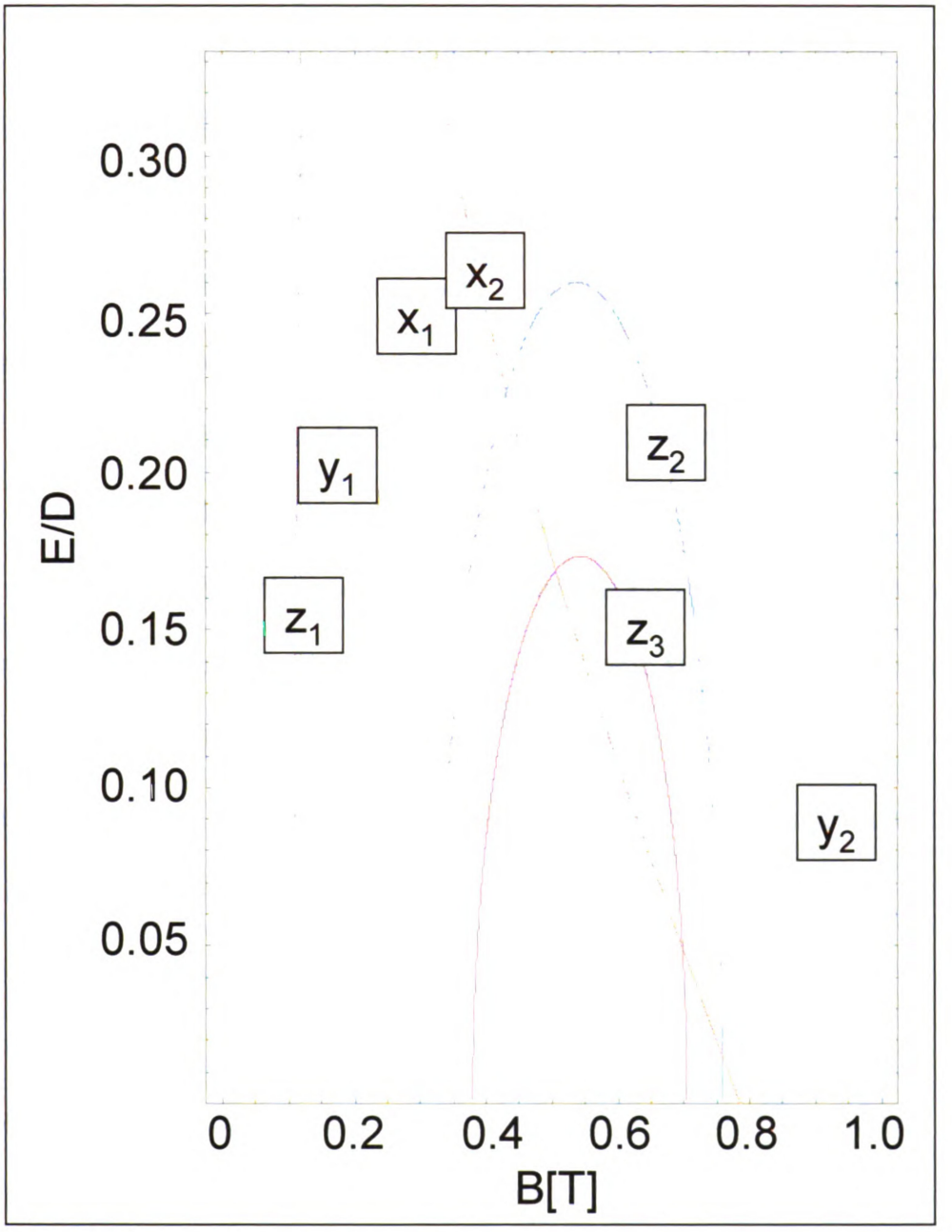

Figure 2-40: Resonant field of transition at X- Band frequency for a quartet spin system with D = 0.50 cm^{-1} and variable E/D.

2.4.6 Conclusions. Electron paramagnetic resonance (EPR) is employed to explore the ground state spin Hamiltonian parameters of **3** and a model complex, [Cr(tren)(DTBCat)](PF_6), as well as several higher symmetry complexes of chromium(III). Using the values obtained and previously reported spin Hamiltonian values for other chromium(III) systems, a systematic study of both axial and rhombic examples of quartet systems was carried out to elucidate the origin of the perpendicular mode EPR transitions. These were explored via energy level diagrams and transition diagrams. Specifically, an approach was implemented to build up the spectra in terms of increasing complexity of the zero field splitting spin Hamiltonian: first a fully isotropic system was explored, then the axial and rhombic zero field splitting parameters were introduced. It is our hope that this study will provide a simple reference tool for understanding and assigning EPR parameters of quartet spin systems.

2.5 Final Remarks

The work presented in this chapter represents the foundation for the rest of the work presented in this dissertation: not only in the sense of characterizing the electronic structures of these complexes from the ground up, but also in the piecewise approach that has been implemented to ultimately understand the electronic structure and dynamics of spin-exchange complexes of chromium(III). This strategy aims to understand physical properties in the absence of spin exchange and thus quantify the effects of the introduction of spin exchange on

electronic structure and kinetics. Chapter 3 characterizes the nonradiative dynamics of quartet chromium(III) complexes, and Chapter 4 utilizes the wealth of knowledge developed in Chapters 2 and 3 (as well as in the literature) to understand the observed physical properties of spin-exchange complexes of chromium(III).

2.6 References

(1.) Guo, D., McCusker, J. K. *Inorganic. Chemistry* **2007,** 46, 3257-3274.

(2.) Wheeler, D. E.; Rodriguez, J. H.; McCusker, J. K. *Journal Of Physical Chemistry A* **1999,** 103, (20), 4101-4112.

(3.) Fehir, R. J.; McCusker, J. K. *Journal Of Physical Chemistry A* **2009,** 113, (32), 9249-9260.

(4.) Fehir, R. J., Ph.D. Thesis, Michigan State University, East Lansing, 2009.

(5.) Brown, M. A.; El-Hadad, A. A.; McGarvey, B. R.; Sung, R. C. W.; Trikha, A. K.; Tuck, D. G. *Inorganica Chimica Acta* **2000,** 300-302, 613-621.

(6.) Mueller, J.; Kikuchi, A.; Bill, E.; Weyermueller, T.; Hildebrandt, P.; Ould-Moussa, L.; Wieghardt, K. *Inorganica Chimica Acta* **2000,** 297, 265-277.

(7.) Antcliff, K. L.; Baker, R. J.; Jones, C.; Murphey, D. M.; Rose, R. P. *Inorganic Chemistry* **2005,** 44, 2098-2105.

(8.) Baker, R. J.; Farley, R. D.; Jones, C.; Kloth, M.; Murphey, D. M. *Journal of the Chemical Society, Dalton Transactions* **2002,** 3844-3850.

(9.) Baker, R. J.; Farley, R. D.; Jones, C.; Mills, D. P.; Kloth, M.; Murphey, D. M. *Chemistry: A European Journal* **2005,** 11, 2972-2982.

(10.) Ozarowski, A.; McGarvey, B. R.; Peppe, C.; Tuck, D. G. *Journal of the American Chemical Society* **1991,** 113, 3288-3293.

(11.) Soedjak, H. S.; Cano, R. E.; Tran, L.; Bales, B. L.; Hajdu, J. *Biochimica et Biophysica Acta* **1997,** 1335, 305-314.

(12.) Weeks, C. L.; Levina, A.; Dillon, C. T.; Turner, P.; Fenton, R. R.; Lay, P. A. *Inorganic Chemistry* **2004,** 43, 7844-7856.

(13.) Andriessen, W. T. M.; Meuldijk, J. *Inorganic Chemistry* **1976,** 15, (9), 2044- 2047.

(14.) Meier-Callahan, A. E.; Bilio, A. J. D.; Simkhovich, L.; Mahammed, A.; Goldberg, I.; Gray, H. B.; Gross, Z. *Inorganic Chemistry* **2001,** 40, (6788-6793).

(15.) Barrera, J. A.; Wilcox, D. E. *Inorganic Chemistry* **1992,** 31, 1745-1752.

(16.) Andriessen, W. T. M. *Journal of Physics and Chemistry of Solids* **1976,** 37, 189-196.

(17.) Riesen, H.; Dubicki, L. *Journal of Physical Chemistry A* **2008,** ASAP.

(18.) Wang, D. M.; Pilbrow, J. R. *Journal of Magnetic Resonance* **1988,** 77, 411-423.

(19.) Mabbs, F.; Collison, D., *Electron Paramagnetic Resonance of d Transition Metal Compounds*. Elsevier: 1992.

(20.) Sander, W.; Grote, D.; Kossmann, S.; Neese, F. *Journal of the American Chemical Society* **2008,** 130, (13), 4396-4403.

(21.) Hans Henning Wenk, W. S. *Angewandte Chemie International Edition* **2002,** 41, (15), 2742-2745.

(22.) Nakazawa, S.; Sato, K.; Shiomi, D.; Franco, M. L. T. M. B.; Lazana, M. C. R. L. R.; Shohoji, M. C. B. L.; Itoh, K.; Takui, T. *Inorganica Chimica Acta* **2008,** 361, (14-15), 4031-4037.

(23.) Fleischhauer, P.; Gehring, S.; Saal, C.; Haase, W.; Tomkowicz, Z.; Zanchini, C.; Gatteschi, D.; Davidov, D.; Barra, A. L. *Journal of Magnetism and Magnetic Materials* **1996,** 159, 166-174.

(24.) Benelli, C.; Dei, A.; Gatteschi, D.; Pardi, L. *Inorganic Chemistry* **1988,** 27, 2831-2836.

(25.) Miller, J. S.; Calabrese, J. C.; Rommelmann, H.; Chittipeddi, S. R.; Zhang, J. H.; Reiff, W. M. *Journal of the American Chemical Society* **1987,** 109, 769.

(26.) Graebe, *Justus Liebigs Annalen der Chemie* **1868,** 146, 31.

(27.) Weider, P. R.; Hegedus, L. S.; Asada, H.; D'Andreq, S. V. *Journal of Organometallic Chemistry* **1985,** 50, 4276.

(28.) Guo, D.; McCusker, J. K. *Inorganic Chemistry* **2007,** *46*, 3257-3274.

(29.) Wheeler, D. E.; McCusker, J. K. *Inorganic Chemistry* **1998,** 37, 2296-2307.

(30.) Schweiger, A.; Jeschke, G., *Principles of Pulse Electron Paramagnetic Resonance*. Oxford University Press: New York, 2001; p 157.

(31.) *XSophe Computer Simulation Software Suite*, 1.1.4; Centre for Magnetic Resonance and Department of Mathematics, The University of Queensland (Brisbane, Queensland, Australia 4072) and Bruker Biospin GMBH (formerly Bruker Analytik; Rheinstetten, Germany): 1993-2004.

(32.) Wang, D.; Hanson, G. *Journal of Magnetic Resonance, Series A* **1995,** 117, 1-8.

(33.) Hanson, G. R.; Gates, K. E.; Noble, C. J.; Griffin, M.; Mitchell, A.; Benson, S. *Journal of Inorganic Biochemistry* **2004,** 98, 903-916.

(34.) McClung, R. E. D. *Canadian Journal of Physics* **1968,** 46, 2271.

(35.) Weltner, W., *Magnetic Atoms and Molecules*. Van Nostrand Reinhold: New York, 1983; p 105.

(36.) Frisch, M. J.; Trucks, G. W.; Schlegel, H. B.; Scuseria, G. E.; Robb, M. A.; Cheeseman, J. R.; Zakrzewski, V. G.; Montgomery, J. A.; Stratmann, R. E.; Burant, J. C.; Dapprich, S.; Millam, J. M.; Daniels, A. D.; Kudin, K. N.; Strain, M. C.; Farkas, O.; Tomasi, J.; Barone, V.; Cossi, M.; Cammi, R.; Mennucci, B.; Pomelli, C.; Adamo, C.; Clifford, S.; Ochterski, J.; Petersson, G. A.; Ayala, P. Y.; Cui, Q.; Morokuma, K.; Malick, D. K.; Rabuck, A. D.; Raghavachari, K.; Foresman, J. B.; Cioslowski, J.; Ortiz, J. V.; Stefanov, B. B.; Liu, G.; Liashenko, A.; Piskorz, P.; Komaromi, I.; Gomperts, R.; Martin, R. L.; Fox, D. J.; Keith, T.; Al-Laham, M. A.; Peng, C. Y.; Nanayakkara, A.; Gonzalez, C.; Challacombe, M.; Gill, P. M. W.; Johnson, B.; Chen, W.; Wong, M. W.; Andres, J. L.; Head-Gordon, M.; Replogle, E. S.; Pople, J. A. *Gaussian 98*, revision A.4; Gaussian, Inc.: Pittsburgh, PA, 1998.

(37.) *GaussView 2.1*, Gaussian, Inc.: Pittsburgh, PA, 2000.

(38.) Wolfram Research, I., *Mathematica*. Version 5.2 ed.; Wolfram Research, Inc. Champaign, Illinois, 2005.

(39.) Broze, M.; Luz, Z. *The Journal of Physical Chemistry* **1967,** 71, (11), 3690-3693.

(40.) Cano, J.; Ruiz, E.; Alvarez, S.; Verdaguer, M. *Comments on Inorganic Chemistry* **1998,** 20, (1), 27-56.

(41.) Ruiz, E.; Cirera, J.; Alvarez, S. *Coordination Chemistry Reviews* **2005,** 249, 2649-2660.

(42.) *CRC Handbook of EPR Spectra of Quinones and Quinols*. CRC Press: Boca Raton, Fl, 1985; p 382.

(43.) Drago, R. S., *Physical Methods for Chemists*. Second ed.; Surfside: Gainesville, 1992; p 381.

(44.) Reitz, D. C.; Dravnieks, F.; Wertz, J. E. *Journal of Chemical Physics* **1960,** 33, 1880-1881.

(45.) Das, M. R.; Fraenkel, G. R. *Journal of Chemical Physics* **1965,** 42, (4), 1350-1360.

(46.) Brown, M. A.; McGarvey, B. R.; Tuck, D. G. *Journal of the Chemical Society, Dalton Transactions* **1998**, 1371-1375.

(47.) Fehir Jr., R. J. PhD Thesis, Michigan State University, East Lansing, 2009.

(48.) Fehir, R. J.; Krzyaniak, M.; Schrauben, J. N.; McCracken, J. L.; McCusker, J. K. *Journal of Physical Chemistry B* **2010,** submitted.

(49.) O'Malley, P. J. *Antioxidants & Redox Signaling* **2001,** 3, (5), 825-838.

(50.) Larson, S. C. *Journal of Physical Chemistry A* **2001,** 105, 8333-8338.

(51.) Saladino, A. C.; Larsen, S. C. *Journal of Physical Chemistry A* **2003,** 107, 1872-1878.

(52.) Fehir, R. J.; McCusker, J. K. *Journal of Physical Chemistry A* **2009,** 113, 9249-9260.

(53.) Ressouche, E.; Schwizer, J., *Molecular Magnets: Recent Highlights*. Springer: New York, 2003; p 119-137.

(54.) Barone, V., *Recent Advances in Density Functional Methods*. World Scientific Publishing: Singapore, 1995.

(55.) Tuononen, H. M.; Armstrong, A. F. *Inorganic Chemistry* **2005,** 44, 8277-8284.

(56.) Tuononen, H. M.; Chivers, T.; Armstrong, A.; Fedorchuk, C.; Boere, R. T. *Journal of Organometallic Chemistry* **2007,** 692, 2705-2715.

(57.) Drago, R. S., *Physical Methods for Chemists.* second ed.; Surfside Scientific Publishers: University of Florida, Gainesville, 1992; p 385.

(58.) Nguyen, M. T.; Creve, S.; Vanquickenborne, L. G. *Journal of Physical Chemistry A* **1997,** 101, 3174-3181.

(59.) Macfarlane, R. M. *Journal of Chemical Physics* **1967,** 47, (6), 2066-2073.

(60.) Brickman, J.; Kothe, G. *The Journal of Chemical Physics* **1973,** 59, (6), 2807-2814.

(61.) Lanciano, P.; Savoyant, A.; Grimaldi, S.; Magalon, A.; Guigliarelli, B.; Bertrand, P. *Journal of Physical Chemistry B* **2007,** ASAP.

(62.) Ikagawa, T.; Otsuka, T.; Kaizu, Y. *Journal of Physical Chemistry A* **1998,** 102, 649-653.

(63.) Singer, L. S. *Journal of Chemical Physics* **1955,** 23, 379-388.

(64.) Elbers, G.; Remme, S.; Lehmann, G. *Inorganic Chemistry* **1986,** 25, (7), 896.

(65.) Jarrett, H. S. *Journal of Chemical Physics* **1957,** 27, (6), 1298-1304.

(66.) McGarvey, B. R. *The Journal of Chemical Physics* **1964,** 40, (3), 809-812.

(67.) Atanasov, M.; Schoenherr, T. *Inorganic Chemistry* **1990,** 29, (22), 4545.

(68.) Fields, R. A.; Haindl, E.; Winscom, C. J.; Khan, Z. H.; Plato, M.; Mobius, K. *The Journal of Chemical Physics* **1984,** 80, (7), 3082-3086.

(69.) Andriessen, W. T. M.; Groenewege, M. P. *Inorganic Chemistry* **1976,** 15, (3), 621-626.

(70.) Schrauben, J. N.; Guo, D.; McCracken, J. L.; McCusker, J. K. *Inorganica Chimica Acta* **2008,** 361, 3539-3547.

Chapter 3: Electronic Structure and Ligand Field Dynamics of High-Symmetry Complexes of Chromium(III)

3.1 Introduction

The work presented in this chapter employs transient absorption spectroscopy to study a series of substituted complexes of the archetypal complex tris(acetylacetonato)chromium(III) in an effort to elucidate mechanisms of nonradiative dynamics. As described in chapter 1, when a system absorbs a photon, the ensuing processes that relax the molecule back to the ground state can be classified as either radiative (fluorescence, phosphorescence) or nonradiative (vibrational cooling, internal conversion, nonradiative intersystem crossing, quenching mechanisms). To achieve rational design of technologies such as solar cell technology, molecular machines, and artificial photosynthesis,[1,2] one must be able to predict and control the initial photophysical events after absorption of a photon. The goal of nonradiative decay theory is the prediction of the rates of state crossing events. In general, for inorganic systems there is a great deal of understanding of the dynamics between the lowest energy excited state, which according to Kasha's rule is the emissive state, and the ground state. However, the theory has never been confirmed for intersystem between two excited states, and furthermore no one has tested the applicability of nonradiative decay theory to nonthermalized excited states. Moreover, there is no general conceptual framework in place describing the ultrafast dynamics in transition metal systems.

A goal of the study of this series is to prove whether the current formalism of nonradiative decay theory is applicable to transitions between nonthermalized, rapidly evolving excited states. In the course of this study it is our hope to establish the foundation of a framework which successfully describes the ultrafast ligand field dynamics in transition metal systems. To determine whether nonradiative decay theory can describe decay dynamics between excited states, a series of molecules with relatively simple ligand field manifolds is required to minimize the number of excited states that could potentially be participating in the photophysics. A high photostability is also desirable to avoid photochemistry. The molecules of study are a series of chromium(III) tris-chelated derivatives of mono-deprotonated 2,4-pentanedione (acac), present in Figure 3-1. Formally, the symmetry of these molecules is D_3, but the local environment around the chromium(III) center, O_6, is effectively O_h. This series was designed with the hope that with modifying the ligand the relative energies (ΔE) and displacements (ΔQ) of the participating states will change enough—thus changing the coupling integral—in order to observe significant changes in k_{nr}. Ligands with π-effects (e.g. phenyl substituted acac) couple to t_{2g} orbitals and will thus modify the energy of the ^2E state, according to the nephelauxetic effect,[3] while σ-modifying groups (CF_3 or CH_3 substituted acac) will inductively modify the energy of the $^4T_2$ state. These systems also provide a conceptual stepping stone to understanding the excited state dynamics of low-symmetry and Heisenberg spin exchange complexes

of chromium(III), discussed in Chapter 4 of this dissertation. In order to observe the anticipated sub-100 femtosecond dynamics of the intersystem crossing in these systems we implemented femtosecond transient absorption.[4] The experiment is described below.[6]

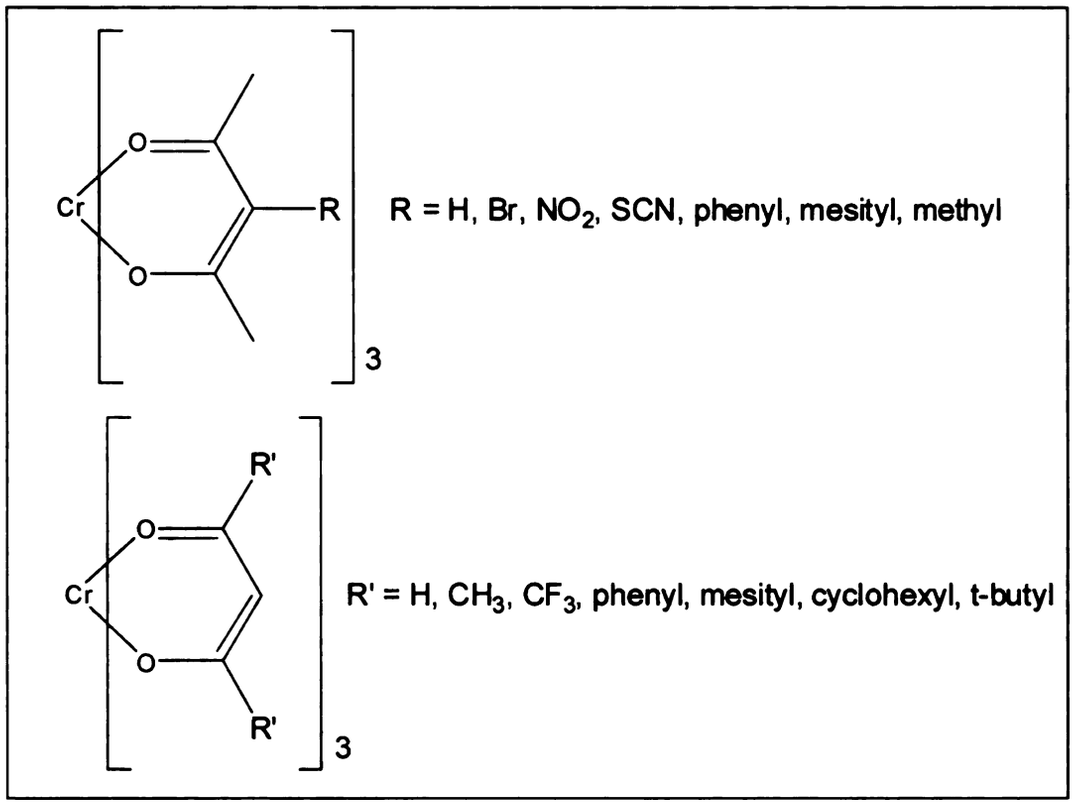

Figure 3-1: Molecules of interest in this study.

For the remainder of this chapter the following abbreviations are employed to represent the mono-anionic, chelating forms of the ligand: acac = of 2,4-pentandione, 3-NO_2ac = 3-nitro-2,4-pentandione, 3-Brac = 3-bromo-2,4-pentandione, hfac = 1,1,1,5,5,5-hexafluoro-2,4-pentandione, dbm = 1,3-benzyl-1,3-propandione, 3-methylac = 3-methyl-2,4-pentandione; 3-Phac = 3-phenyl-2,4-

pentandione; 3-SCNac = 3-thiocyanato-2,4-pentandione; tbutylac = 2,2,6,6-tetramethyl-3,5-heptandione; dcm = 1,3-cyclohexyl-1,3-propanedione; prop = 1,3-propanedione; 3-mesac = 3-mesityl-2,4-pentanedione.

3.2 Background: Ultrafast Transient Absorption Spectroscopy

The concept of the transient absorption experiment is fairly straightforward: an excitation or "pump" pulse prepares an excited state in the sample, and a second "probe" pulse follows which effectively takes a snapshot of the excited state absorption. In reality the experiment is quite difficult and requires a tremendous amount of technology to successfully carry out on the picosecond and sub-picosecond timescales, the timescale of molecular vibrational motion. While many technologies are required (described briefly in the experimental section in the description of the instrument), the arrival of titanium sapphire lasers, whose large bandwidth enabled creation of sub-picosecond pulses, was the first crucial step.[5] After amplification and manipulation of these pulses, the beam is split into pump and probe beams. Eventually the pulses from both beam paths end up overlapped at the sample, and the distance in beam paths gives the timing of the experiment (Figure 3-2). In our case we vary the pump beam path while the probe path stays constant (for stability reasons), so that as the pump beam path is decreased the time between which the two pulses reach the sample increases. The timing nomenclature of a transient absorption experiment is as follows: before the pump pulse hits the sample, but after the probe pulse has, is considered "negative

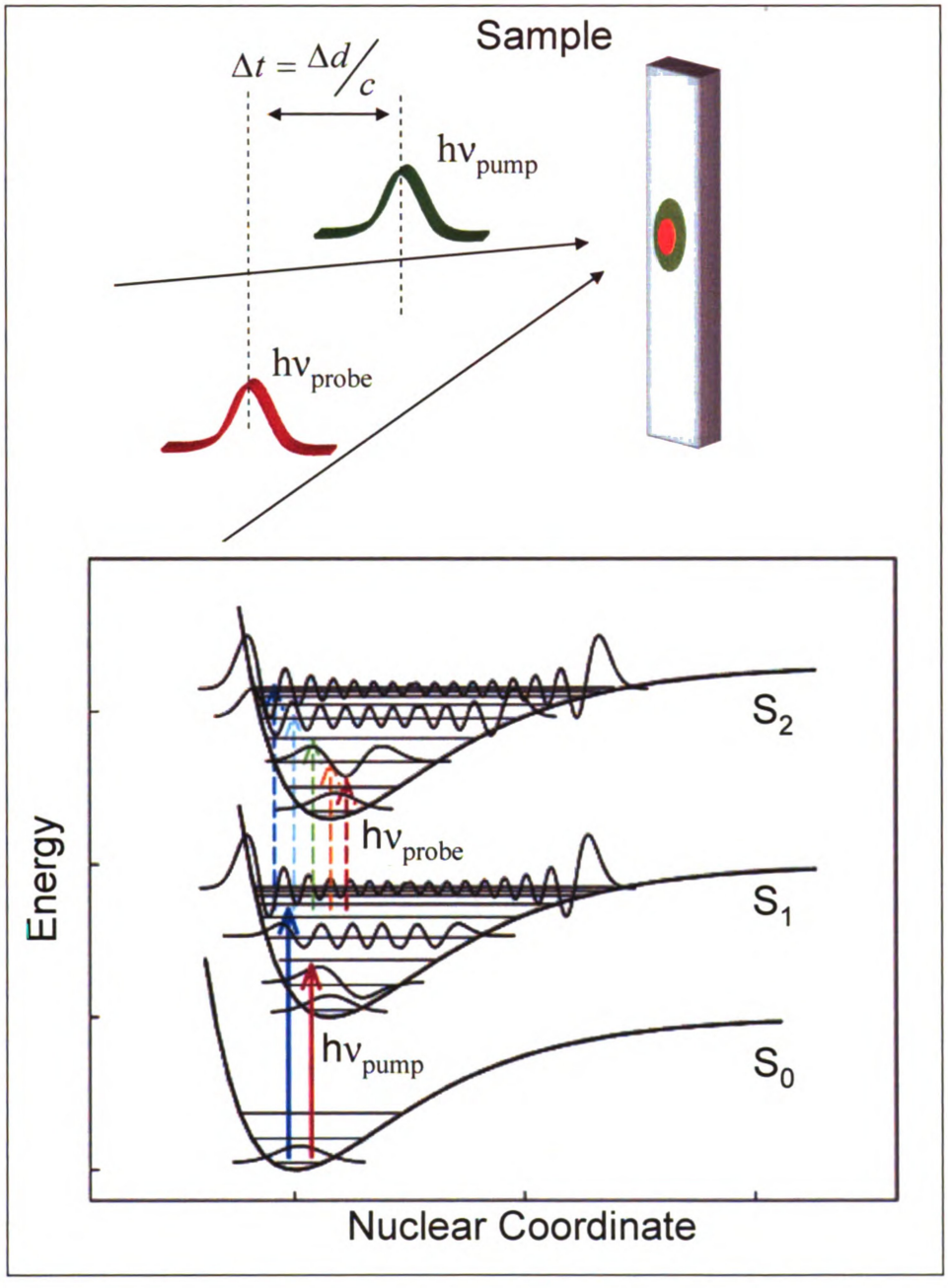

Figure 3-2: The transient absorption experiment employs a pump pulse, which prepares an excited state population, and a probe pulse, which interrogates dynamics within the excited state. Time resolution of the experiment is achieved by varying the distance of the paths traversed between the pump and probe pulses. The potential energy surfaces diagram is reproduced from reference 6.

time," "time zero" occurs when the pump and probe pulses are completely temporally overlapped within the sample, and "positive time" is when the pump pulse proceeds the probe pulse. Data are referenced to the ground state absorption so that changes in the extinction coefficient between the ground and excited state are what are effectively being measured, and the data are thus reported as ΔA (Figure 3-3).

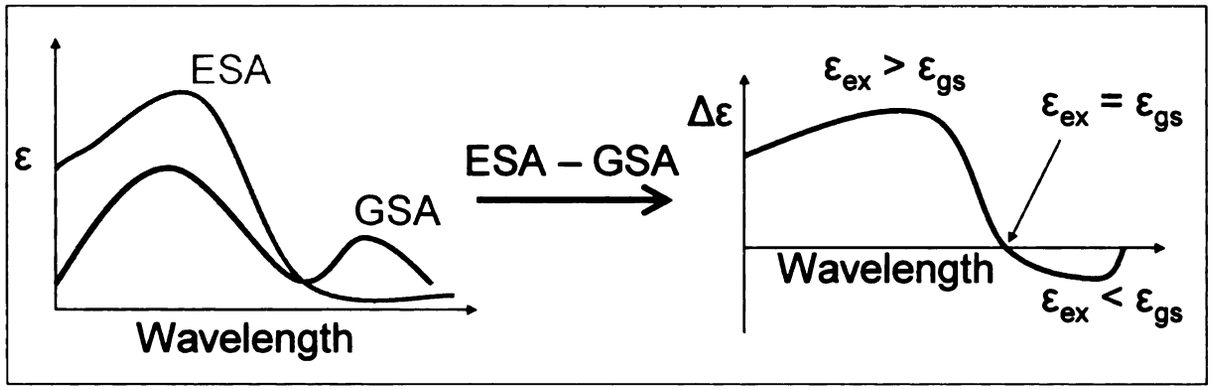

Figure 3-3: Cartoon showing ground state absorption (GSA) and excited state absorption (ESA), plotted in units of extinction coefficient (ε, M^{-1} cm^{-1}) (left graph). The transient absorption experiment effectively measures the difference in the extinction coefficient of these two states (right graph), leading to the possibility of both positive ("ESA") and negative ("bleach") features in the transient spectrum.

As one becomes familiar with the transient absorption experiment, it becomes clear that transient full spectra, i.e. full excited state absorption or bleach features, provide information that is not easily gleaned from a series of single-

wavelength kinetic traces. Discussed below are various scenarios for spectral evolution, which are put into context in terms of the kinetic processes that they represent. A useful gedanken experiment is to consider one-dimensional potential energy surfaces—and the characteristics of these surfaces, i.e. relative energies, displacements and depths of the potential wells—and predict the evolution of the full spectra based on these characteristics. (Whether this exercise is physically meaningful depends on the number of normal modes which are actually involved in facilitating nonradiative decay of the electronic state in question. Nevertheless, this remains a useful tool for developing an understanding of the physical processes, and the observation of these events, that are monitored in the transient absorption experiment.) The possible observable full spectral dynamics depend primarily on the relative displacement and slopes, that is whether one potential is softer than the other, of the evolving electronic surface and the higher-lying electronic state to which the probe pulse absorbs (cf. Figure 3-2). The examples presented below are intended for the reader to gain an understanding of some of the important electronic factors that can influence the observables of the transient absorption experiment. Of course, beside these examples, various other combinations of potential well shape, displacement, and energy separation can be imagined. Considered first are dynamics within a single electronic state which does not evolve to form another electronic state, but rather thermalizes (vibrationally cools) to form a metastable excited state.

In Figure 3-4 are shown two potential energy surfaces with no displacement along the nuclear coordinate. These two wells are identical in depth and separate energetically such that visible light induces transitions from the lower state to upper state. Consider now that the lower state, S_1, is excited into a higher-lying vibrational level, such that a transition from this state to the upper-lying state, S_2, will have maximum probability at energy hν(1). The probability of transition is greatest at this energy because of optimum overlap of the constituent vibrational wavefunctions of S_1 and S_2.

In the case of the transient absorption experiment hν(1) would correspond to a monochromatic probe of S_1, and because the transition probability is highest would also correspond to the maximum intensity of the excited state absorption, $\lambda_{max,ex}$. As the state thermalizes to form the lowest energy vibrational state, $\lambda_{max,ex}$ will not change due to the similar slopes of the potential wells. However, the excited state absorption is expected to narrow as the state thermalizes due to the relatively small overlap of the $\nu = 0$ vibrational wavefunction of S_1 with those of the S_2, limiting energetically the breadth of the transition. Therefore, a narrowing single band without a shifting peak is indicative of vibrational relaxation within a single electronic state. The narrowing of the excited state absorption will manifest itself as a decay in the ESA at most probe wavelengths.

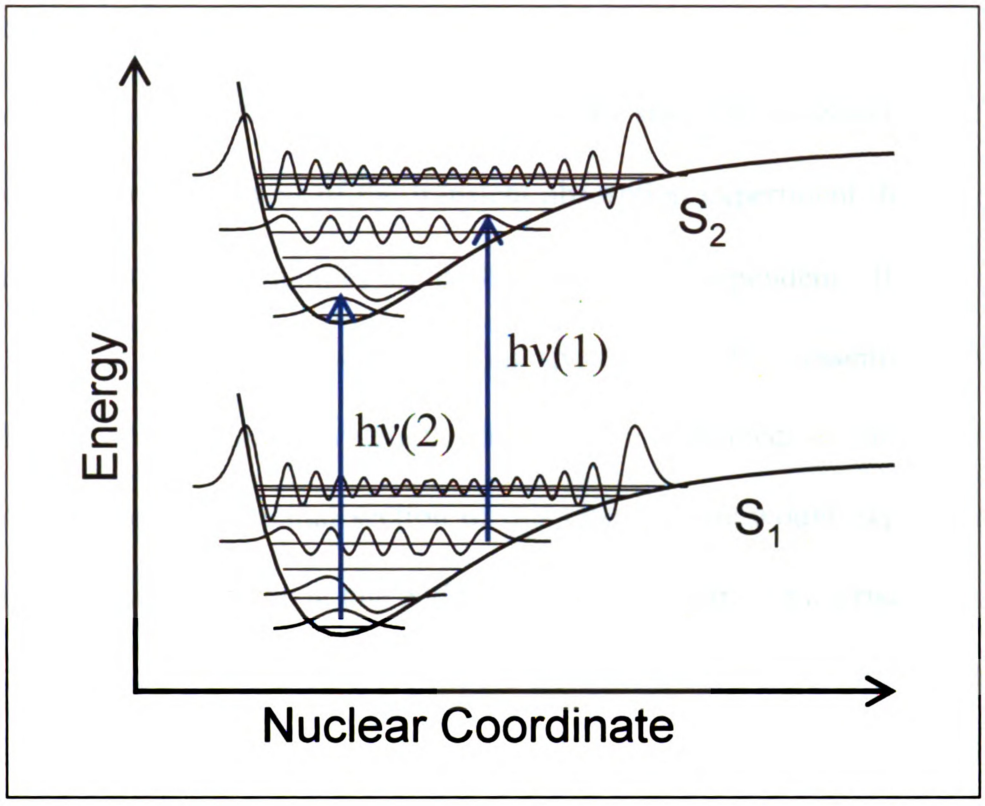

Figure 3-4: Case of two identical electronic potential wells with small relative displacement along the nuclear coordinate. Higher-lying vibrational levels can absorb readily at many wavelengths (hν(1)), but as S_1 vibrationally cools the number of available transitions is limited (hν(2)), and the spectrum of S_2 accordingly narrows. $\lambda_{max,ex}$ does not shift due to the identical slopes of S_1 and S_2.

Again considering vibrational relaxation within a single electronic state, one can envision scenarios in which $\lambda_{max,ex}$ will vary as S_1 thermalizes. Figure 3-5 presents two scenarios in which S_1 is vibrationally cooling but S_1 and S_2 have different well depths, i.e. one potential is softer than the other. One can see that if S_1 represents a softer potential than S_2 a red shift of $\lambda_{max,ex}$ is expected as S_1 cools

(Figure 3-5, upper panel), while a blue shift of $\lambda_{max,ex}$ occurs if the S_2 potential is softer (Figure 3-5, lower panel). In both cases the spectrum is expected to narrow as S_1 cools. In the context of the transient absorption experiment this represents one case in which the dynamics are probe-wavelength dependent. If one were to monitor 10 nm wide window of the full spectra, which is essentially what is carried out when single-wavelength kinetics are collected on the instrument presented in the experimental section of this chapter, one would expect decay in the excited state absorption at one end (window 1 in Figure 3-6), a rise in the other (window 3), and a combination of kinetics in the middle. Therefore, a shift in the transient spectrum, concomitant with a narrowing of this spectrum, is also indicative of decay within a single electronic state.

Electronic surface crossings carry different signatures in full-spectral evolution. Figure 3-7 presents the example of a nonradiative intersystem crossing process, a nonradiative transition between states of different spin, in this case a singlet state and a triplet state. In this diagram the states are displaced along the nuclear coordinate—but this is not necessary to the description of the dynamics in this case but is rather shown this way to more easily distinguish between the states. The singlet state $^1S_1$ is prepared in an excited vibrational level. Laser pulses probing this configuration at energy hν(1) can induce transitions only into the upper singlet state, $^1S_2$, due to the low transition probability between states of different spin. As the state cools, similar dynamics to those described above are

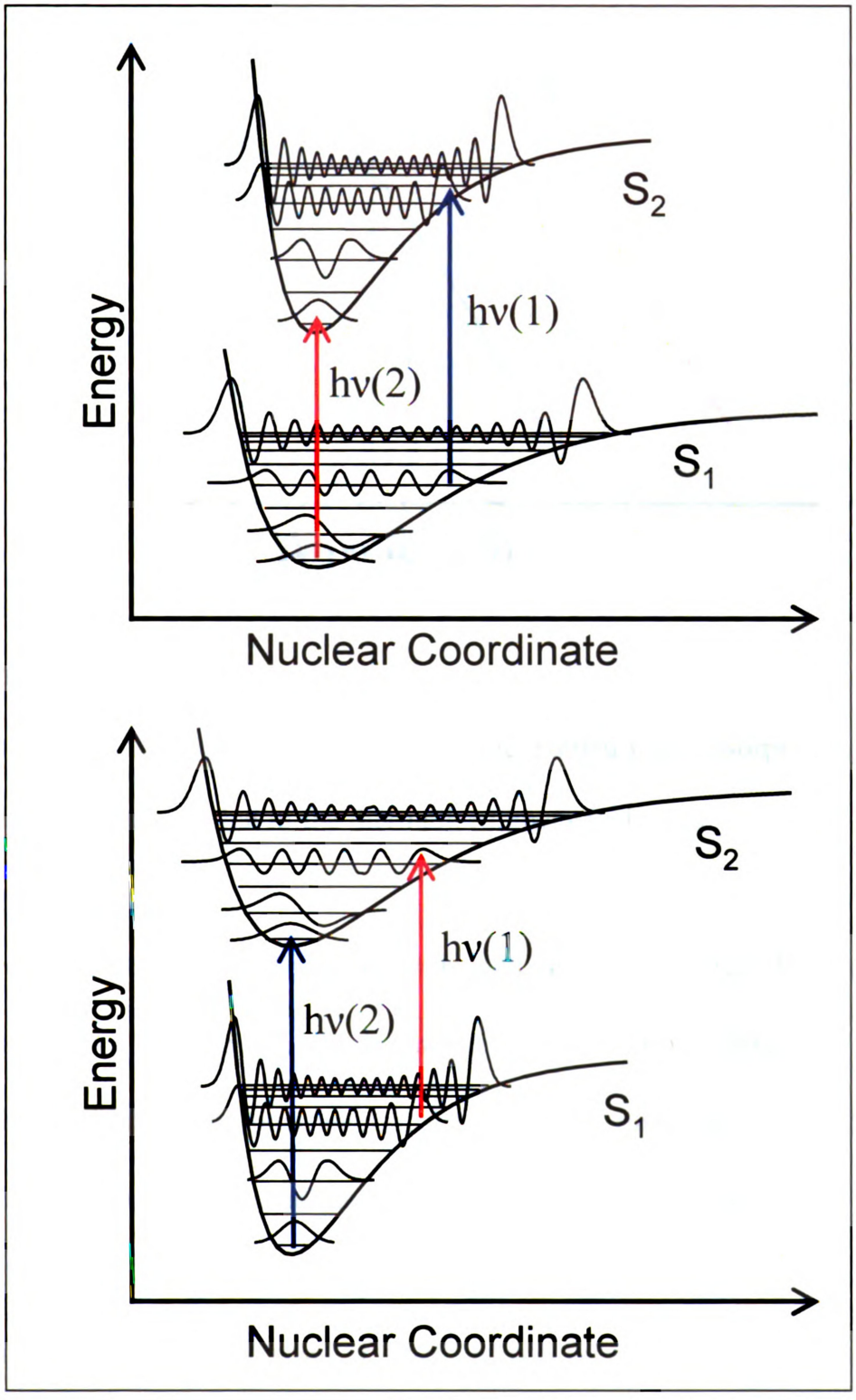

Figure 3-5: Potential energy surface diagrams detailing expected shifts of $\lambda_{max,ex}$ for different slopes of S_1 and S_2.

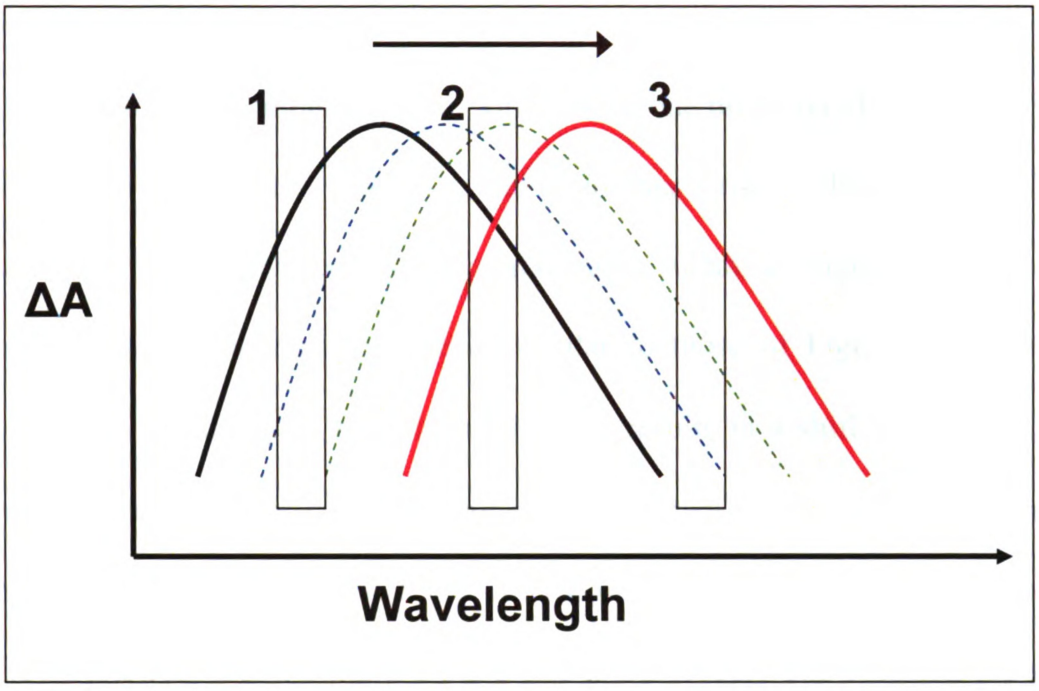

Figure 3-6: Cartoon representing transient full spectra that are red-shifting with time. Black represents the earliest time excited state absorption spectrum while red represents that of the thermalized, metastable state.

observed, namely a narrowing of spectrum without any expected shift in $\lambda_{max,ex}$. In the scenario of Figure 3-7, the thermalized $^1S_1$ has strong vibrational overlap with a higher-lying vibrational level of the $^3S_3$ state; therefore, as the $^1S_1$ cools population will be transferred nonradiatively to the triplet state $^3S_3$. As this population decays, the spectral features characteristic of $^1S_1$ will also decay and features associated with the newly formed $^3S_3$ will arise. $^3S_3$ only has significant transition probability to another triplet state, $^3S_4$, at hν(2). In this scenario a shift in $\lambda_{max,ex}$ is expected. Figure 3-8 represents this case: one band decays while

another grows, clearly indicative of a surface crossing to a new electronic state. Again, if one were to monitor probe windows, at one probe window a decay in the excited state absorption is observed, and at another a rise is observed, exactly the same as the case described above for relaxation within a single electronic state. Therefore, single-wavelength kinetics similar to those of Figure 3-6 would be observed, where decay in one electronic state results in a shift of $\lambda_{max,ex}$. Here, however, the black transition is decaying concomitant with the growth of the red transition, so that in window 1 (far left) a monoexponential decay is observed while on the red edge (window 3) and rise is observed. The fact that the single wavelength kinetics are the same for the two disparate processes of Figures 3-6 and 3-8 emphasizes the need for well-resolved full spectra, the only means of distinguishing between these two cases.

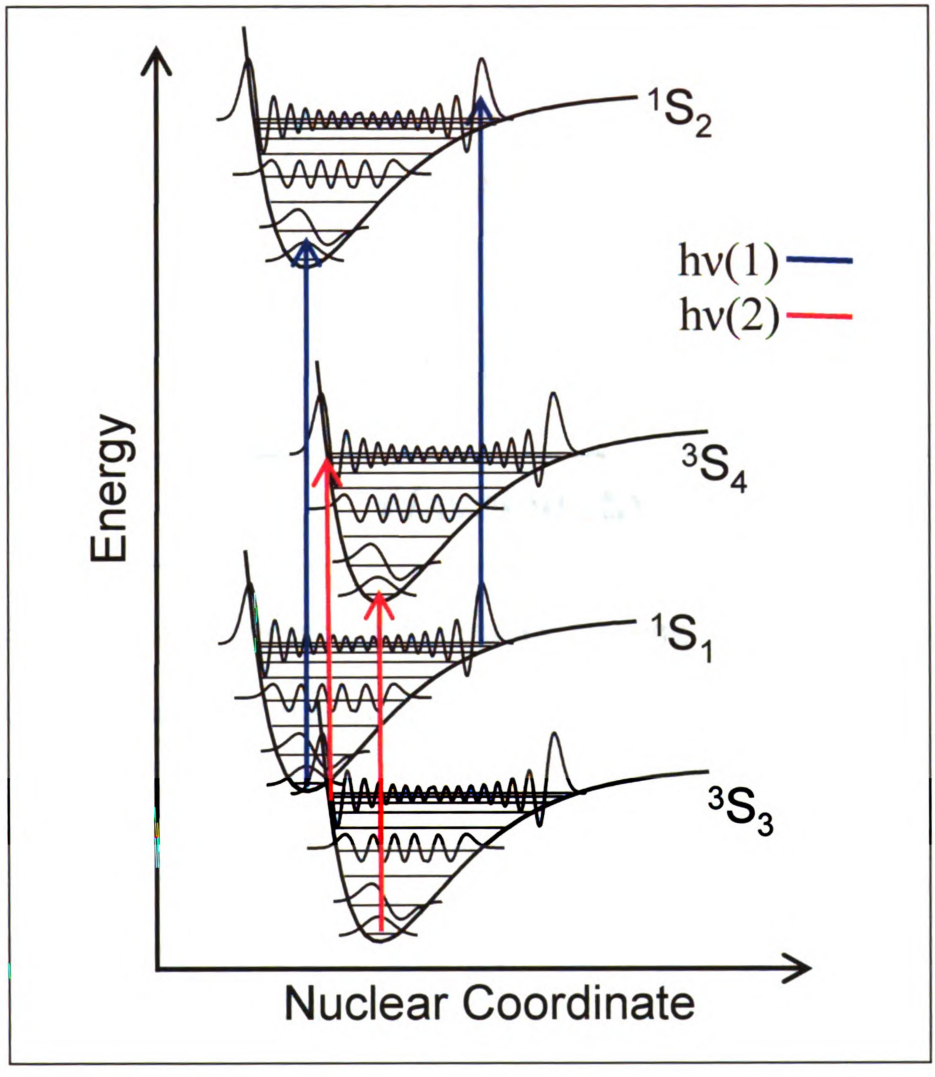

Figure 3-7: Generalized picture revealing how an intersystem crossing event can affect the observed transient spectra.

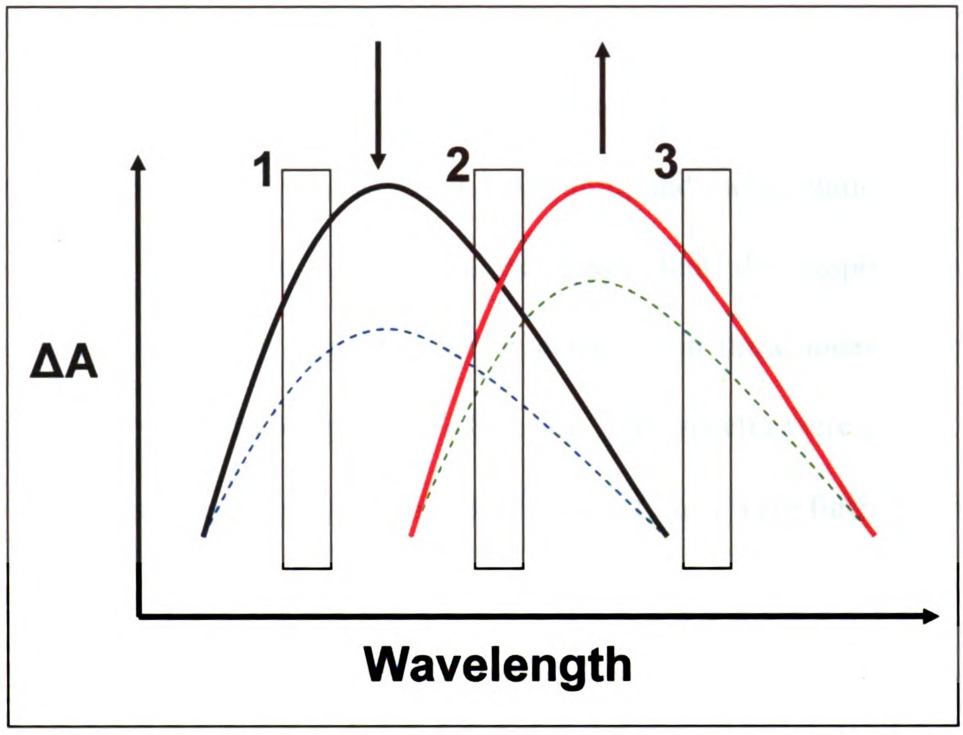

Figure 3-8: Transient full spectra of a surface crossing event, with characteristic spectra from the initial and final electronic states.

3.3 Experimental Section

3.3.1 Physical methods. UV-vis absorption was carried out on a Cary-50. Spectrographic grade dichloromethane or acetonitrile (Jade) was used for all measurements. Emission and excitation spectra were collected on a Spex Fluoromax Spectrofluorometer. All samples were prepared in an inert environment, and such that the absorbance at the excitation wavelength was between 0.1 - 0.2. All emission spectra reported in this dissertation were collected at low temperature (80 K) using a Janis SVT-100 optical dewar. The emission spectra of tris(acetylacetonato)chromium(III) ($Cr(acac)_3$) and related complexes

was collected in an 80 K optical glass of 2-methyltetrahydrofuran. These complexes emit near 800 nm, and a 650 nm long-pass filter was employed. For all measurements the emission slits were set at 0.5 mm, and the excitation slits were set between 0.5 - 1 mm. It should be noted that the response of the photomultiplier tube which is employed for detection in these measurements is quite poor for wavelengths longer than ~ 810 nm. The spectra were corrected for lamp intensity, and spectra plotted in units of energy (cm^{-1}) were further corrected as per Parker and Rees.[6]

All time-resolved spectroscopic measurements were carried out in dichloromethane, unless the samples were shown to photodegrade when exposed to ultrashort pulses. In this case, the sample was flowed and dichloromethane could not be used because it would dissolve the tubing that was employed in the experiment; acetonitrile was used instead. Ultrafast transient absorption data with ~ 100 fs pulse duration were collected as follows. A Ti:sapphire oscillator (Coherent Mira) is pumped at 5.4 W (Coherent Verdi), producing modelocked pulses centered at 803 nm with a FWHM of 13.5 nm at an repetition rate of about 76 MHz. These pulses are fed into a cavity containing a stretcher/compressor and regenerative amplifier (Positive Light Spitfire), pumped by a Coherent Evolution. The output of the regenerative amplifier is again 800 nm, ~100 fs pulses at kilohertz repetition rate. Approximately 70% is fed into an OPA (TOPAS) for generating the appropriate pump wavelength, while the remaining 30% is used to

generate the white light continuum (CaF_2 or sapphire) used for the probe pulse. The pump traverses a delay line (Aerotech ATS100-200 with a Unidex 100 motion controller), providing the timing for the experiment. The full white light continuum can be used as a probe for full spectral transient studies, or a 10 nm bandpass filter can be employed to select a probe wavelength for a "single-wavelength" kinetic trace.

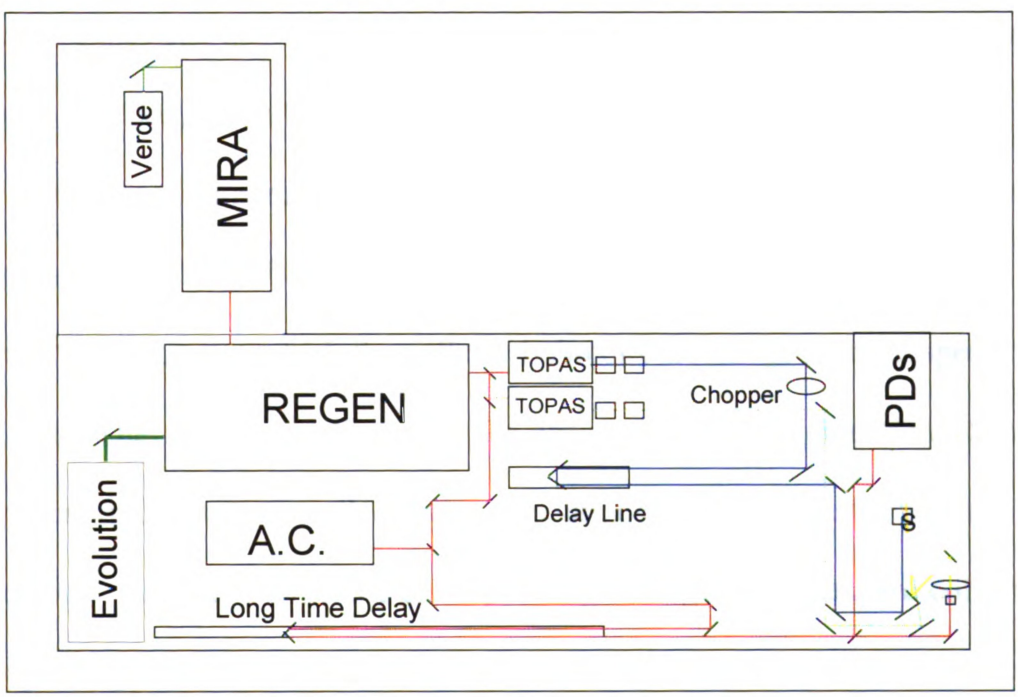

Figure 3-9: Ultrafast transient absorption setup which can achieve ~ 100 fs pulses in the visible.

In the visible, pump powers of 6-7 μJ/pulse are used, while exciting in the ultraviolet requires smaller energies, approximately 1-3 μJ/pulse. Samples were prepared in 1 mm pathlength cells so that the absorbance is 0.4 - 0.7 at the excitation wavelength. For certain complexes a flowing sample was used to avoid

photodecomposition of the sample. A lock-in amplifier and chopper are employed to achieve reasonable S/N, and detection is carried out with two avalanche photodiodes. Labview programs of local origin were used to process all data.[7] In general, fitting of single wavelength kinetic traces with $\tau > 500$ fs was carried out with an exponential function with an additional y-offset. Fitting was started at 300 fs, past the solvent cross-correlation signal. Although not used in this dissertation, faster dynamics can be modeled via convolution of the kinetics and the instrument response function, given by the solvent cross-correlation signal.

Transient full spectra were collected using a fiber-optic cable connected to a Hamamatsu HC233-0900 spectrograph. The spectrograph employs a diode array (C5964 NMOS), upon which the collected photons are imaged after dispersion via a grating. The data was collected in the absence of lock-in detection. Scans of background pump scatter, called dark scans, are collected before the experiment is carried out. Background scans, corresponding to negative times, are collected at the beginning of each scan, and the dark and background scans are both subtracted to calculate the final transient spectra. Sub-ps full spectra must be corrected for the chirp associated with the probe pulse. This is described in detail elsewhere.[7]

Coherence data on $Cr(acac)_3$ were collected on an instrument housed by the Beck group at Michigan State University. The sample was a flowing solution of acetonitrile with an absorbance of ~ 0.7. Femtosecond pump-probe transients with impulsive excitation were recorded using the dynamic-absorption technique, in

which the probe beam is dispersed in a grating monochromator after passing through the sample.[8-10] The pump and probe pulses were obtained from the signal-beam output of an optical parametric amplifier (Coherent OPA 9450), which was pumped by an amplified Ti:sapphire laser (Coherent Mira-seed oscillator and a modified Coherent RegA 9050 regenerative amplifier, with Coherent Verdi V5 and V10 pump lasers, respectively). The laser was operated at a repetition rate of 250 kHz. The pump and probe pulses were corrected for group-delay dispersion on the way to the sample by a SF10 Brewster prism-pair pulse compressor. The pump-probe time delay was scanned using a rapid-scanning delay stage (Clark-MXR, ODL-150) in a modified Mach-Zehnder interferometer with confocal sample and autocorrelation-crystal positions. Calcite polarizers and wave plates in the pump and probe beams set their planes of polarization at 90°; after passing through the sample, the probe beam was analyzed by another calcite polarizer oriented 90° relative to the pump-beam's plane of polarization, and then it was passed through a monochromator (Spex 270M, 4-nm bandpass) and detected by an amplified photodiode (Thorlabs PDA55). The slits of the monochromater were adjusted to obtain a fairly narrow bandpass (4 nm) compared to the width of the laser's spectrum. This approach is similar to that used by Champion and co-workers in their studies of low-frequency vibrational coherence in heme proteins.[11,12] The pump-probe signal was obtained from the photodiode signal using a lock-in amplifier (Femto LIA-MV-200-H); the pump beam was modulated at 50 kHz by a photoelastic modulator (Hinds Instrumentation). Fitting

of the oscillatory component (the residual after subtraction of the exponential components) was accomplished with a program of local origin, and has been described in detail elsewhere.[13] Briefly, the oscillatory residuals were fit with a multicomponent model that contains both slowly damped and rapidly damped components. The slowly damped components were modeled as a simple damped cosinusoid, while the rapidly damped components were modeled in the time domain with inhomogeneously broadened components with asymmetric Gaussian lineshapes.

3.3.2 Computational Methods. All calculations were carried out in Gaussian 03.[14] Crystal structure geometries were used as a starting point for geometry optimization calculations using the B3LYP functional and LANL2DZ basis set to generate a minimized geometry. This geometry was then subjected to a further geometry optimization at the unrestricted B3LYP/6-311g** level, employing a dielectric continuum solvent model for dichloromethane ($\varepsilon = 8.93$) or acetonitrile ($\varepsilon = 35.688$). The optimized geometry was used for time-dependent calculations also employing a dichloromethane dielectric continuum using the unrestricted B3LYP functional and 6-311g** basis set. Images of molecular orbitals and vibrational modes were prepared in GaussView.[15]

3.3.3. Synthesis I. 3-Substituted Complexes of 2,4-pentanedione

i. tris(2,4-pentanediono)chromium(III), $Cr(acac)_3$. $Cr(acac)_3$ was prepared by adapting a previous literature method.[16] In 15 ml of water was added 2 g (7.51 mmol) of chromium(III) chloride hexahydrate, 4.5 g (45 mmol) of acetylacetone (2,4-pentanedione) and 4.5 g (45 mmol) of triethylamine. The solution was stirred with gentle heating and allowed to react overnight. Purple crystals fall out of solution which can be filtered, dried, and recrystallized by dissolving in benzene and slowly adding three volumes of petroleum ether. Yield: 0.57 g (21 %). Anal. Calcd for $C_{15}H_{21}O_6Cr$ expected: C, 51.57; H, 6.06; N, 0.00. Found: C, 51.65; H, 5.94; N, 0.02.

ii. tris(3-phenyl-2,4-pentanedionato)chromium(III), $Cr(3\text{-phenylacac})_3$. This preparation was modified from a previously reported procedure.[17] 0.6 g (10 mmol) of urea was stirred into 1 ml of water and 3 ml of dioxane. 0.176 g (1 mmol) of 3-phenyl-2,4-pentanedione (TCI) was added, then 0.089 g (0.33 mmol) of chromium(III) chloride hexahydrate was added. The reaction was refluxed and stirred for three days. Upon cooling, the product was washed on a fine fritted filter with copious amounts of water to remove any ammonium salts and dried *in vacuo*. Anal. Calc. for $C_{33}H_{33}O_6Cr$ expected: C, 68.62; H, 5.76; N, 0.00. Found: C, 72.60; H, 6.20; N, 0.10. This complex has also previously been prepared using a method developed by Girolami and coworkers.[18,19]

iii. tris(3-methyl-2,4-pentanedionato)chromium(III), Cr(3-methylacac)$_3$. 0.6 g (10 mmol) of urea was stirred into 2 ml of water and 2 ml of dioxane. 0.114 g (1 mmol, 0.116 ml) of 3-methyl-2,4-pentanedione (Aldrich) was added, then 0.089 g (0.33 mmol) of chromium(III) chloride hexahydrate was added. The reaction was refluxed and stirred for three days. Upon cooling, the product was washed on a fine fritted filter with copious amounts of water to remove any ammonium salts and dried *in vacuo*. The product was recrystallized by dissolving the solid in a 5:1 methanol/water solution, and allowing the methanol to slowly evaporate. This yielded brown-green needle-like crystals. Anal. Calc. for $C_{18}H_{27}O_6Cr$ expected: C, 55.24; H, 6.95; N, 0.00. Found: C, 55.26; H, 7.10; N, -0.02.

iv. tris(3-nitro-2,4-pentandiono)chromium(III), Cr(3-NO_2acac)$_3$. This complex was prepared according to literature methods.[20] A slurry of finely divided copper(II) nitrate 2.5-hydrate (2.15 g) in 40 ml of acetic anhydride was stirred for 15 minutes at 0 °C. 1 g (2.87 mmol) of $Cr(acac)_3$ was added and stirring maintained at 0 °C for two hours. After two hours the solution was removed from the ice bath and allowed to stir at room temperature for one hour. The slurry was decomposed by adding 120 ml of water, 120 ml of ice, and 3 g of sodium acetate. The red precipitate was collected, washed with ethanol and water, and air dried. The product is recrystallized from ethanol/chloroform. Yield: 0.57

g (21 %). Anal. Calc. for $C_{15}H_{18}N_3O_{12}Cr$ expected: C, 37.29; H, 3.75; N, 8.68. Found: C, 37.26; H, 3.24; N, 8.84.

v. tris(3-bromo-2,4-pentandiono)chromium(III), Cr(3-Bracac)$_3$. $Cr(Br\text{-}acac)_3$ was prepared according to literature methods.[21] A stirring solution of 0.6 g (1.7 mmol) of $Cr(acac)_3$, 0.51 g sodium acetate, and 15 ml of glacial acetic acid was prepared and cooled to 30 °C. To it was added a solution of 1.21 g (7.6 mmol) of Br_2 in 2 ml of glacial acetic acid. After 5 minutes the precipitates were collected and washed with water, aqueous sodium bicarbonate, aqueous sodium sulfate, and finally water. The brown substance was recrystallized twice from benzene/heptane. Yield: 0.751 g (0.13 mmol, 74.6 %). Anal. Calc. for $C_{15}H_{18}O_6Br_3Cr$ expected: C, 30.74; H, 3.10; N, 0.00. Found: C, 31.03; H, 3.15; N, 0.04.

vi. tris(3-thiocyano-2,4-pentandiono)chromium(III), Cr(3-SCNacac)$_3$. The procedure[22,23] involves preparation of three different solutions, all of which must be cooled in a dry ice/ acetone bath prior to mixing: 1) a vigorously stirring suspension of potassium thiocyanate (10 g, 100 mmol) in absolute methanol; 2) 8 g bromine (200 mmol, 2.66 ml) in absolute methanol; 3) a solution of $Cr(acac)_3$ (5.8 g, 16.5 mmol) in absolute methanol. The bromine solution was added slowly to KSCN/methanol suspension so that the temperature does not go above -60 C.

Then the $Cr(acac)_3$ is added all at once. The mixture is stirred for one hour in the dry ice/acetone bath, then stirring is continued and the solution is allowed to reach room temperature. The room temperature solution is poured onto crushed ice and the precipitate is collected after one hour. The purple solid is recrystallized from benzene/petroleum ether. Yield 3.79 g (7.28 mmol, 44.1%). Anal. Calc. for $C_{18}H_{18}O_6N_3S_3Cr$ expected: C, 41.53; H, 3.49; N, 8.07. Found: C, 42.27; H, 3.38; N, 6.65. An infrared spectrum of this compound shows the characteristic 4.64 μm SCN stretch, a single absorption at 6.40 μm in the 6.25-6.75 region and a lack of peak at 8.25 μm, associated with unsubstituted $Cr(acac)_3$.

vii. 3-mesityl-2,4-pentanedione. This ligand was prepared according to previously published procedures, with slight modifications. [24] Activated copper powder (64 g) was prepared in a 1 L roundbottom flask by suspending copper powder in glacial acetic acid for 15 minutes, decanting the acid and replacing it. After 15 minutes more, the acid was decanted and reagent grade acetone was used to displace the acid. These washings continued until the acetone was colorless, then the copper powder was dried *in vacuo*. After the powder is dry, 5 g of $Cr(3\text{-}Bracac)_3$, prepared as described above, and 10.5 g of iodomesitylene (Alfa Aesar) were stirred into the copper powder. The mixture was heated under positive pressure of Ar for 4 hours at 240 °C. After cooling, the product was broken up and 430 ml of 50% H_2SO_4 solution was added and the mixture heated for 3 hours.

After cooling, the mixture was filtered, and the filtrate washed with water. The dry filtrate was extracted with benzene in a Soxhelet extractor for three hours. Meanwhile, the acidic mother liquor is extracted with benzene, and these organic extracts are washed three times with water and dried over Na_2SO_4. The extracts were combined, the solvent removed, and the residue separated with benzene on a silica column. The second product to come off the column (rf ~ 0.5) is the desired product. The solvent is removed, and a crude solid is obtained by dissolving the oily product in methanol, adding a few drops of water, and letting the methanol slowly evaporate. This brown solid was sublimed under high vacuum at ~ 80 °C to yield a yellow crystalline solid, the desired product. Yield: 120 mg, (2.1 %). ^{1}H NMR (300 MHz, $CDCl_3$); 1.739 (s, 6 H, -CH_3), 2.075 p (s, 6 H, phenyl-CH_3), 2.282 (s, 3H, phenyl-CH_3), 6.910 (s, 2 H, aromatic), 16.597 (1 H, -OH).

viii. tris(3-mesityl-2,4-pentanedionato)chromium(III), Cr(3-mesac)$_3$: This complex, which is purple in color, was achieved according to the method established by Girolami and coworkers,[18,19] (ESI +, m/z = 704.4 MH^+), but also contained a significant amount of an unknown green solid (ESI+, m/z = 1003.5). A cleaner preparation was carried out: 65 mg (0.298 mmol) of 3-mesityl-2,4-pentanedione was added to a stirring solution of 26.5 mg of chromium(III) chloride hexahydrate (9.93×10^{-5} mol) and 0.6 g urea (10-fold excess). Enough methanol was added to the solution to dissolve the ligand (approximately 12 ml)

and the solution was refluxed for 24 hours. A purple precipitate forms during the course of the reaction. After removing the reaction from heat, a stream of nitrogen was blown over the solution and more purple precipitate forms along with the unreacted ligand. The cooled solution is filtered and washed with large amounts of water and methanol. MS (ESI +), m/z = 704.5 (MH^+, 100%). Anal. Calcd for $C_{42}H_{51}CrO_6$ expected: C, 71.67; H, 7.30; N, 0.00. Found: C, 71.33; H, 7.23; N, 0.00.

3.3.4 Synthesis II. Substituted Complexes of 1,3-Propanedione.

i. tris(propandiono)chromium(III). This preparation is modified from a literature procedure.[25] A mixture of 5.084 g (0.031 mol) of tetramethoxypropane, 5 ml water and 2 ml of 1 M HCl were heated in a steam bath until the phases mixed and the solution became lemon yellow. Overheating to produce a darker color will decrease the yield. The solution was cooled to 0 °C in an ice bath then 2.52 g triethylamine was added, which was dried over 4 Å molecular sieves and distilled from P_2O_5. The solution rapidly turns a red-violet color. This solution was added to a 0 °C (again cooled in an ice bath) suspension of 1.30 g anhydrous $CrCl_3$ (mol), 1.635 g Zn dust and 100 ml of ether. After stirring for 30 minutes, the ether layer becomes intensely violet; it is decanted, replaced, and this procedure is repeated until the reaction is exhausted. The solvent is removed and the red residue is dissolved into ~ 25 ml of hot benzene. The solution is allowed

to cool and then poured onto a column of neutral alumina packed with benzene. The red/violet band is eluted with dichloromethane, leaving an orange band remaining on the column. Recrystallization can be carried out by dissolving in isopropanol, adding three times the volume of hot heptane and placing in a freezer. Crystals can be easily grown by slow evaporation of an ether solution. Anal. Calcd for $C_9H_9CrO_6$: C, 40.77; H, 3.42; N, 0.00. Found C, 41.15; H, 3.36; N, -0.02. MS (ESI +), m/z = 266.0 (MH^+).

ii. 1,3-dicyclohexyl-1,3-propanedione. This synthesis is modified from literature procedures.[26] A 500 ml two neck round bottom flask was equipped with a reflux condenser and a rubber septum. 2.74 ml (20 mmol) of cyclohexyl methyl ketone (Alfa Aesar) was put into solution with 200 ml of dry diethyl ether and bubble degassed with nitrogen for ½ hour while stirring. 20 mmol of 2 M LDA (10 ml) was then added dropwise over 10 minutes, and the orange-brown solution was allowed to stir for 10 minutes. Meanwhile, 2.86 ml (20 mmol) of methyl cyclohexanecarboxylate (Aldrich) was bubble degassed in 100 ml of dry ether and added to the solution via cannula transfer. After refluxing for two hours, the solvent was removed and the product was put in water. The product was neutralized with dilute HCl, extracted with ether, and dried over sodium sulfate. This yields the crude product. To purify, put the product in a methanol solution: a white precipitate will form which was shown by NMR to be an aliphatic side

product. The precipitate was filtered off, and to the yellow methanol solution was added a very hot concentrated solution of copper(II) acetate in water. While cooling, a dark precipitate will form which is bis(1,3-dicyclohexyl-1,3-propanedionato)copper(II). Filter and wash with water and a large amount of methanol. (Anal. Calcd for $C_{30}H_{46}CuO_4$: C 67.45, H 8.68; found C 67.30, H 8.86). To liberate the ligand, dissolve the copper complex in ether and add about 50 ml of 10% sulfuric acid (aqueous) and shake until the green color of the copper complex is replaced by the light yellow of the ligand. Extract the ligand with ether, dry over sodium sulfate. The ligand can be recrystallized by dissolving in methanol and adding a small amount of water. Yield: 0.99g (21.2%). Anal. Calcd for $C_{15}H_{24}O_2$: C 76.23, H 10.24; Found C 76.41 H 10.46.

iii. tris(1,3-dibenzoylmethanato)chromium(III), Cr(dbm)$_3$. The synthesis was carried out via a previously published method.[27] Briefly, $Cr(acac)_3$ and a slight excess of 1,3-dibenzoylmethane were ground together, then heated at 175 °C for 4 hrs under a slight stream of N_2. The cooled product was broken up, heated with methanol to extract the starting materials, cooled, then filtered. After washing with acetone the product was recrystallized twice from benzene/cyclohexane. Anal. Calcd for $C_{45}H_{33}CrO_6$: C 74.90, H 4.58; Found C 74.16, H 4.18.

iv. tris(1,3-dibenzoylmethanato)gallium(III), $Ga(dbm)_3$. 1 mmol (0.256 g) of $Ga(NO_3)_3$ hydrate was dissolved in 20 ml methanol, and to it was added dropwise 3 mmol (0.672 g) of dibenzoylmethane in methanol over 15 minutes. A slurry of sodium bicarbonate (0.5 g in 20 ml) in methanol was added dropwise and the reaction was allowed to stir overnight, over which time the product precipitates. The product was filtered and washed with water. To recystallize, dissolve in dichloromethane and slowly add methanol. Yield: 0.35 g, 47%. Elemental analysis: Calculated for $C_{45}H_{33}GaO_6$: C 73.09, H 4.50; Found C 71.69, H 4.50. Note: the unreacted ligand can be recovered by adding water to the mother liquor to crash it out.

v. tris(1,3-dicyclohexyl-1,3-propandionato)chromium(III), $Cr(dcm)_3$. The synthesis can be easily carried out using previously published methods for tris(1,1,1,5,5,5-hexafluoroacetylacetonato)chromium(III).[18,19] Briefly, under inert conditions, $CrCl_2$ (0.1 g, 8.46×10^{-5} mol) was added to a solution of two times excess lithium bis(trimethylsilyl)amine (0.28 g) in 5 ml THF. After 15 minutes of stirring the solution should turn from colorless to purple, and finally to blue after about one hour. The reaction mixture was filtered to remove LiCl that had precipitated, and the mother liquor was cooled with an acetone/dry ice bath. Once cooled, a solution of 1,3-dicyclohexyl-1,3-propandione (60 mg, 2.54×10^{-4} mol) dissolved in a minimum amount of THF was added dropwise to the cold solution.

The color changes from blue to yellow. The solution is removed from the drybox and allowed to stir while exposed to the atmosphere, and the color changes from yellow to green. The solvent was removed, and the crude product washed with methanol and ether, and recrystallized via slow evaporation of 3:1 CH_2Cl_2/methanol solution. Yield. 19.7 mg (31%). Anal. Calcd for $C_{45}H_{69}CrO_6$: C 71.30, H 9.19, Found: C 70.66, H 9.52

vi. tris(1,3-dicyclohexylmethanato)gallium(III), Ga(dcm)$_3$. 0.114 g (0.564 mmol) of $Ga(NO_3)_3$ hydrate was dissolved in 10 ml methanol, and to it was added dropwise to 0.4 g (1.69 mmol) of 1,3-dicyclohexyl-1,3-propanedione in methanol over 15 minutes. A slurry of sodium bicarbonate (0.5 g (excess) in 20 ml) was added dropwise and the reaction was allowed to stir overnight, over which time the product precipitates. The product was filtered, and washed with copious amounts of methanol and water. To recystallize, dissolve in dichloromethane and slowly add methanol. Yield: 0.24 g (55%). Anal. Calcd for $C_{45}H_{69}GaO_6$: C 69.67, H 8.97; Found C 69.58, H 9.22. Note: the unreacted ligand can be recovered by adding water to the mother liquor to crash it out.

vii. tris(2,2,6,6-tetramethyl-3,5-heptanedionato)chromium(III), Cr(tbuylac)$_3$. To a solution of 2 ml water and 2 ml dioxane was added 0.6 g urea (excess), 0.184 g (1 mmol, 0.208 ml) of 2,2,6,6-tetramethyl-3,5-heptanedione, and 0.089 g (0.33

mmol) chromium(III) chloride hexahydrate. The reaction was refluxed for 3 days and the product washed with water and recrystallized from benzene/petroleum ether. Anal. Calcd for $C_{33}H_{57}CrO_6$: C 65.86, H 9.55; Found C 65.85, H 9.29.

viii. tris(1,1,1,5,5,5-hexafluoro-2,4-pentandiono)chromium(III). This method was adapted from the synthesis of tris(1,1,1-trifluoro-2,4-pentandionato)chromium(III).[28] 0.535 g (2 mmol) of chromium(III) chloride hexahydrate is dissolved in about 10 ml of water, to which 3.5 ml of 2 M NH_3 in ethanol is added slowly with shaking. The solution is allowed to stand for 10 minutes, after which the turquoise product, $Cr(OH)_3$, is gravity filtered and washed with water. The moist $Cr(OH)_3$ is added to a solution of 1 ml 1,1,1,5,5,5-hexafluoro-2,4-pentandione (excess) in 20 ml of dimethoxypropane. 0.34 ml of glacial acetic acid is added, and the solution should feel cool while it turns purple as the $Cr(OH)_3$ dissolves. The solution is stoppered and allowed to react overnight. The product is filtered, air dried, and recrystallized by heating the product in ethanol, filtering the solution, and adding hexanes to the filtrate. Yield 0.164 g. The product in stored in an inert atmosphere in the dark, as prolonged exposure results in decomposition of the product. This complex can also be made from a literature preparation utilizing a Cr(II) precursor.[18]

3.4 Results and Discussion

3.4.1 $Cr(acac)_3$. Although the absorption and emission spectra of this complex have been examined previously, this section will explore the excited state electronic structure of $Cr(acac)_3$ in great detail, as the results and concepts developed here will be extremely useful for analysis and assignment of transitions for the other members of this series. The absorption spectrum, shown in Figure 3-10, consists of several transitions in the ultraviolet, centered at 250 nm ($\varepsilon \sim 11100$ M^{-1} cm^{-1}), 270 nm ($\varepsilon \sim 10000$ M^{-1} cm^{-1}) and a more intense band at 330 nm ($\varepsilon \sim 15000$ M^{-1} cm^{-1}). Another transition of much lower intensity, centered at 374 nm with $\varepsilon \sim 430$ M^{-1} cm^{-1}, is observed on the shoulder of the intense band at 330 nm. In the visible one observes a very broad band of low intensity centered at 560 nm with $\varepsilon \sim 65$ M^{-1} cm^{-1}. The emission spectrum is quite narrow with maximum intensity at 775 nm (12907 cm^{-1}).

Starting in the UV, the transitions at 250 nm and 270 nm are assigned as an intraligand $\pi \rightarrow \pi^*$ transition based on the absorption spectrum of $Ga(acac)_3$. In this complex ligand field and charge transfer transitions are precluded due to the closed shell nature of the Ga(III) ion, leaving only the possibility of intraligand transitions. The transition, centered at 280 nm, is quite intense with $\varepsilon \sim 31000$ M^{-1} cm^{-1}. Given this assignment, the other intense transition in the UV, at 330 nm, is assigned as a charge-transfer transition based on its intensity. Given the relatively high oxidation potential of the chromium(III) ion this transition is likely a ligand-

to-metal charge transfer (LMCT) transition, whose orbital parentage is depicted in Figure 3-11.

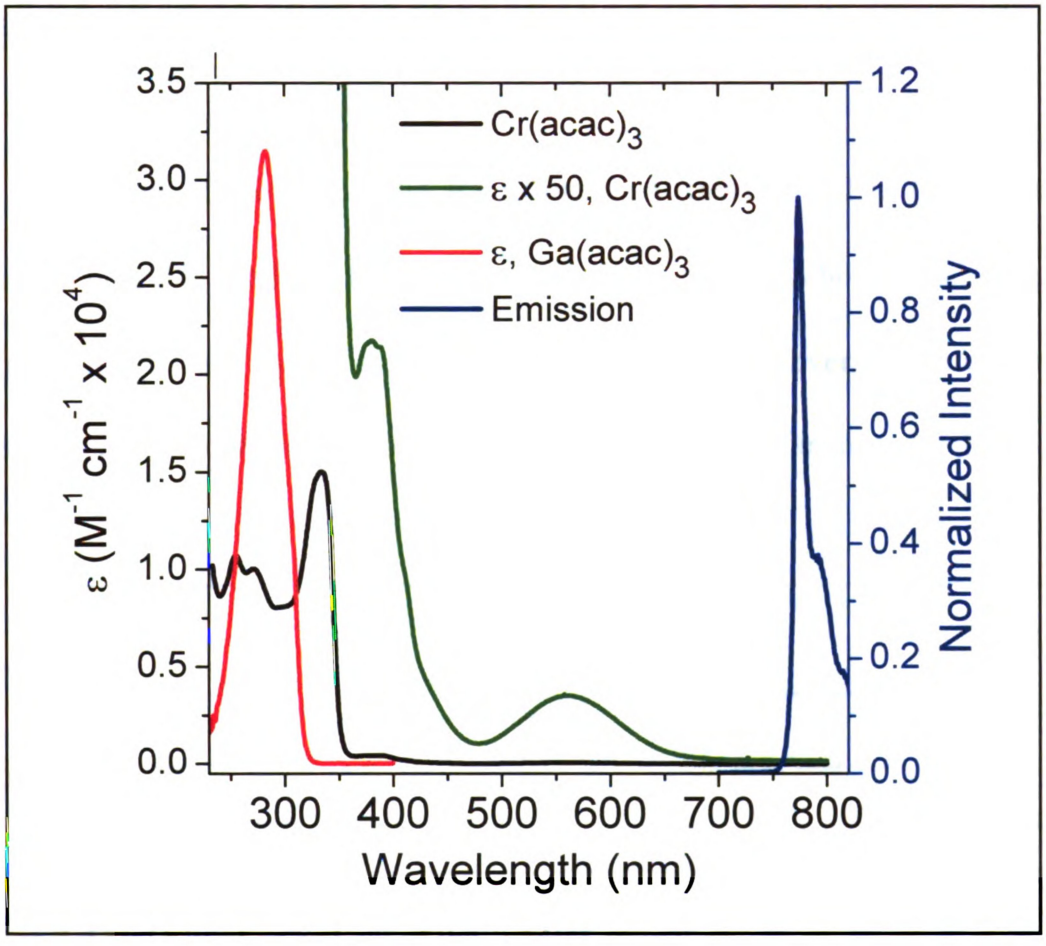

Figure 3-10: Absorption and emission spectra for $Cr(acac)_3$, acquired in dichloromethane and a low-temperature (80 K) optical glass of 2-methyltetrahydrofuran, respectively.

In this drawing, the π orbitals shown on the right are ligand ($acac^-$) based. These assignments have been confirmed in the literature. Barnum[29] assigns the band near 330 nm to a CT type transition despite previous assignment of a $\pi \rightarrow \pi^*$

transition due to the high intensity. All transitions higher in energy he assigns to $\pi \rightarrow \pi^*$ transitions. This corresponds well to the transitions of $Ga(acac)_3$, which can have no CT type transitions due to the redox-inert nature of the gallium(III) ion, and show no strong absorptions near 330 nm. Fleming and Thornton[30] agree with this assignment of the ultraviolet transitions in $Cr(acac)_3$. The transitions of $Cr(acac)_3$ near 345 nm have been assigned in the literature as both metal to ligand charge transfer[31] and ligand to metal charge transfer. However, as stated above, the stability of chromium(III) to oxidation makes a LMCT far more likely (Figure 3-11).

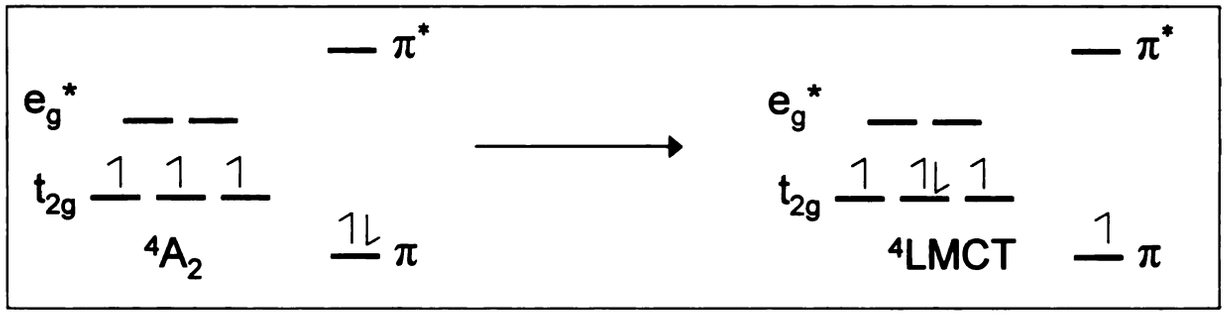

Figure 3-11: Orbital parentage of the ^{4}LMCT transition.

$Cr(acac)_3$ shows a shoulder on this charge-transfer band around 380 nm with intensities 7-8 times that of the $^4A_2 \rightarrow {}^4T_2$. Fleming and Thornton assign this as $^4A_2 \rightarrow {}^4T_1$, but Barnum hesitated to assign the shoulder to a ligand field transition due to the relatively large intensity. This band has even been assigned as a charge-transfer type transition.[31] Hanazaki and coworkers have ascribed the higher extinction coefficient of this transition as due to coupling between the

ligand field and ligand based electrons.[32] This coupling will now be described in detail. Many complexes of aromatic ligands bound to chromium(III) have moderate-strength absorptions (300-2000 $M^{-1}cm^{-1}$) which can not easily be assigned as ligand field (generally $\varepsilon < 100\ M^{-1}\ cm^{-1}$), charge transfer, or ligand based ($> 10^3 - 10^4\ M^{-1}\ cm^{-1}$). These transitions have been observed in chromium(III) complexes of bipyridine,[33-35] phenanthroline,[35] as well as substituted acetylacetonate complexes of chromium(III). In the late 1960's Nagakura and coworkers suggested that these transitions were to an excited state constructed from both triplet intraligand (^{3}IL) character and ligand-field character, arising from direct coupling between the unpaired electrons on the ligand and metal center.[36-38] Twenty years later Hanazaki and coworkers re-examined this problem,[32] with the results presented below.

To estimate the relative probability of a so-called $^4(^3IL)$ transition (i.e. a total spin-allowed transition as a result of coupling between triplet ligand and metal-based spins) the authors start by constructing the relevant zero-order wavefunctions, which include both metal and ligand electrons. As an example, the ground state and one possible charge-transfer state can be expressed as comprised of both d-orbital and ligand-based orbitals. Using this formalism the states $^4(^1IL)$ and $^4(^3IL)$ can be constructed, corresponding to states with total quartet spin which include the ligand frontier orbitals. While the $^4(^1IL)$ state simply corresponds to a ligand localized $\pi \rightarrow \pi^*$ transition, the $^4(^3IL)$ state arises from coupling with the

ligand triplet states, and transition from the ground state to this state is forbidden due to the triplet character of the ligand. However, these states can become optically allowed if ^{4}CT character is mixed in. Using this intensity-borrowing mechanism, the authors were able to develop an equation which gives the ratio of the oscillator strengths of the easily-assignable $^4(^1\text{IL})$ to the more ambiguous $^4(^3\text{IL})$, using only the energies of the $^4(^1\text{IL})$, $^4(^3\text{IL})$, and charge transfer states. The equation they developed results in a ratio of 0.04 for $Cr(bpy)_3$, in reasonable agreement with many of the moderate-strength absorptions observed in both $Cr(acac)_3$ and $Cr(bpy)_3$-type complexes. Therefore, this moderate-strength absorption has been assigned as a transition to a quartet state that possesses quartet charge-transfer and triplet intraligand character, $^4(^3\text{IL})$, the orbital parentage of which is depicted in Figure 3-12.

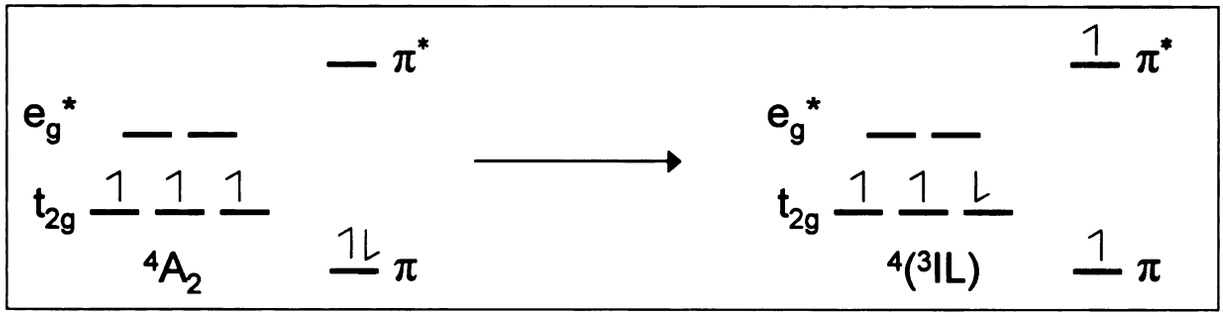

Figure 3-12: Orbital parentage of the $^4(^3\text{IL})$ transition.

In terms of purely ligand field transitions, the weak absorption whose maximum is at 560 nm is assigned as the $^4A_2 \rightarrow {}^4T_2$ transition, the lowest-energy spin-allowed transition for a d_3 ion. This transition is well separated from the others

discussed above, allowing for selective excitation into the $^4T_2$ electronic state using a broadband ultrafast laser pulse. The next highest spin allowed ligand field state in energy is the $^4T_1$, which is likely buried under the $^4(^3IL)$ state near 375 nm. Both states share a $(t_{2g})^2(e_g^*)^1$ orbital parentage, leading to a displacement of the electronic potential wells along the metal-ligand coordinate with respect to the ground state (Figure 3-13). This displacement leads to the broad absorptions observed in the visible region.

The lowest-lying excited state, ^2E, is emissive in low temperature optical glasses. For $Cr(acac)_3$ this emission occurs at 775 nm and is extremely narrow. The narrowness of this transition, as with the breadth of the $^4T_2$ absorption described in the preceding paragraph, can be attributed to the relative geometries of the metal coordination sphere between the two electronic states. For the case of ^2E the orbital parentage is the same as the ground state $^4A_2$ (both are $(t_{2g})^3$, Figure 3-13), leading to very small geometric distortions between these electronic states, and thus the narrow emission spectrum.

Our group has already explored the nonradiative dynamics of $Cr(acac)_3$ using optical ultrafast transient absorption techniques with ~ 100 fs pulses.[4,7] It is well established that the ^2E state recovers to the ground state with $\tau \sim 700$ ps, and Figure 3-14, upper panel, shows that the full transient spectrum at 5 ps corresponds to the nanosecond full spectrum, proving that the ^2E state is fully established by 5 ps. Figure 3-14, lower panel, shows full transient spectra over the

first 5 ps after excitation. These chirp-corrected spectra reveal essentially the same lineshape over this time frame, even as early as 400 fs, showing that the ^{2}E state is established faster than the resolution of the measurement. The slight narrowing and loss of intensity of the spectrum over the first 5 ps was assigned as due to vibrational cooling in the ^{2}E; the signatures of this process were discussed above and will not be elaborated on here. The slight decay of the spectrum was fit to a lifetime of 1.1 ± 0.1 ps.

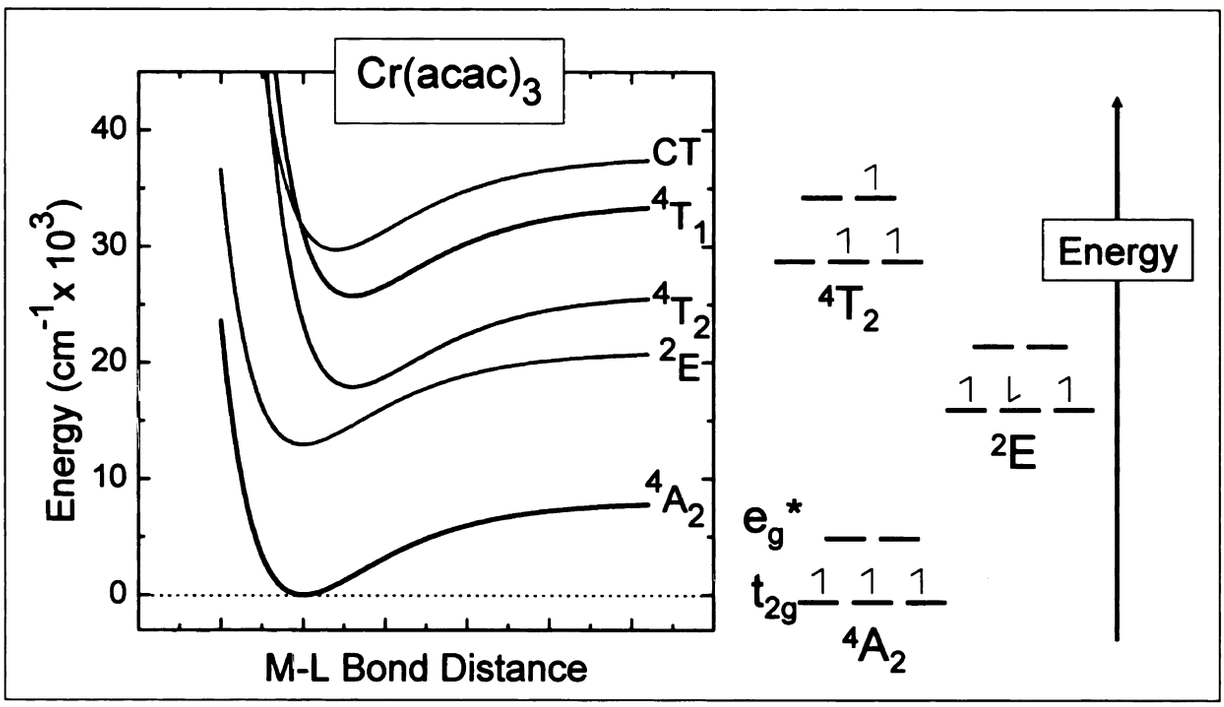

Figure 3-13: Semi-qualitative energy level diagram (left) and diagram showing the orbital parentage of the relevant ligand field electronic states (right) for $Cr(acac)_3$.

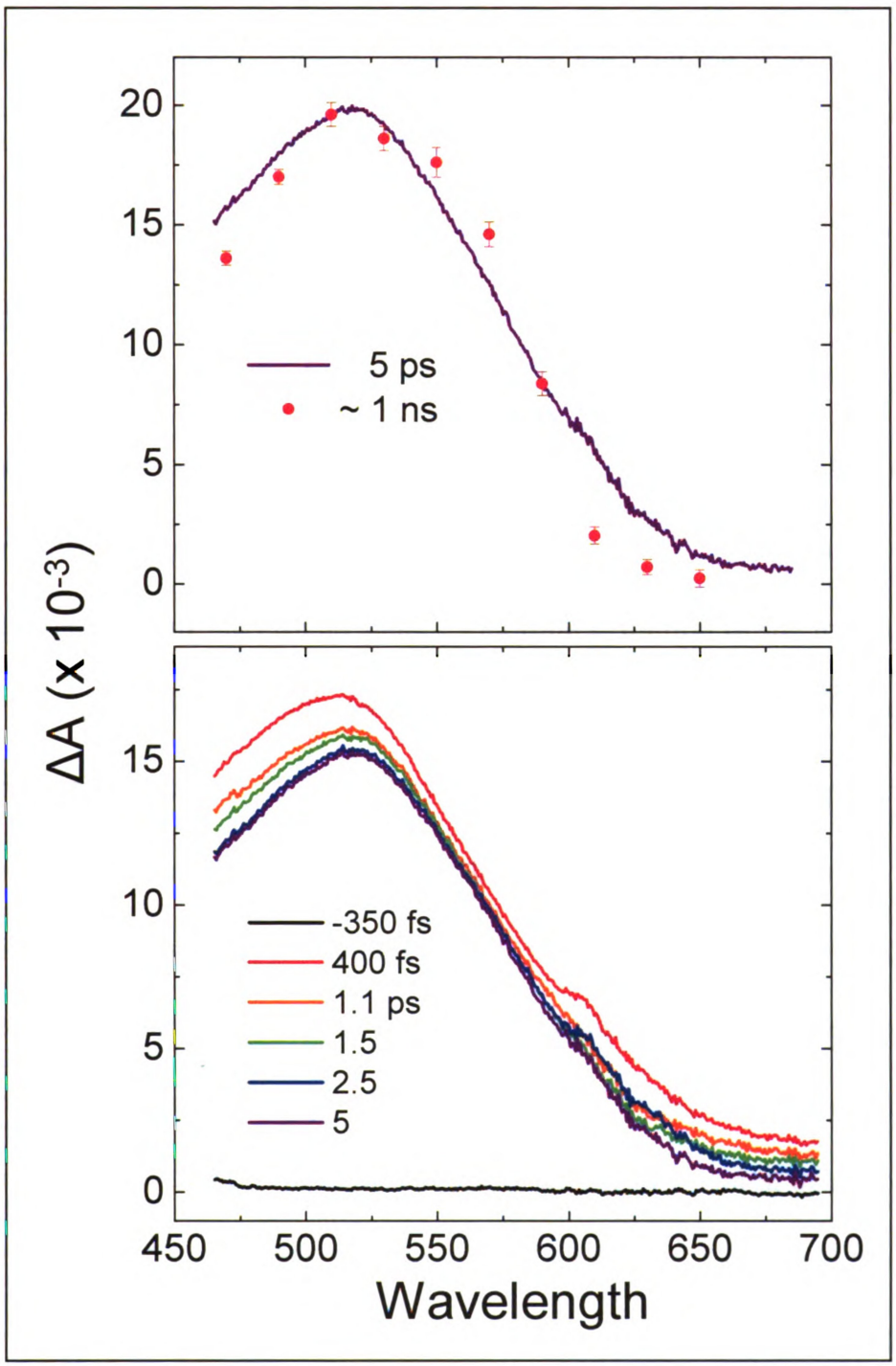

Figure 3-14: Data revealing vibrational cooling dynamics on the ^2E surface of $Cr(acac)_3$ after excitation of the sample at 625 nm, adapted from reference 6. See text for details.

This picture of nonradiative decay in these systems was slightly modified by a report by Kunttu and coworkers,[39] wherein they reported the relaxation dynamics of $Cr(acac)_3$ as probed by ultrafast transient infrared spectroscopy. The question they wished to address was whether relaxation via the ^2E constitutes a major relaxation pathway. By monitoring the υCO and υC=C stretches after pumping into the $^4T_1$ (400 nm) and ^{4}LMCT (345 nm) excited states they were able to address this question, by assuming that the vibrational characteristics of the ^2E state are distinct from those of the ground $^4A_2$ state. The transient data shows complete recovery of the ground state. The time evolution of the transient υC=C stretch (pump at 400 nm and probe at 1521 cm^{-1}) was fit with biphasic kinetics with time constants τ_1 = 15 ps and τ_2 = 760 ps. While the 760 ps component corresponds to ground state recovery via the ^2E state, the authors explain the faster dynamics as follows: after pumping into a high excited state and prompt intersystem crossing into the doublet manifold, redistribution of the excess energy into vibrations leads to a heating of the molecule. This in turn enhances BISC into the quartet manifold until vibrational cooling leads to a trapping of the remaining population in the ^2E state. Most of the ground state (70-85%) population recovers with a time constant of 15 ps, attributed to internal conversion from the $^4T_2$. These results are not at odds with the data acquired in the optical ultrafast transient absorption experiment, and serve to indicate the limitations of the transient absorption experiment in the absence of a definite $^4T_2$ feature. The dynamics of

the low-lying ligand field manifold are summarized in the Jablonski diagram of Figure 3-15.

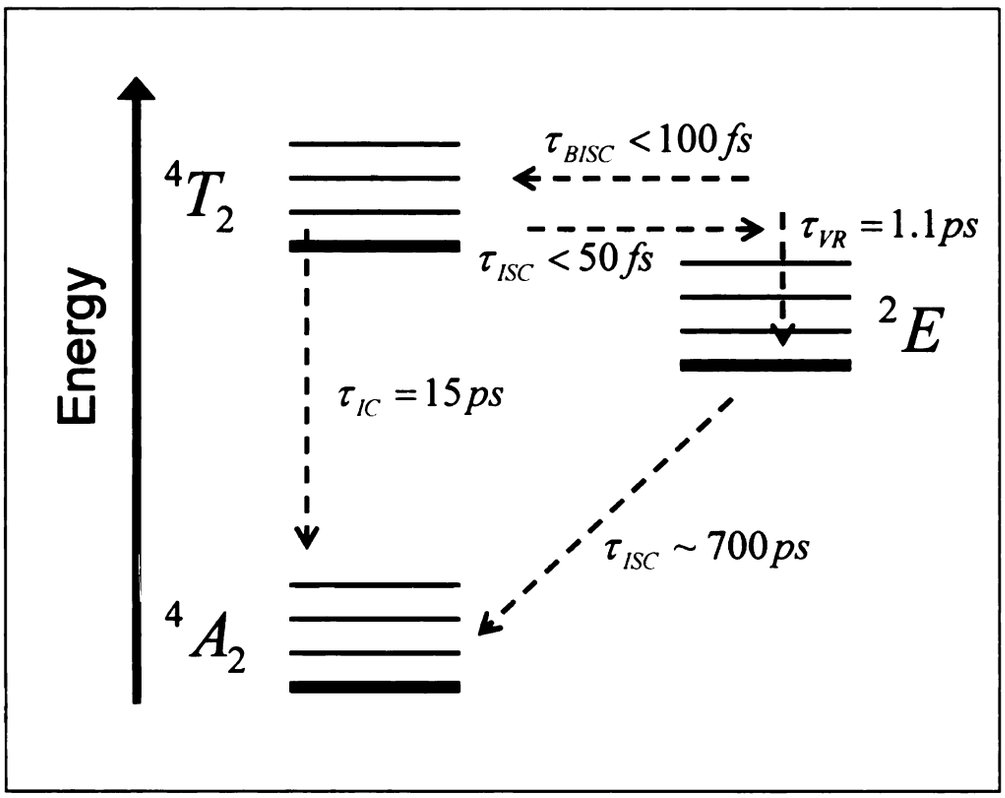

Figure 3-15: Jablonski diagram summarizing the nonradiative rates in the low-lying ligand field manifold of $Cr(acac)_3$.

In an effort to resolve the ultrafast intersystem crossing event for this system, transient absorption experiments were carried out using the ultrafast system of the Beck group at Michigan State University, which produces ~ 50 fs pulses. The sample was prepared in acetonitrile with an absorbance of ~0.7, and flowed during the experiment to prevent any possible signals from photodecomposition. Initial experiments employed excitation at 600 nm (15 nm FWHM), resulting in the preparation of a relatively cool vibrational Frank-Condon state of the $^4T_2$ surface.

The probe pulse was also 600 nm, and a monochromator was employed to select probe wavelengths of 592 ± 2 nm (Figure 3-16) or 608 ± 2 nm (Figure 3-17). The entire probe pulse was also employed as a probe (Figure 3-18). The kinetic trace of Figure 3-16 was obtained by subtracting an exponential decrease in excited state absorption with a time constant of 320 fs to obtain a flat baseline. This time constant is on the appropriate time scale for intramolecular vibrational redistribution processes. Fitting of the oscillatory component (the residual after subtraction of the exponential components) was accomplished with a program of local origin, and has been described in detail elsewhere.[40,41] Briefly, the oscillatory residuals were fit with a multicomponent model that contains both slowly damped and rapidly damped components. The slowly damped components can be modeled as a simple damped cosinusoid, while the rapidly damped components are modeled in the time domain with inhomogeneously broadened components with asymmetric Gaussian lineshapes. The data of Figure 3-16 reveals a rapidly damped oscillation which was fit with two oscillatory components: (1) a frequency of 164 cm^{-1} that damps with τ = 70 fs, and (2) a weaker component that oscillates with 75 cm^{-1}. This weaker, 75 cm^{-1} component has less than 5% of the amplitude of the 164 cm^{-1} oscillation, and functionally serves to model all low-lying modes of the system. The redder probe (Figure 3-17) reveals similar oscillatory kinetics as Figure 3-16, and a 1.6 ps ESA decay was

subtracted from this data. The data acquired with the integrated probe pulse (Figure 3-18) was fit with a biexponential function (τ_1= 50 fs, τ_2= 1.3 ps).

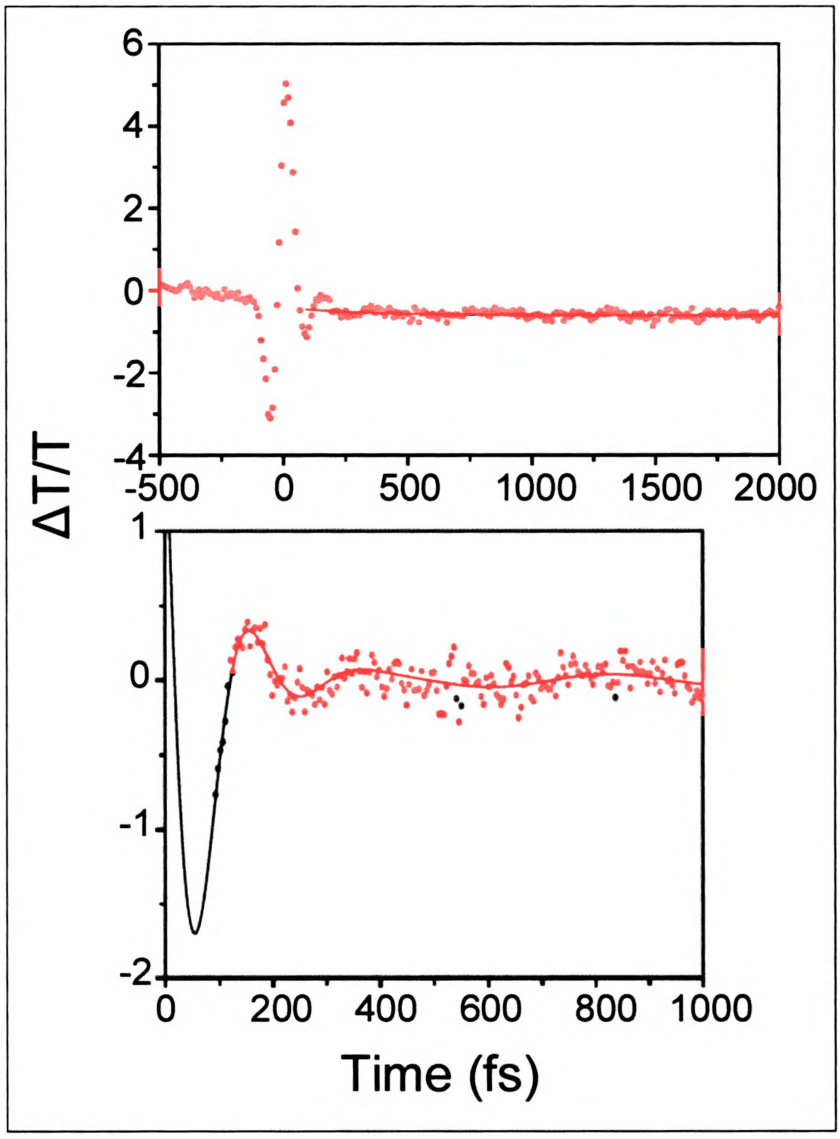

Figure 3-16: Kinetic trace for $Cr(acac)_3$ pumped at 600 nm and probed at 592 ± 2 nm. A monexponential rise (τ = 320 fs) in excited state absorption was subtracted from the raw data (top panel) to obtain a flat baseline. The resulting data (bottom panel) are fit with a rapidly damped oscillatory component (164 cm^{-1}, τ = 70 fs) and one weaker component (75 cm^{-1}).

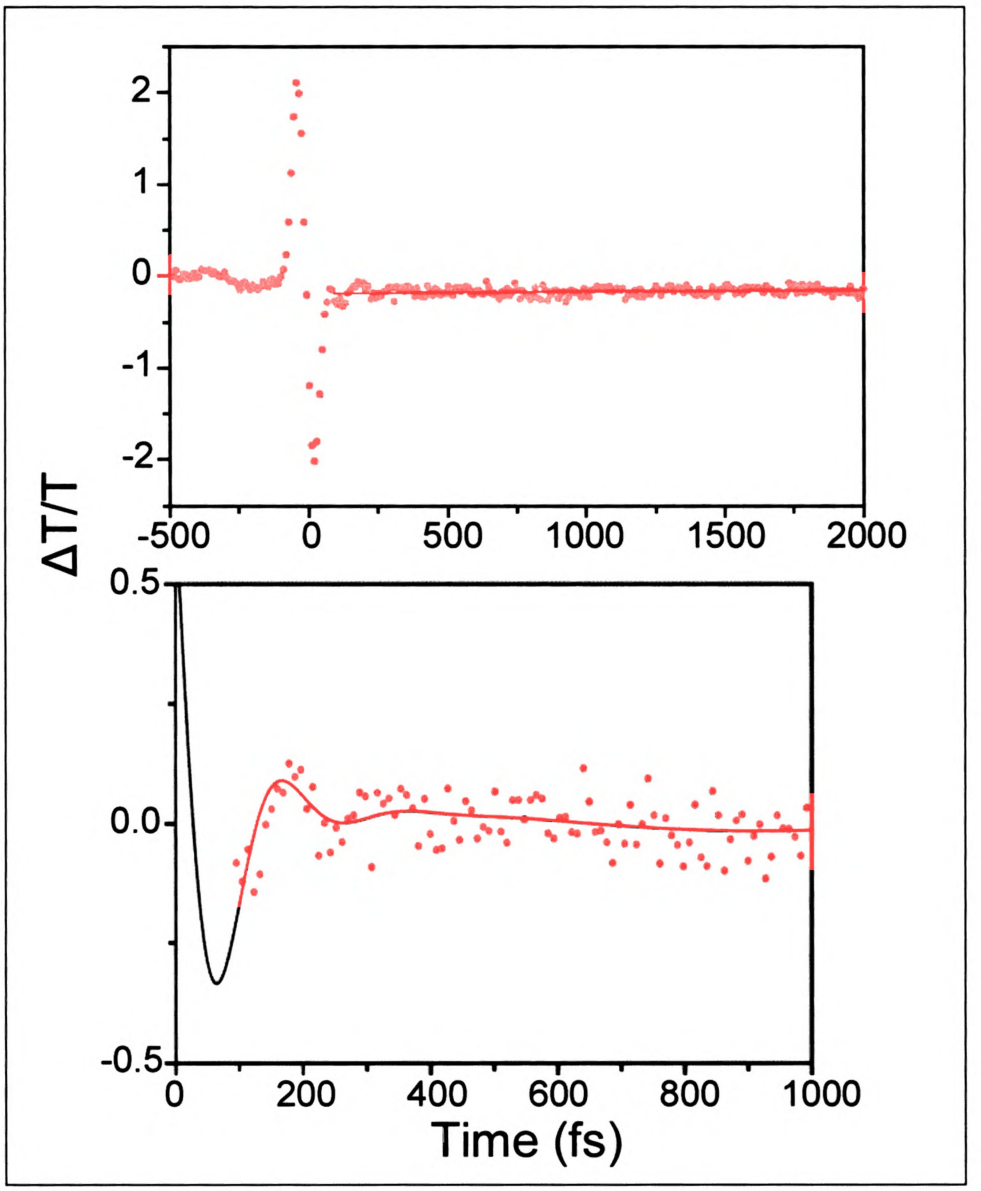

Figure 3-17: Kinetic trace for $Cr(acac)_3$ pumped at 600 nm and probed at 608 ± 2 nm. A 1.6 ps rise in excited state absorption was subtracted from the raw data (top panel) to obtain a flat baseline. The resulting data (bottom panel) are fit with a rapidly damped oscillatory component (165 cm^{-1}, τ = 70 fs) and one weaker component (28 cm^{-1}).

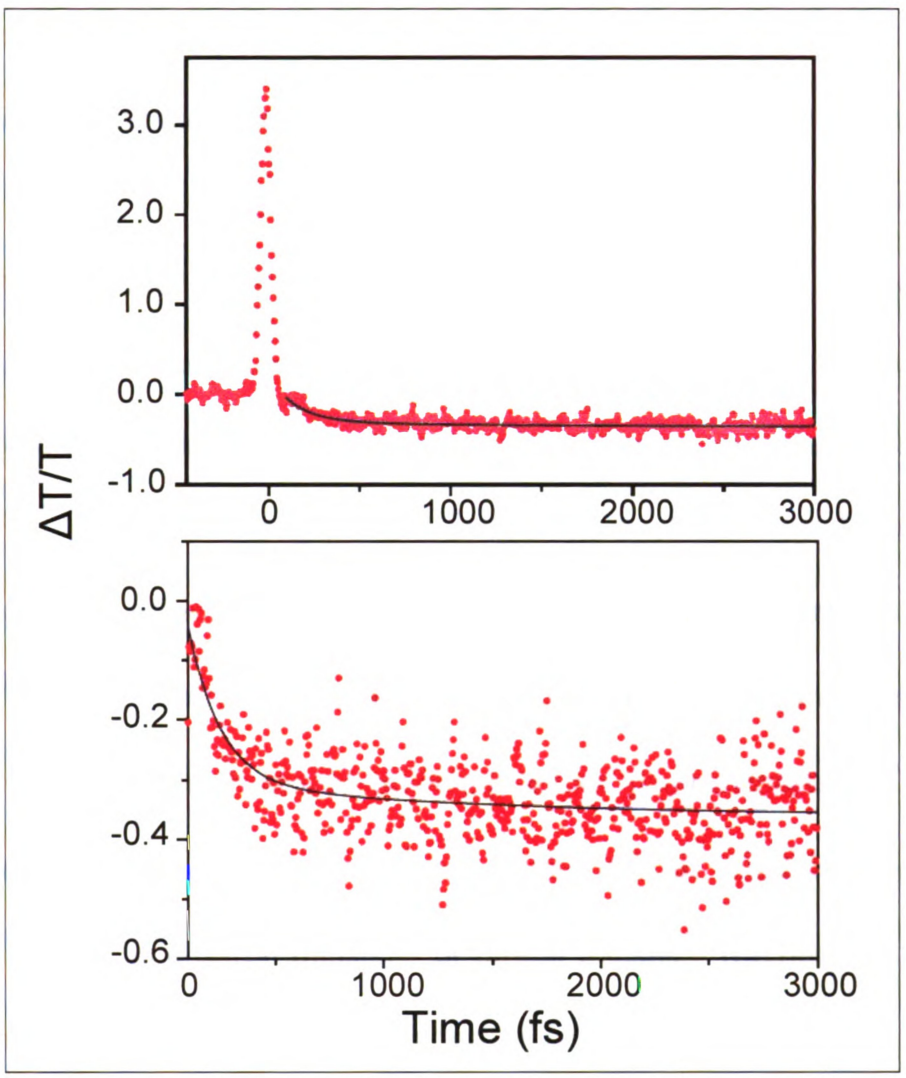

Figure 3-18: Kinetic trace for $Cr(acac)_3$ pumped at 600 nm and utilizing the integrated probe pulse centered at 600 nm (top). The data was fit with a biexponential rise in ESA (τ_1 = 50 fs, τ_2 = 1.3 ps).

These observations likely represents vibrational coherence is this system. In recent years, vibrational coherence has been observed in many transition metal coordination systems: many cases exist of coherence in zinc porphyrins,[41,42] heme

complexes,[11,12,43] other metalloproteins[44] and mixed valence species.[45,46] To date, observation of vibrational coherence is rare for simple coordination complexes, although recently coherence has been reported for $[Fe(bpy)_3]^{2+}$.[47] In most cases coherence is observed on a single electronic state. This state can be the initially populated excited state (so called impulsive absorption), although coherence on the ground state, formed via impulsive stimulated Raman scattering, is also quite common.[40,41,46] Control of relative contributions of excited state and ground state coherence can be achieved by varying excitation pulse duration[48] and introducing chirp.[42,49] Finally, coherence can be produced on other electronic states via indirect coherence mechanisms, involving either photochemistry,[11,50-53] rapid geometric changes,[47] or formation of some other type of product state (e.g. an acceptor state in an electron transfer[54] or proton transfer[55] reaction). A different phenomenon involves so-called "retention of coherence," wherein a vibrational wavepacket is formed on one electronic surface and propagates through a barrier to populate another electronic state, with the wavepacket still intact. Some interesting examples include work on photosynthetic bacterial reaction centers and the FMO photosynthetic model complex, which has shown that coherence is maintained between different excitonic states in these systems, disproving the previously assumed incoherent hopping mechanism.[56-58] This phenomenon has also been observed during internal conversion in cyanine dye molecules,[59]

photochemical rearrangements,[60] photoisomerization (although many such examples involve barrierless isomerization),[61,62] and mixed valence species.[45]

The time scales of ground state recovery (via the $^4T_2$ and ^2E states, as discussed above) are much longer than the observed kinetics, suggesting an excited state coherence. Given the previous studies that have been carried out on this molecule (*vide supra*), it is reasonable to think that a conservative estimate of the lifetime of the $^4T_2 \rightarrow {}^2E$ ISC event is < 100 fs. Again, looking to the kinetic trace of Figure 3-16, it is seen that significant amplitude of the oscillatory component is present at later times (> 400 fs). This observation, coupled with the estimated lifetime for ISC, suggest that coherence is retained during this ISC event, i.e. coherence is taking place on the Franck-Condon state and is maintained during the ultrafast intersystem crossing event that immediately follows excitation, a first for a simple coordination compound. This may be the first reported account of retention of coherence for a spin-forbidden (i.e. intersystem crossing) event.

If retention of coherence is occurring during intersystem crossing, then the frequency of the coherent vibration suggests the nature of the vibrational mode that is coupled to the $^4T_2 \rightarrow {}^2E$ conversion (*vide infra*), revealing significant implications for the mechanism of ultrafast ISC in this complex. Vibrational spectra of tris(acetylacetonato)metal(III) complexes have been extensively studied both experimentally and theoretically.[63-71] The Cr-O stretch is reported as a wide absorption near 250 cm^{-1}, and there are several other low-frequency vibrations of

$Cr(acac)_3$, although no reports (infrared or Raman) of a vibrational mode near 164 cm^{-1}, the observed frequency of both the 592 nm and 608 nm probes, again suggesting an excited state coherence. This value may correspond to the vibrational frequency of the Cr-O stretch in the $^4T_2$ state: this excited ligand field state has occupation of an e_g^* orbital and thus weakened Cr-O bonds are expected. A ground state frequency calculation at the UBLYP/6-311g** level, employing a CPCM solvent model for acetonitrile (Figure 3-19), reveals that the 250 cm^{-1} mode is indeed metal-ligand active, but also includes large amplitude oscillations involving the peripheral methyl groups of the acac ligand (the calculation also reveals several vibrations near 164 cm^{-1}, but these are not metal-ligand active). This observation, along with recent results on substituted complexes of $Cr(acac)_3$, highlighted below, imply a significant role for the structure of ligand backbone in the ultrafast $^4T_2 \rightarrow {}^2E$ conversion.

Although the timescales for the various dynamical events reported above point to retention of coherence, one can not discount coherence on the ^2E surface as a result of an indirect coherence mechanism. Such a mechanism has been reported recently for $[Fe(bpy)_3]^{2+}$, where vibrational coherence was reported on the lowest-energy excited state, $^5T_2$.[47] The authors note that the observed coherent frequency of 130 cm^{-1} was likely due to N-Fe-N bending modes which were coherently excited by the impulsive Fe-N stretch during the change from a low spin to a high spin state. In the case of $Cr(acac)_3$ one would also expect significant geometric

distortions along the Cr-O bonds in the $^4T_2$ excited state. Thus one would anticipate the coherent mode to be metal-ligand active. The question remains whether this coherence is formed on the Franck-Condon state or formed on the ^2E state as a result of an impulsive stretching of the Cr-O bonds on the same timescale as intersystem crossing. Again, given the timescales observed for this system the former is preferred.

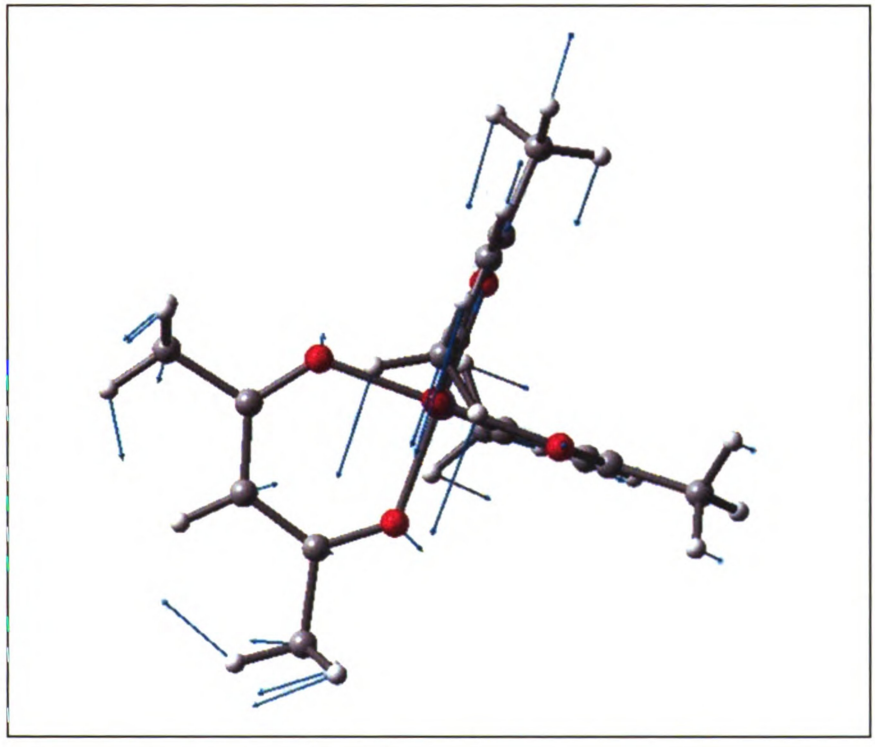

Figure 3-19: Ground state frequency calculation for $Cr(acac)_3$ at 250 cm^{-1} at the UBLYP/6-311g** level, employing a CPCM solvent model for acetonitrile.

This observation has significant implications pertaining to the mechanism of the ultrafast ISC event. Retention of coherence during this event suggests that the $^4T_2$ and ^2E states are very strongly coupled via the observed low frequency

mode (164 cm^{-1}). This further implies that this low frequency mode (or perhaps low-frequency modes) plays a significant role in facilitating ultrafast ISC in this complex. Work by Perkovic and Endicott in the early 1990s on vibrationally constrained complexes of chromium(III) (primarily derivatives of 1,4,7-triazacyclononane, TACN) has implicated low-frequency modes as playing an important role in $^2E \rightarrow {}^4A_2$ conversion.[72] In a non-constrained system, low-frequency modes would produce a trigonal distortion; this distortion would then allow mixing of d-orbital character, making the way for rapid intersystem crossing. The constraining complexes inhibit low-frequency modes, preventing a trigonal distortion, and effectively slowing nonradiative decay via this pathway. It is reasonable to assume that some similar mechanism, coupled with the relative displacement and energies of the $^4T_2$ and ^2E states, may be facilitating ultrafast $^4T_2 \rightarrow {}^2E$.

This description of intense vibronic coupling between two electronic states to facilitate an ultrafast intersystem crossing event is essentially that of a spin-forbidden "conical intersection." Conical intersection simply describes the molecular geometry points at which two potential energy surfaces—of the same spatial and spin symmetry—intersect. These constitute degenerate and intersecting points among the two surfaces, which are characterized by strong vibronic coupling, resulting in an effective breakdown of the separation of electronic and vibrational components of the wavefunction (Born-Oppenheimer

approximation). This strong vibronic coupling provides a facile mechanism for ultrafast interstate crossing (i.e. internal conversion, as observed mainly for organic systems and biological systems[73,74] or intersystem crossing). As a result of this property, conical intersections have also been called "photochemical funnels," because the ultrafast processes that they induce effectively quench other kinetic pathways, and funnel the energy toward a certain photochemical or photophysical path. The breakdown of the Born-Oppenheimer approximation is especially relevant for large polyatomic molecules, which are characterized by a large number of close-lying electronic states and a high number of degrees of freedom, leading to a high density of vibrational states. [75]

This study of coherence in these systems, and the implications of the mechanisms of nonradiative decay that they suggest, are an exciting new avenue for this research and is covered extensively in the future work chapter, Chapter 5.

3.4.2 3-substituted Complexes of 2,4-pentanedione.

$Cr(3\text{-}NO_2ac)_3$. This complex forms purple crystals, and is purple/pink as a powder and in solution. Assignments for the UV-vis absorption spectrum, shown in Figure 3-20, are fairly straightforward due to the similarity of this spectrum to that of $Cr(acac)_3$ (*vide supra*). Starting in the UV there is a transition centered at 272 nm ($\varepsilon \sim 17000\ M^{-1}\ cm^{-1}$), another of slightly lower intensity at 330 nm ($\varepsilon \sim$

13400 M^{-1} cm^{-1}) and an anomalous transition centered near 366 nm ($\varepsilon \sim 4000$ M^{-1} cm^{-1}). In the visible is a low-intensity broad transition centered at 560 nm.

The transition at 272 nm matches well what has been observed in $Cr(acac)_3$ as an intraligand $\pi \rightarrow \pi^*$ type transition: $Cr(acac)_3$ shows two peaks in this region at 255 nm and 275 nm. A lower energy transition as predicted by the nephelauxetic effect is not observed, indicating that the nitro group is not coupling well into the inner π system of the acetylacetonate ligand. This is evident from the x-ray crystal structure of this complex, presented in Appendix C, which reveals that the π orbitals of the nitro groups are close to 90° with respect to the π system of the acetylacetonate core. The apparent orthogonality of the nitro π system to that of the acetylacetonate ligand is further manifested by the rest of the absorption spectrum as well. The absorption at 330 nm is assigned as a ligand-to-metal charge transfer transition based on a similar absorption observed for $Cr(acac)_3$ centered at 333 nm. Any coupling between the nitro and acac π systems should result in a red shift of this peak relative to $Cr(acac)_3$, which is not observed. In fact, a new transition arises centered at 366 nm that has an oscillator strength in the range of charge transfer transitions. It is hypothesized that this transition is due to a charge transfer transition directly from the nitro substituent to the metal center (LMCT). The broad transition at 560 nm is easily assigned as absorption to the spin-allowed $^4T_2$ ligand field state.

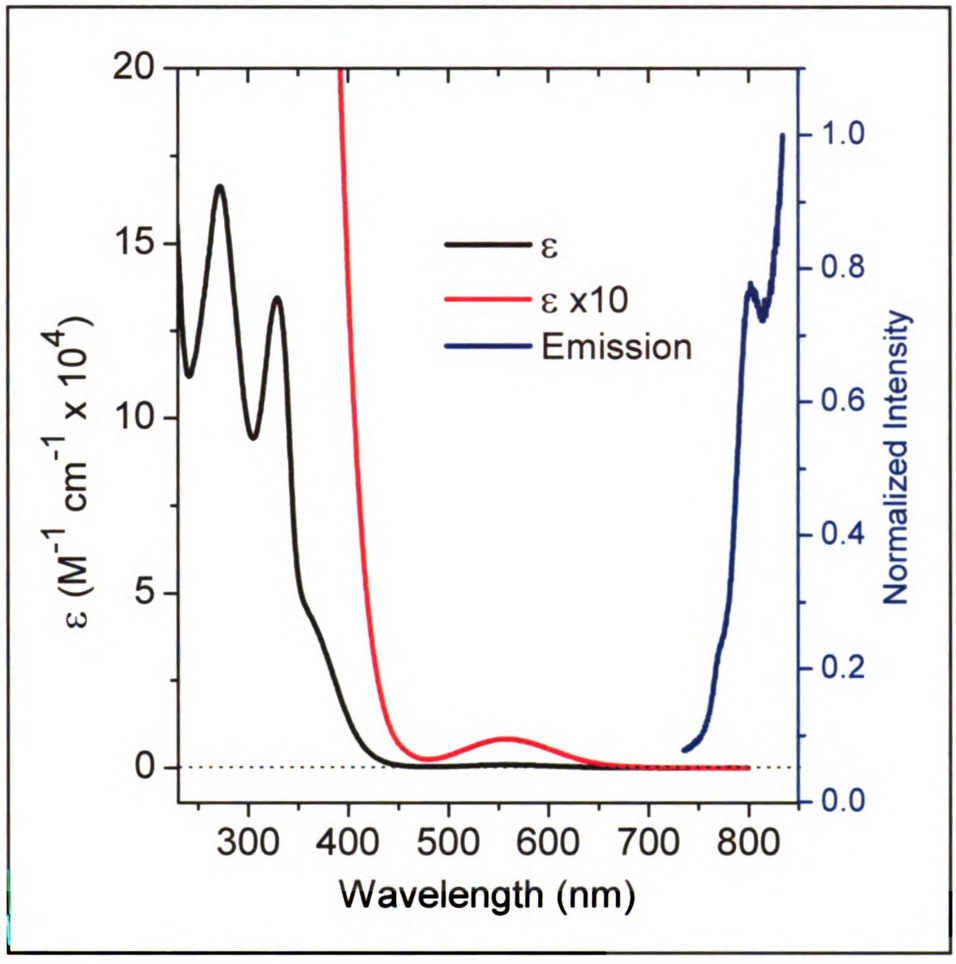

Figure 3-20: UV-vis spectrum recorded in dichloromethane and emission spectrum recorded in a low temperature glass of 2-methyl-tetrahydrofuran for $Cr(3\text{-}NO_2ac)_3$.

Considering the electronic similarities between this complex and $Cr(acac)_3$ one would intuitively expect similar dynamics to those of $Cr(acac)_3$. This is in fact the case. Initial experiments were carried out with ~ 100 fs pulse duration, resulting in an effective resolution (cross correlation of solvent signal) of ~ 250 fs.

Starting with longer timescale data (Figure 3-21), it is observed that ground state recovery occurs with a lifetime of ~730 ps; the value for $Cr(acac)_3$ is ~ 760 ps. The full spectral excited state absorption dynamics (Figure 3-21, left) reveal an excited state absorption that decreases in intensity with time without changing bandshape, indicating absorption from the same excited state at all time points with loss of this state to the ground state. From previous work on $Cr(acac)_3$ this absorption is assigned as originating from the lowest energy excited state, ^2E, and the observed dynamics are due to loss of this state via intersystem crossing to the ground state, $^4A_2$. With regard to the bandshape of the ^2E spectrum it is interesting that it is clearly composed of two different Gaussian lineshapes, perhaps corresponding to transition to two distinct charge-transfer states as discussed above.

Moving on to shorter timescale dynamics, it is seen that the early time full spectra (Figure 3-22, left) are again composed of a very broad absorption with maximum excited state absorption around 510 nm. This bandshape is the same as that observed in the longer time spectra (above), representative of absorption from the ^2E state. This bandshape is also observed in the full spectrum at 300 fs (not shown), the effective resolution of our instrument, indicating that the ^2E state is formed faster than the resolution of the experiment. The early time (1 ps) full spectra are much broader than full spectra for later times: the narrowing of the full spectra with time is indicative of vibrational cooling, which is occurring on the ^2E

surface. Single wavelength kinetics (Figure 3-22, right) show that this cooling occurs with $\tau = 1.65 \pm 0.03$ ps, slightly slower than the same process for $Cr(acac)_3$. These observations were invariant with excitation wavelength across the $^4T_2$ absorption: at all pump wavelengths the full spectra narrowed with time over the first ~ 10 ps, and the lifetime of this process as a function of pump wavelength was essentially invariant (Figure 3-23). All of these observations suggest very similar mechanisms of nonradiative decay to those observed for $Cr(acac)_3$.

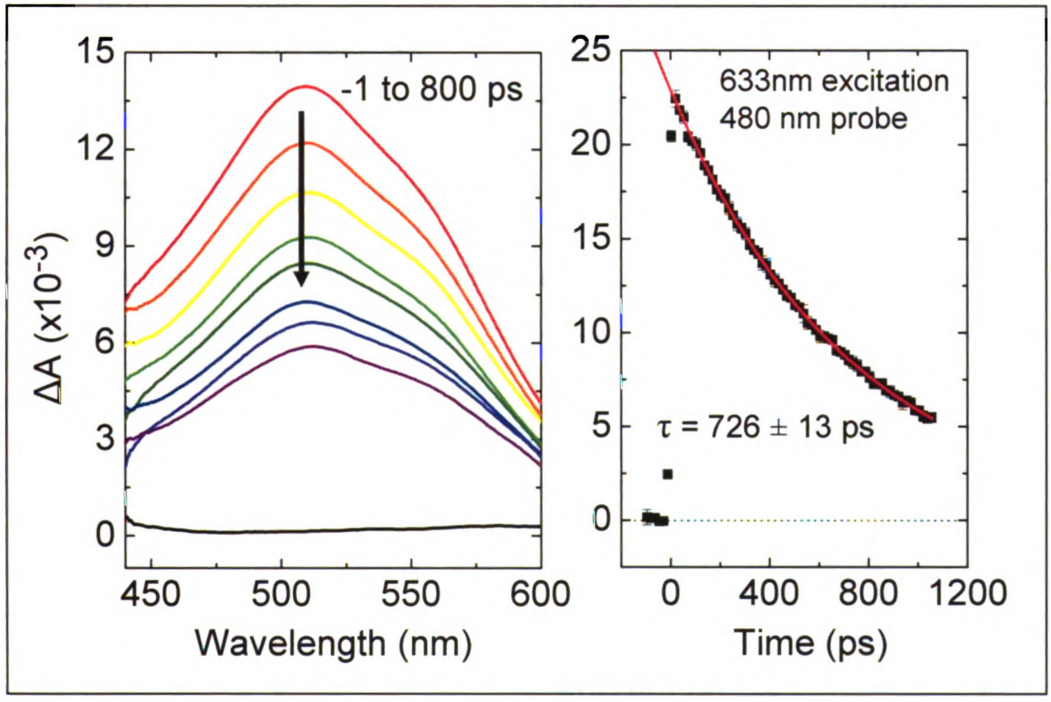

Figure 3-21: Full spectral ground state recovery dynamics for $Cr(3\text{-}NO_2acac)_3$ and long-time single wavelength kinetic trace for $Cr(3\text{-}NO_2ac)_3$ after excitation at 633 nm.

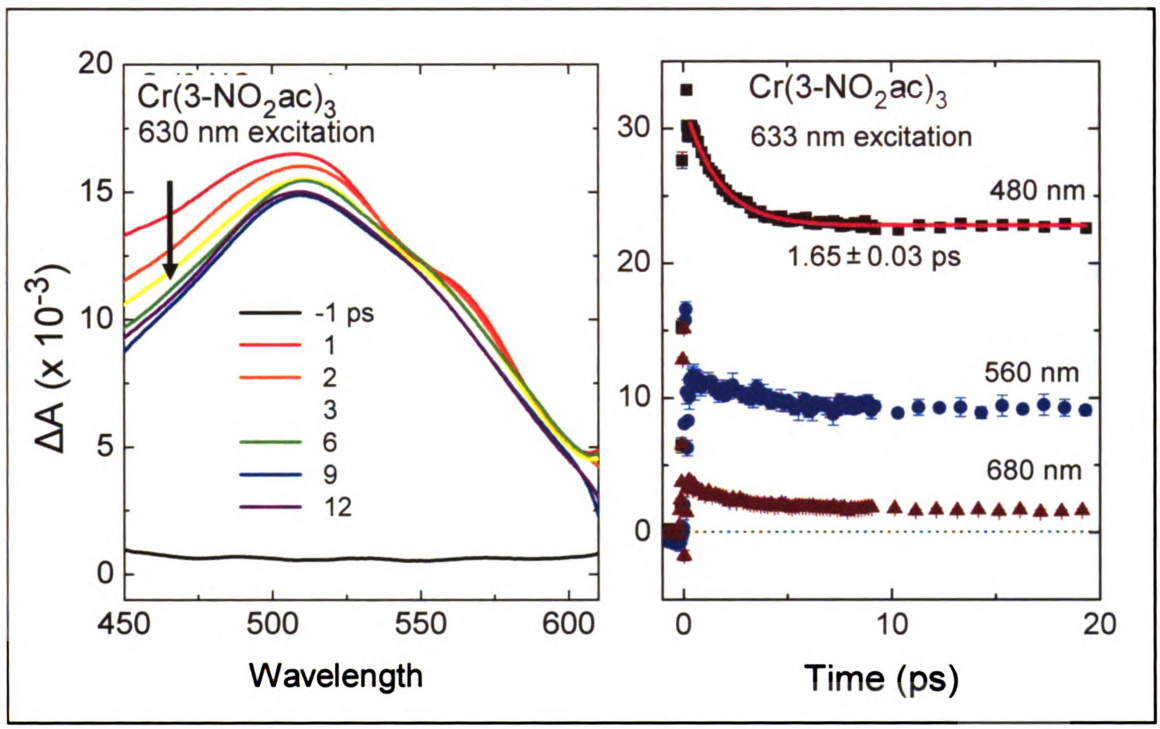

Figure 3-22: Full spectral and single wavelength kinetic data of $Cr(3\text{-}NO_2ac)_3$ in dichloromethane excited at 630 nm and 633 nm, respectively.

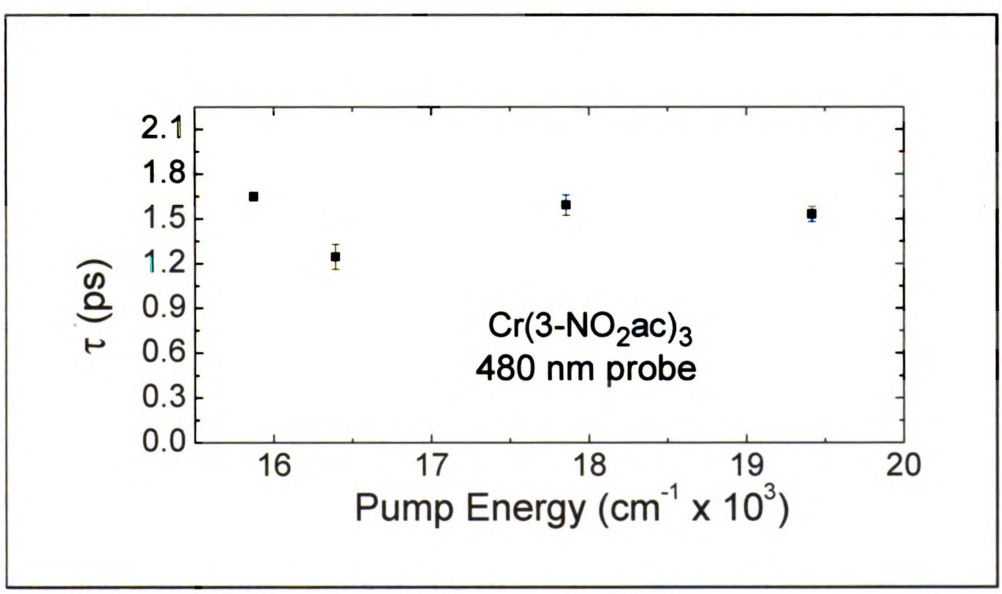

Figure 3-23: Observed lifetime as a function of pump energy at 480 nm probe. All measurements were carried out in dichloromethane.

Cr(3-Brac)$_3$. This complex forms brown crystals, and is brown/yellow as a powder and in solution. The ground state absorption spectrum is similar in most respects to what has been observed for this class of coordination compounds. In the ultraviolet three transitions are observed which are at 270 nm ($\varepsilon \sim 6600\ M^{-1}\ cm^{-1}$), 355 nm ($\varepsilon \sim 8600\ M^{-1}\ cm^{-1}$), and a low-intensity transition centered at 400 nm ($\varepsilon \sim 480\ M^{-1}\ cm^{-1}$) that presents as a shoulder on the much more intense transition at 355 nm. In the visible one observes a low-intensity broad transition centered at 565 nm ($\varepsilon \sim 65\ M^{-1}\ cm^{-1}$).

As shown previously for this class of compounds, the absorption centered at 270 nm is ligand ($\pi \rightarrow \pi^*$) based. The similarity of this value to that of Cr(acac)$_3$ (272 nm) suggests relatively little perturbation in the ligand π system as a result of substitution of Br (a π-donor and σ-acceptor) in the 3-position of the ligand backbone. The absorption at 355 nm is assigned as a LMCT type transition based on typical assignments for this class of compounds, as well as literature assignments. This value is red shifted by ~ 25 nm with respect to the corresponding transition in Cr(acac)$_3$. Again, the broad absorption centered at 565 nm is assigned as a transition into the $^4T_2$ state. Here λ_{max} is red shifted by 5 nm with respect to the same transition in Cr(acac)$_3$. This makes sense given the σ-accepting and π-donating nature of the Br substituent, which acts to decrease 10Dq by lowering the energy of the e_g^* set while raising t_{2g}.

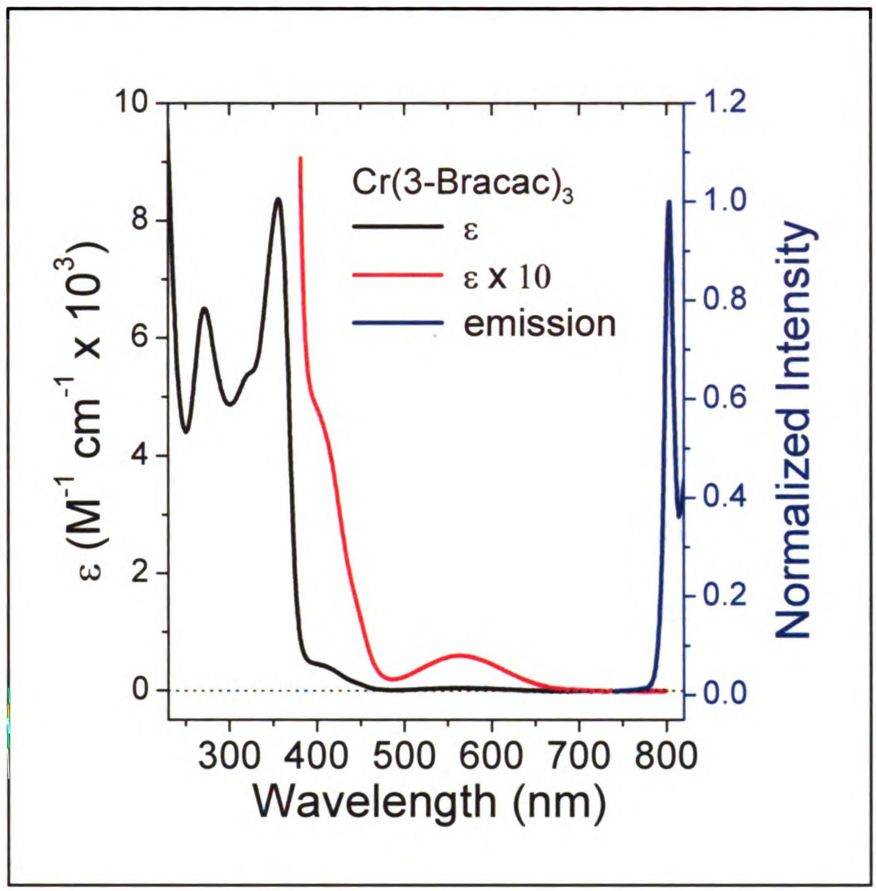

Figure 3-24: Absorption and emission spectra for Cr(3-Brac)$_3$ recorded in dichloromethane and an 80 K optical glass of 2-methyltetrahydrofuran, respectively. See experimental section for details.

The maximum wavelength of emission for this complex has been reported previously by Forster and DeArmond, who recorded the spectrum in a low-temperature glass (5:5:2 ethyl ether: isopentane: ethanol) and reported a value of 12390 cm^{-1}.[76] This compares well to our result (obtained in a low temperature optical glass of 2-methyltetrahydrofuran) of 12450 cm^{-1}. A recent spectroscopic study employing luminescence and excitation line narrowing spectroscopy has

recently been carried out, yielding further insight into the electronic structure of both the $^4A_2$ and ^2E electronic states, [77] revealing a ^2E splitting of 138 cm^{-1} due to a Jahn-Teller interaction and a $^4A_2$ splitting of 1.4 cm^{-1} (corresponding perfectly to the value of $D \sim 0.7$ cm^{-1} reported in Chapter 2, where zero-field splitting is given by 2D). Of general interest, and discussed by Forster and DeArmond,[78] is that the quantum yield of luminescence in this family of complexes is excitation wavelength dependent, i.e. excitation into the ligand field results in a different quantum yield of emission than excitation into the charge-transfer or intraligand transitions. For $Cr(3\text{-}Brac)_3$, the authors report a factor of two increase in the radiative quantum yield from the ^2E state for excitation into the $^4(^3IL)$ / $^4T_1$ transition versus excitation into the $^4T_2$ state, while pumping into the LMCT transition provided a quantum yield in between these two values. A comparison of the excitation scan, (monitoring at 804 nm) and the absorption spectrum (Figure 3-25) reveals that the quantum yield of emission is definitely excitation wavelength dependent: excitation into states with relatively low oscillator strength (such as $^4(^3IL)$ / $^4T_1$ and $^4T_2$) emit competitively with states of much greater oscillator strength (LMCT and IL transitions). This suggests that excitation into these states of lower absorption intensity results in a higher quantum yield of emission. Furthermore, assuming that the $^4T_1$ and $^4T_2$ states have the same oscillator strength, the approximately two-fold increase in the excitation scan intensity of the

$^4T_1$ versus the $^4T_2$ state is qualitatively in line with the report of quantum yield of luminescence reported by Forster.

Nonradiative decay from the ^2E state to recover the ground state was probed using ultrafast transient absorption spectroscopy with ~ 100 fs pulses. Values for ground state recovery between 1.9 – 2.5 ns were obtained for all pump/probe combinations. The relatively large error on this measurement results from the inability of our instrument to scan to times longer than ~ 1.2 ns. Despite this error, it is clear that this value represents about a factor of three increase in the ground state recovery lifetime via the ^2E as compared to $Cr(acac)_3$.

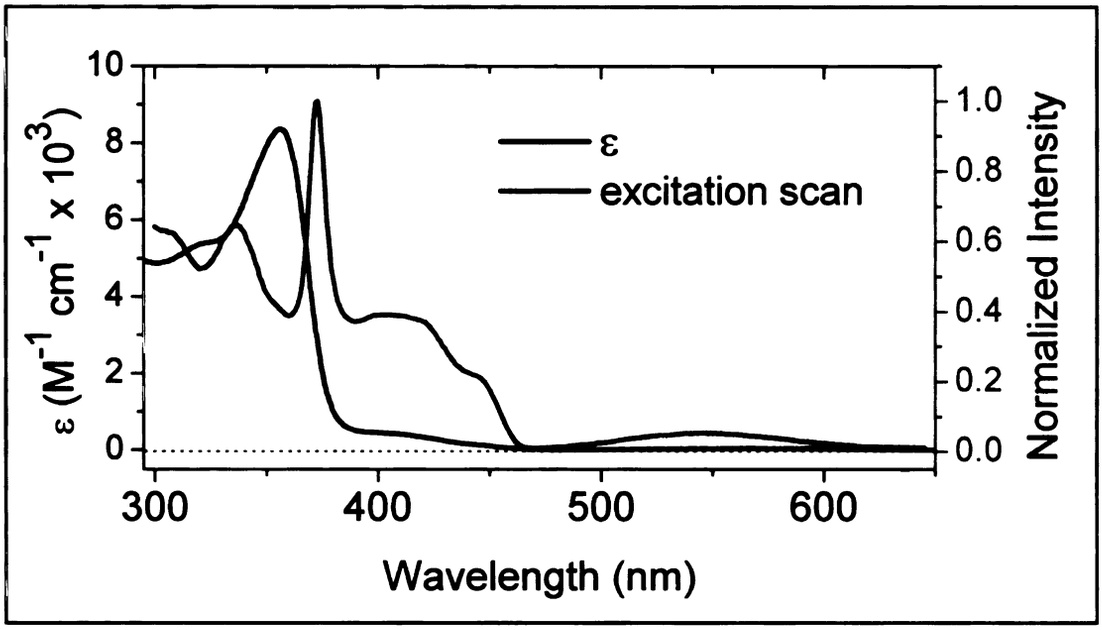

Figure 3-25: Excitation scan of $Cr(3\text{-}Brac)_3$ in an 80 K optical glass of 2-methyltetrahydrofuran. The excitation scan reports the emission intensity (probed near the emission maximum at 804 nm) as a function of the excitation wavelength.

Early time full spectra after excitation at 630 nm, the low-energy should of the $^4T_2$ absorption, are shown in Figure 3-26. The full-spectral bandshape at 1 ps is essentially retained over the entire time frame of the experiment, although within the first 10 ps the spectrum narrows.

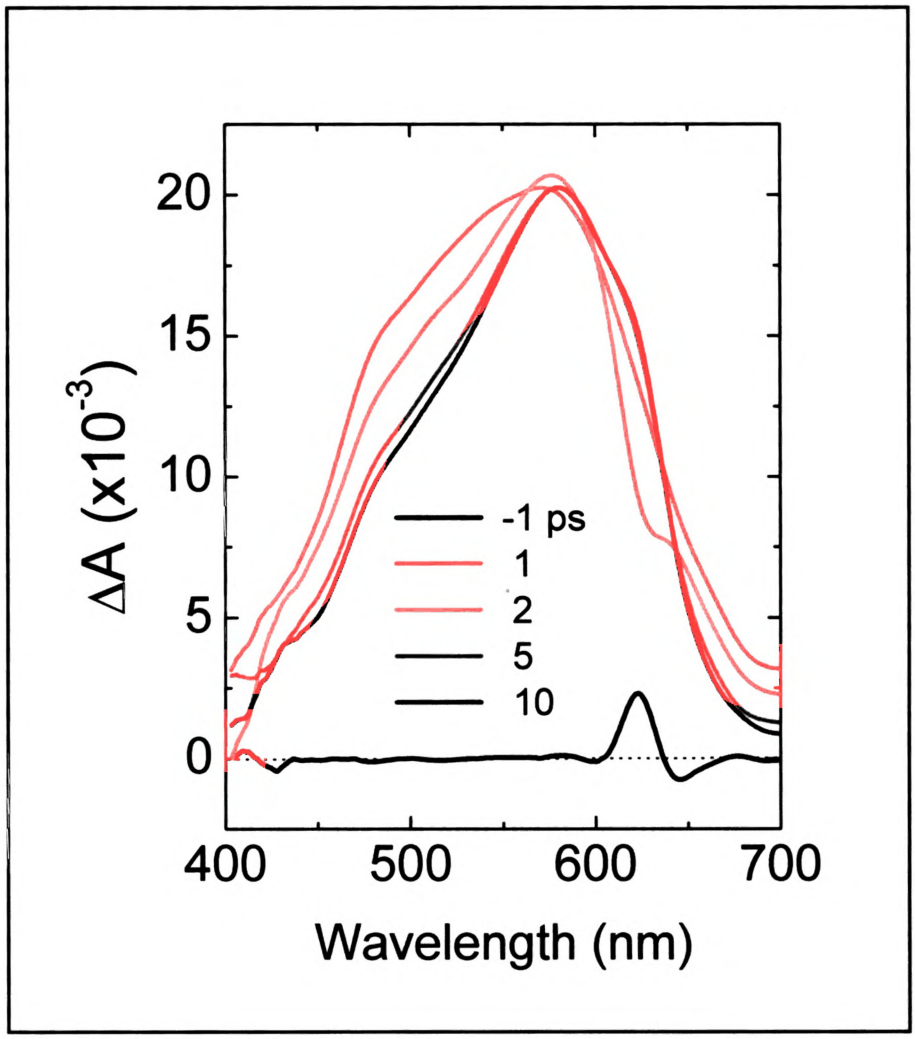

Figure 3-26: Full spectra for $Cr(3\text{-}Brac)_3$ at 630 nm. Anomalies in the full spectra around 630 nm are due to scatter of the pump pulse.

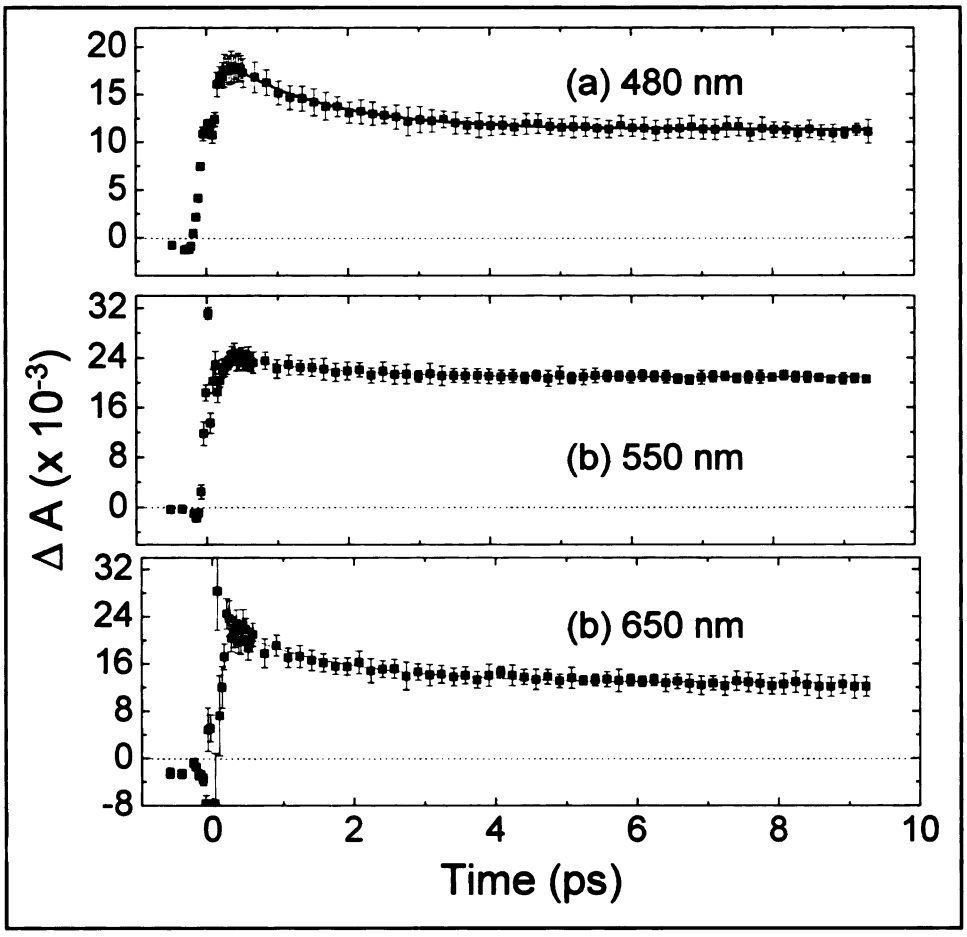

Figure 3-27: Representative single wavelength kinetic data of $Cr(3\text{-}Brac)_3$ in dichloromethane excited at 610 nm, with probe wavelengths reported in the figure. The data were fit with a monoexponential function with lifetime 1.4 ± 0.1 ps.

This indicates an excited state absorbance from the long-lived, lowest energy excited state ^2E, implying that intersystem crossing from the initially formed $^4T_2$ occurs faster than the resolution of our experiment. The dynamics that are observed in the first 10 ps are occurring on the ^2E surface, and are assigned as vibrational cooling within this state. Single wavelength kinetics (Figure 3-27),

which corroborate the full spectral dynamics, reveal that this process occurs on a slightly longer timescale than the corresponding event in $Cr(acac)_3$: approximately 1.4 ps for $Cr(3\text{-}Brac)_3$ versus 1.1 ps for $Cr(acac)_3$. This value was obtained for all excitation wavelengths across the entire $^4T_2$ absorption profile.

$Cr(3\text{-methylac})_3$. $Cr(3\text{-methylac})_3$ forms dark green crystals and powders. The UV-vis absorption and emission spectra of this complex are shown in Figure 3-28. In the ultraviolet one observes two distinct transitions at 270 nm ($\varepsilon \sim 9080\ M^{-1}\ cm^{-1}$) and 350 nm ($\varepsilon \sim 10860\ M^{-1}\ cm^{-1}$). On the low-energy shoulder of the 350 nm absorption is an absorption of much lower intensity centered around 395 nm with $\varepsilon \sim 320\ M^{-1}\ cm^{-1}$. In the optical region is a broad absorption of low intensity centered around 574 nm with $\varepsilon \sim 70\ M^{-1}\ cm^{-1}$. The energy of the transition at 272 nm, which is similar to the value obtained for $Cr(acac)_3$ and assigned as an intraligand transition, is evidence that the ligand π structure is not varying much as a result of the methyl substituent. While this is expected given the σ-donating nature of the methyl substituent, there is ample evidence that the relative energies of the chromium(III) based states and ligand π-based states are shifting as a result of this substitution: the absorption at 350 nm, assigned as a LMCT transition, is red shifted by 20 nm with respect to the same transition in $Cr(acac)_3$. This implies a destabilization of the ligand π-based orbitals with respect to chromium d-based orbitals (or alternatively a stabilization of the chromium orbitals with respect to

the ligand π set). The moderate intensity transition at 395 nm is assigned as $^4(^3IL)$, while the broad weak absorption at 574 nm is assigned as absorption into the $^4T_2$ ligand field state. This state is red-shifted by ~ 15 nm with respect to the same transition in $Cr(acac)_3$.

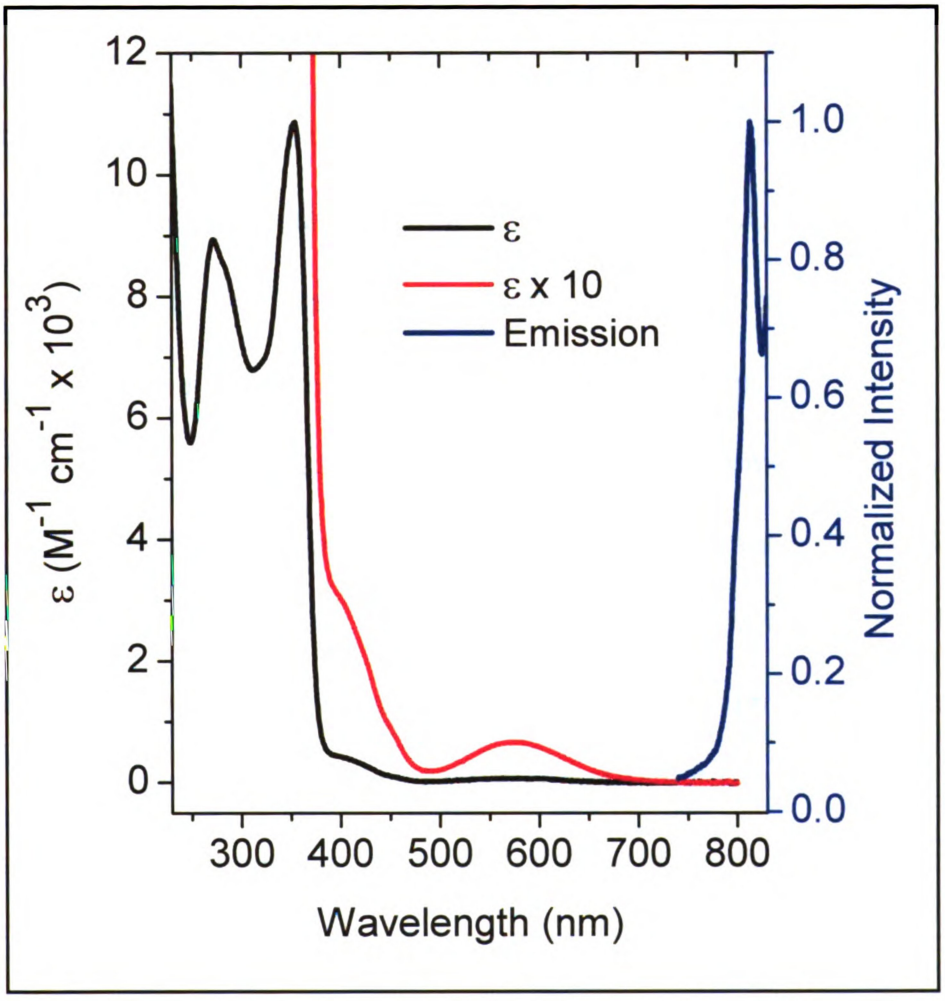

Figure 3-28: Absorption and emission spectra for $Cr(3\text{-methylac})_3$ recorded in dichloromethane and an 80 K optical glass of 2-methyltetrahydrofuran, respectively. See experimental section for details.

The emission spectrum (blue trace, Figure 3-28) was recorded in a low-temperature (80 K) optical glass of 2-methyltetrahydrofuran. It has a maximum intensity at 12280 cm^{-1} (814 nm). This signifies a considerable red shift of the emission maximum from $Cr(acac)_3$, implying that the 3-methylacetoacetonate ligand acts as a better delocalizer of π density that acetylacetonate, according to the nephelauxetic effect.

The stabilization of the ^2E may have major implications for ground state recovery dynamics via this state. These two states are nested, and, according to nonradiative decay theory, stabilizing the ^2E with respect to the ground state (lowering ΔE) would increase the vibrational overlap facilitating faster nonradiative decay. Initial ground state recovery measurements seemed to be confirming this, with monoexponential fits revealing lifetimes on the order of ~ 450 ps. These fits, however, all showed a slight offset from baseline, indicating that the original ground state was not recovered during this process, as a result of either 1) formation of a photoproduct or 2) a completely different set of dynamics from what has been previously observed for these systems, with ground state recovery occurring on a much longer timescale than the experiment. There were no other outward signs of photochemistry, i.e. precipitation of a photoproduct or observation of different pre- and post-experimental absorption spectra. To test these possibilities, future experiments must be carried under flowing conditions.

Cr

spe

ser

wir

sho

abs

abs

410

tran

abs

are

tran

liga

low

$^{4}(^{3}$H

cent

allo

obse

struct

Cr(3-SCNac)$_3$. Cr(3-SCNac)$_3$ forms purple crystals and powders. The absorption spectrum of Cr(3-SCNac)$_3$ conforms completely with the other members of this series, Figure 3-29. In the ultraviolet the spectrum tails up until the solvent window is closed (~220-230 nm for dichloromethane), and on this rise is a shoulder centered around 260 nm with $\varepsilon \sim 10200\ M^{-1}\ cm^{-1}$. A well-defined absorption is centered at 326 nm ($\varepsilon \sim 10300\ M^{-1}\ cm^{-1}$). On the red edge of this absorption are shoulders of much lower intensity at 370 nm ($\varepsilon \sim 480\ M^{-1}\ cm^{-1}$) and 410 nm ($\varepsilon \sim 130\ M^{-1}\ cm^{-1}$). In the visible one observes a broad low-intensity transition centered around 560 nm with $\varepsilon \sim 75\ M^{-1}\ cm^{-1}$. Given the previous absorption spectra for this class of complexes (discussed above), the assignments are straightforward. The shoulder at 260 nm is assigned as a ligand localized transition originating from the delocalized π structure of the acetylacetonate ligand. The absorption at 326 nm is assigned as a LMCT transition, while the lower intensity absorptions on the shoulder of the LMCT transition are assigned as $^4(^3IL)$ at 370 nm and absorption into the $^4T_1$ at 410 nm. The broad absorption centered at 560 nm is again assigned as a transition to the lowest-energy spin allowed ligand field state, $^4T_2$. All of these values match very closely those observed for Cr(acac)$_3$, representing only small perturbations to the electronic structure as a result of substituting thiocyanate into the ligand backbone.

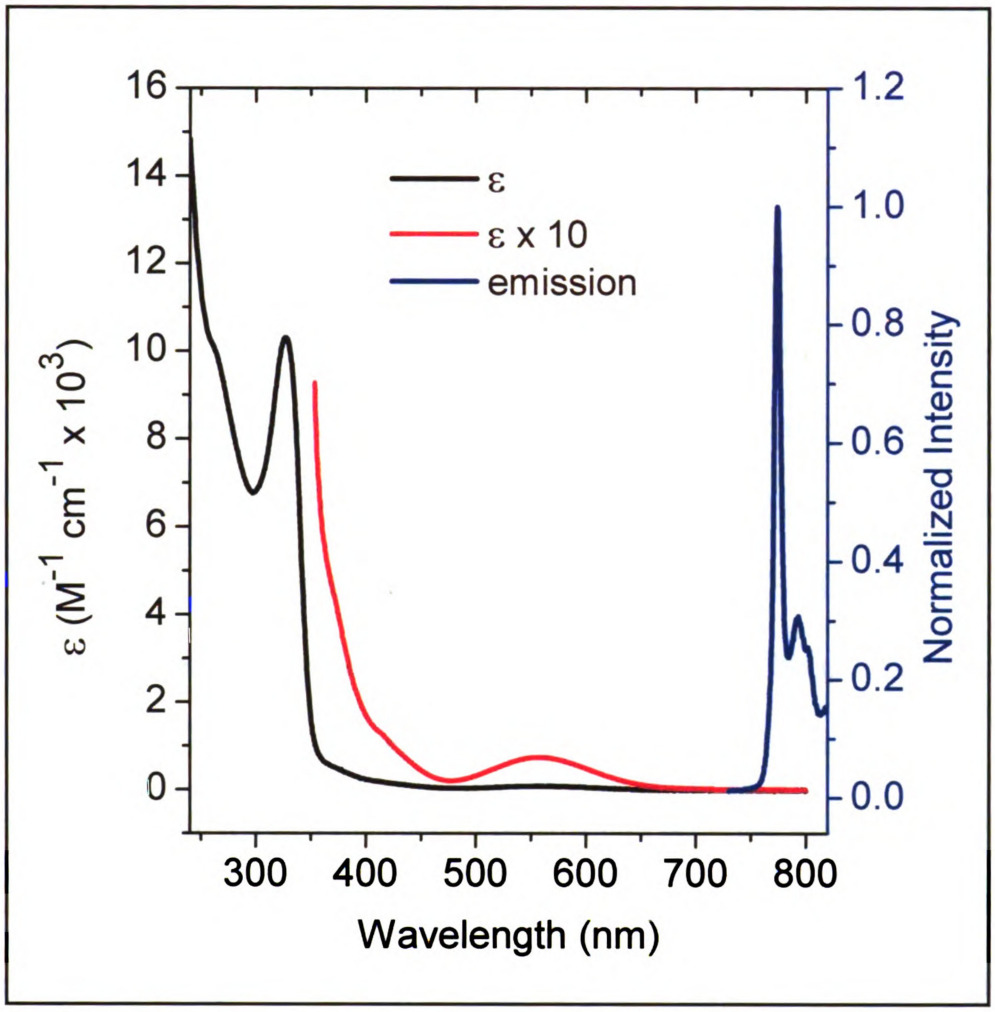

Figure 3-29: UV-vis absorption (black and red traces) and emission spectra of $Cr(SCNac)_3$, collected in dichloromethane and an optical glass of 2-methyltetrahydrofuran, respectively. See text for details.

Like the other complexes in this series, $Cr(3\text{-}SCNac)_3$ emits in a low-temperature optical glass. The emission spectrum (blue trace, Figure 3-29), recorded in an 80 K optical glass of 2-methyltetrahydrofuran, has a maximum intensity at 12920 cm^{-1} (774 nm) and is quite narrow. This value is equivalent to

that observed for $Cr(acac)_3$, suggesting that the thiocyanate group does little to change the π delocalizing ability of the ligand.

Femtosecond transient absorption data are presented in Figures 3-30 and 3-31. A kinetic trace out to 1 ns, after 630 nm excitation, on the low-energy shoulder of the $^4A_2 \rightarrow {}^4T_2$ absorption was collected (not shown). This data was fit with a monoexponential function that has no offset from the baseline at long times, indicating ground state recovery, and decays with a lifetime of 930 ± 100 ps. Early time full transient spectra are shown in Figure 3-30. Despite the noise associated with the measurement, general features can still be gleaned from this data. The data show a broad excited state absorption with a maximum at about 500 nm. Over the first 10 ps the spectra narrow and decrease in intensity, without the bandshape changing significantly. These observations are consistent with absorption from a single electronic state. Single-wavelength kinetic traces (Figure 3-31) confirm the dynamics of the full spectra, revealing a decay in the excited state absorption across the entire probe region. These data were fit with a monoexponential decay function yielding a lifetime of 1.65 ± 0.1 ps. These data are entirely consistent with the picture developed for the nonradiative decay observed in $Cr(acac)_3$, namely ultrafast ($k > 10^{13}\ s^{-1}$) intersystem crossing to the ^2E state and vibrational cooling on the ^2E state with a 1-2 ps lifetime. This vibrational cooling lifetime is constant for all excitation energies across the $^4T_2$ profile, Figure 3-32.

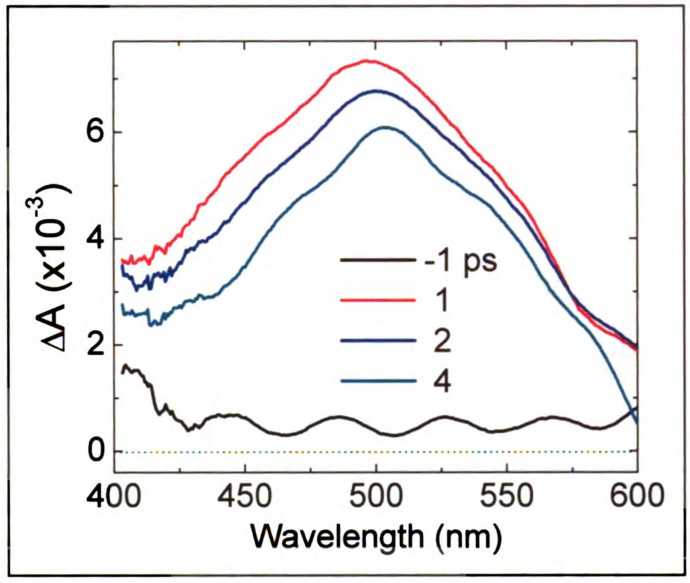

Figure 3-30: Full spectra transient absorption spectra for $Cr(3\text{-}SCNac)_3$ after 635 nm excitation.

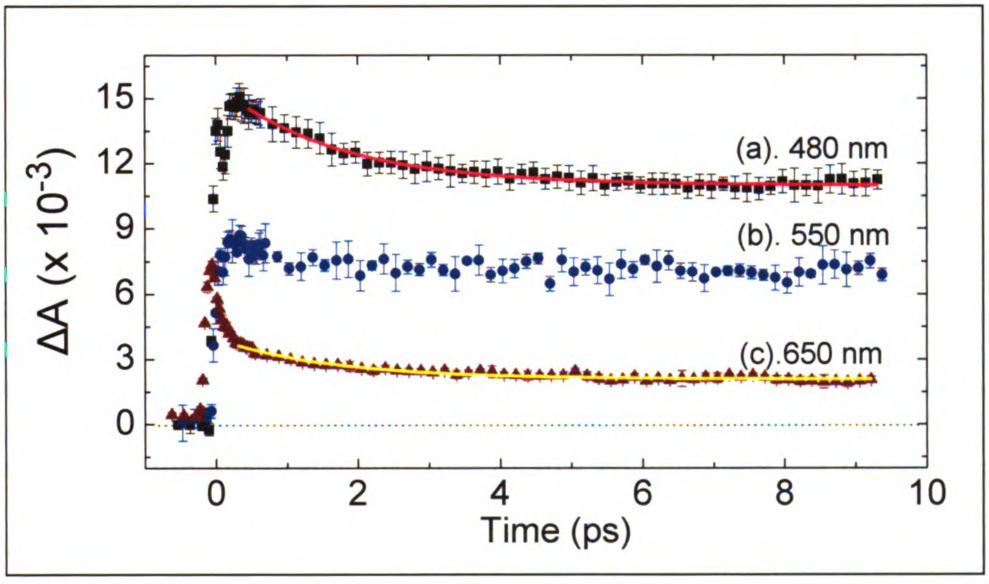

Figure 3-31: Representative single wavelength kinetics for $Cr(3\text{-}SCNac)_3$, excited at 515 nm. All fits were carried out with a monoexponential decay function to yield a lifetime of 1.65 ± 0.1 ps.

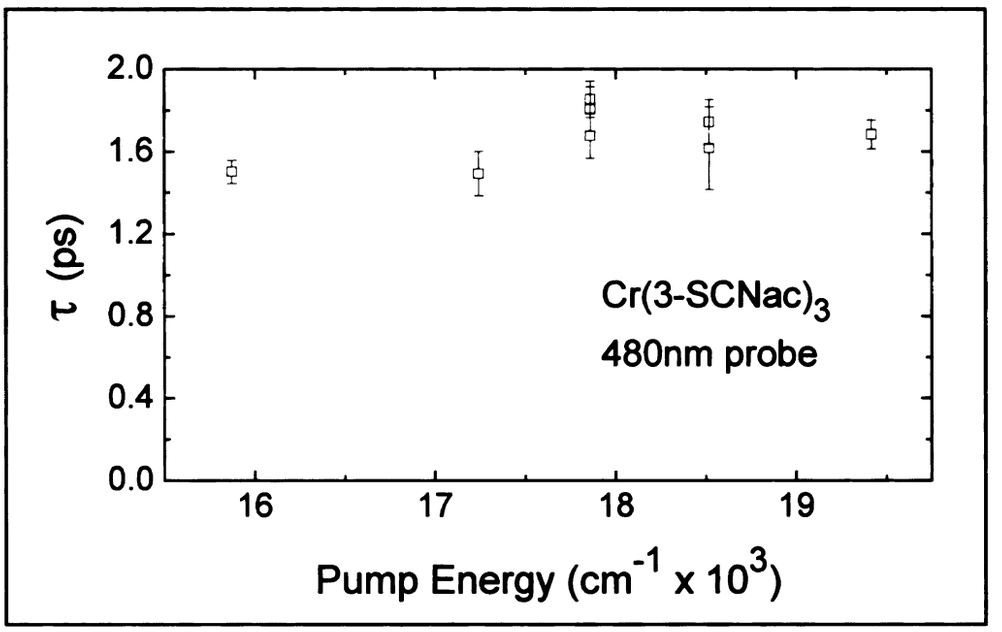

Figure 3-32: Vibrational cooling lifetime as a function of excitation energy for $Cr(3\text{-}SCNac)_3$.

$Cr(3\text{-}Phac)_3$. $Cr(Phac)_3$ forms blue/green powders and blue crystals. The crystal structure, shown in Figure 3-33, shows a highly symmetric environment about the chromium(III) metal center, with typical Cr-O bond lengths of 1.95 Å. Further crystallographic data is presented in Table 3-1 as well as Table C-2 of Appendix C. Of interest to the electronic structure of this complex are the dihedral angles that the phenyl groups make with respect to the inner π system of the acetylacetonate ligand. These three values (75.88°, 68.29°, and 87.40°) indicate that the π structures of the acetylacetonate and phenyl rings are able to couple to some extent. Of course these values are affected by crystal packing forces and all of the subsequent measurements are carried out in solution. The fact that the color

of the solution is dissimilar to that of $Cr(acac)_3$ indicates that the phenyl rings do couple to the acetylacetonate π system system.

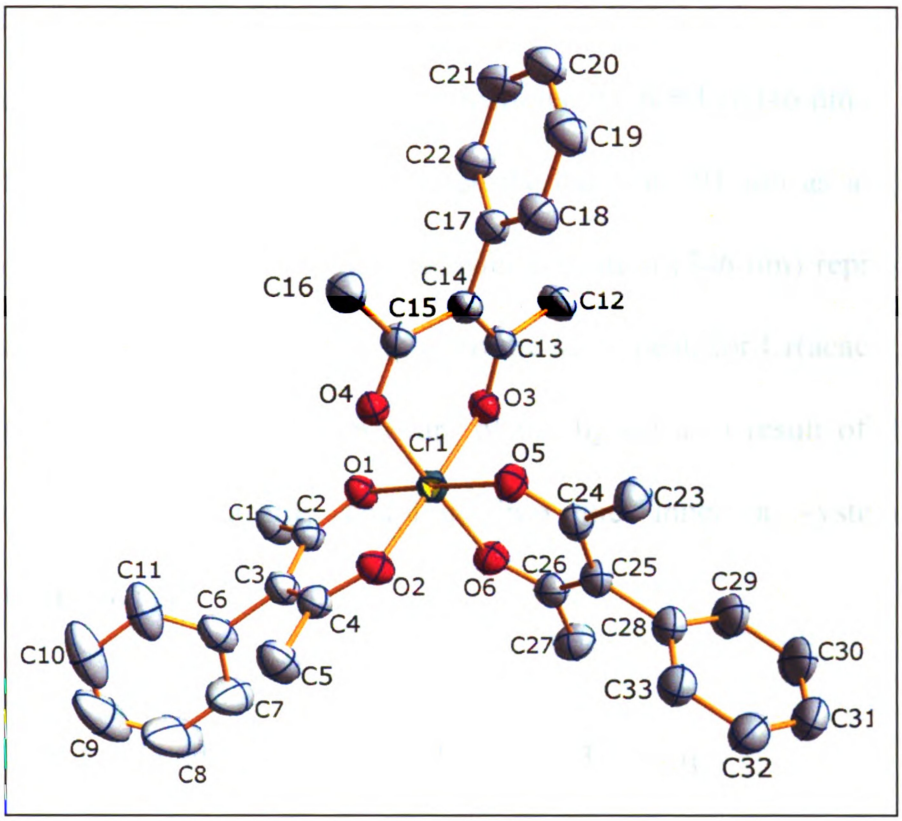

Figure 3-33: Crystal structure of $Cr(3\text{-Phac})_3$. Representative bond lengths and angles are given in Table 3-1.

The absorption and emission spectra for $Cr(3\text{-Phac})_3$ are shown in Figure 3-34. In the ultraviolet is an intense sub-300 nm transition that increases in intensity until the solvent window is closed, while a well-defined transition is centered at 346 nm ($\varepsilon \sim 11400\ M^{-1}\ cm^{-1}$) with a shoulder of much lower intensity on the red edge (394 nm, ($\varepsilon \sim 450\ M^{-1}\ cm^{-1}$). In the visible is a low-intensity transition

centered at 571 nm with $\varepsilon \sim 105\ M^{-1}\ cm^{-1}$. The absorptions correspond broadly in shape and position to those observed for the rest of this series, and the assignments are made accordingly. Namely, in the ultraviolet, the intense sub-300 nm absorptions are assigned as intraligand transitions, the band at 346 nm as a charge-transfer transition, and the moderate intensity band at 394 nm as a $^4(^3IL)$ type transition. The energy of the charge transfer transition (346 nm) represents an ~ 20 nm red shift of this peak with respect to the same peak for $Cr(acac)_3$, which is likely due to the lower-lying π structure of the ligand as a result of the phenyl substituent of $Cr(3\text{-}Phacac)_3$ coupling into the inner π system of the acetylacetonate ligand.

Table 3-1: Select bond lengths and angles for $Cr(3\text{-}Phac)_3$.

Cr-O Bonds (Å)	Cr1-O1	1.9466
	Cr1-O2	1.9555
	Cr1-O3	1.9567
	Cr1-O4	1.9502
	Cr1-O5	1.9391
	Cr1-O6	1.9502
O-Cr-O Angles (°)	O1-Cr1-O5	178.63
	O2-Cr1-O3	176.51
	O4-Cr1-O6	177.56
	O1-Cr1-O4	92.69
	O1-Cr1-O2	88.76
	O2-Cr1-O6	91.57
	O2-Cr1-O5	90.52
Phenyl Dihedral (°)	C2-C3-C6-C11	75.88
	C15-C14-C17-C18	68.29
	C24-C25-C28-C29	87.40

This increased delocalization of the ligand π system is also manifested in the low-temperature emission spectrum, whose maximum intensity is at 12523 nm (798.5 nm), also red-shifted with respect to the emission spectrum of $Cr(acac)_3$. This is not surprising given the moderate coupling of the phenyl and acetylacetonate π systems predicted from the x-ray crystal structure.

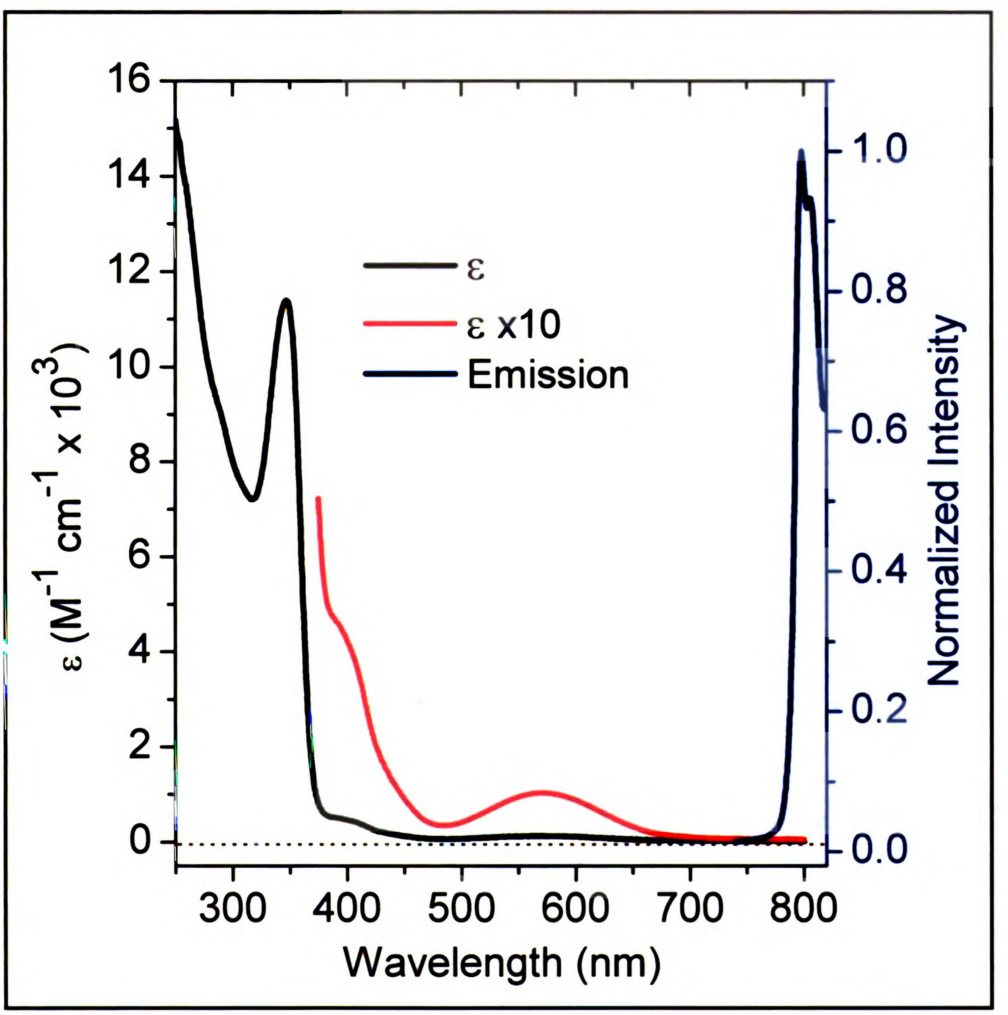

Figure 3-34: UV-vis absorption (black and red traces) and emission spectra of $Cr(3\text{-Phac})_3$, collected in dichloromethane and an optical glass of 2-methyltetrahydrofuran, respectively. See text for details.

Representative long-timescale (ps-ns) time resolved data is shown in Figure 3-35. For all pump/probe combinations a lifetime of 1.7 - 1.9 ns was obtained after fitting the data with a monoexponential function. Again, this value exceeds the limit to which our instrument can scan, resulting in the large error on the measurement. Shorter timescale data are shown in Figure 3-36 (full spectra over the first 5 ps) and Figure 3-37 (single wavelength kinetic traces).

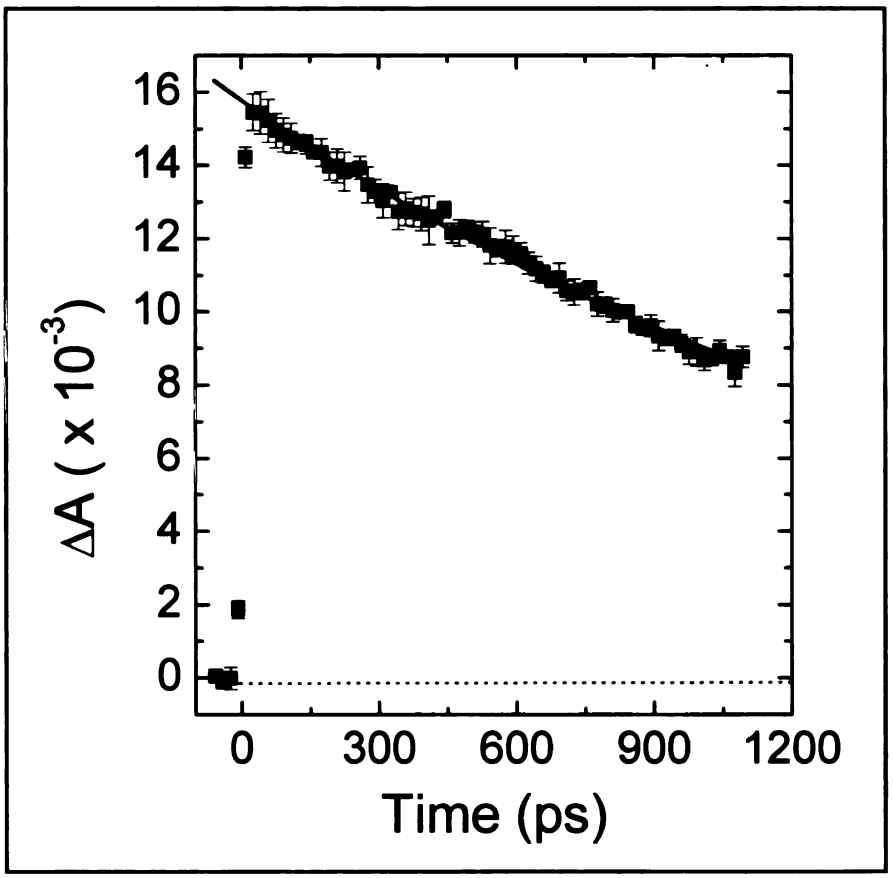

Figure 3-35: Representative data of ground state recovery for $Cr(3\text{-}Phac)_3$. This data was acquired with an excitation wavelength of 610 nm and a probe wavelength of 480 nm. The value of 1.7 - 1.9 ns ground state recovery time was found for all pump/probe combinations.

The full spectra data of Figure 3-36 reveals an excited state absorption that is quite broad and dramatically redshifts and narrows over the first three picoseconds, from a band maximum of 535 nm to 560 nm. This prominent shifting of the full spectrum manifests itself accordingly in single-wavelength kinetics (Figure 3-37): on the blue edge the kinetics reveal a decay in the excited state absorption, while a rise in the excited state absorption is observed on the red edge as the absorption shifts. The lifetime of the decay on the blue edge is constant for excitation across the entire excited state absorption profile, Figure 3-38.

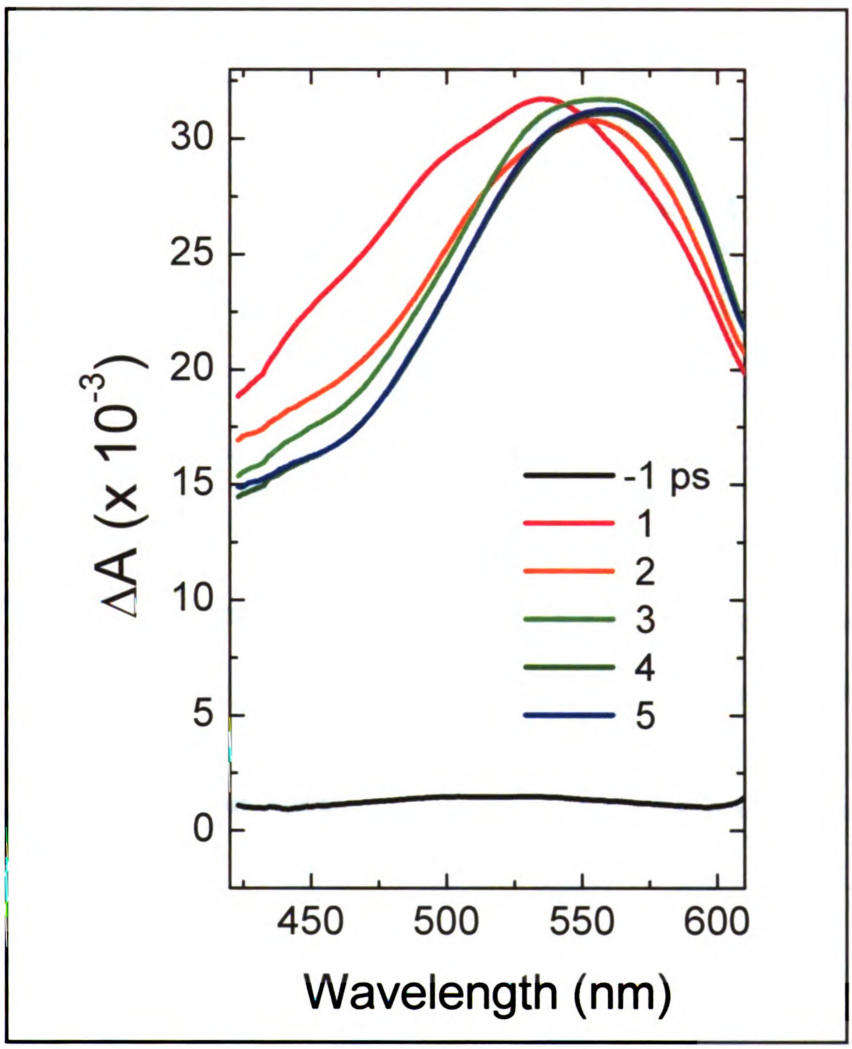

Figure 3-36: Full spectra transient absorption spectra of $Cr(3\text{-}Phac)_3$ at 633 nm excitation in dichloromethane.

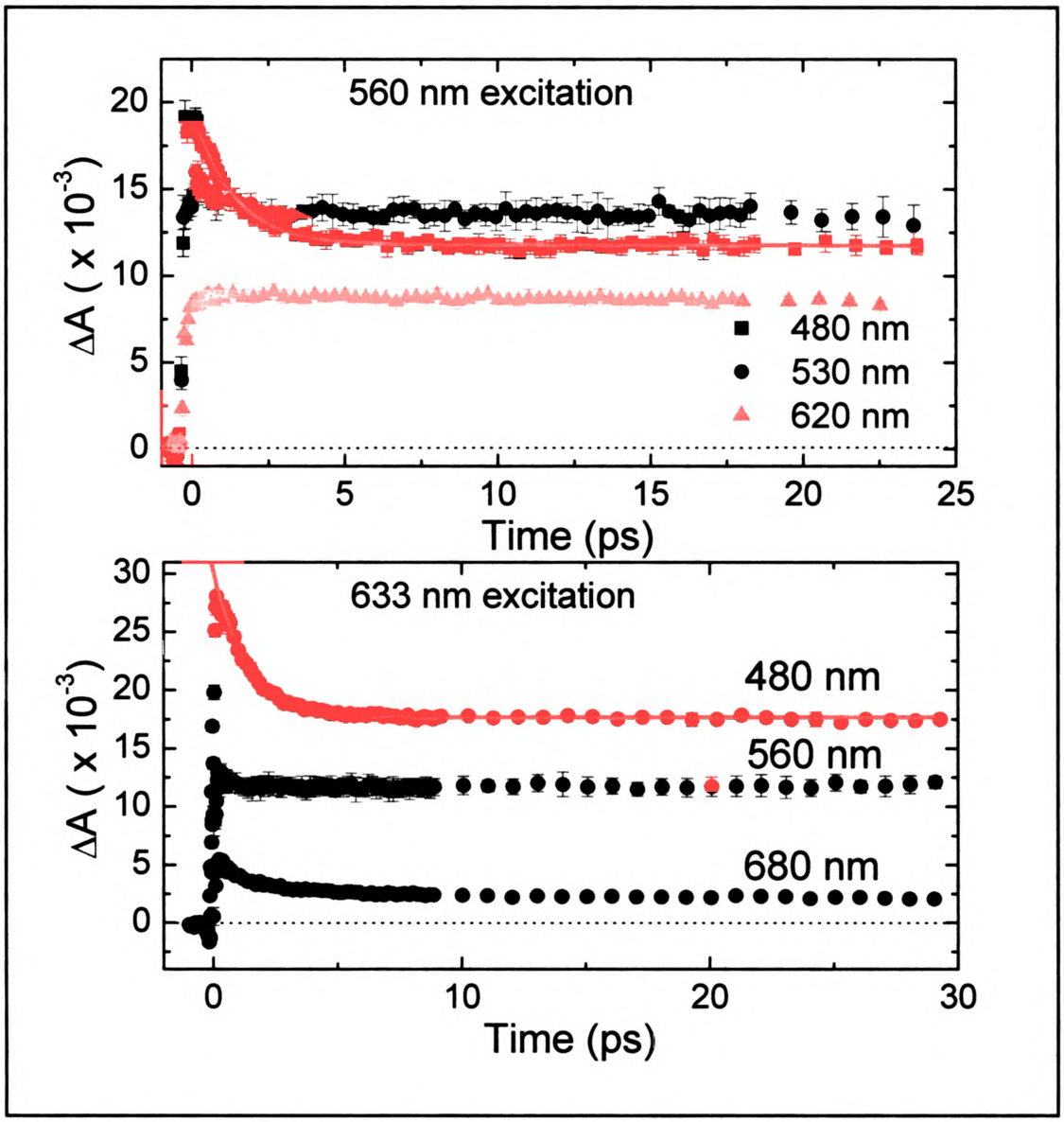

Figure 3-37: Single wavelength kinetics for $Cr(3\text{-Ph-acac})_3$ excited at 560 nm (top) and 630 nm (bottom). All fits at 480 nm probe were carried out with a monoexponential decay function yielding 1.30 ± 0.05 ps.

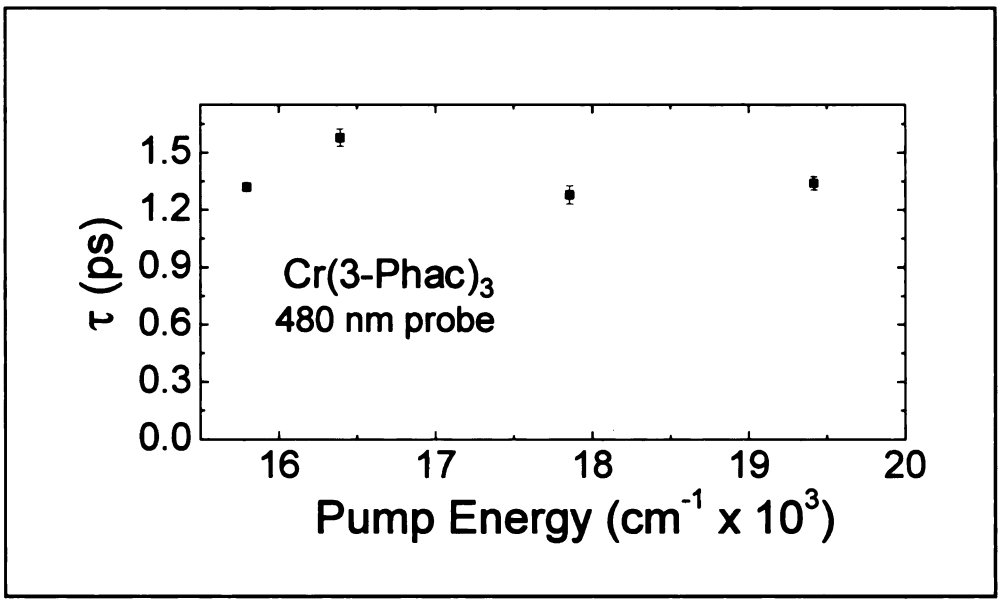

Figure 3-38: Lifetime of transient absorption dynamics on the blue edge of the excited state absorption as a function of excitation wavelength.

The dynamics revealed on long timescales likely correspond to ground state recovery via the ^2E state, as observed in other members of this series. The value of ~ 1.8 ns corresponds to a 2-3 fold increase in ground state recovery lifetime as compared to $Cr(acac)_3$. The shorter timescale dynamics are different than those observed for the rest of this series. The apparent shift in the full spectra could be due to one of the following events: 1) the shifting and narrowing of the spectrum is due to cooling on a single surface, where the surface being probed represents a softer potential than that of the state to which the probe induces a transition, similar to the situation presented in Figure 3-5; 2) the dynamics are occurring on a single electronic surface, and the observed shifting of the full spectra is due to geometrical changes during cooling in this state, while the narrowing is due to

changing Franck-Condon factors as the system cools; 3.) the observed dynamics are the result of a surface crossing in which the initially excited $^4T_2$ state absorbs bluer than the long-lived ^2E. Scenario 3 involves changing populations of the $^4T_2$ and ^2E states occurring over the first few picoseconds causing the apparent shift of the spectrum.

Scenarios 1 and 2 are preferred given the observed dynamics across this series, as well as considering the mode by which the ultrafast intersystem crossing is likely occurring, as revealed by coherence measurements on $Cr(acac)_3$ (*vide supra*): namely, via low-frequency modes involving the methyl groups of the ligand backbone. Scenario 2 can be accounted for if there was some energetic benefit to the phenyl ring on the ligand backbone to be more in-plane with the acetylacetonate π structure in the ^2E state versus the $^4A_2$. In this model the $^4T_2 \rightarrow {}^2E$ ISC occurs faster than the resolution of the instrument, so that only dynamics from the ^2E state are observed. As the state vibrationally cools on the ~ 1 ps timescale the phenyl group begins to rotate in-plane, increasing the coupling between the phenyl group and π system of the acetylacetonate ligand. As this occurs, the excited-state electronic structure changes as well, lowering the energy of the charge-transfer manifold, the state into which excited state dynamics are probed, resulting in the red shift of the spectrum over the first few picoseconds. (The ^2E energy would be lowered as well according to the nephelauxetic effect, but to a lesser extent than the charge-transfer energy.) This phenyl-rotation

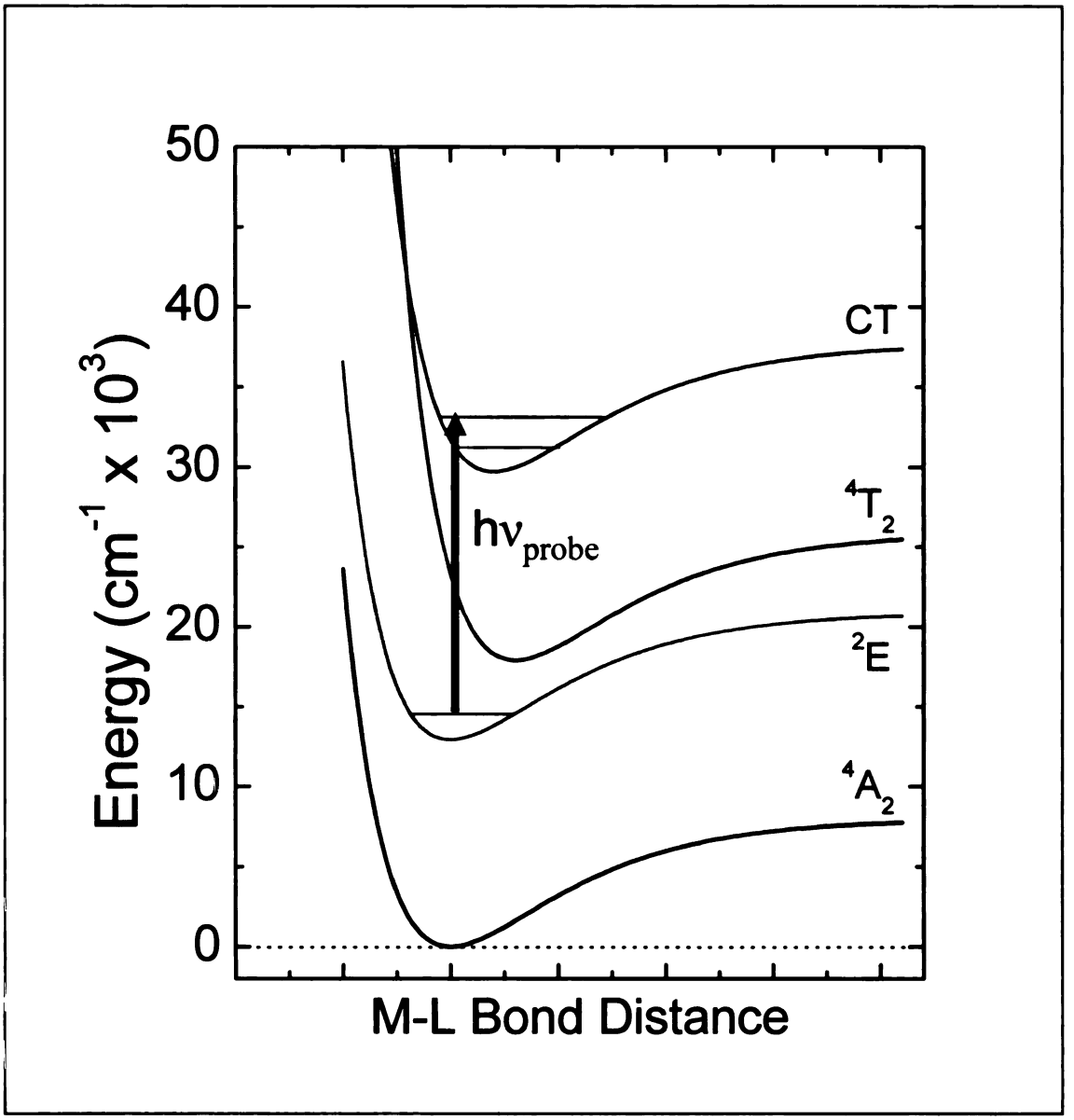

Figure 3-39: Potential energy surfaces diagram highlighting the charge-transfer transition that is employed to monitor dynamics on the ^{2}E surface. If the phenyl group of the 3-phenyl-acetylacetonate ligand rotates more in-plane with the core of the acetylacetonate ligand the energy of the charge-transfer transition employed as a probe lowers with respect to the ligand field manifold, resulting in a red-shift of the excited state spectrum.

hypothesis will be tested by using $Cr(3\text{-mesac})_3$, a complex in which rotation of the phenyl rings would be sterically hindered by the ortho-methyl groups of the mesityl ring. Initial characterization of the electronic structure of this complex is presented in the following section.

$Cr(3\text{-mesac})_3$. This complex forms purple powders and crystals similar in color to $Cr(acac)_3$. Single crystals can easily be grown by slow evaporation of an approximately 5:1 dichloromethane/methanol solution. While a crystal structure is not presented (collection is currently underway during writing of this section), the fact that the color of this complex is more similar to that of $Cr(acac)_3$ (purple) than that of $Cr(3\text{-Phac})_3$ (blue/green) suggests that the mesityl group is more orthogonal to the acetylacetonate π system than the unsubstituted phenyl ring. This is expected from simple steric arguments, but nevertheless a crystal structure is required to definitively make this assignment.

The UV-vis absorption spectrum of this complex is shown in Figure 3-40. The main features of the absorption spectrum are an intense absorption at 354 nm ($\varepsilon \sim 12311\ M^{-1}\ cm^{-1}$), a moderate intensity absorption on the low-energy onset of the intense transition (390 nm, $\varepsilon \sim 550\ M^{-1}\ cm^{-1}$), and a broad, weak absorption in the visible at 564 nm with $\varepsilon \sim 100\ M^{-1}\ cm^{-1}$. From characterization of members of this series, these features are assigned as charge transfer, $^4(^3IL)$, and $^4A_2 \rightarrow {}^4T_2$ transitions, respectively.

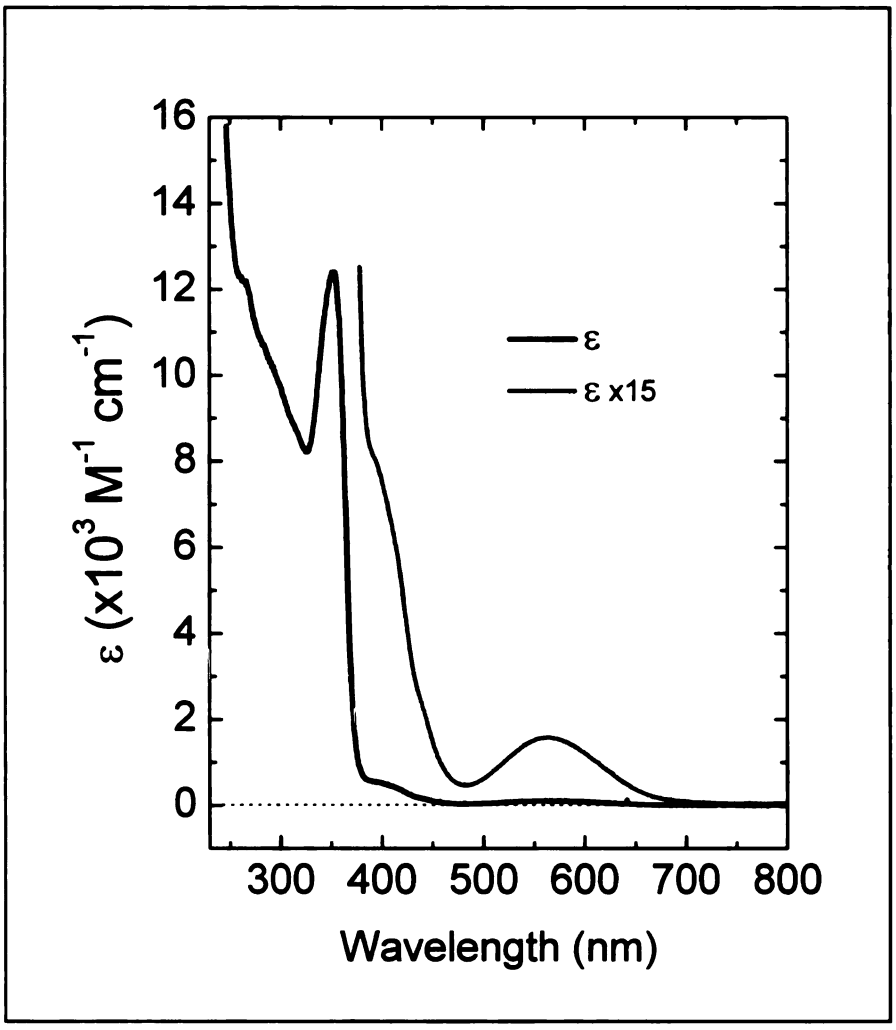

Figure 3-40: Absorption spectrum of $Cr(3\text{-mesac})_3$ in dichloromethane.

3.4.3 1,3-substituted complexes of 1,3-propanedione

$Cr(t\text{-butylac})_3$. The absorption and emission spectra of $Cr(t\text{-butylac})_3$ are shown in Figure 3-41. The appearance of these spectra should be fairly familiar to the reader of the previous section. In the ultraviolet one finds two absorption peaks of large intensity at 279 nm (10300 M^{-1} cm^{-1}) and 335 nm (13100 M^{-1} cm^{-1}) and a moderate strength absorption at 379 nm (450 M^{-1} cm^{-1}). From previous

assignments, and given that the π structure of the ligand is essentially unchanged from acetylacetonate, these absorptions are assigned as ligand $\pi \rightarrow \pi^*$, ^{4}CT, and $^4(^3$IL), respectively.

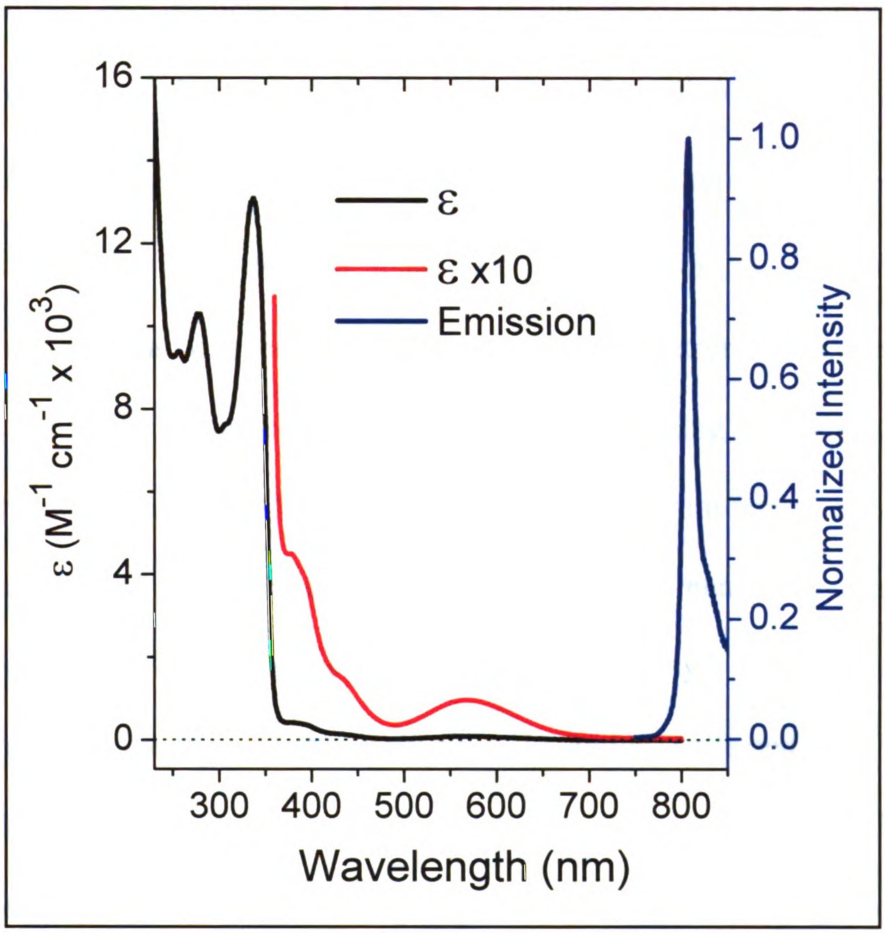

Figure 3-41: UV-vis and emission spectra of Cr(tbutylac)$_3$ in dichloromethane and 2-methyltetrahydrofuran.

In fact, the energies of the absorption maximum reported above represent a very small perturbation to the ligand π structure. In the visible one observes two low-intensity transitions: one on the low-energy shoulder of the $^4(^3$IL) absorption and

another, more well-defined peak centered at 570 nm with $\varepsilon \sim 95\ M^{-1}\ cm^{-1}$. These features are assigned as the spin allowed $^4T_2$ and $^4T_1$ transitions, respectively. An emission spectrum was collected in an 80 K optical glass of 2-methyl-tetrahydrofuran, and is shown in Figure 3-41, blue trace. The spectrum is quite narrow, consistent with emission from the intraconfigurational ^2E state, with the emission maximum at 12389 cm^{-1} (807 nm). This value represents a ~500 cm^{-1} redshift to that of the emission maximum of $Cr(acac)_3$ at 775 nm. This observation is curious because a shift of the emission spectrum from one complex to another is usually explained in terms of the π-delocalizing ability of the ligand vis-à-vis the nephelauxetic effect: a red-shift of the spectrum represents a more π-delocalizing ligand. In this case the aforementioned argument can not be applied as the t-butyl groups have no effective π-delocalizing ability.

Representative data of the early time dynamics, collected with ~ 100 fs optical pulses, is shown in Figure 3-42. These data were excited at 633 nm (full spectra) or 610 nm (single-wavelength kinetics), on the red edge of the $^4T_2$ absorption. The transient full spectra show a broad spectrum at early times (300 fs), which narrows, red shifts, and increases in intensity with a maximum absorption at 530 nm. Single-wavelength kinetic traces confirm that these dynamics are real: probing at 450 nm reveals a decay in the excited state absorption, and probing at 550 nm reveals a rise in the excited state absorption. Both the rise and the decay components are occurring with $\tau \sim 2$ ps. The profile of

the spectrum at 12 ps is also observed at much later times, confirming that this transient spectrum originates out of the long-lived ^2E state. There are two distinct possibilities to account for the dynamics observed in the transient full spectra: 1) the dynamics are taking place on a single electronic surface, and the observed narrowing, red-shifting, and growth of the signal in the red represents vibrational cooling dynamics on this surface; 2) the dynamics represent absorption from two different excited states, one whose excited state absorption is decaying with time and another that has increasing excited state absorption with time.

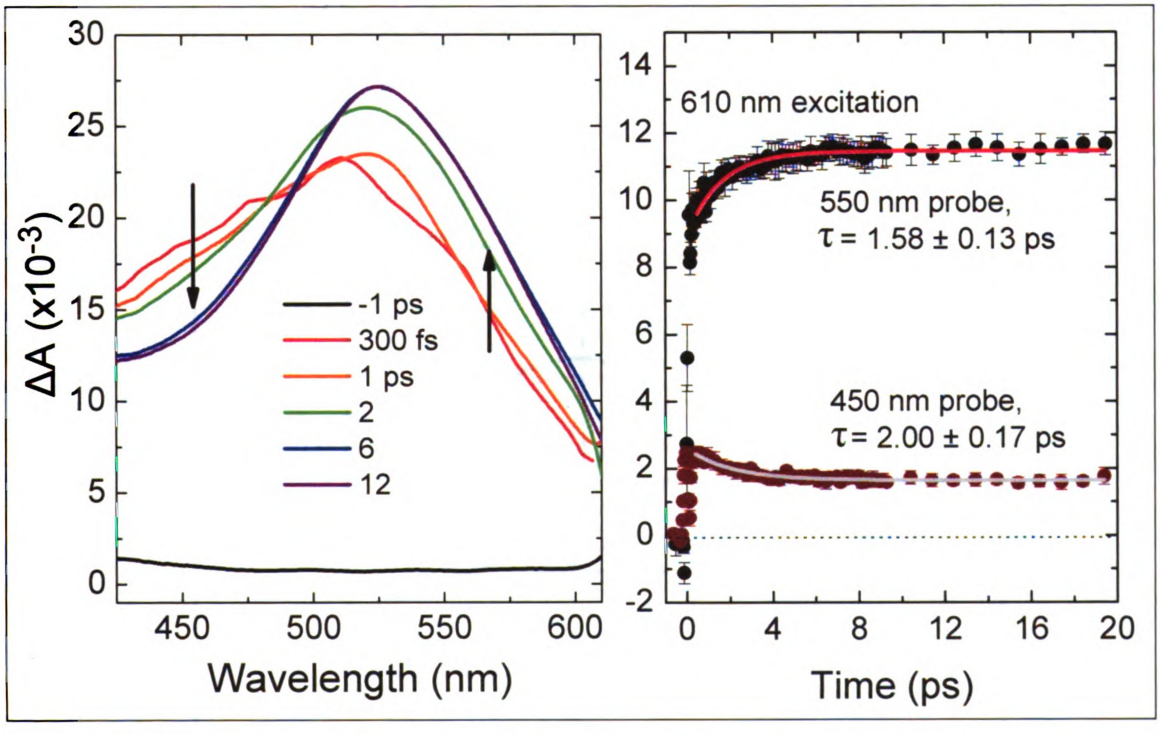

Figure 3-42: Full spectra of $Cr(tbutylac)_3$ after excitation 633 nm and select single wavelength kinetic traces after 610 nm excitation. Similar evolution of the full spectra were observed for other excitation wavelengths across the $^4A_2 \rightarrow {}^4T_2$ transition.

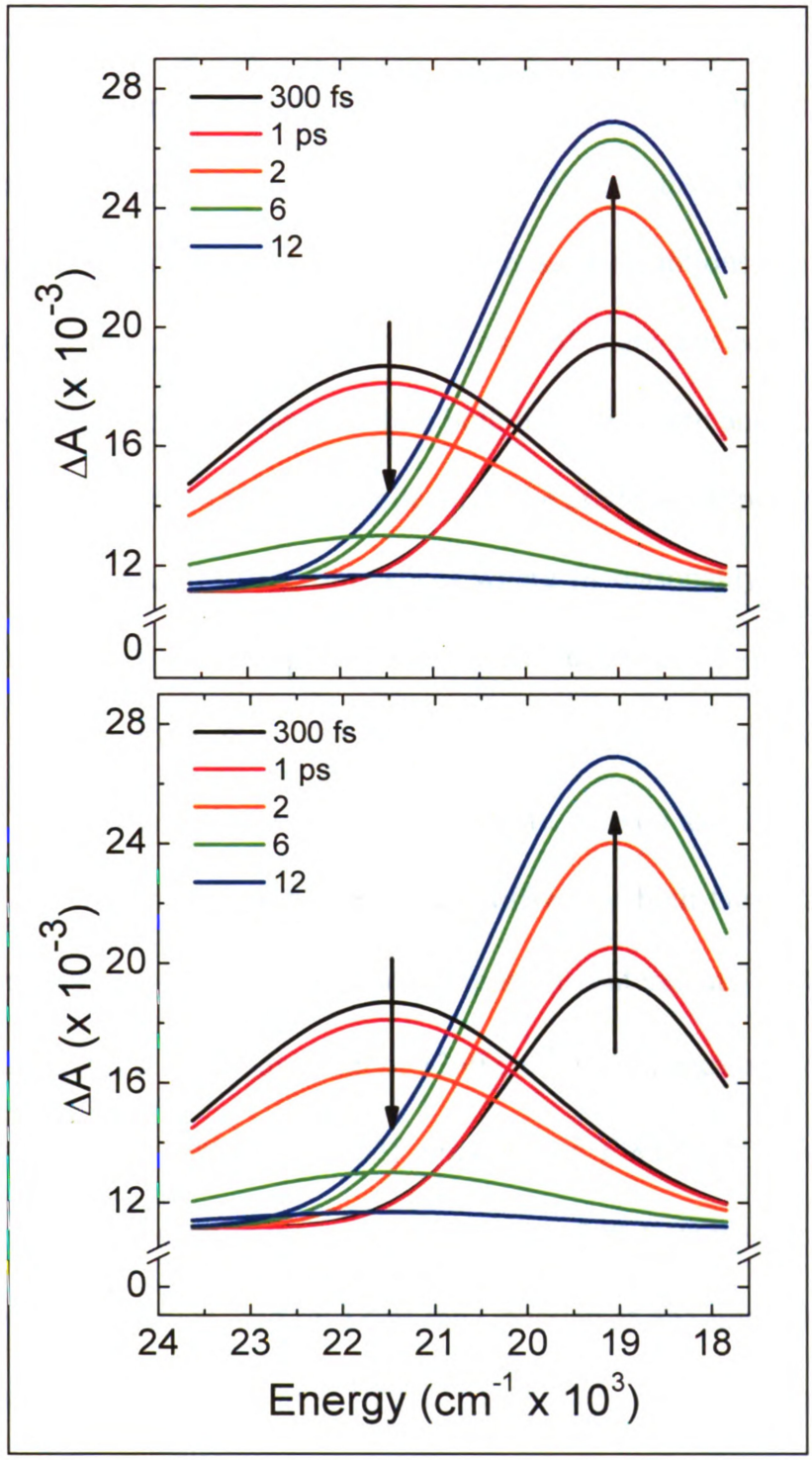

Figure 3-43: Gaussian deconvolution of the transient full spectra. An example fit for the transient spectrum at 2 ps is shown. See text for details of the fits.

Gaussian deconvolution of the transient spectra was carried out by assuming absorption from two different electronic states, with the additional assumption that the peak maximum and the width of these absorption profiles are essentially unchanged during the dynamics. These assumptions are crude and unfortunate given that the evolution of an excited state necessarily leads to changing absorption cross-section, affecting both the bandwidth and peak position of the absorption profile. However, despite all of the crude assumptions employed in the fitting procedure, all of the time slices where fit reasonably well with this model. Fitting of a transient spectrum at much later times (~ 20 ps), which corresponds to absorption from the ^2E only, revealed the peak position and bandwidth of the transient absorption from this state, as well as a long-time offset of ΔA (= 0.011), which was employed as the offset for both Gaussian features. The fits, figure 3-43, reveal one Gaussian component centered at 21500 cm^{-1} (465 nm), with a full width at half-maximum of 1750 cm^{-1}, which decays over time, and a second component at 19050 cm^{-1} (525 nm), whose FWHM is between 1100-1300 cm^{-1} and increases in intensity over time. At 300 fs these two Gaussians have nearly equal amplitude, and by 12 ps the Gaussian at 465 nm only makes up a very small contribution of the total signal. The success of this fitting procedure strengthens the argument that absorption from two different excited states is observed. If indeed this is the case, the bluer feature is absorption from the $^4T_2$ state, and decay of this feature represents depopulation of this state. The

concomitant growth of the redder feature therefore represents population of ^2E state and likely encompasses vibrational cooling dynamics on this state as well.

$Cr(prop)_3$. This complex forms reddish-purple crystals and powders, similar to $Cr(acac)_3$. The UV-Vis and low temperature emission spectra are reported in Figure 3-44. In the ultraviolet one observes a series of peaks of high intensity, with a maximum at 265 nm (8900 cm^{-1} M^{-1}), and another well-defined intense peak at 345 nm (11300 cm^{-1} M^{-1}). The series of peaks are assigned as intraligand $\pi \rightarrow \pi^*$ transitions based on their energies, while the peak at 345 nm is assigned as a ^4CT transition. The fine structure observed in $Cr(prop)_3$ is apparent both in the 250 – 350 nm range as well as on the low energy shoulder of the charge transfer transition. The absorption spectrum in these ranges, plotted in energy units, is reproduced in greater detail in Figure 3-44. In the ultraviolet, the splitting between the peaks is ~ 2700 cm^{-1}, likely due to a C-H stretch of the ligand backbone.

In the visible there are several transitions. As aforementioned, there is a moderate strength absorption composed of a vibronic progression of 1000 cm^{-1} splitting on the low-energy shoulder of the charge transfer transition, centered at about 400 nm with $\varepsilon \sim 380$ M^{-1} cm^{-1}. It should be noted that the lowest-energy component may be primarily $^4T_1$ in nature, and only coincidentally at the appropriate energy to fit into the vibronic progression. This splitting of ~ 1000

cm^{-1} likely represents C=C stretches of the ligand ring system: DFT calculations reveal modes near 1000 cm^{-1} that are due to bending and stretching of the ligand backbone. The well-resolved low intensity feature at 555 nm (60 M^{-1} cm^{-1}) is assigned as absorption into the $^4T_2$.

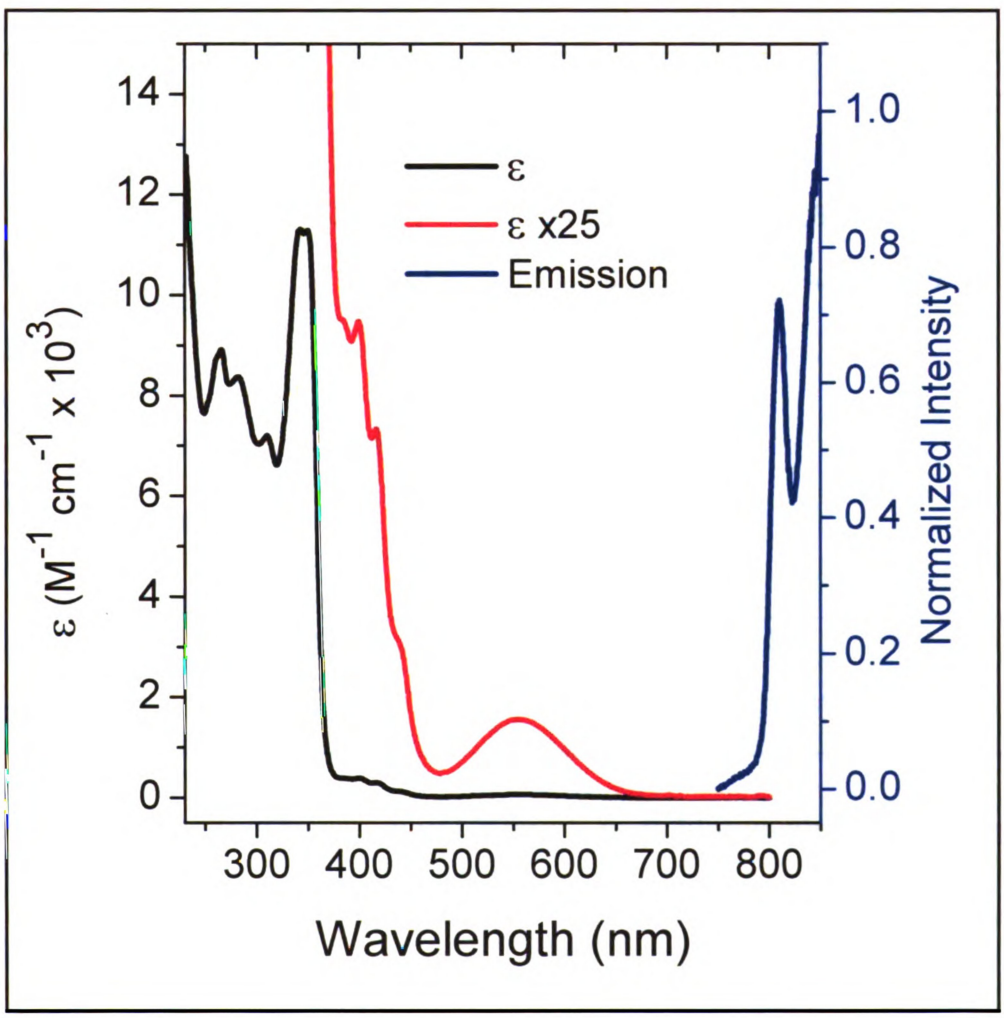

Figure 3-44: Absorption and emission spectra of $Cr(prop)_3$ recording in dichloromethane and an 80 K optical glass of 2-methyltetrahydrofuran, respectively.

An emission spectrum was collected in a low-temperature (80 K) optical glass of 2-methyltetrahydrofuran. The spectrum has one resolvable peak centered at 12330 cm^{-1} (811 nm) and another, more intense peak that is beyond the trustworthy range of our detector (>815 nm).

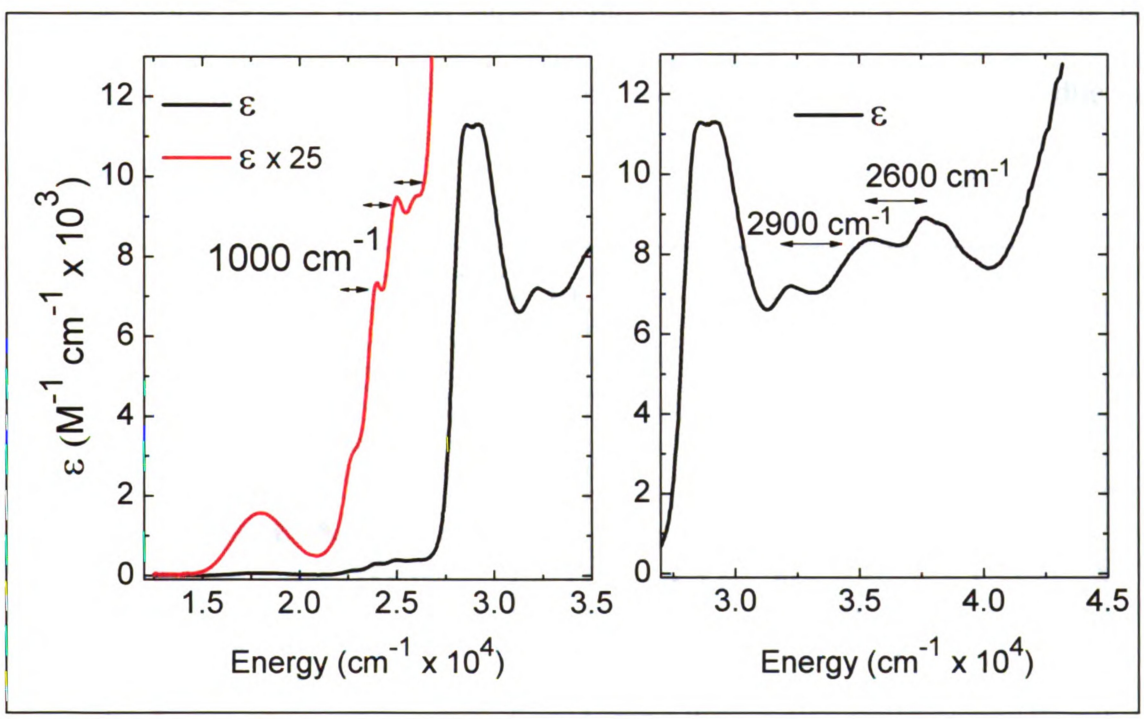

Figure 3-45: Absorption spectrum of $Cr(prop)_3$ in dichloromethane, revealing the vibronic structure with ~ 1000 cm^{-1} splitting on the red edge of the charge transfer band.

Ultrafast transient absorption spectroscopy of this complex, utilizing ~ 100 fs optical pulses, was initially carried out in dichloromethane in a static quartz cuvette; however the sample showed signs of photodecomposition after a few

minutes. The solvent was changed to acetonitrile so that the sample could be flowed. Long time single wavelength kinetics occur on a much longer timescale than our ultrafast instrument (τ is likely greater than 5 ns). Preliminary study of shorter timescale dynamics (Figure 3-46) reveal biphasic kinetics, with a fast decay component ($\tau \sim 700$ fs) and an order of magnitude slower rise in the excited state absorption ($\tau \sim 7$ ps). At bluer wavelengths only the fast component is observed, and the slower component is observed only in a narrow window due to the small change in amplitude.

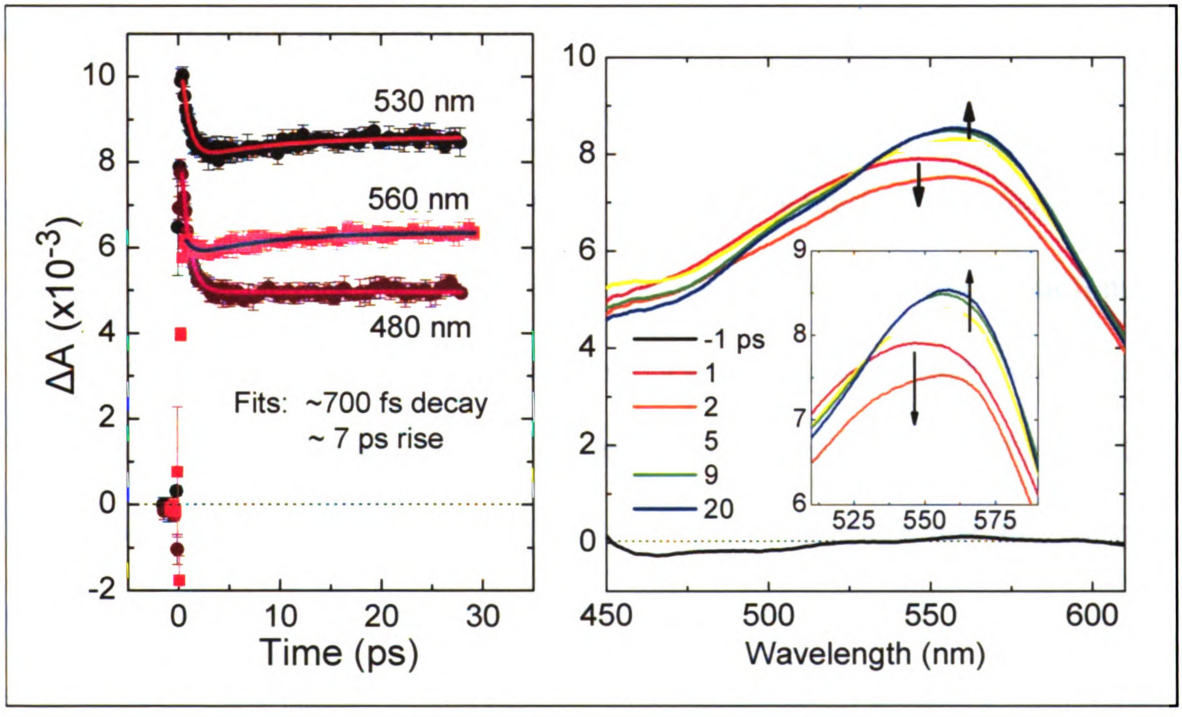

Figure 3-46: Short timescale dynamics of a flowing sample of $Cr(prop)_3$ in acetonitrile after excitation at 633 nm.

Given the paucity of electronic states involved, as well as the low-energy excitation of the $^4T_2$ state, only a handful of scenarios exist to account for the observed dynamics. The biexponential kinetics suggest dynamics originating from two different electronic states. One such scenario would involve the ~0.7 ps component corresponding to depopulation of the $^4T_2$ state—either via internal conversion to reform the ground state or via intersystem crossing to form the ^2E state. Given the trends observed for this series, namely that the intersystem crossing time is varying with substitution, it is not unreasonable that the faster 700 fs component is due to $^4T_2 \rightarrow {}^2E$ intersystem crossing. The long time offset of the kinetics suggests population of the long-lived ^2E state, therefore the slower ~7 ps component is likely vibrational cooling in ^2E, which is much slower than that of $Cr(acac)_3$. The disparate timescale for this complex as compared to $Cr(acac)_3$ may be due to a of lack of low-frequency modes by which to distribute excess vibrational energy. This relates to the notion of "vibrationally deficient" molecules which was introduced in chapter 1. It has been suggested that this slower component may be due to a photochemical reaction involving chelation of a solvent acetonitrile molecule to the metal center. While displacement of one of the chelating ligand oxygen sites is unlikely, Kirk[79] points to the possibility of 7-coordinate photochemical intermediates. Such a photochemical intermediate is much more likely for this complex than others in the series due to the relatively open coordination sphere as a result of the sterically smaller propanedione ligands.

Future experiments must employ a non-bonding solvent in order to test this possibility.

$Cr(dcm)_3$. The absorption and low-temperature emission spectra of $Cr(dcm)_3$ are shown in Figure 3-47. In the ultraviolet one observes a high-intensity peak at 280 nm (12770 M^{-1} cm^{-1}) which matches closely to that of the gallium(III) analog, which has an absorption maximum at 282 (43800 M^{-1} cm^{-1}). The peaks in this region are therefore assigned as intraligand transitions. Also observed in the ultraviolet is an intense peak at 338 nm (17200 M^{-1} cm^{-1}). Based on previous assignments of similar peaks across this series, as well comparison with the gallium(III) analog, this absorption is assigned as transition to a ^{4}CT state. On the edge of the visible spectrum one observes a moderate intensity transition at 380 nm with $\varepsilon \sim 540$ M^{-1} cm^{-1}, assigned as absorption into the $^4(^3$IL). A low-intensity shoulder, assigned as absorption into the $^4T_1$ state, is also observed. Finally, absorption into the $^4T_2$ is seen at 570 nm with $\varepsilon \sim 90$ M^{-1} cm^{-1}. All of these values represent very small deviations from the values observed for $Cr(acac)_3$. The emission spectrum (blue trace, Figure 3-47), collected in an 80 K optical glass of 2-methyltetrahydrofuran, is quite narrow, consistent with emission from the intraconfigurational ^{2}E state. The emission maximum is at 12500 cm^{-1} (800 nm), redshifted by several hundred wavenumbers from the emission maximum of $Cr(acac)_3$.

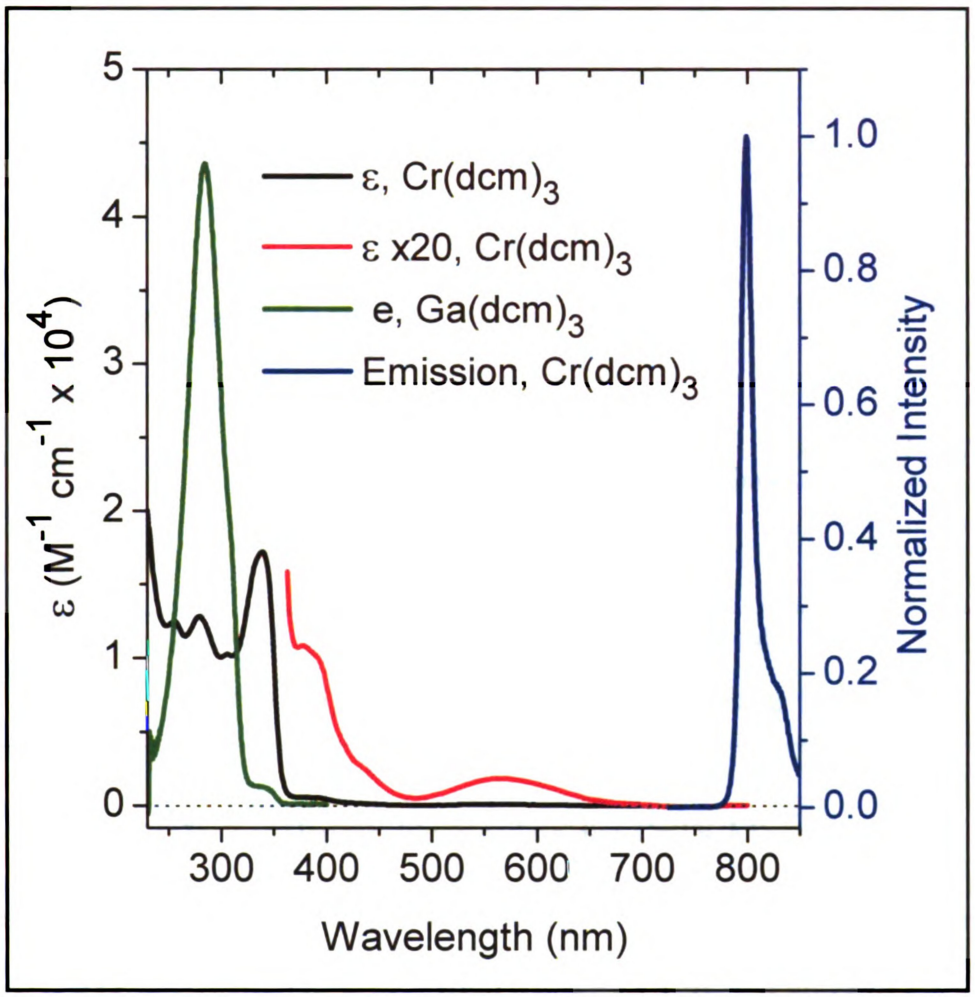

Figure 3-47: UV-vis and emission of $Cr(dcm)_3$ in dichloromethane and a low-temperature glass of 2-methyltetrahydrofuran. The electronic absorption spectrum of $Ga(dcm)_3$ reveals the relative energy of the intraligand transition.

Long-time (ps-ns) transient absorption kinetics (not shown) were fit with a monoexponential decay function which showed a negligible offset from the baseline, indicating ground state recovery with a lifetime of 1.22 ± 0.03 ns. Shorter timescale (-1 to 10 ps after excitation) single wavelength data for

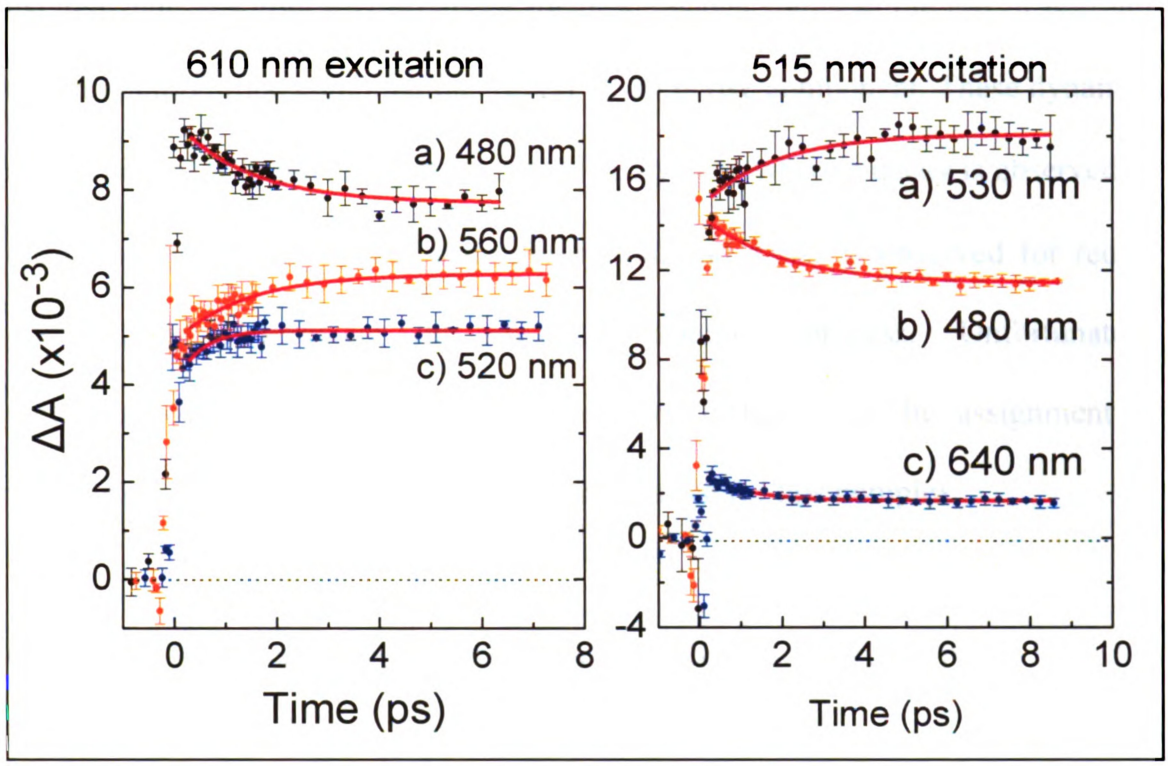

Figure 3-48: Single wavelength kinetic data for $Cr(DCM)_3$ excited at 515 nm (right) and 610 nm (left). All data were fit with monoexponential decay functions. The data at 515 nm excitation reveal lifetimes of a.) 1.78 ± 0.50 (530 nm probe), b.) 1.93 ± 0.25 ps (480 nm probe) and c.) 1.02 ± 0.14 ps (640 nm probe). At 610 nm excitation the lifetimes are a.) 1.43 ± 0.26 ps (480 nm probe), b.) 1.40 ± 0.25 ps (560 nm probe) and c.) 0.49 ± 0.12 ps (520 nm probe). See text for details.

excitation at 515 nm and 610 nm, at the blue and red edges of the $^4T_2$ absorption, are shown in Figure 3-48. These data reveal, in general, decay in the ESA with a lifetime between 1.3 - 2 ps for bluer probes, and a rise in the ESA for probe wavelengths between 500-600 nm, which has an ~1 ps lifetime. A decay in the

excited state absorption is observed for probe wavelengths to the red of 600 nm. Certain pump/probe combinations reveal a 500 fs rise component. These dynamics are consistent with those observed for Cr(t-butylac)$_3$, where a decay is observed on the blue edge of the excited state absorption, and a rise is observed for redder portions, and is consistent with a two-state dynamical process. Unfortunately, collection of full spectra proved to be very difficult, so the assignment of intersystem crossing dynamics remains speculative for this complex.

Cr(dbm)$_3$. This complex forms brown crystals, brown/yellow powders and is brown/yellow in solution. Crystals for this complex can be grown by slow evaporation from a methanol/dichloromethane solution for both Cr(dbm)$_3$ and its gallium(III) analog. The crystal structure of Cr(dbm)$_3$ is shown in Figure 3-49, crystallographic data for Cr(dbm)$_3$ and Ga(dbm)$_3$ are given in Table C-3 of appendix C, and relevant bond lengths and angles are presented in Table 3-2. The crystal structure reveals a highly symmetric environment around the metal center, with all M-O bond lengths 1.95 ± 0.02 Å, and O-M-O bond angles averaging ~ 90° and ~ 177°. Another important observation with pertinence to the electronic structure is the dihedral angle of the phenyl groups of the ligand to the inner π structure of the ligand. This shallow angle (~ 20°) ensures that the phenyl rings are coupling effectively into the inner π system of the ligand, drastically changing the ligand electronic structure (with respect to acetylacetonate), as discussed

below. A DFT calculation was carried out at the UB3LYP/6-311g** level employing a CPCM solvent model of dichloromethane in order to determine the solution-phase structure of this complex. The bond lengths and angles of the minimized geometry correlate well to the average values of the crystal structure geometry (Table 3-2).

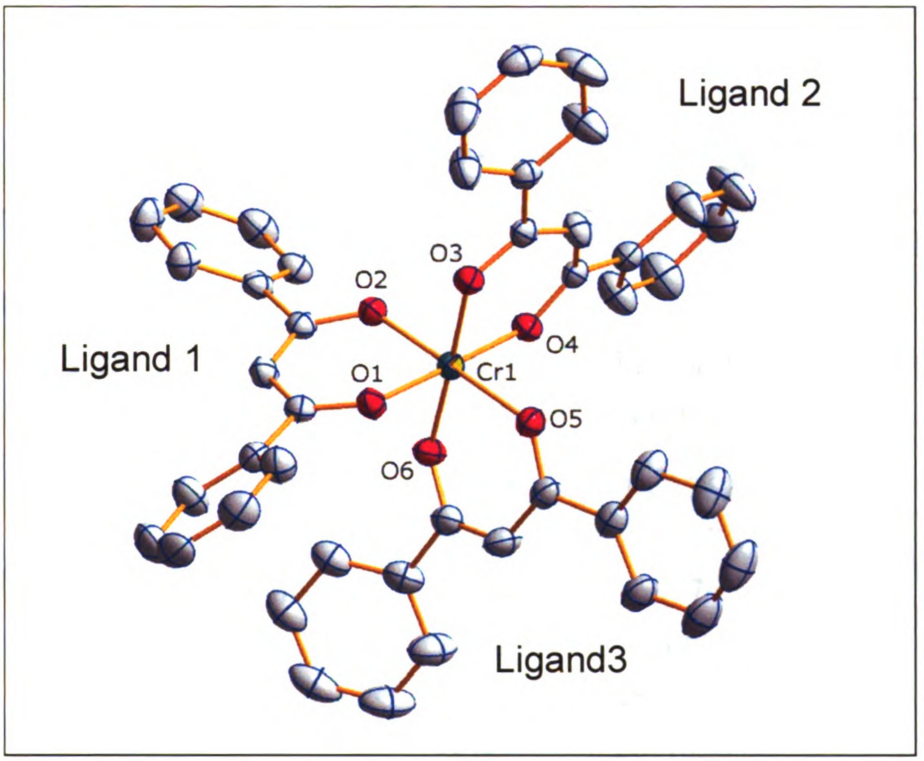

Figure 3-49: $Cr(DBM)_3$ crystal structure.

Absorption and emission spectra for this complex, as well as the absorption spectrum of the gallium(III) analog, are shown in Figure 3-50. The gallium(III) complex of this ligand absorbs intensely out to about 400 nm. In the chromium(III) complex this intensity is quenched and further high-intensity transitions arise which extend out to about 450 nm. The high-intensity band

centered at 400 nm is likely due to a low-energy charge transfer transition, facilitated by the low-lying π structure of the ligands. This band resides where the

Table 3-2: Relevant average bond lengths and bond angles for $Cr(DBM)_3$ and $Ga(DBM)_3$. Calculated values were obtained at the UB3LYP/6-311g** level employing a CPCM solvent model of dichloromethane.

		$Ga(dbm)_3$	**$Cr(dbm)_3$**	**$Cr(dbm)_3$ calc**
M-O (avg. Å)		1.954567	1.9568	1.9568
O-M-O (avg °)		90.014 177.03	177.689 90.00373	89.86584 179.5245
Phenyl Dihedral (°)	Ligand 1	-25.68 1.05	-26.2762 4.7167	17.83 19.00
	Ligand 2	19.83 28.45	5.6976 -8.3421	
	Ligand 3	25.99 15.59	29.7017 28.4038	

moderate-strength transitions of $Cr(acac)_3$ and $Cr(dcm)_3$ are found (as well as many other member of this series), and in fact low-temperature absorption spectra of $Cr(dbm)_3$ reveal a structured shoulder on the low-energy edge of the charge-transfer band whose spacing is ~ 1300 cm^{-1}, corresponding to the C=C stretch of the monodeprotonated dibenzoylmethane ligand. The implications of this fine

structure have been discussed (*vide supra*), leading to an assignment of absorption in this region as being partially due to a transition into the mixed $^4(^3IL)$ state. Similar to $Cr(acac)_3$, the $^4A_2 \rightarrow {}^4T_2$ absorption occurs near 560 nm, although the extinction coefficient is around 100 M^{-1} cm^{-1}, larger than the ~60 M^{-1} cm^{-1} of both $Cr(acac)_3$ and $Cr(dcm)_3$. The $^2E \rightarrow {}^4A_2$ emission is nearly 1000 cm^{-1} red of $Cr(acac)_3$ emission, which is expected from the extended π structure of the ligand according to the nephelauxetic effect. This emission appears broader than that of other members of this series, but this is likely an artifact of the low detector response to the red of ~ 810 nm.

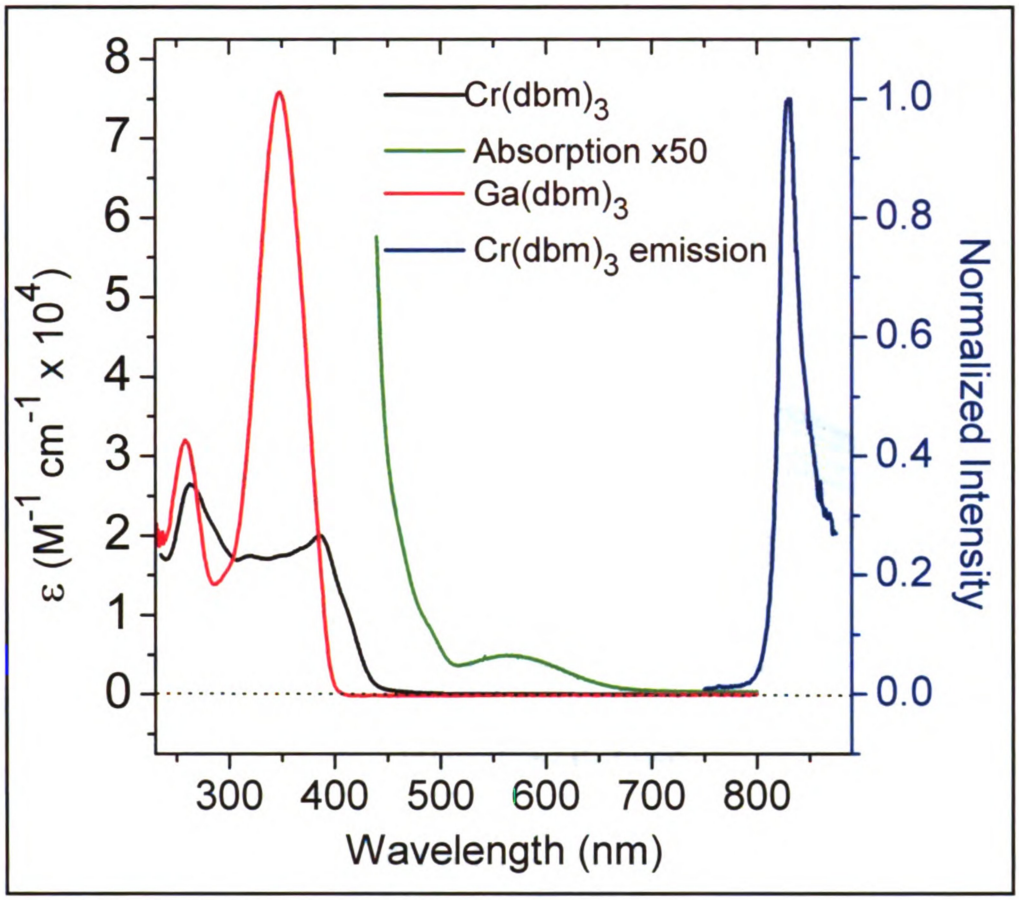

Figure 3-50: UV-vis absorption and emission for $Cr(DBM)_3$ acquired in dichloromethane solution and a low-temperature optical glass of 2-methyl-tetrahydrofuran.

Transient absorption spectroscopy reveals that a ground state recovery lifetime for $Cr(DBM)_3$ 3-6 times as long as that of $Cr(acac)_3$ (approximately 3.5 ns versus approximately 0.7 ns). Clearly better data must be acquired in order to better compare the ground state recovery times for these three molecules, but these time constants fall within the "dark" range of our current laser lab setup, as discussed above. Shorter timescale dynamics are shown in Figures 3-51 and 3-52.

Full excited state transient absorption spectra, Figure 3-51, clearly show two different absorption bands.

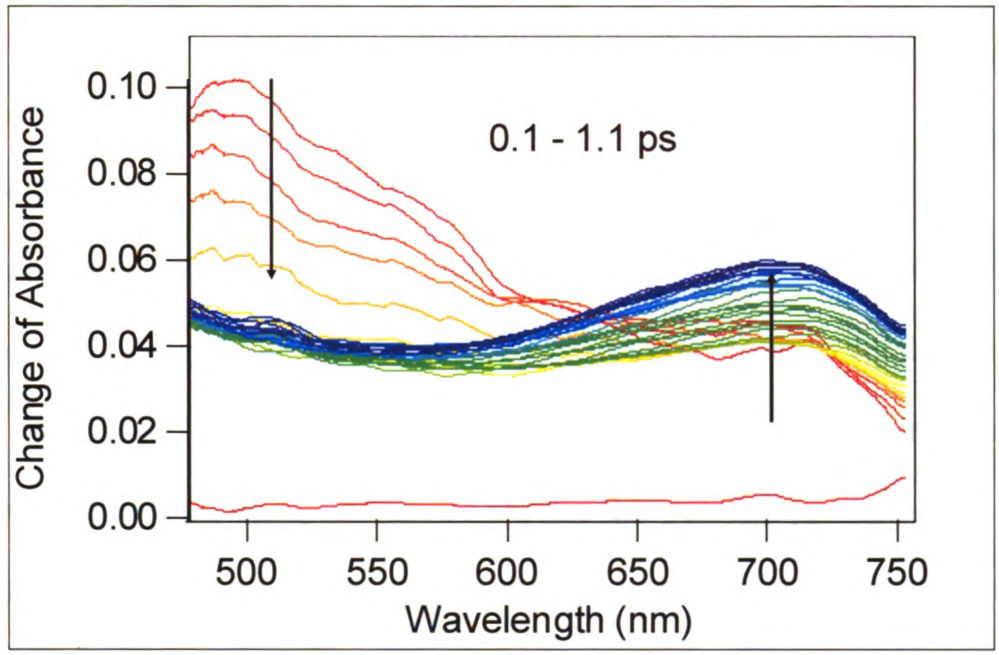

Figure 3-51: Full spectra of $Cr(dbm)_3$ in dichloromethane solution after excitation at 515 nm. The red spectrum near the baseline is at negative time, and the other spectra are spaced by 30 fs, with red being the earliest and blue the latest, starting at 0.1 ps and ending at 1.1 ps. Similar full spectra were observed for other excitation wavelengths across the $^4A_2 \rightarrow {}^4T_2$ absorption.

The bluer band, centered around 500 nm, decays very quickly while retaining its shape. A second band, centered at 700 nm grows in over a much longer timescale. Single-wavelength kinetics confirm this picture, Figure 3-52: the data reveals instrument-limited formation dynamics for probes bluer than ~550 nm and a ~1.3 ps rise in the excited state absorption for redder probes. The lifetime of the rise of

this redder component was found to be consistent for all excitation wavelengths across the $^4T_2$ absorption, Figure 3-53.

The full spectra dynamics share many of the characteristics of the other members of this series, namely a feature that decays and gives rise to a redder feature that grows in on a longer timescale than the first component. Given the results presented above for other members of this series the full spectra dynamics are remarkable only in the fact that the timescales are so different for the evolution of the two features. One possible explanation of the slower component is that it is due to rotation of the phenyl rings. To explore this possibility, single wavelength kinetic traces at 530 nm pump and 700 nm probe were collected in two different solvents: dichloromethane ($\mu = 0.4$) and the more viscous N-methylpyrollidinone ($\mu = 1.4$). If the phenyl rings were rotating, then presumably the more viscous solvent would inhibit rotation and slow down this process. While the data for N-methylpyrollidinone did reveal a slightly slower process, the fits were not outside the margin of error for the measurement. Regardless of interpretation, this complex presents the clearest example from this series of excited state absorption from two different excited states.

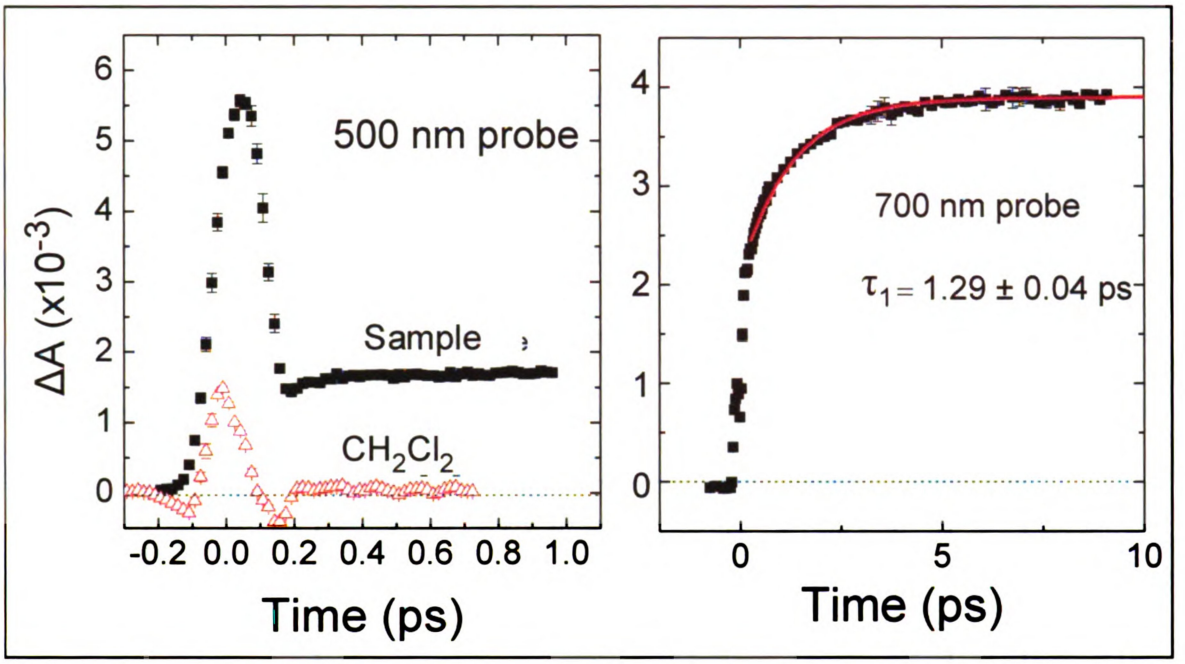

Figure 3-52: Representative single wavelength kinetic traces for $Cr(dbm)_3$ in dichloromethane for excitation at 610 nm.

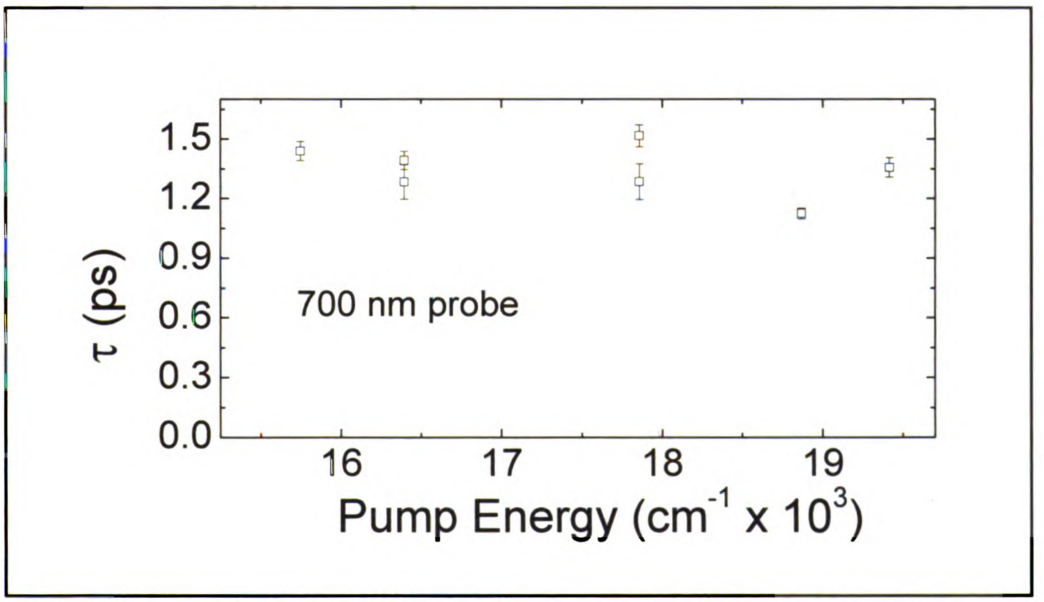

Figure 3-53: Lifetime values for various excitation energies across the $^4T_2$ absorption for 700 nm probe.

Cr(hfac)$_3$. This complex forms green powders and is quite difficult to crystallize due to its high solubility in most common solvents. The green powder will decompose in air over the course of several weeks to give a colorless crystalline material (presumably the free ligand). The UV-Vis absorption spectrum is shown in Figure 3-54.

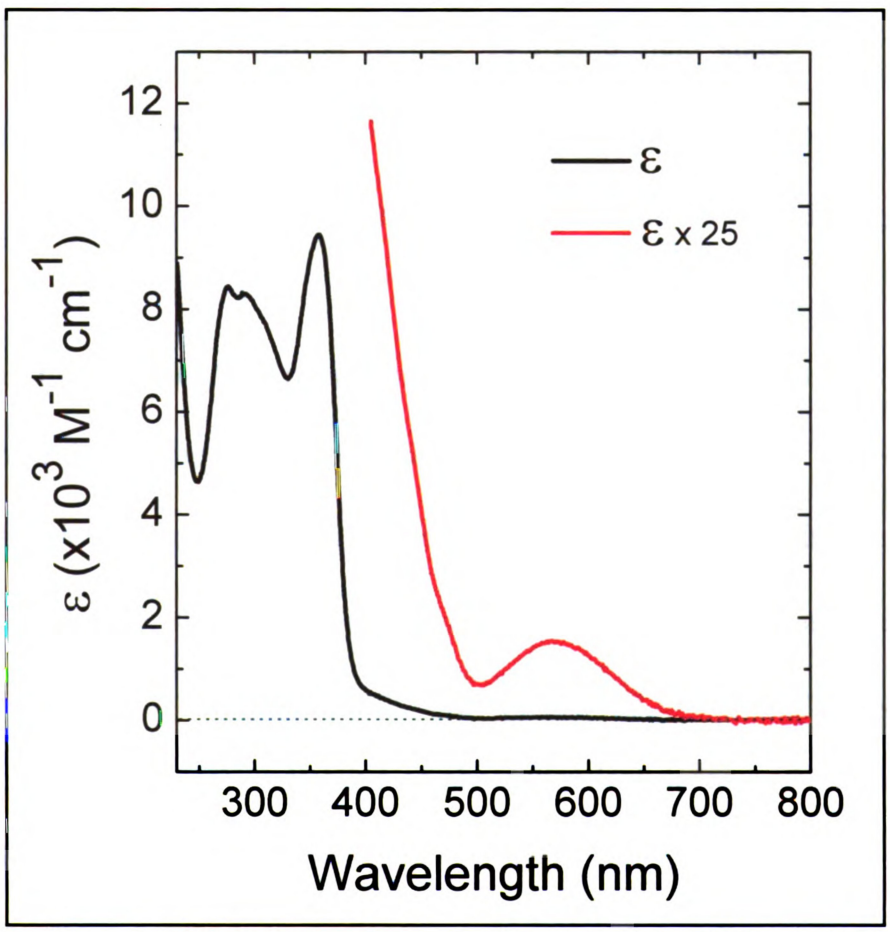

Figure 3-54: UV-vis absorption spectrum for Cr(hfac)$_3$ in dichloromethane.

As expected, it conforms with other members of this series with the exception that most peaks are red-shifted relative to those of $Cr(acac)_3$ due to the electron withdrawing ability of the $-CF_3$ substituent. In the ultraviolet one observes two peaks at 273 nm ($\varepsilon \sim 8420\ M^{-1}\ cm^{-1}$) and 291($\varepsilon \sim 8290\ M^{-1}\ cm^{-1}$) assigned as ligand-based transitions and a more intense peak at 360 nm ($\varepsilon \sim 9460\ M^{-1}\ cm^{-1}$) assigned as charge-transfer in nature. A broad, low-intensity band at 567 nm (61 $M^{-1}\ cm^{-1}$) is due to a transition to the $^4T_2$ ligand field state. The emission maximum for this complex, at 12300 cm^{-1}, has been reported before.[76] We were unable to observe any emission from this complex in an 80 K optical glass of 2-methyltetrahydrofuran.

Preliminary ultrafast measurements showed complex kinetics at early times, while long-time scans revealed a baseline offset after an ~ 400 ps component, similar to what was observed for $Cr(3\text{-Methylac})_3$ in the previous series. Furthermore, samples which underwent ultrafast experiments were shown to have a different absorption spectrum (as well as a colorless microcrystalline precipitate in some cases), indicative of photochemical decomposition to produce the free ligand. Therefore, future experiments require flowing of the sample to reduce this photochemical damage. The presence of free ligand suggests some source of protons in solution which may be due to some acidic impurities in the dichloromethane solvent—future experiments using acetonitrile may avoid this problem.

3.5 Comparison of Complexes. The initial goal of this research was to quantify whether nonradiative decay theory was applicable to the ultrafast events occurring after excitation of these systems. This quantitative aspect has proven quite difficult to implement, due to a number of chemical and technological hurdles, namely 1) the emission spectra in many cases are too red to be reliable given the detection limit of our instrument; 2) the energy gaps for these complexes are not that disparate; 3) as shown for $Cr(acac)_3$, the $^4T_2$ state is likely not thermalizing prior to intersystem crossing, making determinations of Franck-Condon overlap speculative at best; 4) for the 3-substituted $Cr(acac)_3$ series chemical modification did very little to change the dynamics, and in all cases the $^4T_2 \rightarrow {}^2E$ intersystem crossing event was not observed for the ~ 100 fs pulses used. The result is that qualitative differences dominate the discussion.

First the ground state recovery dynamics, i.e. those corresponding to the $^2E \rightarrow {}^4A_2$ transition, are considered. Given the emission data presented above, one would expect from nonradiative decay theory, considering only a two-state system at this point, that the ground state recovery time constants would vary systematically from $Cr(dbm)_3$ (being the fastest) to $Cr(acac)_3$, the slowest: for nested potential energy surfaces, such as the $^4A_2$ ground state and lowest energy excited state ^2E, a lowered zero point energy corresponds to greater vibrational overlap of the component electronic potentials. In fact, from the data below, the

opposite trend appears to hold. It is possible that the breadth of emission data for $Cr(dbm)_3$ shows that the potential is not as nested, but breadth is likely due to an extremely low response past 825 nm for the photomultiplier tube that is employed in our fluorescence experiment. In fact, as described in Chapter 1, quenching of the ^2E state can occur through a variety of mechanisms which are thermally activated.[72,80,81] Therefore, at ambient temperature one can expect not only a decay component corresponding to nonradiative decay from the low-temperature regime (dependent on factors such as potential well displacement and relative energy which affect vibrational overlap), but also thermally-induced quenching events (BISC, quenching via reaction, etc.). The fact that these events occur on a timescale several times greater than the capabilities of the instrument also leads to quite a bit of uncertainty: the dynamics were fit with monoexponential decays, but this model can not be confirmed until the timescale capabilities of the instrument are increased. Once this is achieved, the best way to parse out the low-temperature dynamics from those of the possible thermally-activated pathways, and to test the applicability of nonradiative decay theory to this ground state recovery event, would be to carry out the experiment at low-temperature.

The ultrafast dynamics present an equal challenge. The 3-substituted $Cr(acac)_3$ series was originally chosen for comparison to the previous work on $Cr(acac)_3$ not only for potential ease of synthesis, but because it was speculated that substitution at the 3-position would provide the most direct access to the inner

π-system of the acetylacetonate ligand, thus modifying the electronic structure and dynamics most dramatically. Clearly, this assumption proved to be incorrect: the dynamics observed for the 3-substituted series are qualitatively all very similar, lacking any biphasic kinetics, and are therefore given the same interpretation, i.e. that of $Cr(acac)_3$. Coherence data of $Cr(acac)_3$ collected with ~ 50 fs optical pulses provides some insight into why this may be. An oscillation of 164 cm^{-1}, assigned as vibrational coherence, was observed. This frequency may correlate to a metal-ligand active vibrational mode observed in the ground state infrared spectrum but in the e_g^*-populated $^4T_2$ sate. DFT frequency calculations of $Cr(acac)_3$ indicate that this mode, while M-L active, also includes a large amplitude motion of the acetylacetonate methyl groups. If indeed this mode is active in facilitating ultrafast intersystem crossing in the complex, then perturbation to the ligand structure at the 3-position (especially the sterically small substituents that were chosen for this study) is likely to not drastically change this mode. Assuming that electronic differences normally considered for nonradiative decay theory (E_0 and ΔQ) are negligible for this series, the intersystem crossing rate is expected to be same across the 3-substituted series based solely on the promoting ability of the ligand backbone vibrational modes.

There are clear differences between the 3-substituted and the substituted propanedione series: 1) different dynamics are observed for every member of this series, despite electronic similarities, implying a role for the ligand structure in at

the 1,3-positions in nonradiative dynamics; 2) transient spectra from different electronic states are observed; 3) there are varying timescales of dynamics across the series. Given the previous results for the 3-substituted series, these differences are not surprising, and in fact reinforce the interpretation of the $Cr(acac)_3$ coherence data. The fact that biphasic kinetics are observed for both large (R = cyclohexyl) and small (R = H) ligands reveals that the ultrafast kinetics are not simply a matter of electronics, but also of vibrational motion of the molecule on the timescale of the observed dynamics.

Several points must be made about the fitting procedure employed throughout this chapter. The single wavelength kinetic data were fit with either a mono- or biexponential function with a baseline offset, i.e

$$y = y_0 + A_1 \exp(-x/\tau_1) + A_2 \exp(-x/\tau_2) \quad (3.1)$$

For example, $A_1 \exp(-x/\tau_1)$ may correspond to depopulation of the $^4T_2$ state (and concomitant population of the ^2E state) while $A_2 \exp(-x/\tau_2)$ corresponds to vibrational cooling the in ^2E state. This model likely does not represent a correct physical picture of the dynamics, as this fitting model has both kinetic components with amplitude at time zero, implying that both physical processes are initiated at time zero, immediately following excitation. Assuming that the observed dynamics are due to intersystem crossing followed by vibrational cooling in the ^2E state, a correct model of state evolution would involve 1) a fast exponential decay

component with amplitude at time zero which decays to baseline, corresponding to depopulation of the $^4T_2$ state (this assumes that there is no thermalization of $^4T_2$ prior to intersystem crossing); 2) a second component on the same timescale as the first, which is delayed and has no amplitude at time zero, and grows in corresponding to population of the ^2E; 3) a third component with a different timescale than 1) and 2) corresponding to vibrational cooling of the ^2E. A similar model has been developed by Mathies and coworkers[82] to account for the ultrafast initial dynamics of ruthenium(II) polypyridyl chromophores, where the initial ^{1}MLCT state passes through a second CT state before the lowest-energy ^{3}MLCT is formed (equation 3.2). From this kinetic picture the authors developed equation 3.3 which describes the population of the ^{3}MLCT.

$$^1MLCT \xrightarrow{k_1} X \xrightarrow{k_2} {}^3MLCT \tag{3.2}$$

$$[^3MLCT] = [^1MLCT]_0\{1-(k_2-k_1)^{-1}[k_2\exp(-k_1t)-k_1\exp(k_2t)]\} \tag{3.3}$$

This basic picture can be applied to the two-state evolution of this system wherein the intermediate state X and ^{3}MLCT are replaced by initially populated and thermalized vibrational levels of the ^2E state, i.e.

$$^4T_2 \xrightarrow{k_{ISC}} {}^2E_0 \xrightarrow{k_{VC}} {}^2E_{therm} \tag{3.4}$$

In this equation $^2E_0$ represents the initially populated vibrational level (or, more likely, levels) of the ^2E electronic state while $^2E_{therm}$ represents the thermalized ^2E

state. Substitution of the corresponding terms for this system to equation 3.3 results in equation 3.5. Of course, correct fitting of the data requires convolution of this equation with an instrument response function.

$$[^2E_{therm}] = A_1\{1-(k_{VC}-k_{ISC})^{-1}[k_{VC}\exp(-k_{ISC}t)-k_{ISC}\exp(k_{VC}t)]\} \qquad (3.5)$$

In this equation A_1 is essentially the long-time baseline offset of the kinetic trace. While equation 3.5 accounts for the ^2E population, the full evolution of the dynamics can be described by including a second monoexponential term to account for depopulation of the $^4T_2$ state, and a third term corresponding to the concentration of the "intermediate" $^2E_0$ state, equation 3.6.

$$y = IRF \otimes ([^4T_2]+[^2E_0]+[^2E_{Therm}]) \qquad (3.6)$$

Attempts are currently underway to implement this new fitting model. One drawback of this model is that is does not account for back intersystem crossing from the ^2E state to the $^4T_2$ state, which Kunttu and coworkers have shown for $Cr(acac)_3$ to be important process (at least for high-energy excitations).[83] This model is appropriate for all systems, but necessary for those in which the k_1 and k_2 are very different ($Cr(dbm)_3$ and $Cr(prop)_3$, as well as every member of 3-substitued $Cr(acac)_3$ series). For systems in which the intersystem crossing dynamics are occurring on the same timescale as thermalization of the ^2E state (e.g. $Cr(tbutylac)_3$), the $[^2E_0]$ concentration can be assumed to be a steady-state. Cleary, this model is not perfect for all systems, but represent a much more

physically sound model of intersystem crossing dynamics than a simple biexponential function.

3.6 Final Remarks

The work presented in this chapter represents the initial efforts toward uncovering mechanisms of ultrafast nonradiative decay in transition metal systems. Qualitative trends were observed which seem to be indicating that certain low-frequency metal-ligand active modes are facilitating the ultrafast intersystem crossing event. Future work, described in Chapter 5, will benefit from increased spectroscopic capabilities, such as shorter pulses which will potentially enable further coherence measurements and present a more quantitative analysis of the series.

3.7 References

(1) Meyer, T. J. *Accounts of Chemical Research* **1989**, *22*, 163-170.

(2) Alstrum-Acevedo, J. H.; Brennaman, M. K.; Meyer, T. J. *Inorganic Chemistry* **2005**, *44*, 6802-6827.

(3) Forster, L. S. *Chemical Reviews* **1990**, *90*, 331-353.

(4) Juban, E.; McCusker, J. *Journal of the American Chemical Society* **2005**, *127*, 6857-6865.

(5) Zewail, A. H. *Journal Of Physical Chemistry A* **2000**, *104*, 5660-5694.

(6) Parker, C. A.; Rees, W. T. *Analyst* **1960**, *85*, 587-600.

(7) Juban, E., Ph.D. Thesis, University of California, 2006.

(8) Fragnito, H. L.; Bigot, J. Y.; Becker, P. C.; Shank, C. V. *Chemical Physics Letters* **1989**, *160*, 101-104.

(9) Dexheimer, S. L.; Wang, Q.; Peteanu, L. A.; Pollard, W. T.; Mathies, R. A.; Shank, C. V. *Chemical Physics Letters* **1992**, *188*, 61-66.

(10) Schoenlein, R. W.; Peteanu, L. A.; Mathies, R. A.; Shank, C. V. *Science* **1991**, *254*, 412-415.

(11) Zhu, L.; Sage, J. T.; Champion, P. M. *Science* **1994**, *266*, 629-632.

(12) Rosca, F.; Kumar, A. T. N.; D., I.; Ye, X.; Demidov, A. A.; Sjodin, T.; Wharton, D.; Barrick, D.; Sligar, S. G.; Yonetani, T.; Champion, P. M. *Journal of Physical Chemistry A* **2002**, *106*, 3540-3552.

(13) Dillman, K. L.; Shelly, K. R.; Beck, W. F. *Journal Of Physical Chemistry B* **2009**, *113*, 6127-6139.

(14) M. J. Frisch, G. W. T., H. B. Schlegel, G. E. Scuseria; M. A. Robb, J. R. C., J. A. Montgomery, Jr., T. Vreven; K. N. Kudin, J. C. B., J. M. Millam, S. S. Iyengar, J. Tomasi; V. Barone, B. M., M. Cossi, G. Scalmani, N. Rega; G. A. Petersson, H. N., M. Hada, M. Ehara, K. Toyota; R. Fukuda, J. H., M. Ishida, T. Nakajima, Y. Honda, O. Kitao; H. Nakai, M. K., X. Li, J. E. Knox, H. P. Hratchian, J. B. Cross; V. Bakken, C. A., J. Jaramillo, R. Gomperts, R. E. Stratmann; O. Yazyev, A. J. A., R. Cammi, C. Pomelli, J.

W. Ochterski; P. Y. Ayala, K. M., G. A. Voth, P. Salvador, J. J. Dannenberg; V. G. Zakrzewski, S. D., A. D. Daniels, M. C. Strain; O. Farkas, D. K. M., A. D. Rabuck, K. Raghavachari; J. B. Foresman, J. V. O., Q.Cui, A. G. Baboul, S. Clifford; J. Cioslowski, B. B. S., G. Liu, A. Liashenko, P. Piskorz; I. Komaromi, R. L. M., D. J. Fox, T. Keith, M. A. Al-Laham; C. Y. Peng, A. N., M. Challacombe, P. M. W. Gill; B. Johnson, W. C., M. W. Wong, C. Gonzalez, and J. A. Pople; Revision D.01 ed.; Gaussian, Inc.: Wallingford CT, 2004.

(15) Gaussview 2.1; Gaussian, Inc.: Pittsburgh, PA, 2001.

(16) Fernelius, W. C.; Blanch, J. E. *Inorganic Syntheses* **1958**, *5*, 130-131.

(17) Nakamura, K.; Murakami, Y. *Technology Reports of the Kyushu University* **1965**, *38*, 329-336.

(18) Harada, Y.; Girolami, G. S. *Polyhedron* **2007**, *26*, 1758-1762.

(19) Bradley, D. C.; Hursthouse, M. B.; Newing, C. W.; Welch, A. J. *Journal of the Chemical Society, Chemical Communications* **1972**, 567-568.

(20) Collman, J. P.; Marshall, R. L.; William L. Young, I.; Goldby, S. D. *Inorganic Chemistry* **1962**, *1*, 704-710.

(21) Collman, J. P.; Moss, R. A.; Maltz, H.; Heindel, C. C. *Journal of the American Chemical Society* **1960**, *83*, 531-534.

(22) Kluiber, R. W. *Journal of the American Chemical Society* **1961**, *83*, 3030-3032.

(23) Grant, M. S.; Synder, H. R. *Journal of the American Chemical Society* **1960**, *82*.

(24) Kuhr, M.; Bock, B.; Musso, H. *Chemische Berichte* **1976**, *109*, 1195-1203.

(25) *Inorganic Syntheses* **1966**, *8*, 141.

(26) Angela, M.; Jean-Pierre, G.; Sébastien, J.; Delphine, B.; Virginie, R.-V. *Chemistry - A European Journal* **1999**, *5*, 1160-1165.

(27) Charles, R. G. *Inorganic Syntheses*, *8*, 135-138.

(28) Charles, R. *Inorganic Syntheses*, *8*, 138-140.

(29) Barnum, D. W. *Journal of Inorganic and Nuclear Chemistry* **1961**, *21*, 221-237.

(30) Fleming, C. A.; Thornton, D. A. *Journal of Molecular Structure* **1975**, *25*, 271- 279.

(31) Fatta, A. M.; Lintvedt, R. L. *Inorganic Chemistry* **1971**, *10*, 478-481.

(32) Ohno, T.; Kato, S.; Kaizaki, S.; Hanazaki, I. *Inorganic Chemistry* **1986**, *25*, 3853- 3858.

(33) Konig, E.; Herzog, S. *Journal of Inorganic and Nuclear Chemistry* **1970**, *32*, 585-599.

(34) Juban, E. A., Ph.D. Thesis, University of California, Berkeley, 2006.

(35) Serpone, N.; Jamieson, M. A.; Hoffman, M. Z.; Bolletaa, F.; Maestri, M. *Journal of the American Chemical Society* **1979**, *101*, 2907-2916.

(36) Hanazaki, I.; Hanazaki, F.; Nagakura, S. *Journal of Chemical Physics* **1969**, *50*, 265-276.

(37) Hanazaki, I.; Hanazaki, F.; Nagakura, S. *Journal of Chemical Physics* **1969**, *50*, 276-286.

(38) Hanazaki, I.; Nagakura, S. *Inorganic Chemistry* **1969**, *8*, 648-654.

(39) Macoas, E. M. S.; Kananavicius, R.; Myllyperkio, P.; Pettersson, M.; Kunttu, H. *Journal of the American Chemical Society* **2007**, *129*, 8934-8935.

(40) Shelly, K. R.; Golovich, E. C.; Dillman, K. L.; Beck, W. F. *Journal of Physical Chemistry B* **2008**, *112*, 1299-1307.

(41) Dillman, K. L. *Journal of Physical Chemistry B* **2009**, *113*, 6127-6139.

(42) Yoon, M.; Jeong, D.; Cho, S.; Kim, D.; Rhee, H.; Joo, T. *Journal of Chemical Physics* **2003**, *118*, 164.

(43) Gruia, F.; Ionascu, D.; Kubo, M.; Ye, X.; Dawson, J.; Osborne, R. L.; Sligar, S. G.; Denisov, I.; Das, A.; Poulos, T. L.; Terner, J.; Champion, P. M. *Biochemistry* **2008**, *47*, 5156-5167.

(44) Delfino, I.; Manzoni, C.; Sato, K.; Dennison, C.; Cerullo, G.; Cannistraro, S. *Journal of Physical Chemistry, B* **2006**, *110*, 17252-17259.

(45) Marin, T. W.; Homoelle, B. J.; Spears, K. G.; Hupp, J. T. *Journal of Physical Chemistry A* **2002**, *106*, 1131-1143.

(46) Reid, P. J.; Silva, C.; Barbara, P. F.; Karki, L.; Hupp, J. T. *Journal of Physical Chemistry* **1995**, *99*, 2609-2616.

(47) Consani, C.; Premont-Schwarz, M.; ElNahhas, A.; Bressler, C.; van Mourik, F.; Cannizzo, A.; Chergui, A. *Angewandte Chemie, International Edition* **2009**, *48*, 7184-7187.

(48) Pollard, W. T.; Dexheimer, S. L.; Wang, Q.; Peteanu, L. A.; Shank, C. V.; Mathies, R. A. *Journal of Physical Chemistry* **1992**, *96*, 6147-6158.

(49) Bardeen, C. J.; Wang, Q.; Shank, C. V. *Journal of Physical Chemistry A* **1998**, *102*, 2759-2766.

(50) Champion, P. M.; Rosca, F.; Ionascu, D.; Cao, W.; Ye, X. *Faraday Discussions* **2004**, *127*, 123-135.

(51) Trushin, S. A.; Fuss, W.; Schmid, W. E.; Kompa, K. L. *Journal of Physical Chemistry A* **1998**, *102*, 4129-4137.

(52) Banin, U.; Waldmann, A.; Ruhmann, S. *Journal of Chemical Physics* **1992**, *96*, 2416.

(53) Pugliano, N.; Palit, D. K.; Szarka, A. Z.; Hochstrasser, R. M. *Journal of Chemical Physics* **1993**, *99*, 7273.

(54) Rubstov, I. V.; Yoshihara, K. *Journal of the Chinese Chemical Society* **2000**, *47*, 673-677.

(55) Chudoba, C.; Riedle, E.; Pfeiffer, M.; Elsaesser, T. *Chemical Physics Letters* **1996**, *263*, 622-628.

(56) Cheng, Y.; Fleming, G. R. *Annual Review of Physical Chemistry* **2009**, *60*, 241-262.

(57) Engel, G. S.; Calhoun, T. R.; Read, E. L.; Ahn, T.; Mancal, T.; Cheng, Y.; Blankenship, R. E.; Fleming, G. R. *Nature* **2007**, *446*, 782-786.

(58) Lee, H.; Cheng, Y.; Fleming, G. R. *Science* **2007**, *316*, 1462-1465.

(59) Fuji, T.; Jin Ong, H.; Kobayashi, T. *Chemical Physics Letters* **2003**, *380*, 135-140.

(60) Takeuchi, S.; Tahara, T. *Journal of Physical Chemistry A* **2005**, *109*, 10119-10207.

(61) Kobayashi, T.; Saito, T.; Ohtani, H. *Nature* **2001**, *414*, 531-534.

(62) Lenderink, E.; Duppen, K.; Wiersma, D. A. *Journal of Physical Chemistry* **1995**, *99*, 8972-8977.

(63) Nakamoto, K.; McCarthy, P. J.; Martell, A. E. *Journal of the American Chemical Society* **1961**, *83*, 1272-1276.

(64) Dismukes, J. P.; Jones, L. H.; Bailar, J. C. *Journal of Physical Chemistry* **1961**, *65*, 792-795.

(65) Diaz-Acosta, I.; Baker, J.; Cordes, W.; Hinton, J. F.; Pulay, P. *Spectochimica Acta, Part A* **2003**, *59*, 363-377.

(66) Diaz-Acosta, I.; Baker, J.; Cordes, W.; Pulay, P. *Journal of Physical Chemistry, A* **2001**, *105*, 238.

(67) Tayyari, S. F.; Milani-nejad, F. *Spectochimica Acta, Part A* **2000**, *56*, 2679.

(68) Tayyari, S. F.; Raissi, H.; Ahmaabadi, Z. *Spectochimica Acta, Part A* **2002**, *58*, 2669.

(69) Thornton, D. A. *Coordination Chemistry Reviews* **1990**, *104*, 173-249.

(70) Sato, H.; Taniguchi, T.; Nakahashi, A.; Monde, K.; Yamagishi, A. *Inorganic Chemistry* **2007**, *46*, 6755-6766.

(71) Nakamoto, K.; Udovich, C.; Takemoto, J. *Journal of the American Chemical Society* **1970**, *92*, 3973-3976.

(72) Perkovic, M. W.; Endicott, J. F. *The Journal of Physical Chemistry* **1990**, *94*, 1217.

(73) Hare, P. M.; Crespo-Hernandez, C. E.; Kohler, B. *Proceedings Of The National Academy Of Sciences Of The United States Of America* **2007**, *104*, 435-440.

(74) Kang, H.; Jung, B.; Kim, S. K. *Journal Of Chemical Physics* **2003**, *118*, 6717- 6719.

(75) Worth, G. A.; Cederbaum, L. S. *Annual Review of Physical Chemistry* **2004**, *55*, 127-158.

(76) DeArmond, K.; Forster, L. S. *Spectrochimica Acta* **1963**, *19*, 1403-1406.

(77) Riesen, H.; Dubicki, L. *Journal of Physical Chemistry A* **2008**, *ASAP*.

(78) DeArmond, K.; Forster, L. S. *Spectrochimica Acta* **1963**, *19*, 1687-1693.

(79) Kirk, A. D. *Chemical Reviews* **1999**, *99*, 1607-1640.

(80) Endicott, J. F.; Lessard, R. B.; Lynch, D.; Perkovic, M. W.; Ryu, C. K. *Coordination Chemistry Reviews* **1990**, *97*, 65-79.

(81) Endicott, J. F.; Tamilarasan, R.; Lessard, R. B. *Chemical Physics Letters* **1984**, *112*, 381-386.

(82) Yoon, S.; Kukura, P.; Stuart, C. M.; Mathies, R. A. *Molecular Physics* **2006**, *104*, 1275-1282.

(83) Macoas, E. M. S.; Kananavicius, R.; Myllyperkio, P.; Pettersson, M.; Kunttu, H. *Journal of the American Chemical Society* **2007**, *129*, 8934-8935.

Chapter 4: Electronic Structure and Nonradiative Dynamics of Heisenberg Spin Exchange Complexes of Chromium(III)

4.1 Introduction

As described previously, the main theme of the research presented in this dissertation is correlation of the electronic structure of transition metal complexes to nonradiative dynamics in these systems. The previous chapters have been devoted to exploring the electronic structure and nonradiative dynamics in quartet chromium(III) complexes, as well as the ground state electronic and magnetic structure of gallium(III) semiquinone complexes (gallium(III) has an almost identical charge-to-radius ratio as chromium(III), and was therefore chosen as a diamagnetic analog of chromium(III)). We now hope to combine the knowledge of the previous chapters to be applied to the study of the magnetic and electronic structures and nonradiative dynamics of spin-exchange complexes of chromium(III), i.e. complexes with two or more interacting spin centers. This chapter represents the initial efforts toward the synthesis and characterization of a series of chromium-semiquinone complexes. This series will be employed to study the effects of Heisenberg spin exchange interactions on the photophysical properties of a transition metal system. These systems are of interest because Heisenberg spin exchange is operative not only in the ground state (although most examples in the literature only study the phenomena in the ground state), but also in excited states, which has been shown conclusively by Güdel and coworkers.[1-4]

It is thus apparent that introduction of spin exchange can tremendously affect the photophysical as well as photochemical properties of molecular systems. Metal-quinone complexes are ideal for the study of physicochemical properties of exchange-coupled molecules because the redox activity of the quinone ligand provides a facile mechanism for turning the exchange interaction on or off, i.e. in the systems of study in this chapter one is able to selectively turn on spin exchange with incorporation of the paramagnetic species chromium(III) and semiquinone, or turn off exchange interactions by substituting in the diamagnetic analogs gallium(III) and catechol. In this manner a series of controls can be established, which allows one to identify and differentiate properties endemic to the constituents of the molecule and those which arise due to exchange interactions between the constituents.

The main impetus for the dynamical study of these systems arose from a kinetic study of $[Cr(tren)(3,6\text{-DTBCat})]^+$ (where DTBCat = 3,6-di-*tert*-butyl-1,2-orthocatechol and tren is tris(2-aminoethyl) amine) and its semiquinone analog, $[Cr(tren)(3,6\text{-DTBSQ})]^{2+}$, (*vide infra*). These data show the effect of spin exchange on ground-state recovery dynamics in this system: the semiquinone and catechol analogs return to baseline, indicating ground state recovery within ~3 ps and ~6 ps, respectively. This is compared to the approximately 500 ps lifetime observed for $^2E \rightarrow {}^4A_2$ relaxation in a low-symmetry analog, $[Cr(tren)(acac)]^{2+}$. Models for these dynamics are presented below, but it seems apparent from a first

glance that inductive effects and spin exchange are playing a role in modifying these dynamics from those of the related low-symmetry complex $[Cr(tren)(acac)]^{2+}$.

This chapter will focus primarily on the synthesis and characterization of chromium(III)-catechol and chromium(III)-semiquinone complexes. A series of chromium(III)-catechols (from which one can prepare the chromium(III)-semiquinone complexes via a one electron oxidation) and was produced in order to study the effects of modifying spin distribution in these systems. This series utilizes the $[Cr(tren)(3,6\text{-R-Q})]^{+1/+2}$ motif, where 3,6-R-Q represents an ortho-quinone substituted at the three and six positions and either in the catechol (-2) or semiquinone (-1) form (Figures 4-1 and 4-2).

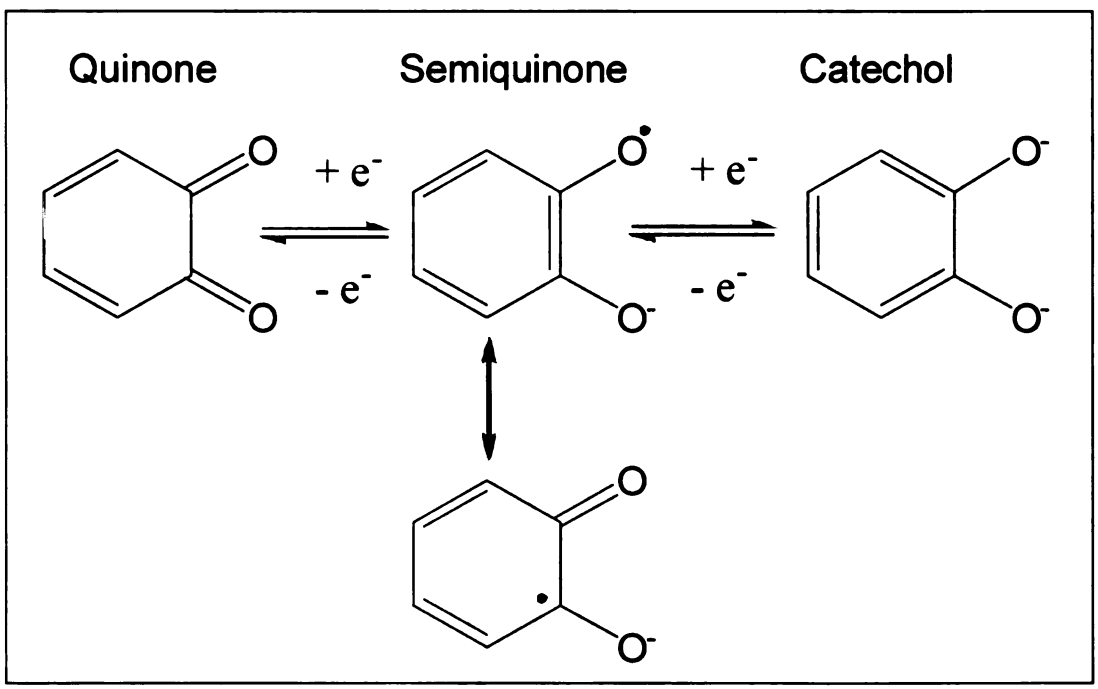

Figure 4-1: The redox states of the ortho-quinone ligands.

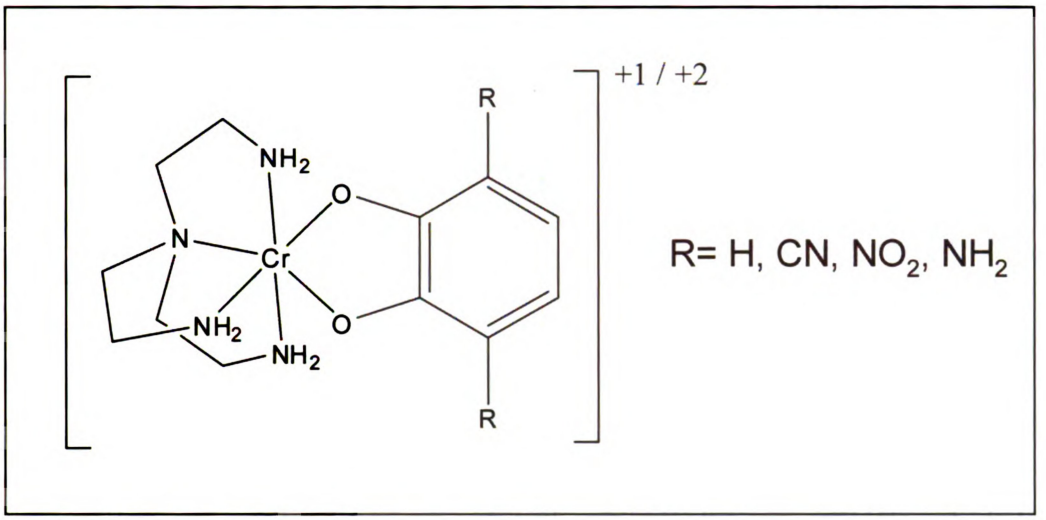

Figure 4-2: Members of the $[Cr(tren)(3,6\text{-}R\text{-}Q)]^{+1/+2}$ series employed in this study.

While this chapter will focus primarily on chromium(III) semiquinone complexes, metal-metal as well as other spin-exchange complexes will be explored, such as the spin-exchange complexes of the aforementioned $[M_1M_2(tren)_2(CA^{n-})]^{m+}$ series, where M = gallium(III) or chromium(III) and CA^{n-} is the chloranilate anion, the bridging chelate between the two metal ions (Figure 4-3). This series was introduced in Chapter 2, which explored the ground states of some of the (magnetically) simpler members of this series via electron spin resonance techniques: the doublet system **2** and the quartet system **3**. While we have characterized the simpler, "magnetically dilute" paramagnetic systems, i.e. those that display no exchange coupling,[5,6] we have yet to explore the effects of "turning on" exchange coupling within this series, namely

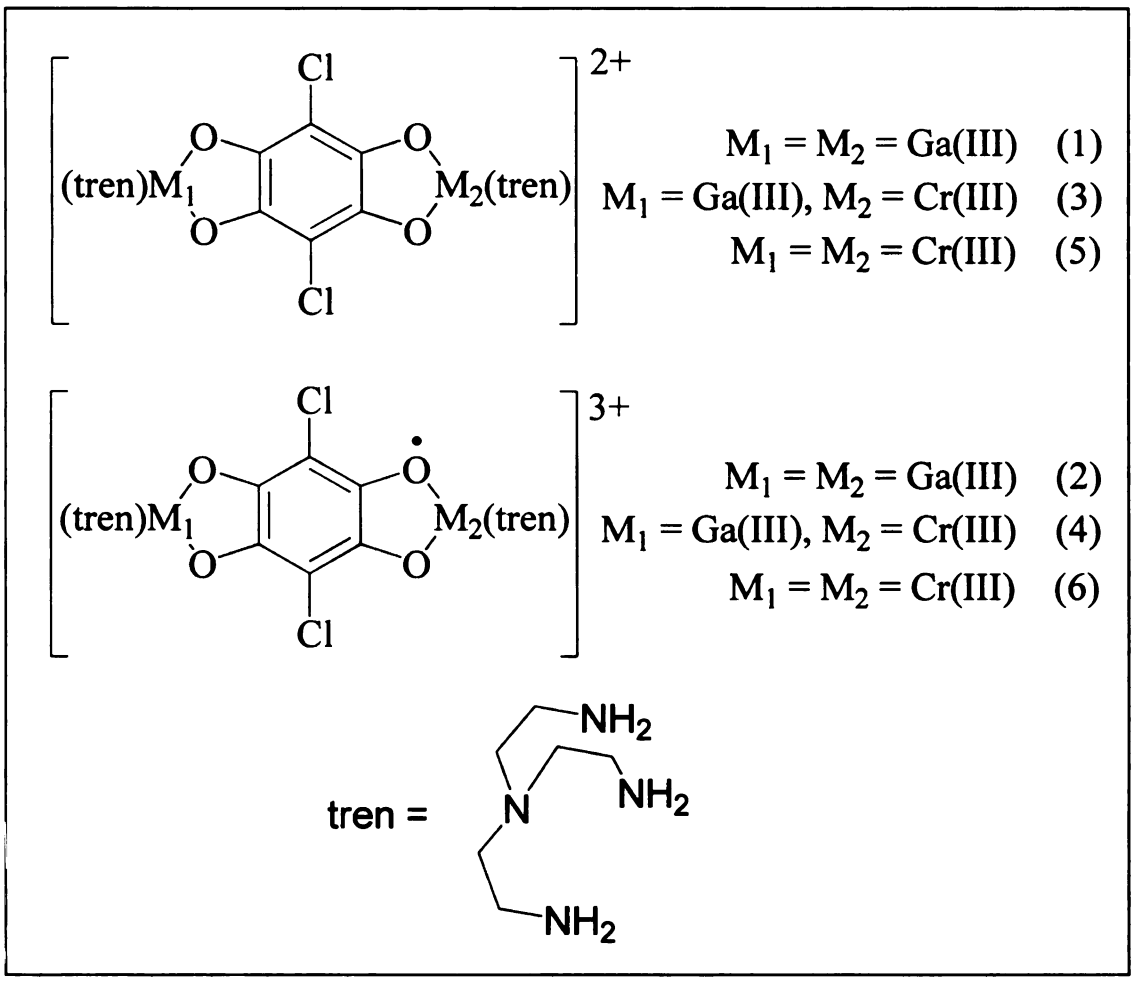

Figure 4-3: Members of the bimetallic $[M_1M_2(tren)_2(CA^{n-})]^{m+}$ series.

$[GaCr(tren)_2(CA^{sq,cat})](BPh_4)_2(BF_4)$ **(4)**, $[Cr_2(tren)_2(CA^{cat,cat})](BPh_4)_2$ **(5)**, and $[Cr_2(tren)_2(CA^{sq,cat})](BPh_4)_2(BF_4)$ **(6)**. In this chapter, X-Band EPR spectroscopy is the main tool utilized to study these magnetically complex ground states. An approached of "building up" the physical interactions in these systems in a piecewise fashion is applied: the physical properties of semiquinone complexes and quartet complexes of chromium(III) were extensively studied before moving on to the study of spin-exchange systems. As such, much of the work presented in

this chapter remains incomplete; a section of chapter 5 is devoted to the future study of these systems. EPR has been implemented to characterize the ground states of magnetic systems similar to those of molecules within this series that display exchange coupling: 1.) exchange-coupled metal-semiquinone complexes including binuclear Cr^{III}-semiquinone species[7,8] (like complexes **4** and **6**) and binuclear Fe^{III}- and Co^{III}-semiquinone species[8,9] and Cu^{II}-semiquinones[10]; 2) exchange coupled metal centers including Cr^{III} dimers[11-13] (like complexes **5** and **6**). This fund of knowledge provides a useful starting point for the analyses of these complexes.

4.2 Experimental Section

4.2.1 Synthetic Methods.

General. All reagents and materials were used as received unless otherwise noted. Solvents were purchased from Aldrich Chemical Co. and distilled and degassed by the freeze-pump-thaw method. The ligand tris(2-aminoethyl)-amine (tren) was purchased from Aldrich and vacuum-distilled prior to use. All synthetic procedures involving hydrochloranilic acid were performed under an inert atmosphere. Hydrochloranilic acid was synthesized by a modification of a previously reported method.[14,15] $Ga(tren)(NO_3)_3$ was prepared according to our previous paper.[16] $[Cr(tren)Cl_2]Cl$ was prepared according to literature

procedures.[17] Synthesis of the bimetallic complexes **4 - 6** and the model complex of **4** were synthesized according to previously published procedures.[16,18]

[Cr(tren)(pyrocatecholate)]BPh_4. This complex was made by adapting a procedure which had been utilized previously to the synthesis of chromium(III)-phenanthrenecatechol and –semiquinone systems.[19] 130 mg (0.43 mmol) of [Cr(tren)Cl_2]Cl is dissolved in 60 ml of 2:1 methanol:water in a 2 neck 250 ml roundbottom flask equipped with a reflux condenser. This solution is rapidly stirred and bubble de-gassed with N_2 for 30 minutes. Meanwhile, a 20 ml solution of 53 mg pyrocatechol (0.48 mmol) and 38 mg sodium hydroxide (0.96 mmol) is prepared under inert conditions in a 50 ml roundbottom flask equipped with a vacuum adaptor and septum. Note: if this solution is exposed to oxygen it will turn green in a matter of minutes (semiquinone form) and eventually brown (quinone). This solution is allowed to stir for approximately ten minutes and is then cannula transferred to the pink solution of [Cr(tren)Cl_2]Cl. The solution rapidly turns purple. The reaction is refluxed under positive N_2 pressure for approximately 16 hours, over which time it turns a dark blue/green color. The solution is filtered under N_2 onto 1.3 g (excess) $NaBPh_4$, and nitrogen is allowed to pass over the solution until it cools and most of the methanol has evaporated. Blue/green microcrystals precipitate, which are collected on a frit and washed with copious amounts of water. Yield: 160 mg (59.4%) Anal. Calc. for

$C_{36}H_{42}BCrN_4O_2 \cdot 3\ H_2O$ expected: C, 63.62; H, 7.12; N, 8.24. Found: C, 63.50; H, 6.20; N, 8.19. Mass spectroscopy (ESI, positive): m/z 306.1 (M-BPh_4, 100%). Crystals suitable for x-ray crystallography were grown by slow evaporation of a methanol/$NaBPh_4$ solution. The product appears to be stable in air as a solid and in solution.

2,3-dihydroxyterephthalonitrile (3,6-cyano-1,2-orthocatechol). This catechol was prepared according to a previously published method.[20] Anal. Calc. for $C_8H_4N_2O_2 \cdot 0.2\ H_2O$ expected: C, 58.68; H, 2.71; N, 17.11. Found: C, 58.28; H, 2.68; N, 16.32. NMR(500 MHz, d_6-DMSO): 7.19 (s), 10.89 (broad, -OH).

[Cr(tren)(3,6-CN-1,2-catecholate)]BPh_4. This complex was prepared in a similar fashion to [Cr(tren)(pyrocatecholate)]BPh_4. 65 mg (0.22 mmol) of [Cr(tren)Cl_2]Cl was dissolved in 30 ml of 1:1 MeOH:H_2O and degassed with N_2 for approximately 30 minutes. A 10 ml methanol solution containing 38.4 mg (0.24 mmol) 3,6-cyano-1,2-orthocatechol and 19.0 mg (0.48 mmol) NaOH was prepared under inert conditions. This dark orange solution was cannula transferred to the pink [Cr(tren)Cl_2]Cl solution, which instantly turns a dark purple/brown color. After refluxing for 30 minutes the solution turns orange, and refluxing is continued for another day. The hot solution is Schlenk filtered under N_2 onto solid $NaBPh_4$ and nitrogen was allowed to blow over the hot solution to

drive off methanol. Brown microcrystals precipitate which were washed with water, dried *in vacuo*, and stored under N_2, although the product does not appear to be air sensitive. Anal. Calc. for $C_{38}H_{40}BCrN_6O_2$ expected: C, 67.56; H, 5.97; N, 12.44. Found: C, 67.89; H, 5.93; N, 12.30. Mass spectroscopy (ESI, positive): m/z 356.1 (M-BPh_4, 100%). Crystals suitable for x-ray crystallography were grown by slow evaporation of an acetonitrile/$NaBPh_4$ or methanol/$NaBPh_4$ solution.

2-methoxy-3-nitrophenol (3-nitroguaiacol). This precursor to 2-methoxy-3,6-dinitrophenol was prepared by a previously published method from ortho-methoxyacetate (Alfa).[21] Anal. Calc. for $C_7H_7NO_4$ expected: C, 49.71; H, 4.17; N, 8.28. Found: C, 49.57; H, 4.09; N, 8.24. NMR(300 MHz, $CDCl_3$): 3.95 (s, 3H, methoxy), ~6 (broad, -OH), 7.09 (t, 1 H, aromatic), 7.21 (d, 1H, aromatic), 7.44 (d, 1H, aromatic).

2-methoxy-3,6-dinitrophenol (3,6-dinitroguaiacol). This precursor to 3,6-dinitro-1,2-orthocatechol was prepared according to a published method from 2-methoxy-3-nitrophenol.[21] The product was extracted from the crude material using hot petroleum ether. This solution was placed in a freezer and yellow microcrystalline material precipitated, which was shown by NMR to contain only the desired product and a small amount of water. NMR (500 MHz, $CDCl_3$): 4.10

(s, 3H, methoxy), 7.26 (d, 1H, aromatic), 7.96 (d, 1H, aromatic), 10.86 (s, 1H, -OH).

3,6-dinitrobenzene-1,2-diol (3,6-dinitro-1,2-orthocatechol). This catechol was prepared from 2-methoxy-3,6-dinitrophenol using a published method.[22] Recrystallization from ethanol resulted in a yellow crystals that were clean by NMR. NMR (500 MHz, $CDCl_3$): 7.71 (s, 2H, aromatic), 10.80 (s, 2H, -OH).

3,6-diaminobenzene-1,2-diol dihydrochloride (3,6-diamino-1,2-orthocatechol·2HCl). 88.3 mg (0.44 mmol) of 3,6-dinitro-1,2-orthocatechol was dissolved in 50 ml of concentrated HCl. With rapid stirring, 0.42 g (3.5 mmol) of tin metal was added slowly over 10 minutes. The reaction was refluxed for approximately 45 minutes. During the reflux, the solution turns from a bright yellow color to colorless. The volume of the solution is reduced slowly to approximately 10 ml by blowing nitrogen over it, and a colorless microcrystalline material precipitates which was collected, washed with ethanol, and dried *in vacuo.* Yield: 68.9 mg (73.5%). Anal. Calc. for $C_6H_8N_2O_2 \cdot 2HCl$ expected: C, 33.82; H, 4.73; N, 13.15. Found: C, 33.61; H, 4.66; N, 12.89. The product is soluble in water but decomposes in solution over several hours to yield a brown solution.

[Cr(tren)(3,6-dinitro-1,2-orthocatecholate)]BPh_4. 65 mg (0.22 mmol) [Cr(tren)Cl_2]Cl was dissolved into 20 ml methanol and 10 ml water in a 2-neck 100 ml roundbottom flask equipped with a reflux condenser. This solution was bubble de-gassed with N_2 for 30 minutes. Meanwhile, a solution of 48 mg (0.24 mmol) 3,6-dinitro-1,2-orthocatechol and 19 mg (0.48 mmol) NaOH in 10 ml methanol was prepared in the drybox. Addition of NaOH to the yellow catechol solution turns the solution red/orange. This solution was cannula transferred to the pink/purple [Cr(tren)Cl_2]Cl solution, which rapidly turns a dark red color. The solution was refluxed under nitrogen for approximately two days, at which point a purple precipitate forms and the solution turns dark purple/brown. The reaction was filtered while hot under N_2 onto solid $NaBPh_4$ (0.7 g). Nitrogen was blown over the solution for several hours to drive off methanol, and a red/brown microcrystalline material precipitates. This product was filtered and washed with copious amounts of water. The product was dried *in vacuo* to yield a burnt orange powder. Yield: 97 mg (63%). Anal. Calc. for $C_{36}H_{40}BCrN_6O_6$ expected: C, 59.94; H, 5.86; N, 11.48. Found: C, 60.43; H, 5.63; N, 11.74. Mass spectroscopy (ESI, positive): m/z 396.1 (M-BPh_4, 100%).

[Cr(tren)(3,6-diamino-1,2-orthocatecholate)]BPh_4. This preparation was carried out in a similar manner to those of the other members of this series. A solution of 86.3 mg (0.292 mmol) of [Cr(tren)Cl_2]Cl in 40 ml methanol and 20 ml

water was degassed with nitrogen for approximately 30 minutes. In the drybox a solution of 62.3 mg (0.292 mmol) of 3,6-diamino-1,2-orthocatechol·2HCl and 46.7 mg of NaOH (1.17 mmol, 4 equivalents) in 20 ml of methanol was prepared. This solution should be colorless. When exposed to air it rapidly turns blue (semiquinone form) and eventually brown (quinone form). This solution was removed from the drybox and transferred via cannula to the solution of $[Cr(tren)Cl_2]Cl$. The combined reaction solution was refluxed under positive nitrogen pressure for 24 hours, over which time the solution turns a dark green color. While hot, the solution is filtered under nitrogen onto solid $NaBPh_4$ (~ 1 g), and nitrogen is allowed to pass over the solution for several hours. As the methanol is driven off the product precipitates as a purple solid, which is filtered and washed with water. The product is stored under inert conditions, and solutions of the product are air sensitive, eventually decomposing to a brown solution. Yield: 120 mg (0.183 mmol, 63%). Anal. Calc. for $C_{36}H_{44}BCrN_6O_2 \cdot 0.5$ $NaBPh_4 \cdot 2$ H_2O: C, 66.77; H, 6.78; N, 9.74. Found: C, 66.80; H, 6.21; N, 9.56. Mass spectroscopy (ESI, positive): 336.2 m/z (M-BPh_4, 85%), m/z = 656.4 (MH^+, 60%).

The UV-vis absorption and electrochemical properties of this complex (see below) are not entirely consistent with the rest of the series. These data are presented below, but until a crystal structure can be obtained these measurements should be taken with a grain of salt.

4.2.2 Physical Measurements.

UV-vis spectra were acquired on a Cary-50. X-band EPR samples were prepared in a dry, inert atmosphere (N_2) by dilution in a mixture of butyronitrile and propionitrile (9:2), both of which had been distilled from CaH_2, degassed, and stored under an inert atmosphere. The resulting sample concentration was approximately millimolar. Continuous-wave X-band EPR spectra were obtained with a Bruker ESP300E spectrometer using a perpendicular-mode cavity (Bruker 4102ST/9516) with resonances around 9.458 GHz. For each compound an appropriate power was chosen to avoid saturation of the signal. An Oxford ESR A900 helium cryostat was employed to maintain the temperature at 4 K.

Cyclic voltammetry was carried out under inert conditions using a CHI Electrochemical Workstation (model CHI620D). Solutions of the compounds were dissolved in acetonitrile containing tetrabutylammonium hexafluorophosphate as the supporting electrolyte. A standard three-electrode setup was employed with a platinum working electrode, graphite counter electrode and Ag/AgCl reference electrode.

4.3 Theory of Heisenberg Spin-Exchange.

Exchange interactions essentially form weak bonds, in the same sense as spin pairing is characteristic of bond formation.[23] For example, two hydrogen radicals,

each having S = ½, come together to form a hydrogen molecule with singlet (S = 0) ground state. A triplet state is also formed, although at a much greater energy, existing as an excited state in this system. Likewise, when two unpaired spins are in close proximity a weak bond is formed. However, unlike exchange of σ- or π-bonds, these interactions are generally on the order of kT. Several criteria must be satisfied for this interaction to occur: 1) the obvious observation that unpaired electrons must reside on each substituent participating in the interaction; 2) an orbital pathway for the exchange must exist; 3) energetic matching of the magnetic orbitals (i.e. those containing unpaired spin). The theoretical physical picture of this phenomenon is well established, and is described by Anderson's Theory.[24] Goodenough[25,26] and Kanamori[27] later gleaned criteria for spin-exchange interactions from this formalism, which qualitatively express the outcome of a spin-exchange interaction from a molecular orbital perspective. For two magnetic orbitals (those containing unpaired spin) that have a large overlap integral, the interaction is antiferromagnetic, while if the overlap integral is zero, the interaction in ferromagnetic. Finally, if a magnetic orbital overlaps with an empty orbital, the interaction is ferromagnetic. These rules are discussed more thoroughly below in terms of metal-semiquinone systems.

In some instances paramagnetic centers are directly bound, resulting in a through-bond spin exchange interaction that is appropriately named "direct exchange." However, in the majority of cases the exchange interaction is facilitated by a diamagnetic bridge between the paramagnetic centers. This is

quite common in multinuclear transition metal systems, and is referred to as "superexchange." Considering the interaction of two centers of spin S_1 and S_2, the exchange interaction will, according to the angular momentum addition rules, produce a "spin ladder" of states.

$$|S_1 + S_2|, |S_1 + S_2 - 1|, \ldots, |S_1 - S_2|$$

The energetic ordering of these states is determined by using the Heisenberg Hamiltonian (also called the Heisenberg-Dirac Hamiltonian), which was originally derived from the exchange Hamiltonian for the hydrogen molecule ($S_1 = S_2 =$ ½),[28,29] but has been applied widely and successfully to many more complicated spin systems. For two interacting spin centers S_1 and S_2, the isotropic Heisenberg Hamiltonian is given by equation 4.1.

$$\hat{H} = J_{12} S_1 \bullet S_2 \qquad 4.1$$

Here J_{12} is a coupling constant which gauges the interaction between the two spin centers. This Hamiltonian has also been represented by various other coupling constants ($2J_{12}$, $-J_{12}$, $-2J_{12}$), lending confusion to the application. In the formalism presented above in equation 4.1, a negative value of J_{12} indicates ferromagnetic exchange coupling, leading to stabilization of the highest total spin state, while a positive value of J_{12} designates antiferromagnetic exchange, wherein the lowest total spin state is stabilized.

In the direct (through-bond) exchange regime the lowest-lying total spin of the system is predicted by examination of the symmetry of the constituent magnetic orbitals. This is essentially a summation of the aforementioned Goodenough and Kanamori rules. Considering only two spin centers, S_1 and S_2, an antiferromagnetic interaction will occur if the magnetic orbitals (i.e. those containing unpaired electrons) of the spin centers are of the appropriate energy and symmetry to interact. This interaction leads to an anti-parallel alignment of the spin dipoles, resulting in the lowest total spin state, $|S_1 - S_2|$, being lowest in energy. This situation is realized in the diagram of Figure 4-4. On the other hand, ferromagnetic exchange stems from complete orthogonality of magnetic orbitals. The non-interacting nature of these orbitals stabilizes the highest possible total spin state, $|S_1 + S_2|$, according to Hund's rule, as depicted in Figure 4-5. The spatial aspect is reflected, for example, in the well-understood role of orbital symmetry of metal-semiquinone complexes of the first row. For example, complexes of $[Ni(II)(tren)(psq)]^+$ (psq = phenanthrenesemiquinone) display ferromagnetic exchange coupling, while the analogous complexes of chromium(III) display antiferromagnetic exchange coupling (*vide infra*).[19,30,31] The energetic consequences of Heisenberg spin exchange can be determined by applying the so-called Kambe approximation, which defines the total spin operator S_t as a sum of spin operators, analogous to the total spin vector.[32] For a two-

component spin exchange system, this approximation yields eigenvalues of the form given by equation 4.2.

$$E = \frac{J}{2}[S_t(S_t+1) - S_1(S_1+1) - S_2(S_2+1)] \qquad (4.2)$$

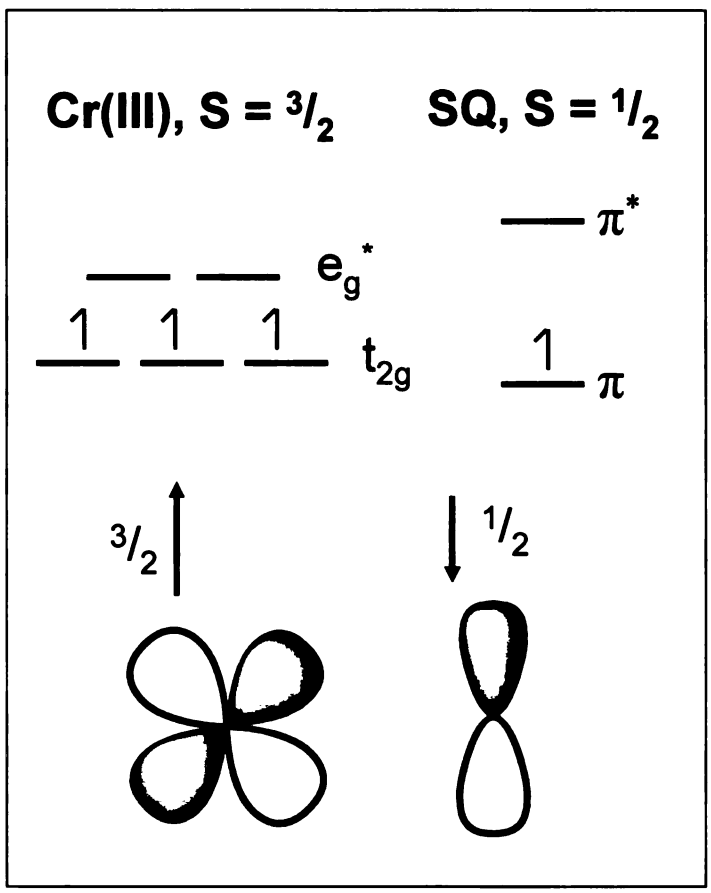

Figure 4-4: Antiferromagnetic exchange arises from non-orthogonality of constituent spin orbitals, resulting in the stabilization of the lowest total spin state.

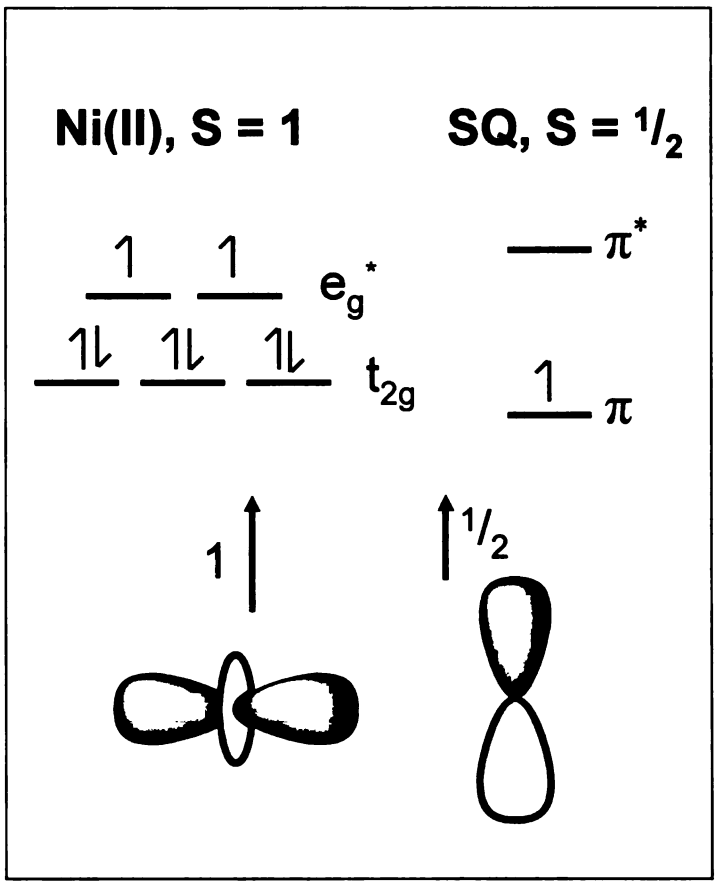

Figure 4-5: Ferromagnetic exchange arises from complete orthogonality of constituent spin orbitals. The highest total spin state is stabilized according to Hund's rule.

Before moving on one last point of interest must be made. In transition metal-semiquinone systems there is often confusion as to the oxidation states of the constitutents of the system due the redox active nature of both transition metals and quinoid ligands. An example (albeit somewhat unrealistic) that pertains to the systems of interest in this chapter is the theoretical resonance formulations of the chromium-semiquinone system to yield other redox states, Figure 4-6. Two of

these states would have no spin exchange interaction, as the ligands would be diamagnetic in nature. Fortunately, due to the relative redox inertness of the chromium(III) ion, this issue does not cause a concern for these studies. In fact, as discussed below, there are characteristic spectrographic and structural signatures that can be employed to very quickly determine whether the ortho-quinone ligand is in its fully reduced catechol form or radical semiquinone form.

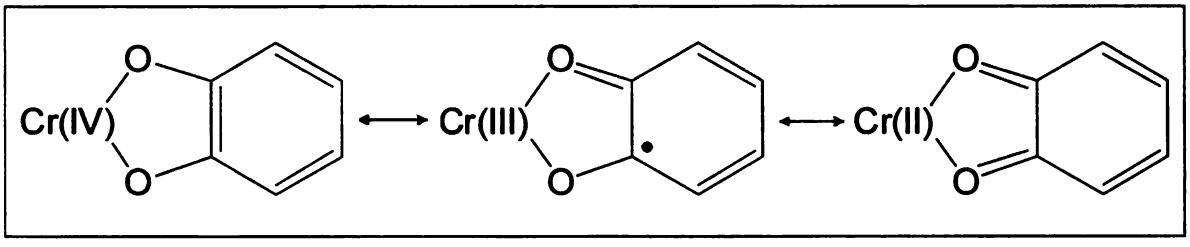

Figure 4-6: Possible redox formulations of the chromium(III)-semiquinone exchange-coupled species. Of these, the only realistic formulation is that of the chromium(III) species due to the relatively redox inert nature of this ion.

4.4 Results and Discussion

4.4.1 Previous Results: [Cr(tren)(3,6DTBCat)](PF_6) and [Cr(tren)(3,6DTBSQ)](PF_6)$_2$. As noted in the introduction to this chapter, the impetus for the research presented in this chapter arose from an ultrafast transient absorption study of [Cr(tren)(3,6DTBCat)](PF_6) and its semiquinone analog, [Cr(tren)(3,6DTBSQ)](PF_6)$_2$. This section will present information on these systems which will prove relevant to the interpretation of similar systems presented throughout this study. The UV-vis spectrum of

[Cr(tren)(3,6DTBCat)](PF_6) has been reported previously, and is reproduced in Figure 4-7(a).[18]

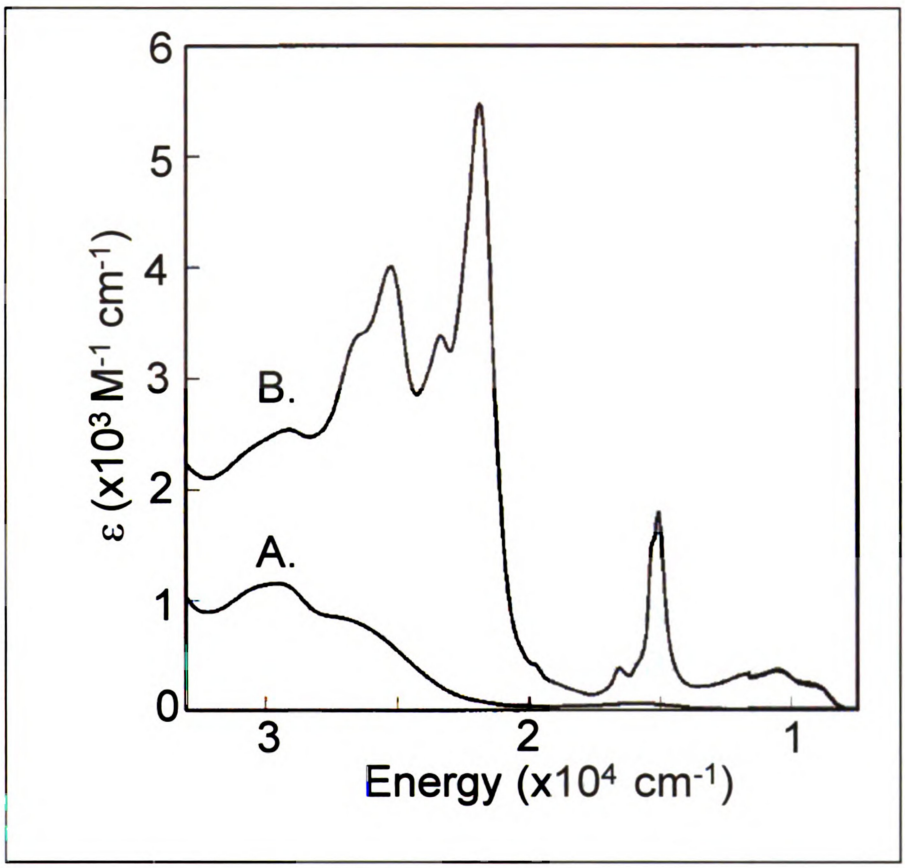

Figure 4-7: UV-vis absorption spectra of [Cr(tren)(3,6DTBCat)](PF_6) (a) and its semiquinone analog, [Cr(tren)(3,6DTBSQ)](PF_6)$_2$ (b), adapted from reference 19.

The spectrum is similar to that of $Cr(acac)_3$, which exhibits a single broad, weak absorption (epsilon ~60 M^{-1} cm^{-1}) corresponding to the spin allowed $^4A_2 \rightarrow {}^4T_2$ ligand field transition, a medium intensity transition (~ 400 nm), and higher energy absorptions of much greater oscillator strength corresponding to charge transfer and ligand-based transitions. In this system, however, the term symbols

are different due to the lowered symmetry of the system: the first spin-allowed excited ligand field state in octahedral symmetry, $^4T_2$, correlates to the states $^4B_1$, $^4A_2$, and $^4B_1$, while the ground state has the term symbol $^4B_2$. The effects of lowered symmetry are shown in Figure 4-8.

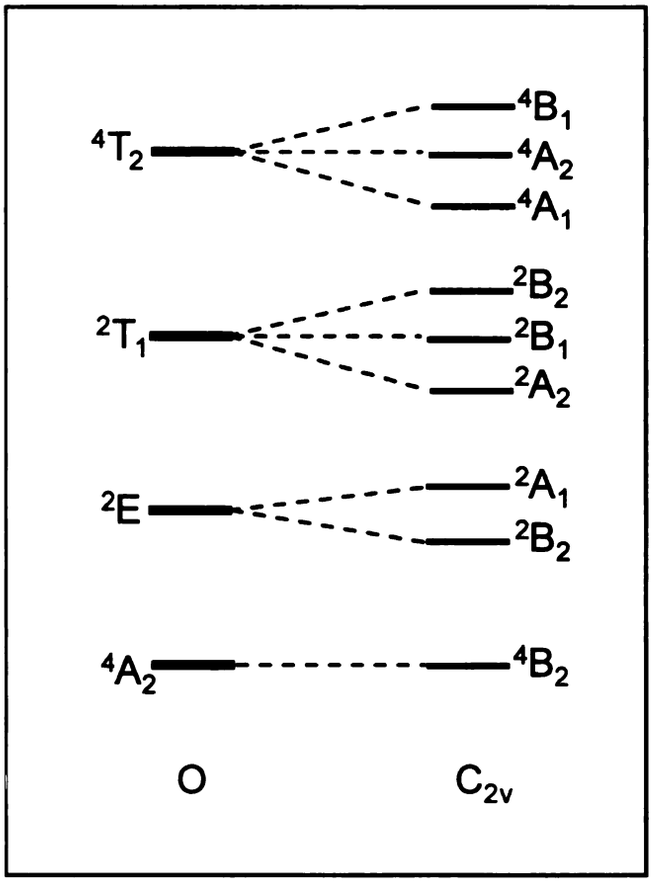

Figure 4-8: Energy-level diagram of a chromium(III) system under C_{2v} symmetry, showing the three lowest-lying ligand field excited states.

It should be kept in mind that the ^2E and $^2T_1$ states, which are usually referred to collectively as the ^2E, are separated by only a few hundred wavenumbers. Therefore, the low-symmetry splittings of these states represents a high density of

doublet excited states. The fact that the width of the ligand field absorption in this system is not markedly different from that of $Cr(acac)_3$ indicates that the splitting of this transition due to lowered symmetry is not that significant. Assignments in the ultraviolet region of the spectrum were assigned as ligand-centered transitions due to lack of Cr^{III}/Cr^{II} and Cr^{III}/Cr^{IV} redox couples and lack of solvatochromatic behavior ruling out charge-transfer transitions.

While the absorption spectrum of the chromium(III)-catechol complex displays many features similar to the corresponding spectrum for $Cr(acac)_3$, the spectrum of the chromium(III)-semiquinone complex is markedly different: extinction coefficients are much greater across the entire visible and near-infrared spectrum, the transitions are, in general, much narrower and structured, and of most interest is an extremely sharp transition that occurs near 15000 cm^{-1}, in the energetic range of the lowest-lying ligand field transitions. While an increase in 10Dq, and thus the energy of states derived from the $^4T_2$ state, is expected due to the weaker π-donating ability of the semiquinone ligand another effect is deemed to be much more important. To begin to understand the differences between these spectra, an appreciation and understanding of the requirements to obtain exchange coupling is necessitated. These requirements, which were outlined above, can be reiterated in one sentence-fragment: each moiety must have unpaired spins and there must be an energetic and spatial matching of the orbitals involved. While this formalism is usually thought of only in terms of the ground state, the

phenomenon is not limited to acting only on ground states as long as the requirements listed above are met. This, therefore, allows for the drastic changes observed in the absorption spectrum, as new spin-allowed transitions arise due to the spin exchange interaction. The visible part of the spectrum can be understood in terms of exchange coupling operating to split the ligand field states under C_{2v} symmetry, as shown in the energy level diagram below (Figure 4-9).[16] It is important to note that coupling is expected to be weaker in states with chromium e_g^* occupation due to lowered overlap of the magnetic orbitals of these states with those of the π-based semiquinone magnetic orbitals.

Experimental proof of this mechanism can be found in single-crystal polarized absorption studies of spin-exchange complexes of chromium(III).[2,3,33,34] In general, as noted by McCarthy and Güdel,[34] spin allowed transitions appear to be less perturbed by spin-exchange interactions than spin-forbidden transitions. One can easily imagine the transition derived from the $^4A_2 \rightarrow {}^4T_2$ transition to persist under the features of the Cr-SQ absorption spectrum near 15000 cm^{-1}. As has been shown in other spin-exchange complexes of chromium(III), introduction of spin exchange can essentially break spin restrictions as the spin-exchange interaction produces both ground and excited states of new spin. In several cases, transitions to ^2E and $^2T_1$-derived states have been observed, which usually present as sharp absorptions due to the intraconfigurational nature of the transition. This

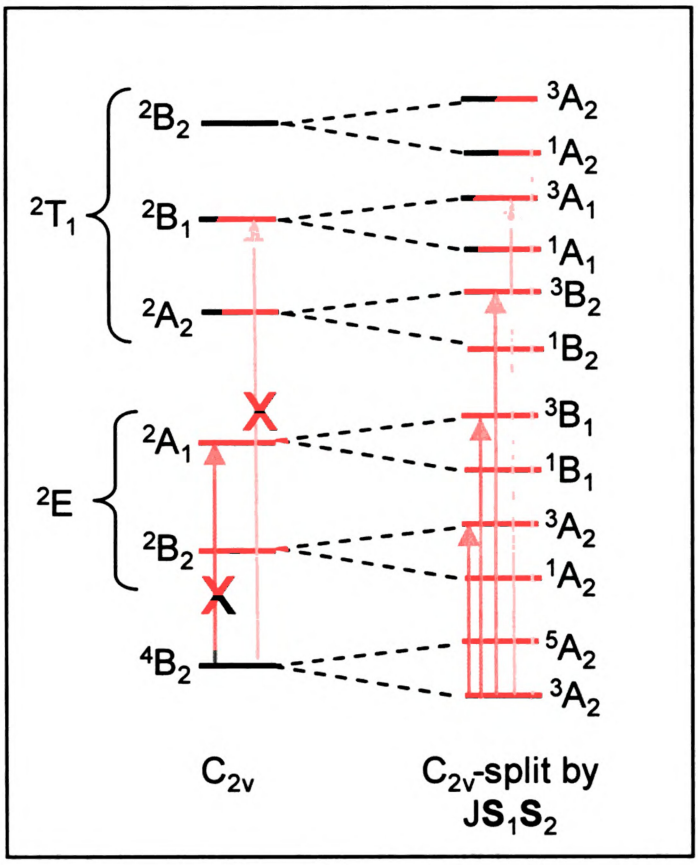

Figure 4-9: Splittings of the C_{2v} electronic components as a result of anti-ferromagnetic coupling between the chromium ligand field states (left side) and the semiquinone π magnetic orbital. The diagram reveals that many spin-allowed transitions are possible as a result of the spin-exchange interaction, whereas energetically similar transitions in non-exchanged system are forbidden.

appears to be the case in this complex as well. In this system, the π-donating ability of the quinoid ligand serves to raise the energy of the t_{2g} orbital set, lowering the energy of the $^4T_2$-derived states (of $(t_{2g})^2(e_g^*)^1$ parentage) and raising the energy of the ^2E- and $^2T_1$-based states (of $(t_{2g})^3$ origin) relative to

acetylacetonate. The narrow breadth of the transition, as well as the π-donating ability of the ligand, point to the fact that these transitions are to states derived from ^2E. The observation of these new features provides insight into the energy of the ^2E state in the catechol complex, which is non-emissive. Given that the low-energy semiquinone absorption features are due to states derived from the ^2E term, then according to Figure 4-8 the nominal $^4T_2$ state (or some component thereof) of the catechol complex is lying below the ^2E state.[35] This is in agreement with the lack of emission from the catechol complex: a lowest-energy quartet excited state would provide excellent coupling to the ground state and thus facilitate rapid nonradiative ground state recovery.

While this previously made assignment conforms with the non-emissive character of this complex, the assignments of excited state energy and splittings for both the catechol and semiquinone complexes remains uncertain without polarized single crystal absorption spectra to quantify the state splittings. For chromium systems this technique has been applied to many different systems, including crystals of chromium(III) oxide[36] and chloride[37-39] materials (which have been studied as potential laser media, but mainly to explore fundamental aspects of electronic structure), as well as many spin-exchange chromium(III) dimers[34] (*vide infra*). One recent example is that of trans-$[Cr(H_2O)_4Cl_2]$, studied by Reber and coworkers.[40] Using low-temperature polarized absorption and

luminescence spectroscopy the authors were able to quantify the splitting due to lowered symmetry of states arising from the $^4T_2$ state.

Preliminary ultrafast transient absorption studies on [Cr(tren)(3,6DTBCat)](PF_6) and [Cr(tren)(3,6DTBSQ)](PF_6)$_2$ have been carried out.[35] This study compared the nonradiative dynamics of these complexes to a low-symmetry redox innocent analog, [Cr(tren)(acac)](PF_6)$_2$. Results for [Cr(tren)(3,6DTBCat)](PF_6) and [Cr(tren)(3,6DTBSQ)](PF_6)$_2$ after excitation at 333 nm are presented in Figure 4-10. In both cases the single-wavelength kinetic traces were fit with a monoexponential decay function, revealing a lifetime of ~ 1.5 ps for the catechol complex and ~ 6 ps for the semiquinone analog. Both traces decay back to the baseline (no long time y-offset), implying ground state recovery that is complete within 10 ps for the catechol and within 25 ps for the semiquinone. The dynamics of the catechol complex mesh well with the general picture outlined above, namely that of a $^4T_2$-derived electronic state lying lowest in energy and providing a facile mechanism for ground state recovery. The comparable dynamics of the semiquinone complex suggest a similar mechanism of ultrafast ground state recovery, although, as discussed above, the electronic structure is greatly affected by the presence of spin exchange. The major goals of this research project are 1) elucidation of electronic structure in these complexes and 2) correlation of this structure to excited state dynamics. This work led us to develop the [Cr(tren)(3,6-R-Q)]$^{+1/+2}$ series in the hopes of elucidating the excited

electronic structure, and thereafter ascertaining mechanisms of nonradiative decay in these complexes.

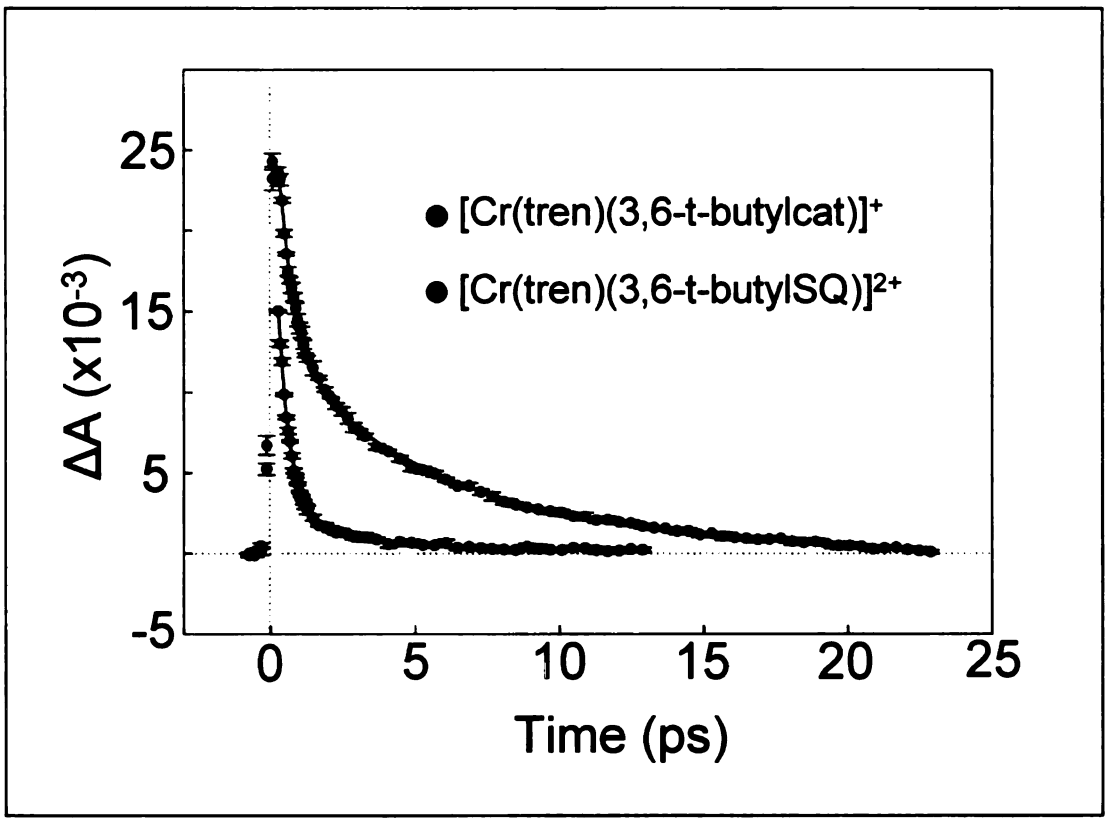

Figure 4-10: Ultrafast transient absorption dynamics of [Cr(tren)(3,6DTBCat)](PF_6) and [Cr(tren)(3,6DTBSQ)](PF_6)$_2$ in acetonitrile solution after excitation at 333 nm.

4.4.2 [Cr(tren)(3,6-R-Q)]$^{+1/+2}$ series

Synthesis. Only the chromium-catechol members of this series have been synthesized to date. For all four catechol members of this series the complexes were prepared using the same general procedure, namely refluxing a solution of the sodium catecholate complex with [Cr(tren)Cl_2]Cl in a methanol/water solution

under inert conditions. This was quite fortuitous given the electronic differences across the series, and likely speaks to this method being a general preparation for this class of molecules. Furthermore, high-quality crystals of all of these complexes (with BPh_4 as the counter-anion) can be grown from a methanolic solution of the complex and $NaBPh_4$. Unfortunately, only crystallographic data of $[Cr(tren)(pycat)]^+$ and $[Cr(tren)(3,6\text{-}CNcat)]^+$ were available for this dissertation. Also remarkable was the general stability of these complexes to oxidation under ambient conditions, with the exception of the 3,6-amino-1,2-catechol complex, which is discussed further below as the electrochemistry of these complexes is explored.

[Cr(tren)(pyrocatecholate)]BPh_4. This complex forms blue/green powders and sky blue crystals. The crystal structure of this complex is presented in Figure 4-11, which also shows some selected bond lengths and angles for this complex. Full crystallographic data is presented in Appendix C. Starting with the metal coordination bonds, the Cr-O bond lengths of approximately 1.92 Å are within the range of values reported for other chromium complexes (such as the high-symmetry $Cr(acac)_3$-type complexes of Chapter 3, with typical bond lengths of 1.95 Å) while the Cr-N are also fairly typical of chromium-am(m)ine complexes with bond lengths of ~ 2.10 Å.[41] The bond lengths of the catechol complex correspond to the double bond delocalized π structure of the ligand, with all values

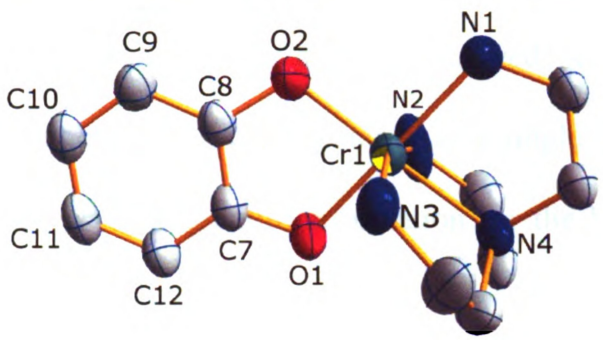

M-L Bonds (Å)	Cr1-O1	1.9244
	Cr1-O2	1.9226
	Cr1-N1	2.093
	Cr1-N2	2.124
	Cr1-N3	2.071
	Cr1-N4	2.077
M-L Angles (°)	O1-Cr1-N1	179.28
	O2-Cr1-N4	176.46
	N2-Cr1-N3	160.90
	O1-Cr1-O2	85.21
	O1-Cr1-N3	87.31
	O1-Cr1-N2	85.77
Ligand Bonds (Å)	O2-C8	1.364
	O1-C7	1.352
	C7-C8	1.400
	C8-C9	1.379
	C7-C12	1.389
	C9-C10	1.396
	C11-C12	1.394
	C10-C11	1.375

Figure 4-11: Crystal structure and selected bond lengths and angles for [Cr(tren)(pycat)]BPh_4.

for bond lengths around 1.4 Å. This is in contrast to the alternating bond lengths of a semiquinone species, representing a more localized picture of the double bonds, with values of either 1.45 Å, corresponding to a single bond, or 1.35 Å for a double bond.[18] This crystallographic information for the ligand confirms the catechol oxidation state.

The ligand oxidation state is further confirmed by the UV-vis absorption spectrum. As described above, the presence of spin exchange affects not only the ground state electronic structure but also the excited state electronic structure, leading to observation of previously spin-forbidden transitions. A quick glance at the absorption spectrum of Figure 4-12 reveals that the spectrum has none of the features associated with a chromium(III)-semiquinone complex, discussed above for the case of $[Cr(tren)(3,6\text{-}DTBSQ)]^{2+}$.

In the ultraviolet one observes a peak near 290 nm (ε ~2650 M^{-1} cm^{-1}) and a more clearly defined absorption peak centered at 340 nm (ε =1650 M^{-1} cm^{-1}). On the red shoulder of this transition is another peak. Finally, a broad, weak featureless transition is centered at 612 (ε = 71 M^{-1} cm^{-1}). Given the trends observed for the high-symmetry systems of Chapter 3, is speculated that the feature at 340 nm is a charge-transfer transition while the peak at 290 nm is an intraligand transition. The low-intensity absorption at 612 nm is clearly a transition into the lowest-energy $^4T_2$ state (O notation), which in this complex of C_{2v} symmetry is split into three singly-degenerate term states ($^4B_1$, $^4A_2$ and $^4A_1$).

This splitting is not observed in the room-temperature absorption spectrum of Figure 4-12.

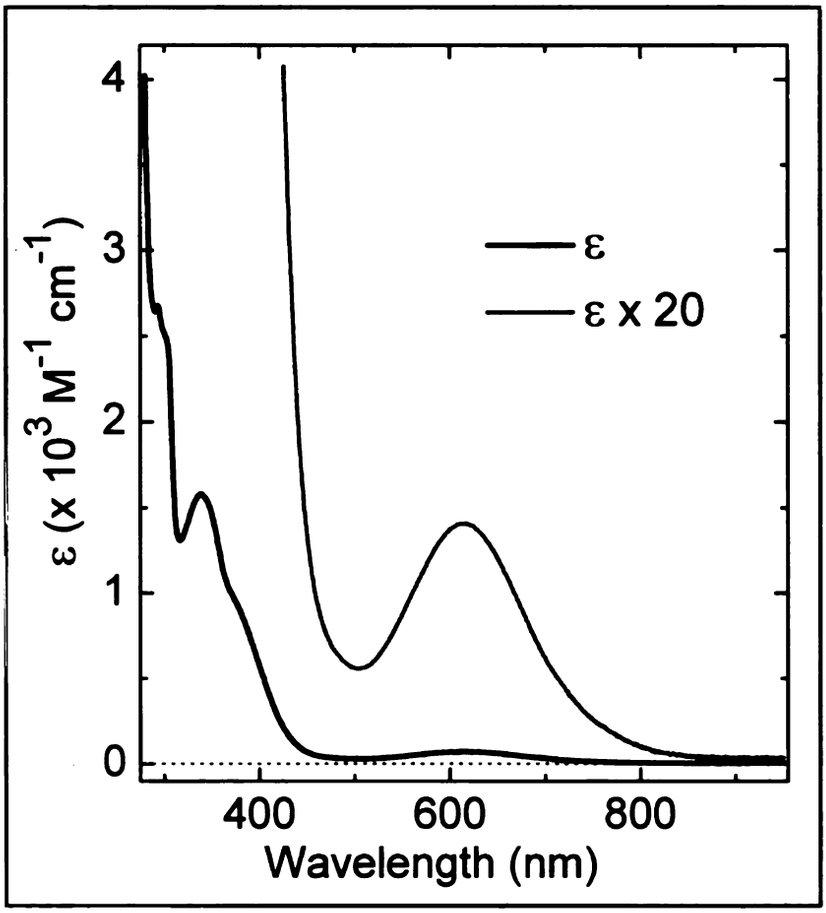

Figure 4-12: UV-vis absorption spectrum of [Cr(tren)(pyrocatecholate)]BPh_4 in acetonitrile.

A cyclic voltammogram of this complex is shown in Figure 4-13. The figure reveals a reversible process with $E_{1/2}$ = + 323 mV (vs Ag/AgCl) and a peak separation (ΔE_p) of 62 mV. This value corresponds to the one-electron catechol to semiquinone oxidation. A second scan to more oxidizing potentials (not shown) reveals a second, irreversible oxidation process at 873 mV, corresponding to

oxidation of the semiquinone complex to the quinone complex. It has been shown that the neutral quinone ligand has very little binding affinity for the chromium(III) metal center, and therefore this oxidation results in decomposition of the metal complex, reflected by the irreversible nature of the oxidation. These oxidative steps are shown in equations 4.3 and 4.4, and were described previously for [Cr(tren)(3,6-DTBSQ)](PF$_6$).[18]

$$[Cr(tren)(pySQ)] \underset{-e^-}{\overset{+e^-}{\rightleftarrows}} [Cr(tren)(pycat)] \qquad E_{1/2} = +0.323\,V \qquad (4.3)$$

$$[Cr(tren)(pySQ)] \overset{-e^-}{\rightarrow} [Cr(tren)(pyQ)] \qquad E_{ox} = +0.873\,V \qquad (4.4)$$

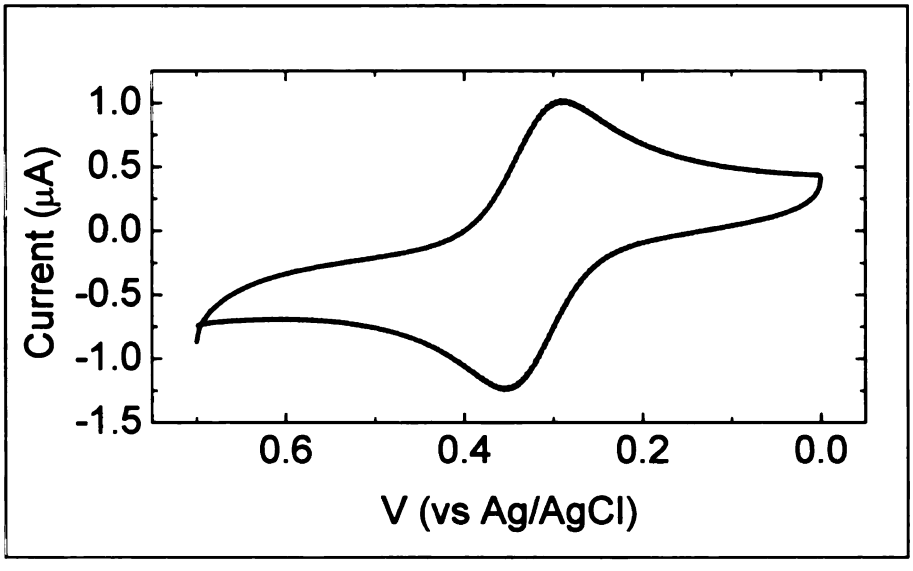

Figure 4-13: Cyclic voltammogram of [Cr(tren)(pyrocatecholate)]BPh$_4$ in acetonitrile. The values are references of Ag/AgCl.

[Cr(tren)(3,6-CN-1,2-catecholate)]BPh_4. This complex is brown both as powders and crystals. The crystal structure and selected bon lengths and angles are shown in Figure 4-14. In many respects metal-ligand bond lengths and angles are similar to those observed for $[Cr(tren)(pycat)]^+$ and will not be elaborated on here. Unlike the pyrocatecholate complex, the C-C bond lengths of the ligand do have alternating character, but not to the extent observed for a semiquinone system. These bond lengths are consistent with the delocalized π-bonding of a catechol complex, with deviations perhaps arising from the electron-withdrawing capability of the neighboring substitutents, which weaken the bonds via introduction of δ+ charges, as discussed in the literature.[42]

The lack of sharp features to the red of 650 nm in the UV-vis absorption spectrum of this complex confirms that a semiquinone species was not formed. These features arise in chromium(III) complexes due to the presence of spin exchange. In the UV one observes an intense transition with two sharp peaks near 365 nm ($\varepsilon \sim 8530\ M^{-1}\ cm^{-1}$). The two sharp peaks are separated by about 1200 cm^{-1}, the frequency of a C=C stretch. This feature is tentatively assigned as a charge transfer feature given the intensity and observation of energetically similar transitions in other chromium complexes explored throughout this dissertation. On the low-energy shoulder of this feature, near 450 nm, are two peaks of relatively low-intensity ($\varepsilon \sim 200\ M^{-1}\ cm^{-1}$), while further into the visible is a broad transition centered at 567 nm ($\varepsilon \sim 93\ M^{-1}\ cm^{-1}$).

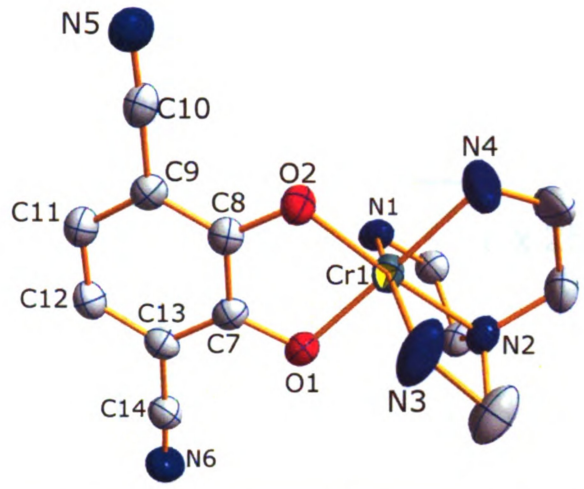

M-L Bonds (Å)	Cr1-O1	1.9568
	Cr1-O2	1.9176
	Cr1-N1	2.083
	Cr1-N2	2.0942
	Cr1-N3	2.087
	Cr1-N4	2.060
M-L Angles (°)	O1-Cr1-N4	178.14
	O2-Cr1-N2	176.19
	N1-Cr1-N3	163.22
	O1-Cr1-O2	84.73
	O1-Cr1-N1	87.02
	O1-Cr1-N3	88.22
Ligand Bonds (Å)	O2-C8	1.325
	O1-C7	1.336
	C7-C8	1.424
	C8-C9	1.395
	C7-C13	1.397
	C9-C11	1.411
	C12-C13	1.423
	C11-C12	1.363

Figure 4-14: Crystal structure and selected bond lengths and angles for [Cr(tren)(3,6-CN-1,2-catecholate)]BPh_4.

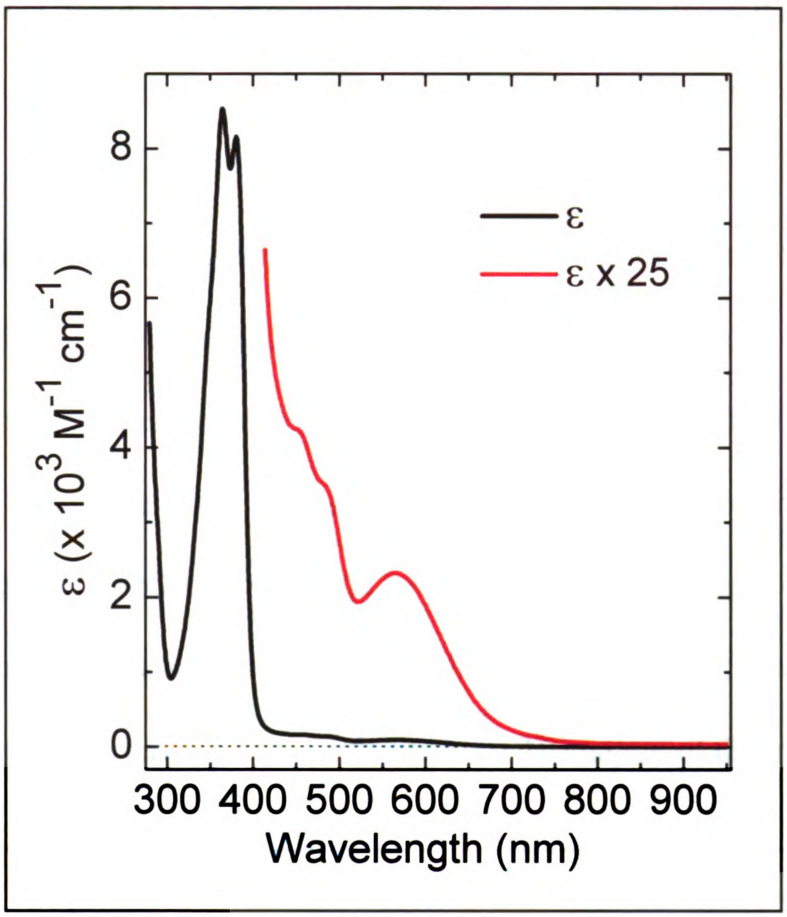

Figure 4-15: UV-vis absorption spectrum of [Cr(tren)(3,6-CN-1,2-orthocatecholate)]BPh_4 in acetonitrile.

The peaks near 450 nm are likely $^4T_1$-based ligand field states; the spacing of about 1500 cm^{-1} could be tied to effects of lowered symmetry, but it is more likely given the energetic proximity to the nominally charge-transfer transition that this splitting is in fact vibronic structure as a result of mixing of ligand- and metal-based orbitals. The broad feature at 567 nm is clearly due to a transition into $^4T_2$-based ligand field states. The splitting due to lowered symmetry is not observed,

but the expected trend of a blue-shift of this peak, a result of the stronger π accepting ability (increasing 10Dq) relative to the unsubstituted catechol, is observed.

The cyclic voltammogram of [Cr(tren)(3,6-CN-1,2-orthocatecholate)]BPh_4 in acetonitrile is presented in Figure 4-16. An irreversible oxidation is observed at + 0.620 V, in close proximity to a reversible wave with $E_{1/2}$ = + 0.703 V and ΔE_p = 59 mV. This reversible process is easily assigned as originating from catechol/semiquinone redox couple. The potential is shifted by approximately 380 mV relative the unsubstituted catechol complex, $[Cr(tren)(pycat)]^+$ as a result of strongly electron-withdrawing cyano substituents. The nature of the irreversible

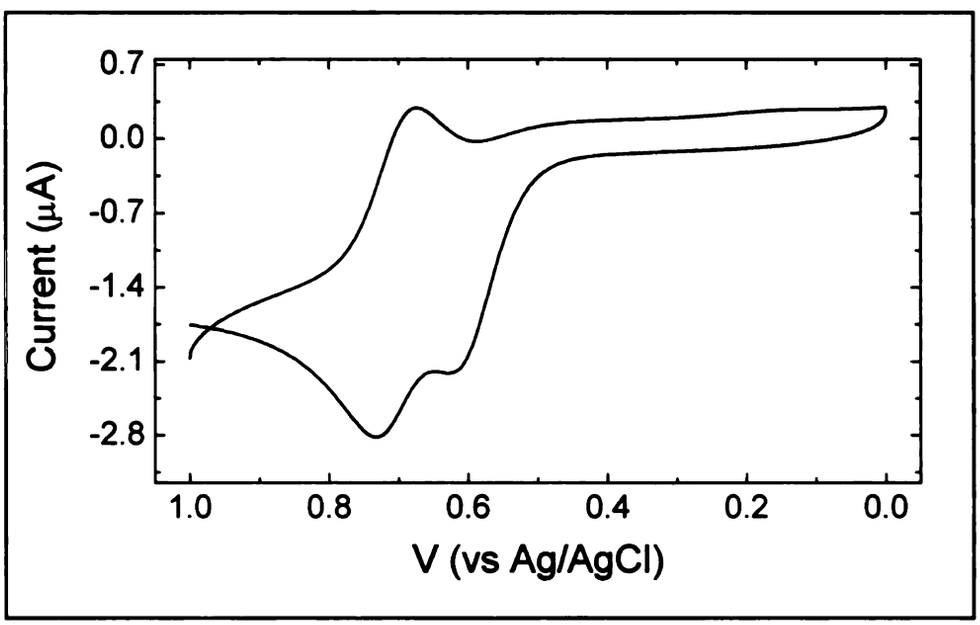

Figure 4-16: Cyclic voltammogram of [Cr(tren)(3,6-CN-1,2-orthocatecholate)]BPh_4 in acetonitrile. Potentials are referenced versus Ag/AgCl.

process observed at + 0.620 V is not apparent, but a similar peak observed for [Cr(tren)(3,6-dinitro-1,2-orthocatecholate)]BPh_4 (see below) suggests a common impurity in both samples. A very irreversible oxidation process is observed at + 1.73 V, corresponding to the semiquinone/quinone redox couple, which results in decomposition of the complex due to the low binding affinity of the fully oxidized quinone ligand.

$$[Cr(tren)(3,6-CNSQ)] \underset{-e^-}{\overset{+e^-}{\rightleftarrows}} [Cr(tren)(3,6-CNCat)] \qquad E_{1/2} = +703\,mV \qquad (4.5)$$

$$[Cr(tren)(3,6-CNSQ)] \overset{-e^-}{\rightarrow} [Cr(tren)(3,6-CNQ)] \qquad E_{ox} = +1.72V \qquad (4.6)$$

[Cr(tren)(3,6-dinitro-1,2-orthocatecholate)]BPh_4. The UV-vis absorption spectrum of this complex is presented in Figure 4-17. In general, two high-intensity absorption features are observed with maximum absorption at 340 nm (ε = 7610 M^{-1} cm^{-1}) and 450 nm (4600 M^{-1} cm^{-1}). To the blue of the 340 nm feature are a series of sharper peaks—these features do not show a constant spacing, and therefore likely do not represent a vibronic progression. These peaks are tentatively assigned as arising from intraligand transitions of the catechol ligand. An absorption spectrum of the sodium salt of the catechol ligand reveals similar features to those observed at 340 nm and 450 nm, and therefore the assignment of these absorptions as due to intraligand transitions is made. However, there are undoubtedly charge transfer transitions in this energetic range as a result of the

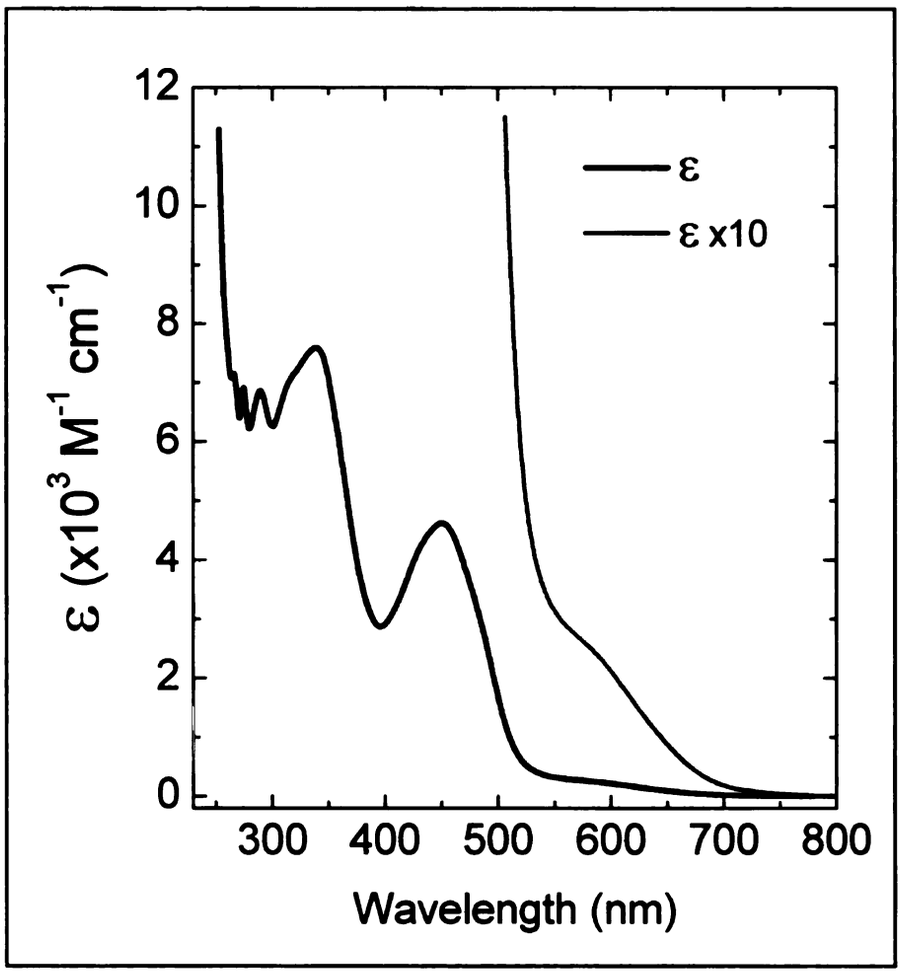

Figure 4-17: UV-vis absorption spectrum of [Cr(tren)(3,6-dinitro-1,2-orthocatecholate)]BPh_4 in acetonitrile.

extended π structure and π-accepting ability of the dinitrocatechol ligand. A comparison of the absorption spectrum with a gallium(III) analog would perhaps provide a means of parsing out charge transfer and intraligand transitions.An absorption of much weaker intensity, centered near 560 nm (290 M^{-1} cm^{-1}), resides on the low energy onset of the more intense absorption features. This absorption represents a transition to $^4T_2$-derived ligand field states, and the large intensity

(compared to the ~ 60 M^{-1} cm^{-1} observed for $Cr(acac)_3$) is likely a result of significant mixing with charge transfer and intraligand transitions of similar energy, i.e. intensity stealing from these states. The energy of the transition is similar to that observed for the 3,6-CN-1,2-catecholate derivative, reflecting a high degree of π accepting ability for both ligands.

The cyclic voltammogram of [Cr(tren)(3,6-dinitro-1,2-orthocatecholate)]BPh_4 in acetonitrile is presented in Figure 4-18. An irreversible oxidation is observed at + 0.636 V, in close proximity to a reversible wave with $E_{1/2}$ = + 0.807 V and ΔE_p = 59 mV. This reversible oxidation is easily assigned as the typical catechol to semiquinone oxidation. In this case, the potential is shifted by approximately 480 mV relative the unsubstituted catechol complex, $[Cr(tren)(pycat)]^+$, as a result of strongly electron-withdrawing nitro substituents. It remains unclear what physical process is occurring for the irreversible oxidation at + 0.636 V, although it is similar to the irreversible process observed for $[Cr(tren)(3,6\text{-}CNcat)]^+$ (at + 0.620 mV vs Ag/AgCl), suggesting a common impurity between both samples. A second irreversible oxidation is seen at 1.717 V, corresponding to the semiquinone to quinone one electron oxidation. This value represents an 840 mV shift relative to the same value for $[Cr(tren)(pycat)]^+$, again as a result of the electron withdrawing nature of the nitro substituents. These two one-electron processes are summarized in equations 4.8 and 4.9.

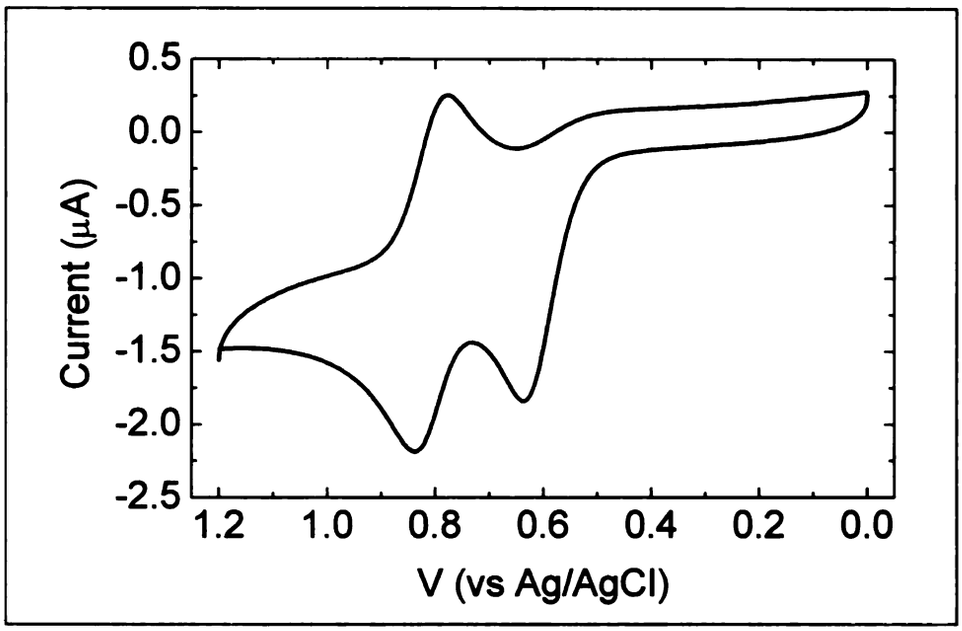

Figure 4-18: Cyclic voltammogram of [Cr(tren)(3,6-NO_2-1,2-orthocatecholate)]BPh_4 in acetonitrile. Potentials are referenced versus Ag/AgCl.

$$[Cr(tren)(3,6-NO_2SQ)] \underset{-e^-}{\overset{+e^-}{\rightleftarrows}} [Cr(tren)(3,6-NO_2Cat)] \qquad E_{1/2} = +0.807\,V \qquad (4.8)$$

$$[Cr(tren)(3,6-NO_2SQ)] \overset{-e^-}{\rightarrow} [Cr(tren)(3,6-NO_2Q)] \qquad E_{ox} = +1.717\,V \qquad (4.9)$$

[Cr(tren)(3,6-diamino-1,2-orthocatecholate)]BPh_4. This complex was prepared as a dark purple powder. The absorption spectrum, Figure 4-19, represents a dramatic shift from those of the other members of this series. High intensity (> 10^3 M^{-1} cm^{-1}) absorptions are observed across the entire ultraviolet, visible, and out to nearly 850 nm. As a result, a solution of this complex has a much more intense color than that of other members of this series. In acetonitrile there are three main, broad features centered at 29790 cm^{-1} (335 nm, $\varepsilon \sim 2500$ M^{-1} cm^{-1}),

19305 cm^{-1} (518 nm, $\varepsilon \sim 1240\ M^{-1}\ cm^{-1}$) and 13200 cm^{-1} (758nm, $\varepsilon \sim 850\ M^{-1}\ cm^{-1}$). Given that the sodium salt of the diaminocatechol ligand is colorless, showing only absorptions in the ultraviolet, the higher energy transitions at 335 nm and 518 nm are generally assigned as charge transfer in nature, although preparation of a d^{10} analog complex would provide the best means of distinguishing charge transfer and intraligand transitions. The shift to higher energy of the feature near 750 nm (in acetonitrile) to approximately 630 nm (in methanol) may be indicative of this transition originating out of a non-bonding orbital (in this case on the amino group): the higher hydrogen-bonding ability of methanol versus acetonitrile would stabilize these orbitals, increasing the energy of the transition. This transition is therefore assigned as an $n \rightarrow \pi^*$ transition, or perhaps a LMCT originating out of the amino nonbonding orbitals. In the acetonitrile spectrum one observes a flat region between 12500 – 15000 cm^{-1}. This is generally indicative of multiple Gaussian lineshapes summing together. In fact, Gaussian deconvolution of this region of the spectrum reveals a broad low-intensity (90 – 120 $M^{-1}\ cm^{-1}$) absorption, centered at about 15470 cm^{-1} (646 nm). This feature has the correct intensity and energy, given the π-donating ability of the amino substituents, to correspond to the $^4T_2$ absorption.

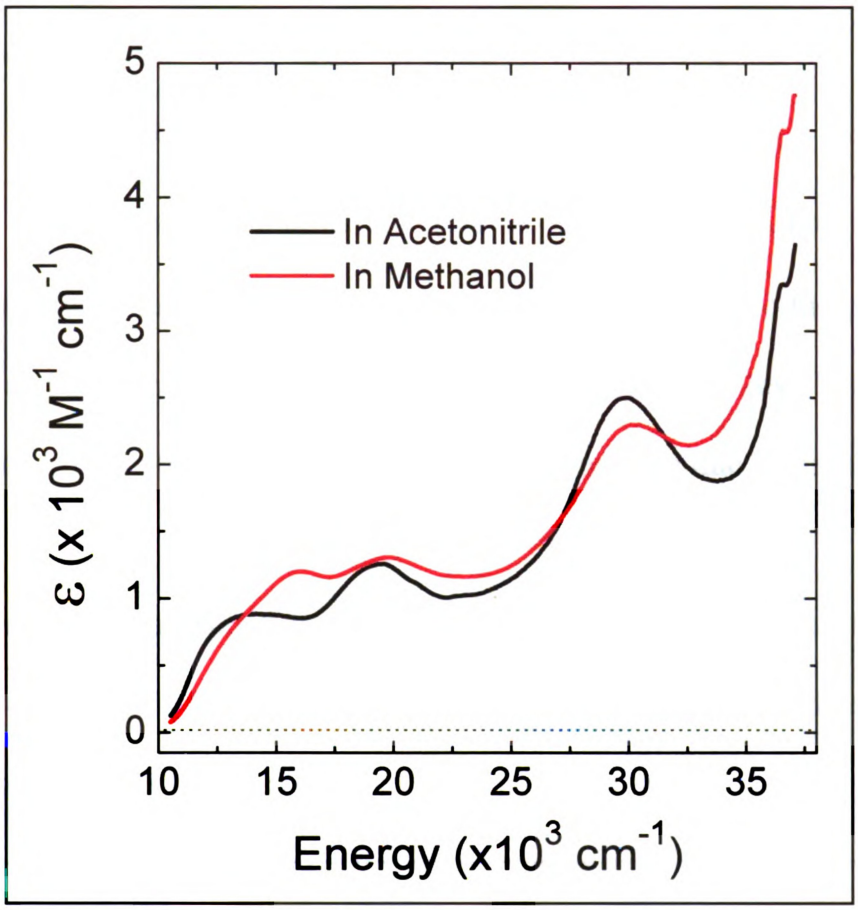

Figure 4-19: UV-vis absorption spectrum of [Cr(tren)(3,6-diamino-1,2-orthocatecholate)]BPh_4 in acetonitrile.

The cyclic voltammogram of this complex in an acetonitrile solution is shown in Figure 4-20. All potentials are versus Ag/AgCl. Not shown is a highly irreversible oxidation process at 0.764 V, corresponding to the semiquinone → quinone oxidation. This value is approximately 1 V less than that of the nitro- and cyano-substituted catechol complexes, and about 100 mV less than the pyrocatechol complex. Given the π-donating ability of the amino substituents the

value of 764 mV reflects the expected trend. In the region of the reversible catechol/semiquinone redox pair (Figure 4-20), one observes irreversible processes at 219 mV and -449 mV. A reversible wave with $E_{1/2}$ = - 457 mV and ΔE_p = 95 mV is observed and assigned as the catechol/semiquinone redox pair. This value represents an approximately 800 mV shift relative to the pyrocatechol complex, and accounts for the air sensitive nature of this complex. No assignment is made for irreversible processes, although these may be due to impurities in the sample.

Given the data presented above, as well as the potential for multiple binding modes of this ligand, it is suggested that future efforts be directed toward other π-donating substituents (methoxy or dimethylamino).

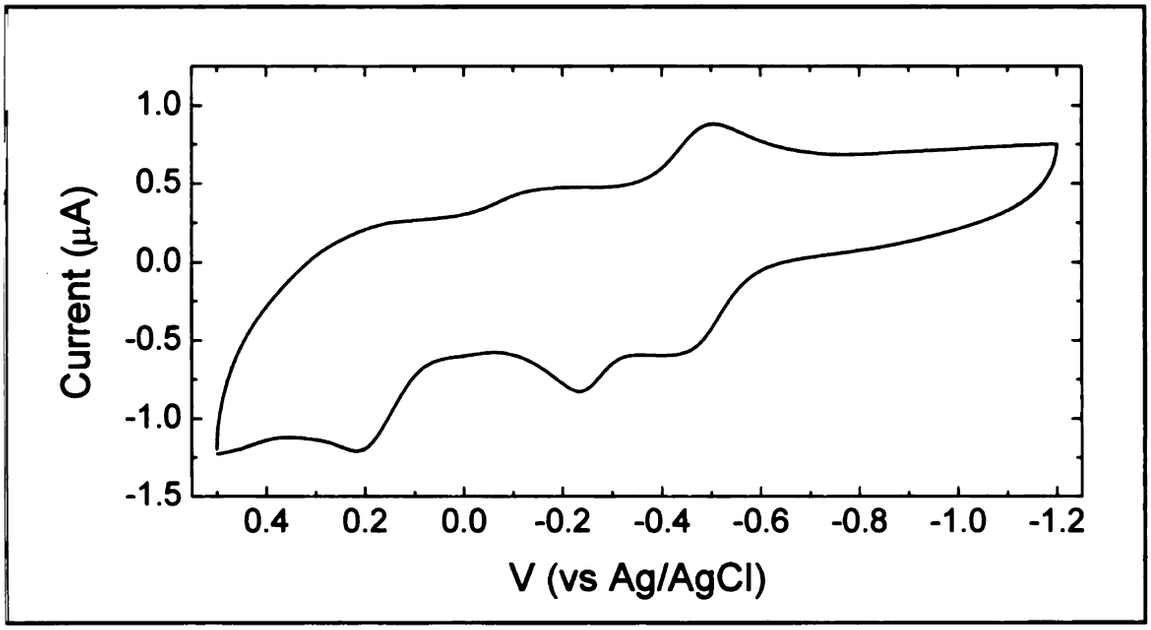

Figure 4-20: Cyclic voltammogram of [Cr(tren)(3,6-NH_2-1,2-orthocatecholate)]BPh_4 in acetonitrile. Potentials are referenced versus Ag/AgCl.

$$[Cr(tren)(3,6-NH_2SQ)] \underset{-e^-}{\overset{+e^-}{\rightleftarrows}} [Cr(tren)(3,6-NH_2Cat)] \quad E_{1/2} = -457\ mV \qquad (4.10)$$

$$[Cr(tren)(3,6-NH_2SQ)] \xrightarrow{-e^-} [Cr(tren)(3,6-NH_2Q)] \quad E_{ox} = +764\ mV \qquad (4.11)$$

4.4.3 Spin Exchange Members of the $[M_1M_2(tren)_2(CA^{n-})]^{m+}$ Series. $[GaCr(tren)_2(CA^{sq,cat})](BPh_4)_2(BF_4)$ (4). Magnetic susceptibility of **4** from 2 – 350 K indicates a temperature-independent value of $\mu_{eff} = 2.72 \pm 0.05\ \mu_B$ ($\mu_{spin\text{-}only}$ for S = 1 is 2.83 μ_B) , characteristic of an S = 1 state.[16] This implies an antiferromagnetic interaction between chromium(III) and the trianionic $CA^{sq,cat}$ bridge and a ΔE between S = 1 and S = 2 states exceeding k_BT at 350 K (~240 cm^{-1}), leading to an essentially isolated triplet ground state, with the quintet state far above it. This corroborates what we[18] and others[1,43] have observed for other Cr^{III}-semiquinone complexes. As expected for **4** the X-band perpendicular- and parallel-mode spectra revealed no features unique to this molecule (Figure 4-21). Instead, the spectra reveal impurities corresponding to other semiquinone species, namely the Cr^{III} dimer **6** and the Ga^{III} dimer **2**. This is in contrast to the ESI-MS data for this complex presented previously,[16] which exhibited a single molecular peak corresponding to complex **4**, with no indication of complexes **2** or **6**, and testifies to the higher sensitivity of EPR as compared to mass spectroscopy techniques. Parallel-mode spectra indicate a transition around g' = 2 (where g' is

the effective g-value and is given by g'= hν/βH, so that for X-Band frequency g' = 2 corresponds to about 3300 G) that is likely a "leaking" of the perpendicular-mode spectrum of the gallium(III) dimer. If this is the case, then zero-field splitting between the $|0\rangle$ and $|\pm 1\rangle$ states within the triplet manifold is large enough that no transitions are observed at X-band frequency, and the signs of the zero-field splitting parameters D and E are unknown. It is also possible that the observed transition in the parallel mode spectrum is due to the $|-1\rangle \rightarrow |+1\rangle$ transition. However, the parallel-mode signal is very weak, and has the same temperature dependence as the main line of the perpendicular mode X-band spectrum of **2**, leading to the conclusion that this observed signal is in fact due to a leaking of the perpendicular mode transition. High-frequency, high-field measurements will be required to address the magnitude of the zero-field splitting in this complex.

This series offers the possibility of fully characterizing the spin Hamiltonian parameters for the chromium(III)-semiquinone system. In this case the spin Hamiltonian parameters can be considered in the strong exchange limit, i.e. where the effect of other operators acts as a perturbation of the isotropic exchange Hamiltonian $J_{12}S_1 \cdot S_2$, the following linear relationships hold for the various spin-exchange levels:

$$g_S = c_1 g_A + c_2 g_B \tag{4.12}$$

$$D_S = d_1 D_A + d_2 D_B + d_{12} D_{AB} \tag{4.13}$$

where g_S and D_S are the g and zero-field splitting tensors, respectively, g_A and g_B are the g-tensors of the individual spin centers, and D_A and D_B are the zero-field splitting tenors of the individual spin centers. D_{AB} is the asymmetric exchange tensor, and arises via the exchange interaction. Bencini and Gatteschi[30] provide the scalar values c_1, c_2, d_1, d_2, and d_{12} for various spin pairs ($d_1 = 0$ in this system because the semiquinone doublet state does not have any zero-field splitting (L = 0), so there is no "D_{SQ}" contribution). The strong exchange limit is a good approximation for **4**, given that the exchange coupling between the chromium(III) center and the semiquinone ligand has been shown to be much greater the k_BT at room temperature, and that other operators in the spin Hamiltonian operate at much smaller scales (less than 1 cm^{-1}). The g and D tensors for the S = 1 and S = 2 states of this system are given by:

$$g_1 = -\frac{1}{4}g_{SQ} + \frac{5}{4}g_{Cr} \tag{4.14}$$

$$D_1 = \frac{3}{2}D_{Cr} - \frac{1}{4}D_{SQ\text{–}Cr} \tag{4.15}$$

$$g_2 = \frac{1}{4}g_{SQ} + \frac{3}{4}g_{Cr} \tag{4.16}$$

$$D_2 = \frac{1}{2}D_{Cr} + \frac{1}{4}D_{SQ\text{–}Cr} \tag{4.17}$$

The tensors $\tilde{g}_{SQ}$, $\tilde{g}_{Cr}$ and $\tilde{D}_{Cr}$ have already been determined in the electron spin resonance studies of chapter 2. $\tilde{D}_{SQ\text{–}Cr}$ is the lone tensor that needs to be determined. Therefore, successful collection and simulation of an EPR spectrum

for this complex allows one to effectively reconstruct the zero field splitting of a spin-exchange complex in a piece-wise fashion, speaking to the utility of the various "control complexes" in this series.

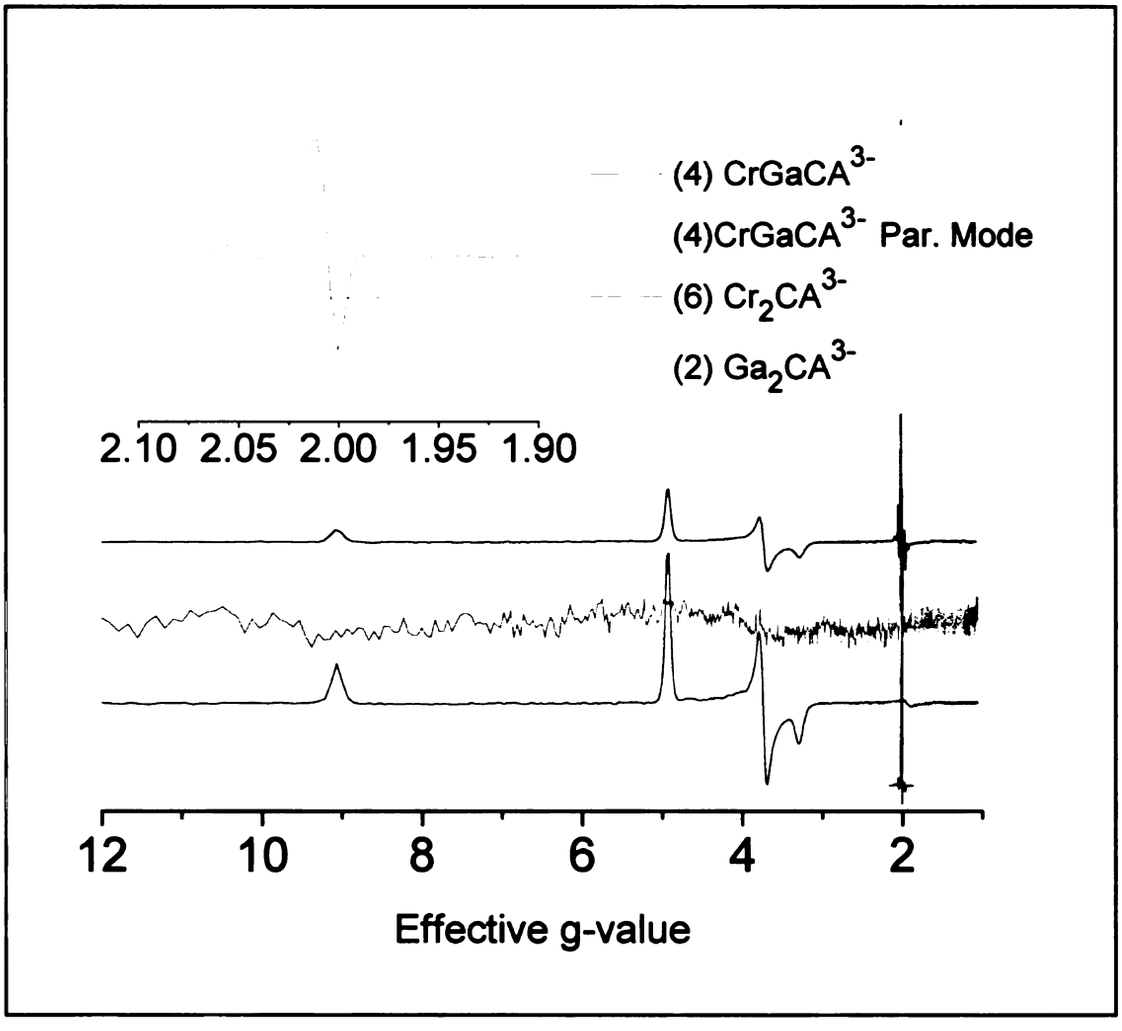

Figure 4-21: Comparison of bimetallic semiquinone complexes, showing that the signals of both the parallel mode and perpendicular mode spectra of complex 4 can be attributed to impurities in the sample. Experimental conditions: Complex 6: 9.4595 GHz, 0.30 mW, 4K; Complex 4 perpendicular mode: 9.6250 GHz, 62.8 mW, 4 K; Complex 4 parallel mode: 9.3941 GHz, 63 mW, 4 K; Complex 6: 9.4595 GHz, 0.63 mW.

$[Cr_2(tren)_2(CA^{cat,cat})](BPh_4)_2$ (5). Exchange coupled dimers of chromium(III) have been explored extensively in the literature.[34] Common motifs include ion-pairs in doped crystals[44-48] and triply bridged μ-hydroxo[2,3,49,50] and halo-bridged[33,51-54] systems consisting of face-shared octahedra. These halo-bridged complexes fall into the well-known family of $A_3Cr_2X_9$ compounds (where A is a singly charged cation and X is the halogen anion). The system presented herein represents one of the few exchange-coupled chromium(III) dimer systems that does not fall into one of the above mentioned categories, other notable complexes being $[Cr_2L_3]^{3+}$ (L = 2,6-bis(aminomethyl)-4-tert-butyl-thiophenolate)[4] and the quinone-bridged $[Cr_2(CTH)(DHBQ)]^{2+}$ complex reported by Dei and coworkers.[55]

$[Cr_2(tren)_2(CA^{cat,cat})](BPh_4)_2$ (**5**) consists of two Cr^{III} nuclei bound by the diamagnetic $CA^{cat,cat}$ bridging ligand. Fitting of the magnetic susceptibility data of **5** indicates an antiferromagnetic interaction on the order of 4 cm^{-1} (for $H = J_{12}S_1 \cdot S_2$), resulting in a singlet ground state and higher-lying states that are populated at low temperatures. The 4 K X-band EPR spectrum of this complex is presented in Figure 4-22. The figure shows that a majority of the peaks in this spectrum can be attributed to the other chromium(III) dimer system of this series, complex **6**, wherein the bridging ligand is in its $CA^{sq,cat}$ form. A number sharp features near $g_{eff} = 2$ can be assigned as arising from **5**, as well as perhaps several broader features at lower fields.

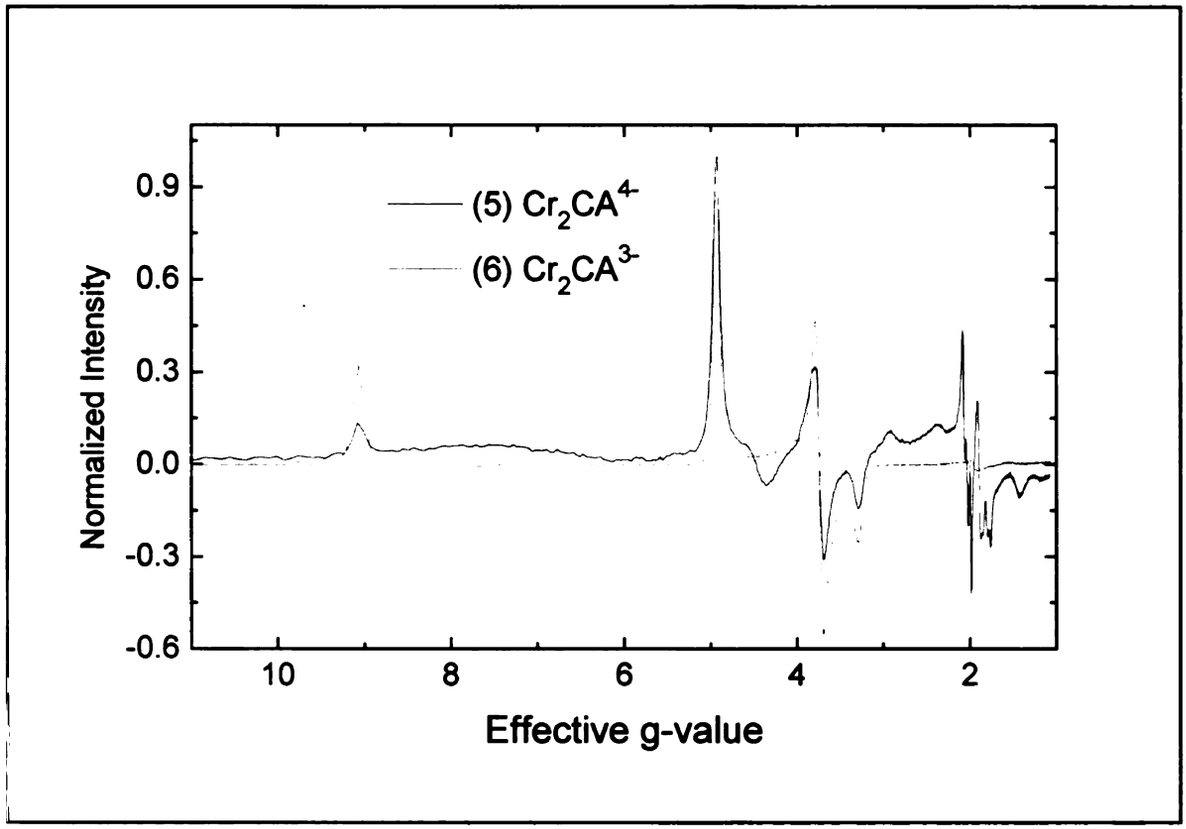

Figure 4-22: X-band perpendicular mode EPR spectrum of **5** at 4 K. This spectrum is plotted against the corresponding X-band spectrum for **6**, revealing that many of the observed features in the spectrum of **5** can be attributed to complex **6** as an impurity.

Applying the Kambe approximation to the Heisenberg coupling Hamiltonian of equation 4.1 and considering only the isotropic component yields eigenvalues of the form given by equation 4.2, where $S_t = 3, 2, 1, 0$ and $S_1 = S_2 = {}^3/_2$. This yields the energy-level diagram in the absence of zero-field splitting effects, i.e. splitting of the m_s sublevels. However, these effects are likely important to the description of the ground state electronic structure because the splitting is expected to be on

the order of the coupling constant due to the integer spin nature of the states. To determine which states contribute to the observed X-band signal, a Boltzmann distribution analysis was carried out by integrating the EPR spectra and monitoring characteristic peaks over the temperature range 4 - 100 K, and comparing the intensities with the anticipated Boltzmann distribution given the calculated energy levels. Thus far the results remain unclear, which is unsurprising given the complicated nature of this spin system.

Exchange-coupled transition metal systems with $|J| < kT$ can be simulated according to the spin Hamiltonian

$$H = \beta_e \vec{B} \cdot \tilde{g} \cdot \vec{S} + \vec{S} \cdot \tilde{D} \cdot \vec{S} + \vec{S}_1 \cdot \tilde{J} \cdot \vec{S}_2 \qquad (4.18)$$

Exchange coupling between the two Cr^{III} centers results in Heisenberg spin manifolds of $S_t = 3, 2, 1, 0$, and each spin manifold can have its own unique g-tensor and zero-field splitting parameters, due to different spin-orbit coupling contributions within each state. Furthermore, in the weakly coupled regime there likely exists extensive mixing between the various spin sublevels. At the moment simulation of the data to obtain this information is not possible, but it is our hope that higher-field (W-band) spectra of this complex will allow for higher resolution and thus easier characterization of each of the Heisenberg spin levels.

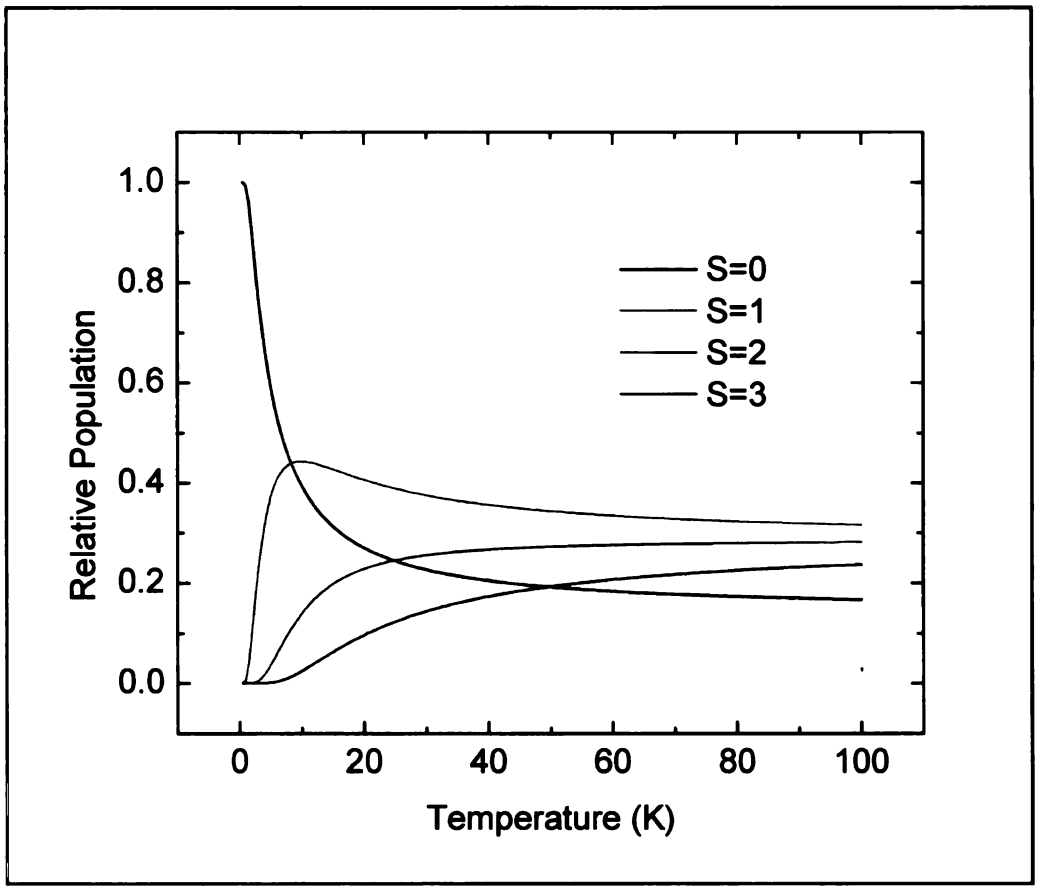

Figure 4-23: Boltzmann distribution of spin states as a function of temperature for complex 5 assuming an antiferromagnetic coupling of J = 4 cm^{-1} and no further zero field splitting of the m_s sublevels.

For this system the strong exchange limit approximation can also be made, but any results should be taken with a grain of salt: the value of 4 cm^{-1} for the isotropic exchange value in this system still represents the largest magnitude interaction in the spin system, but is less than an order of magnitude larger than the other forces operating. For example, the axial zero field splitting of each chromium(III) center is 0.4 cm^{-1}, only an order of magnitude smaller than the J

value. A rigorous treatment would involve diagonalization of the full Hamiltonian matrix.

$[Cr_2(tren)_2(CA^{sq,cat})](BPh_4)_2(BF_4)$ (6). As discussed previously, exchange coupling arising from the interaction of the unpaired spin on the bridging ligand with the S = $^3/_2$ ground state of chromium(III), as in complex **4**, is antiferromagnetic in nature. The same is true for exchange coupling between two chromium(III) centers, as in complex **5**, again due to the shared symmetry of the HOMO orbitals. For $[Cr_2(tren)_2(CA^{sq,cat})](BPh_4)_2(BF_4)$ (**6**), which has both interactions, all values of exchange interactions are antiferromagnetic, resulting in a so-called spin-frustrated S = $^5/_2$ ground state.[56-60] The perpendicular mode X-Band spectrum is presented in Figure 4-24 (and has been invoked in previous sections of this chapter to account for impurities observed in the EPR spectra of complexes **4** and **5**). This spectrum was simulated assuming a sextet spin state, with simulation parameters g_{xx} = 1.98, g_{yy} = 1.975, g_{zz} = 1.97; D = 0.458 cm^{-1}, E = 0.1008 cm^{-1}. The magnetic susceptibility data from 10-100 K corroborate this assignment with a magnetic moment of μ_{eff} = 5.60 μ_B ($\mu_{spin\text{-}only}$ for S = $^5/_2$ is 5.92 μ_B). Like many high-spin ferric complexes this spectrum reveals a resonance near g'= 4.2,[61-65] confirming the sextet nature of the ground state of this complex. Using a procedure described previously for this system,[16] the eigenvalues for the various spin states are given by:

$$E = \frac{J}{2}[S_T(S_T+1) - S_A(S_A+1) - S_3(S_3+1)] + \frac{J^*}{2}[S_A(S_A+1) - S_1(S_1+1) - S_2(S_2+1)] \quad (4.19)$$

where $J = J_{Cr\text{-}SQ}$ is the coupling between the chromium(III) centers and the semiquinone bridge, $J^* = J_{Cr\text{-}Cr}$ is the coupling between the chromium centers, S_3 is the spin on the $CA^{sq,cat}$ bridge, $S_t = {}^7/_2, {}^5/_2, \ldots, {}^1/_2$ and $S_A = S_1 + S_2$, where $S_1 = S_2 = {}^3/_2$. Magnetic susceptibility of compounds **4** and **5** implies values of $J^* = 4\ cm^{-1}$ and $|J| > k_BT$ at 350 K. The magnitude of J effectively isolates the sextet ground state with respect to EPR transitions. Variable temperature EPR data reveal a simple decay in the peak intensities as a function of temperature, indicating no population of higher energy spin states as the temperature increases, and further supporting the high value of J. Simulation of the spectrum at 4 K was carried out using the spin Hamiltonian of equation 2.5 (including electronic Zeeman and zero field splitting terms) and assuming an isolated sextet ground state. Perpendicular and parallel mode spectra were simulated in this manner, and using the same parameters (Figures 4-24 and 4-25). The energy-level diagrams along the x, y, and z axes, presented in Figure 4-26, indicate extensive mixing among the various spin states of the sextet manifold as a result of the small zero-field splitting ($D = 0.458\ cm^{-1}$, $E = 0.1008\ cm^{-1}$). This is evidenced most clearly by the observed parallel mode transition which is formally a $\Delta m_s = +4$ ($S = -{}^5/_2 \rightarrow S = {}^3/_2$) transition.

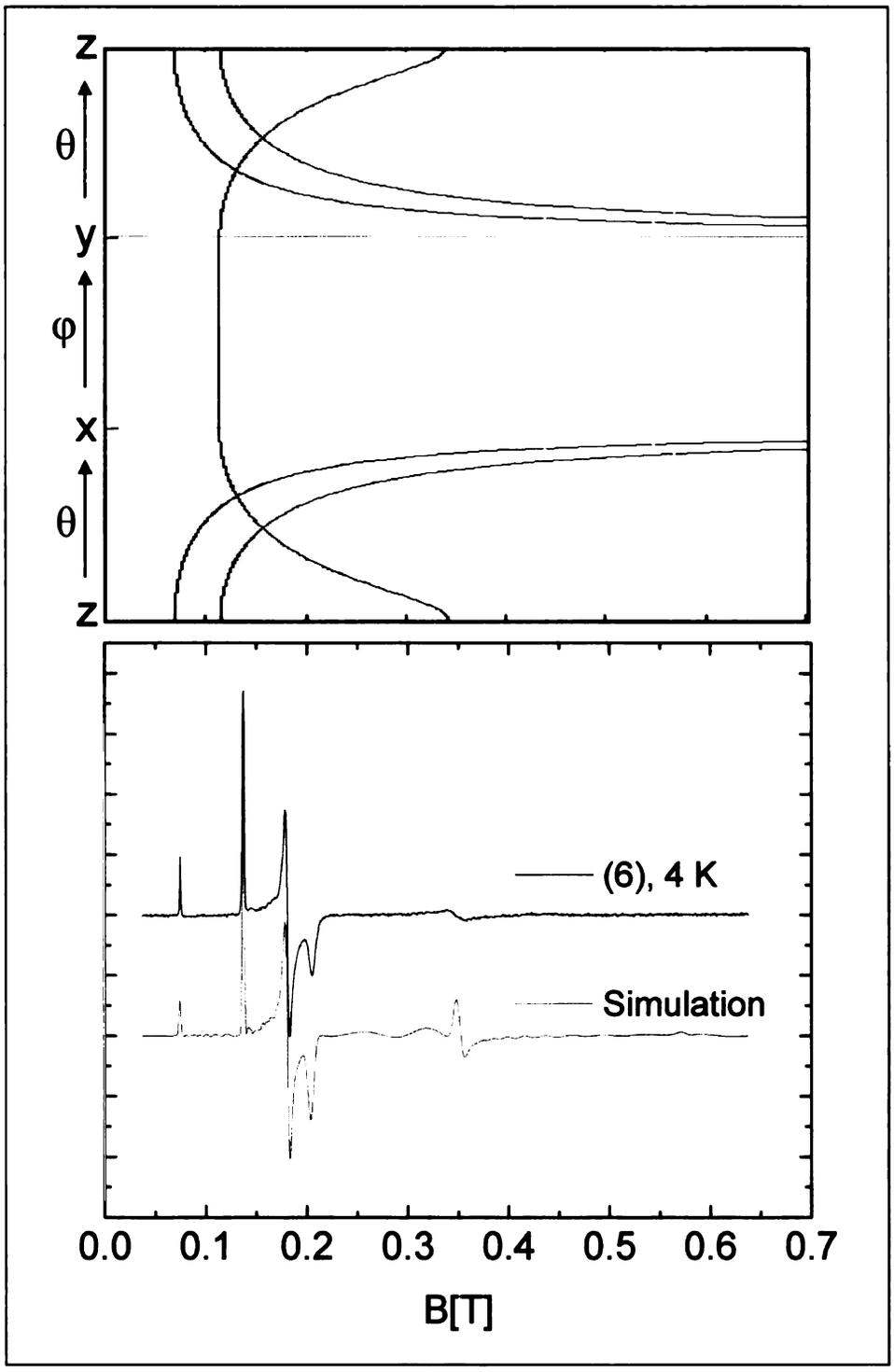

Figure 4-24: Perpendicular mode X-band spectrum of compound 6 (9.458 GHz, 4 K, 0.3 mW). The spectrum was simulated assuming an isolated sextet ground state using the following parameters: $g_{xx} = 1.98$, $g_{yy} = 1.975$, $g_{zz} = 1.97$; $D = 0.458$ cm^{-1}, $E = 0.101$ cm^{-1}.

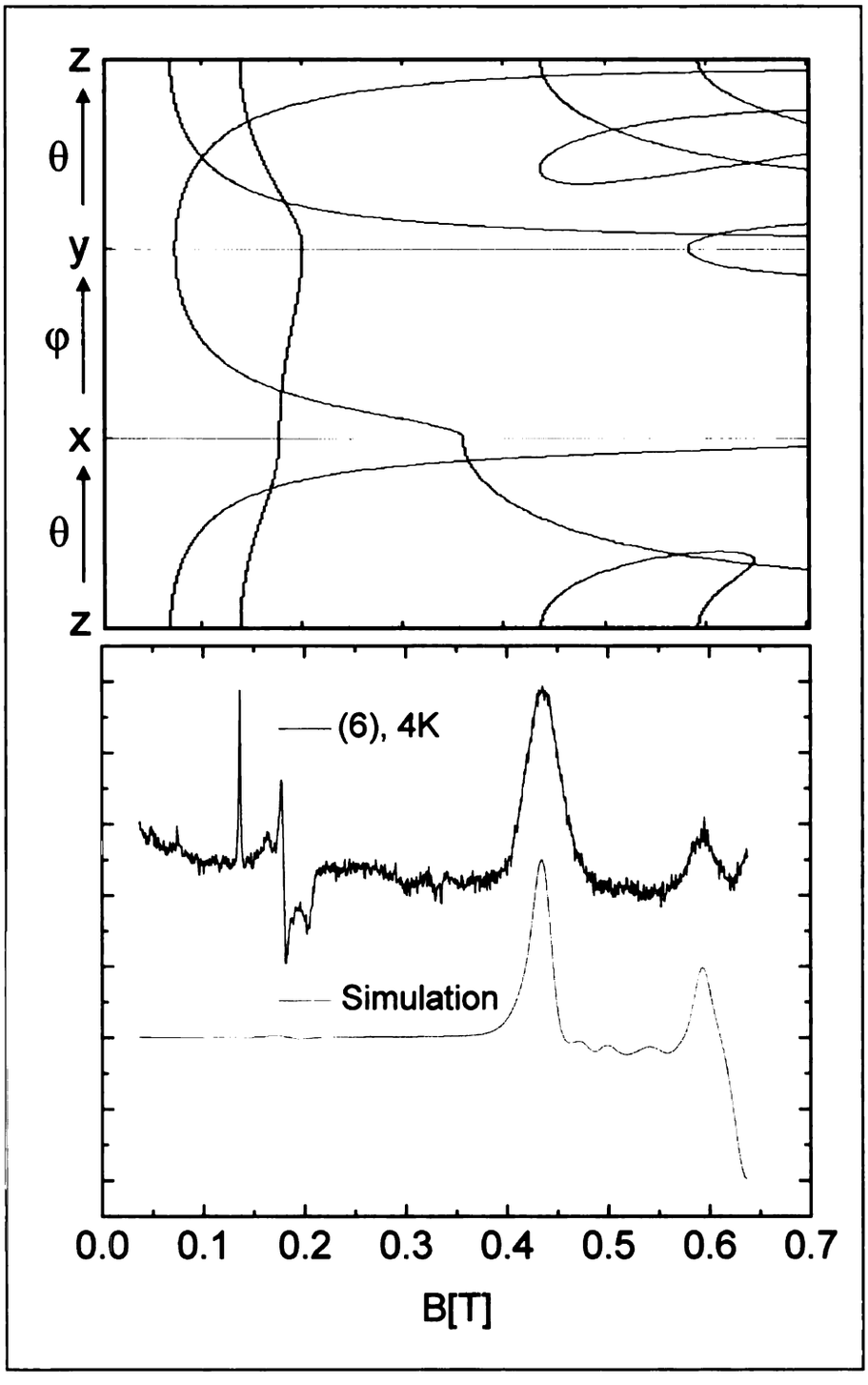

Figure 4-25: Parallel mode X-band spectrum of compound 6 (9.394 GHz, 4 K, 3.16 mW). The spectrum was simulated assuming an isolated sextet ground state using the following parameters: g_{xx} = 1.98, g_{yy} = 1.975, g_{zz} = 1.97; D = 0.458 cm^{-1}, E = 0.101 cm^{-1}.

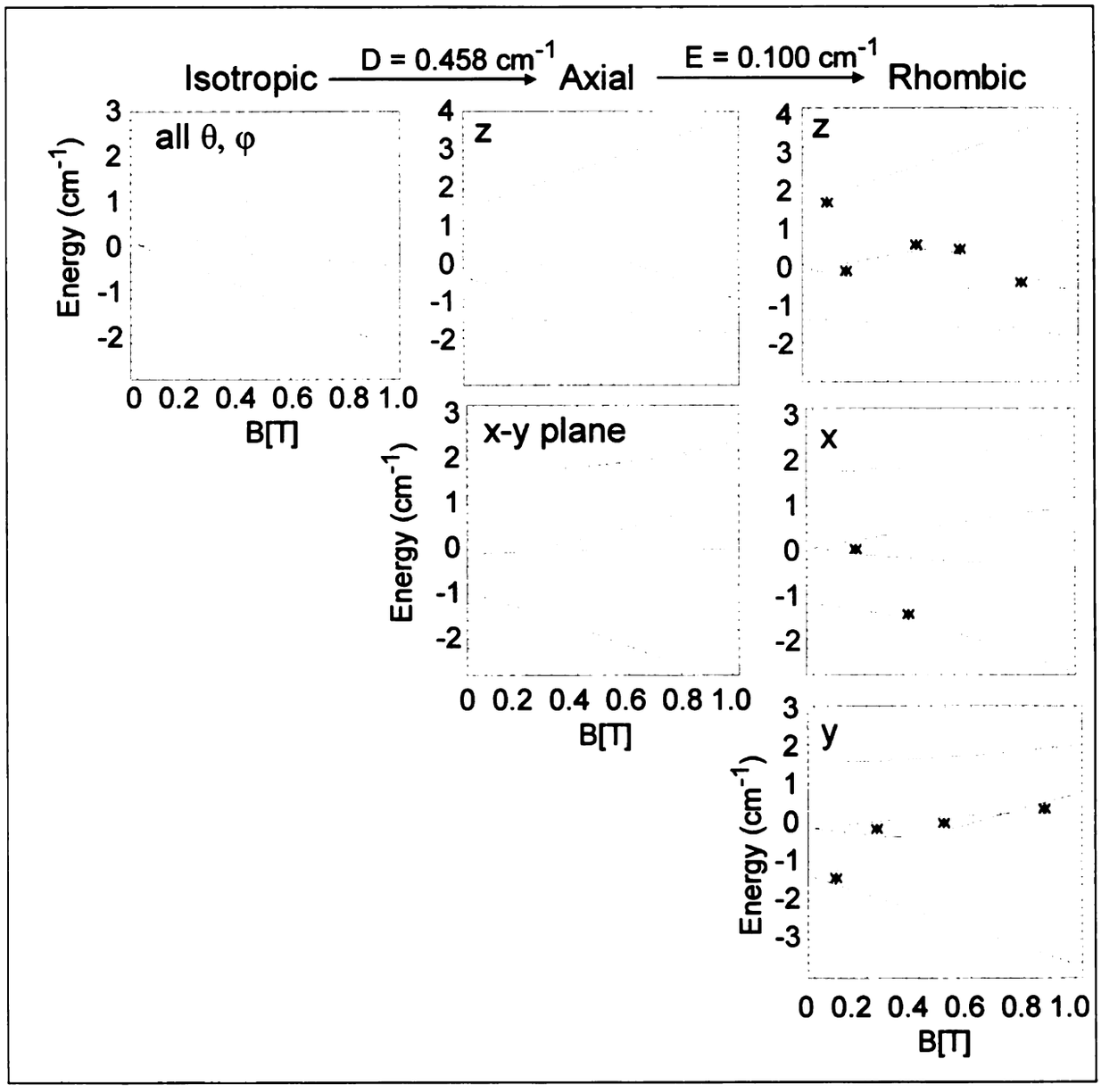

Figure 4-26: Energy level diagram of the ground state of complex 6 as a function of magnetic field, calculated from the simulation parameters.

4.5 Final Remarks.

Initial efforts toward the $[Cr(tren)(3,6\text{-R-Q})]^{+1/+2}$ series, mainly synthetic in nature, are presented in this chapter. This series was synthesized to systematically tune the exchange coupling interaction while essentially retaining the same geometry

across the series. While some spectroscopic characterization of these complexes has been carried out, the majority is yet to be done, and the reader is directed to Chapter 5 for future directions on this project.

The ground states of the majority of the members of the bimetallic $[M_1M_2(tren)_2(CA^{n-})]^{m+}$ series have been characterized using X-band EPR spectroscopy in this chapter as well as chapter 2. This series allows for a broad diversity of ground states, ranging from the diamagnetic species **1** to the paramagnetic sextet ground state of **6**. Magnetic susceptibility indicate an antiferromagnetic exchange interaction between the chromium spin centers of -2 cm^{-1}, although this has not yet been confirmed by EPR spectroscopy for compounds **5** and **6**. The exchange interaction between the chromium spin centers and the $CA^{sq,cat}$ bridge is large enough to isolate the ground state at X-band frequency and the temperatures at which the experiments were carried out. Magnetic susceptibility confirms an isolated triplet state and an isolated sextet state for **4** and **6**, respectively, although this remains unconfirmed by X-band EPR spectroscopy for complex **4** as a result of exceedingly large zero-field splitting within the triplet state. Future work on this area will likely require high-field high-frequency EPR techniques.

4.6 References

(1) Benelli, C.; Dei, A.; Gatteschi, D.; Gudel, H. U.; Pardi, L. *Inorganic Chemistry* **1989**, *28*, 3089-3091.

(2) Schenker, R.; Weihe, H.; Gudel, H. U. *Chemical Physics Letters* **1999**, *303*, 229-234.

(3) Schenker, R.; Weihe, H.; Gudel, H. U. *Inorganic Chemistry* **1999**, *38*, 5593-5601.

(4) Schenker, R.; Weihe, H.; Gudel, H. U.; Kersting, B. *Inorganic Chemistry* **2001**, *40*, 3355.

(5) Schrauben, J. N.; Guo, D.; McCracken, J. L.; McCusker, J. K. *Inorganica Chimica Acta* **2008**, *361*, 3539-3547.

(6) Schrauben, J.; Guo, D.; McCracken, J.; McCusker, J. *Inorganic Chemistry,* Submitted **2010**.

(7) Bencini, A.; Daul, C. A.; Dei, A.; Mariotti, F.; Lee, H.; Shultz, D. A.; Sorace, L. *Inorganic Chemistry* **2001**, *40*, 1582-1590.

(8) Dei, A.; Gatteschi, D.; Pardi, L.; Russo, U. *Inorganic Chemistry* **1991**, *30*, 2589-2594.

(9) Min, K. S.; DiPasquale, A. G.; Golen, J. A.; Rheingold, A. L.; Miller, J. S. *Journal of the American Chemical Society* **2007**, *129*, 2360-2368.

(10) Piskunov, A. V.; Cherkasov, V. K.; Druzhkov, N. O.; Abakumov, G. A.; Ikorskii, V. N. *Russian Chemical Bulletin, International Edition* **2005**, *54*, 1627-1631.

(11) Kremer, S. *Inorganic Chemistry* **1985**, *24*, 887-890.

(12) Glerup, J.; Goodson, P. A.; Hodgson, D. J.; Masood, M. A.; Michelson, K. *Inorganica Chimica Acta* **2005**, *358*, 295-302.

(13) Bolster, D. E.; Gütlich, P.; Hatfield, W.; Kremer, S.; Müller, E. W.; Wieghardt, K. *Inorganic Chemistry* **1983**, *22*, 1725-1729.

(14) Graebe *Justus Liebigs Annalen der Chemie* **1868**, *146*, 31.

(15) Weider, P. R.; Hegedus, L. S.; Asada, H.; D'Andreq, S. V. *Journal of Organometallic Chemistry* **1985**, *50*, 4276.

(16) Guo, D.; McCusker, J. K. *Inorganic Chemistry* **2007**, *46*, 3257-3274.

(17) Zipp, S. G.; Madan, S. K. *Inorganic Chemistry* **1976**, *15*, 587.

(18) Wheeler, D. E.; McCusker, J. K. *Inorganic Chemistry* **1998**, *37*, 2296-2307.

(19) Fehir, R. J., Ph.D. Thesis, Michigan State University, 2009.

(20) Loudon, J. D.; Steel, D. K. V. *Journal of the Chemical Society* **1954**, 1163-1164.

(21) Oxford, A. E. *Journal of the Chemical Society* **1926**, 2004-2011.

(22) Heertjes, P. M.; Nijman-Knape, A. A.; Talsma, H.; Faasen, N. J. *Journal of the Chemical Society* **1955**, 1313-1316.

(23) Bencini, A.; Gatteschi, D. *EPR of Exchange Coupled Systems*; Springer: New York, 1990.

(24) Anderson, P. W. *Solid State Physics-Advances In Research And Applications* **1963**, *14*, 99-214.

(25) Goodenough, J. B. *Physical Review* **1955**, *100*, 564-573.

(26) Goodenough, J. B. *Journal Of Physics And Chemistry Of Solids* **1958**, *6*, 287-297.

(27) Kanamori, J. *Journal Of Physics And Chemistry Of Solids* **1959**, *10*, 87-98.

(28) Heisenberg, W. *Zeitschrift Fur Physik* **1926**, *38*, 411-426.

(29) Dirac, P. A. M. *Proceedings Of The Royal Society Of London Series A-Containing Papers Of A Mathematical And Physical Character* **1926**, *112*, 661-677.

(30) Bencini, A.; Gatteschi, D. *EPR of Exchange Coupled Systems*; Springer: New York, 1990.

(31) Benelli, C.; Dei, A.; Gatteschi, D.; Pardi, L. *Inorganic Chemistry* **1988**, *27*, 2831-2836.

(32) Kambe, K. *J. Phys. Soc. Japan* **1950**, *5*, 48.

(33) Schenker, R.; Heer, S.; Gudel, H. U.; Weihe, H. *Inorganic Chemistry* **2001**, *40*, 1482-1488.

(34) McCarthy, P. J.; Gudel, H. U. *Coordination Chemistry Reviews* **1988**, *88*, 69-131.

(35) Juban, E., Ph.D. Thesis, University of California, 2006.

(36) Wang, G.; Long, X.; Zhang, L.; Wang, G.; Polosan, S.; Tsuboi, T. *Journal of Luminescence* **2008**, *128*, 1556.

(37) Guedel, H. U.; Snellgrove, T. R. *Inorganic Chemistry* **1978**, *17*, 1617.

(38) Oliver, S. W.; Hans, U. G. *The Journal of Chemical Physics* **2001**, *114*, 5832-5841.

(39) Oliver, S. W.; Rafael, V.; Hans, U. G. *The Journal of Chemical Physics* **2001**, *115*, 3819-3826.

(40) Beaulac, R. m.; Reber, C. *Inorganic Chemistry* **2008**, *47*, 5048.

(41) Sofen, S. R.; Ware, D. C.; Cooper, S. R.; Raymond, K. N. *Inorganic Chemistry* **1979**, *18*, 234.

(42) Wheeler, D. E.; Rodriguez, J. H.; McCusker, J. K. *Journal Of Physical Chemistry A* **1999**, *103*, 4101-4112.

(43) Buchanan, R. M.; Claflin, J.; Pierpont, C. G. *Inorganic Chemistry* **1983**, *22*, 2552-2556.

(44) Naito, M. *Journal Of The Physical Society Of Japan* **1973**, *34*, 1491-1502.

(45) Van der Ziel, J. P. *Physical Review B* **1974**, *9*, 2846-2862.

(46) Van der Ziel, J. P. *Journal Of Chemical Physics* **1972**, *57*, 2442-&.

(47) Van der Ziel, J. P. *Physical Review B* **1971**, *4*, 2888-&.

(48) Van Gorkom, G. G. P.; Henning, J. C. M.; Van Stapele, R. P. *Physical Review B* **1973**, *8*, 955-973.

(49) Glerup, J.; Larsen, S.; Weihe, H. *Acta Chemica Scandinavica* **1993**, *47*, 1154-1161.

(50) Riesen, H.; Gudel, H. U. *Molecular Physics* **1987**, *60*, 1221-1244.

(51) Dubicki, L.; Ferguson, J.; Harrowfield, B. V. *Molecular Physics* **1977**, *34*, 1545-1561.

(52) Dean, N. J.; Maxwell, K. J.; Stevens, K. W. H.; Turner, R. J. *Journal Of Physics C-Solid State Physics* **1985**, *18*, 4505-4519.

(53) Johnstone, I. W.; Maxwell, K. J.; Stevens, K. W. H. *Journal Of Physics C-Solid State Physics* **1981**, *14*, 1297-1312.

(54) Briat, B.; Russel, M. F.; Rivoal, J. C.; Chapelle, J. P.; Kahn, O. *Molecular Physics* **1977**, *34*, 1357-1389.

(55) Dei, A.; Gatteschi, D.; Pardi, L.; Russo, U. *Inorganic Chemistry* **1991**, *30*, 2589.

(56) Guo, D.; McCusker, J. K. *Inorg. Chem.* **2007**, *46*, 3257-3274.

(57) McCusker, J. K.; Vincent, J. B.; Schmitt, E. A.; Mino, M. L.; Shin, K.; Coggin, D. K.; Hagen, P. M.; Huffman, J. C.; Christou, G.; Hendrickson, D. N. *Journal Of The American Chemical Society* **1991**, *113*, 3012-3021.

(58) McCusker, J. K.; Christmas, C. A.; Hagen, P. M.; Chadha, R. K.; Harvey, D. F.; Hendrickson, D. N. *Journal Of The American Chemical Society* **1991**, *113*, 6114-6124.

(59) Libby, E.; McCusker, J. K.; Schmitt, E. A.; Folting, K.; Hendrickson, D. N.; Christou, G. *Inorganic Chemistry* **1991**, *30*, 3486-3495.

(60) McCusker, J. K.; Jang, H. G.; Wang, S.; Christou, G.; Hendrickson, D. N. *Inorganic Chemistry* **1992**, *31*, 1874-1880.

(61) Wickman, H. H.; Klein, M. P.; Shirley, D. A. *Journal of Chemical Physics* **1965**, *42*, 2113-2117.

(62) Pilbrow, J. R. *Journal of Magnetic Resonance* **1978**, *31*, 479-490.

(63) Troup, G. J.; Hutton, D. R. *British Journal of Applied Physics* **1964**, *15*, 1493-1499.

(64) Dowsing, R. D.; Gibson, J. F. *Journal of Chemical Physics* **1969**, *50*, 294-303.

(65) Aasa, R. *Journal of Chemical Physics* **1970**, *52*, 3919-3930.

Chapter 5: Future Work

5.1 Introduction

The results presented in this dissertation represent only the beginning of a potentially very rich field of study. Future studies will benefit from enhanced capabilities in the McCusker group laser lab, namely a new ultrafast system that will offer ~ 35 fs pulses in the visible, as well as tunabiltity into the infrared. Furthermore, our current ~100 fs system is being enabled with a longer delay line to achieve longer timescale studies and overcome the "dark window" of 1 – 10 ns that has plagued our research. This chapter, much like the dissertation as a whole, is broken into two general subsections: high-symmetry complexes and low-symmetry, spin-exchange complexes. While study of the high-symmetry complexes will benefit most immediately from the enhanced technological capabilities of our laser lab, much more fundamental work on understanding the electronic structure and spin distribution of spin-exchange complexes is required before meaningful dynamical studies can be performed. Specific future directions of these projects are presented below.

5.2 High-Symmetry Complexes

Of the work on the high symmetry complexes (chapter 3), the most interesting and potentially revealing data was uncovered employing 50 fs pulses, resulting in coherent oscillations. These coherent oscillations may be providing insight into the

reaction coordinate of the ultrafast intersystem crossing in this system. In order to more fully characterize this phenomenon, future work must expand upon the pump/probe combinations employed in chapter 3. Vibrational spectroscopies, namely resonance Raman spectroscopy, could be employed as well to more clearly assign the nature of the coherence. While these measurements may be quite difficult due to the small enhancement afforded by the ligand field absorption, this method would provide the clearest characterization of the $^4T_2$ vibrational structure. In the absence of resonance Raman data, TD-DFT techniques must be employed to gain access to the excited state vibrational frequencies. An example of this technique is shown in Figure 5-1.

Of course, as shown in Chapter 3, synthetic modifications to the acetylacetonate ligand backbone can change the dynamics. In order to test the impact of ligand vibrational modes on ultrafast intersystem crossing dynamics, coherence measurements must be carried out on heavier analogs of $Cr(acac)_3$. The first "heavy" model for $Cr(acac)_3$ will be $Cr(d_7\text{-acac})_3$, synthesized via the route of Figure 5-2. Other potential heavy models for $Cr(acac)_3$, some of which have already been studied, are shown in Figure 5-3. Ground state DFT frequency calculations of some isotopically-enriched heavy $Cr(acac)_3$ analogs at the UB3LYP/6-311g** level, employing a CPCM solvent model of acetonitrile are showin in Figure 5-4. Key vibrational modes between 150 cm^{-1} and 300 cm^{-1}, which may correspond to the vibrational mode observed in the coherence data of

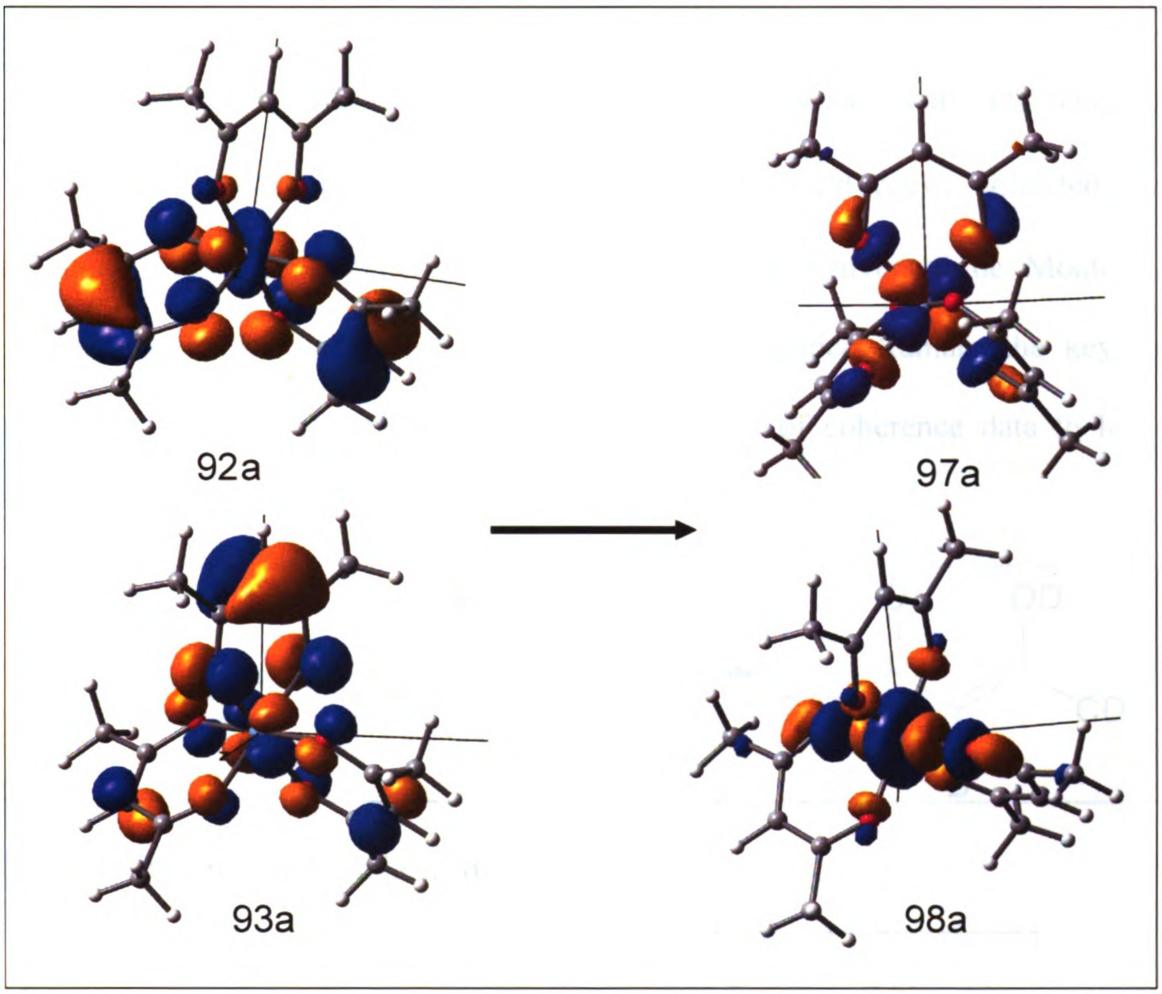

Figure 5-1: The lowest-energy spin-allowed transition for $Cr(acac)_3$, as calculated at the UB3LYP/6-311g** level (employing a CPCM solvent model for acetonitrile) reveals that 92α and 93α molecular orbitals (major contributors to the HOMO) have π-antibonding symmetry while the 97α and 98 α orbitals (major contributors to this transition) have σ-antibonding symmetry. This is qualitatively in line with a transition resulting in population of an e_g^* orbital. Geometry minimization of these MOs effectively constitutes the $^4T_2$ geometry, upon which a frequency calculation can be carried out.

$Cr(acac)_3$ presented in Chapter 3, are highlighted. These values are referenced to the low-frequency portion of Raman spectrum of $Cr(acac)_3$, collected by Alexandre Rodrigue-Witchel of the Reber group at Université de Montréal. Again, due to the likely low enhancement of resonance Raman, the key to characterizing these complexes will the comparison of coherence data to low-frequency Raman spectra, as well as DFT techniques.

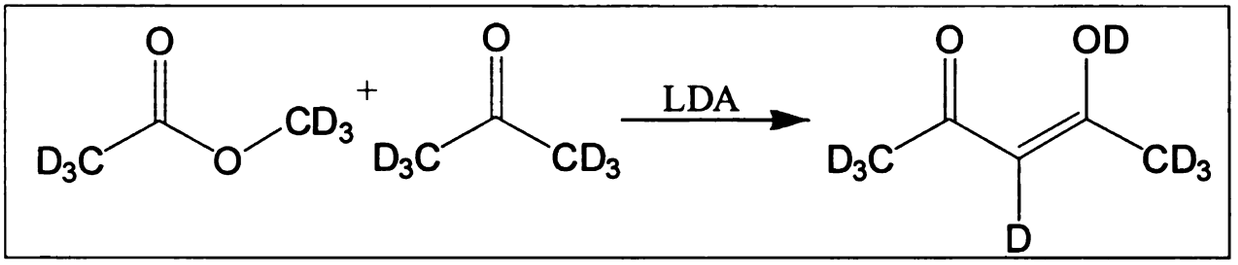

Figure 5-2: Proposed synthesis of d_8-acac.

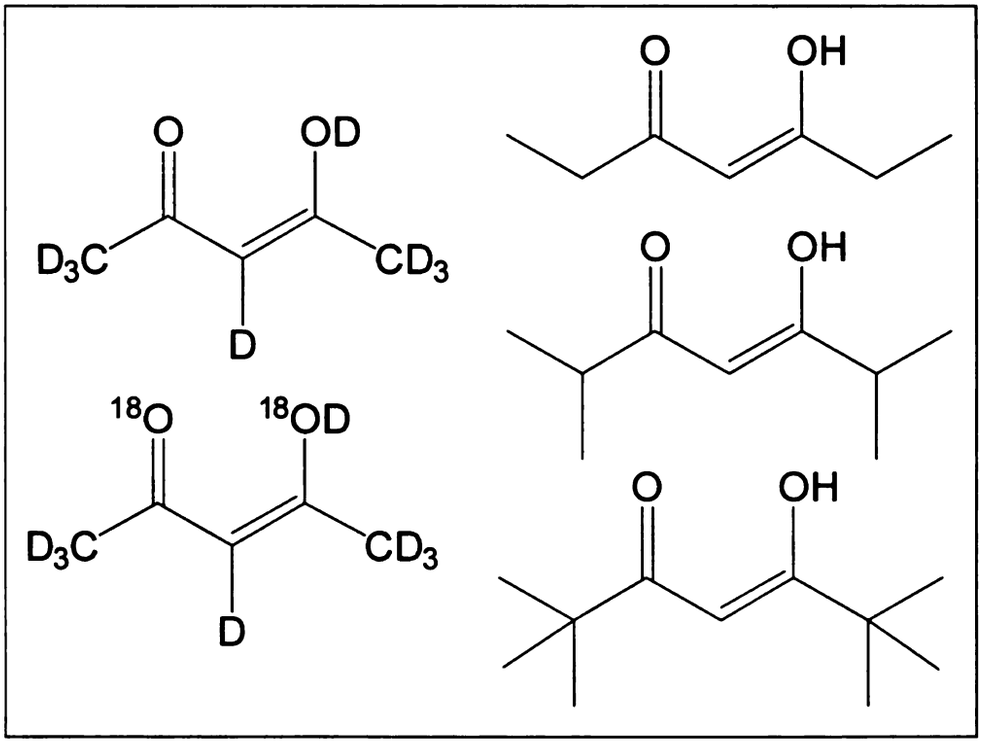

Figure 5-3: "Heavy" analogs of $Cr(acac)_3$.

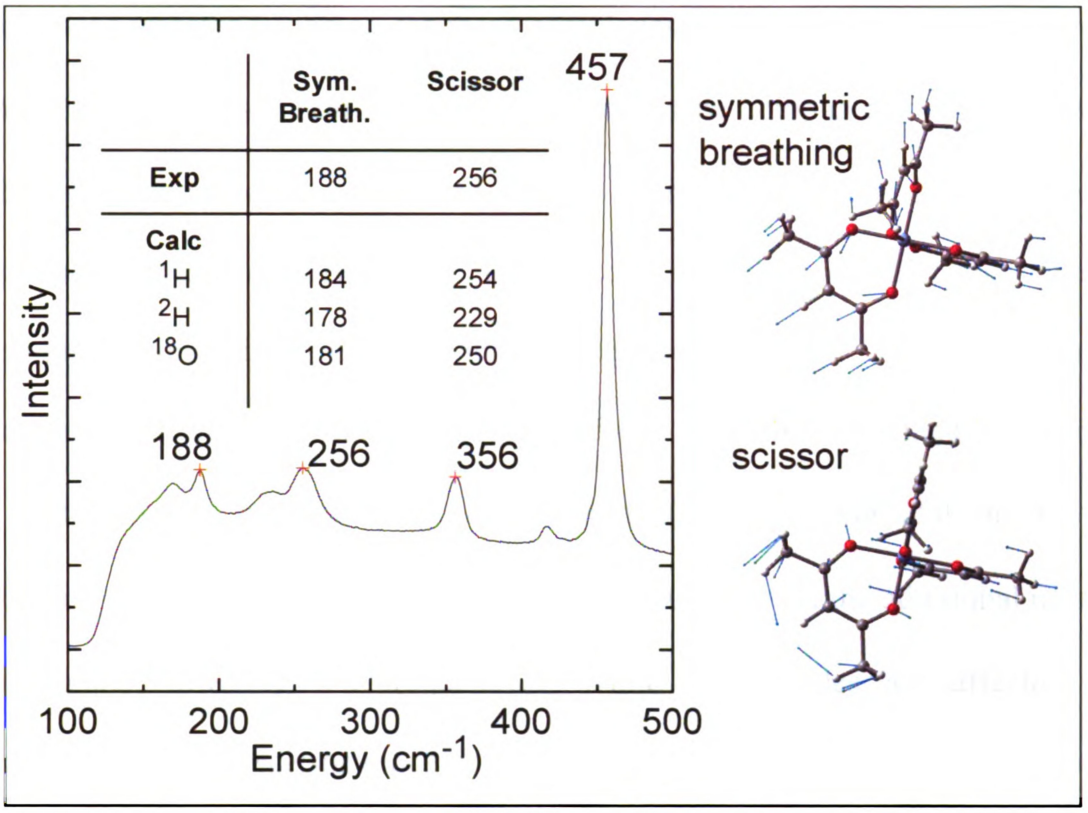

Figure 5-4: Ground state DFT frequency calculations for $Cr(acac)_3$ and isotropically-enriched analogs of $Cr(acac)_3$, referenced to the Raman spectrum.

Further studies could make use of more drastic synthetic modifications to produce vibrationally constrained ligands, in the hope of experimentally determining the coherent mode through suppression of this mode. One possible series would be the hexaamine complexes which were thoroughly studied throughout the latter third of the twentieth century, most notably by Endicott and coworkers.[1-4] For example, a series of increasingly constrained ligands can be envisioned by systematically bonding the ligands to one-another (Figure 5-5). One potential drawback of this series is the lack of ligand π-structure, leading to

no charge-transfer transition for these complexes. This will likely lead to a very small transient absorption signal: in $Cr(acac)_3$-type complexes the excited state absorption corresponds to a ligand field to charge transfer transition, hence the positive excited state absorption. To overcome this obstacle, one could envision employing constraining ligands with an acetylacetonate motif so that the charge-transfer manifold of states remains (Figure 5-6). The series presented in Figure 5-6 systematically suppresses the scissor mode (observed near 250 cm^{-1}) while affecting the symmetric breathing mode (near 190 cm^{-1}) via the additional mass of the ligand, lowering the frequency. While both modes are affected, the suppression of the scissor mode should be more dramatic, allowing one to parse out what mode is active in excited state dynamics.

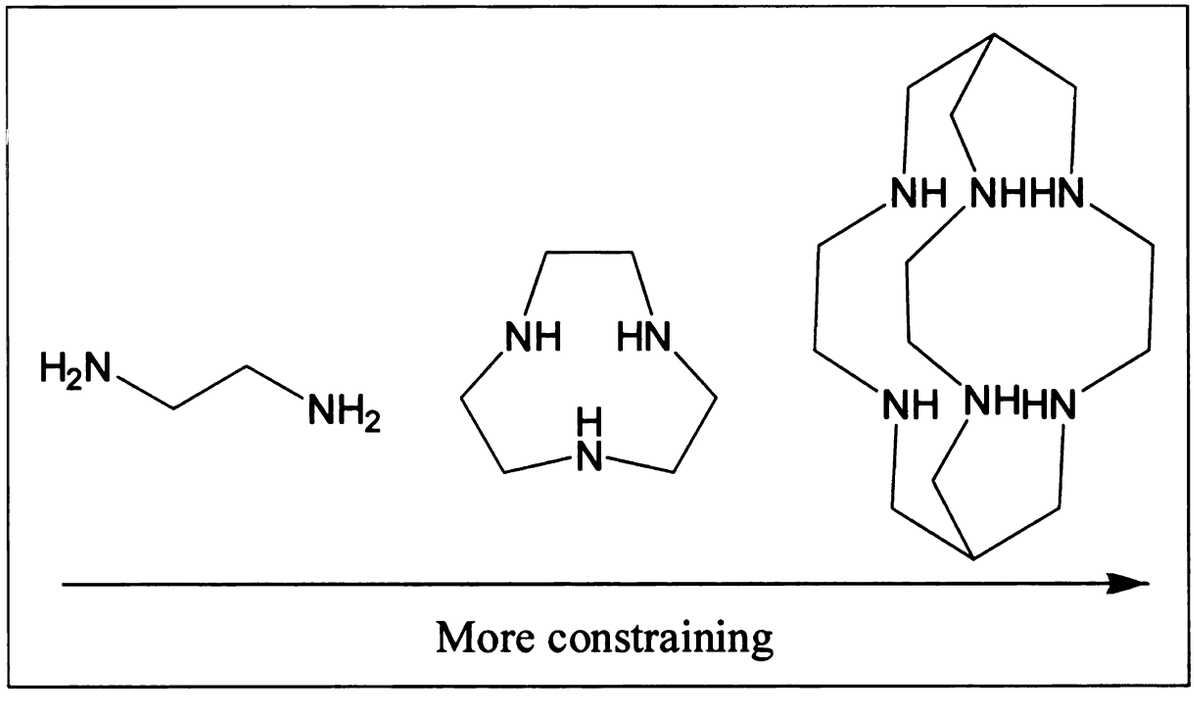

Figure 5-5: $[N_6\text{-chromium(III)}]^{3+}$ series of variable ligand rigidity.

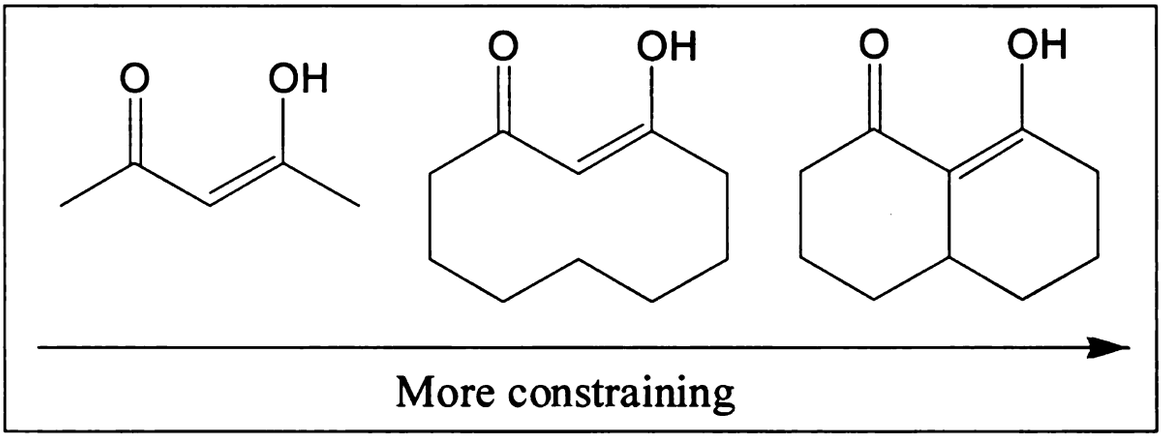

Figure 5-6: A series of increasing constrained acetylacetonate-type complexes.

Another potential future direction of this project is direct observation of vibrational relaxation using ultrafast IR techniques. The best starting point would be an attempt to reproduce the results of Kunttu[5] on $Cr(acac)_3$. Ultrafast IR studies on substituted complexes may be especially fruitful. Many of the 3-substituted complexes would be useful for such a study as they offer unique vibrational modes (C-Br, NO_2, SCN, etc) that could be used as IR tags to potentially witness the vibrational redistribution, and address the role of the 3-substituted position in the vibrational relaxation of these complexes. Once ligand field dynamics are worked out, excitation in charge-transfer and ligand localized transitions can be explored. Rapid decay to the ligand field manifold of electronic states is expected, and many of the same questions outlined above must be again asked, but with respect to ultrafast dynamics between charge-transfer (or ligand localized) and ligand field manifolds. Another potential avenue of study is to address whether these modes of excited state deactivation are generally applicable

to other metal-acetylacetonate complexes, with potential applications to dye-sensitized solar cells.

5.3 Low-Symmetry and Spin-Exchange Complexes. This project can be broken up into two distinct yet interconnected studies: 1) ground state characterization and manipulation of spin polarization and 2) excited state electronic structure and dynamics. The work presented in Chapter 2 of this dissertation, as well as the work of Fehir,[6-8] provides the starting point for the first half of this project, revealing guidelines for manipulation of spin distribution in these systems as well as the experimental techniques for verification of spin distribution.

The ground state characterization of the spin exchange complexes was discussed in Chapter 4. For strongly coupled systems, a better characterization of ground states will include high-field high-frequency EPR, and temperature-dependent EPR studies. Simulations of high-field EPR spectra employing the spin Hamiltonian parameters of low-symmetry chromium-catechol complexes suggest that high-field "field sweep" experiments would be successful in elucidating spin Hamiltonian parameters for these spin-exchange complexes. Of course, these studies will likely do little to address the magnitude to the Heisenberg exchange constant, which has been shown to be larger than k_BT for [Cr(tren)(3,6-di-tert-butylcatechol)](PF_6).[9] Variable temperature magnetic susceptibility measurements

must be carried out to address this. In the absence of conclusive variable temperature magnetic susceptibility data, DFT methods must be applied to estimate J.

The second, kinetic aspect of the project remains in its infancy. Further efforts on this project must begin with characterization of the excited state electronic structure of the low-symmetry chromium-catechol complexes. This can most effectively be carried out using polarized single crystal absorption spectroscopy. Initial studies of this sort can be carried out on the [Cr(tren)(3,6-R-Q)]$^{+1}$ series, which has already been initially characterized spectroscopically in Chapter 4. Furthermore, it has been found that relatively large single crystals can be grown for members of this series by slow evaporation of the complex in a methanol/$NaBPh_4$ solution. As discussed in Chapter 4, transitions between low-symmetry components can be characterized by their allowedness in polarized light. Once a grasp of the electronic structure is obtained, dynamical studies can be carried out. This study, wherein electronic structure is varied while maintaining the same coordination sphere about the chromium ion, would represent a systematic study of the effects of lowered symmetry on ultrafast dynamics of transition metal systems.

The semiquinone analogs of these complexes can be prepared via one electron oxidation of the parent catechol complexes. The electrochemical data presented in Chapter 4 should provide some clear choices of oxidants for this purpose. Again, the first crucial step to understanding the time-resolved dynamics

is elucidation of the excited electronic structure of these complexes. This will likely involve polarized single-crystal absorption spectroscopy, a detailed understanding of chromium-catechol electronic structures, and some additional help from TD-DFT techniques. These same techniques can be applied to the spin-exchange complexes of the $[M_1M_2(tren)_2(CA^{n-})]^{m+}$ series. The study of these spin-exchange complexes will in all likelihood represent one of the most well-rounded projects to be found in the McCusker group, involving synthesis, magnetism, computational work and time-resolved spectroscopies.

5.4 References

(1) Endicott, J. F.; Tamilarasan, R.; Lessard, R. B. *Chemical Physics Letters* 1984, *112*, 381-386.

(2) Endicott, J. F.; Lessard, R. B.; Lynch, D.; Perkovic, M. W.; Ryu, C. K. *Coordination Chemistry Reviews* 1990, *97*, 65-79.

(3) Perkovic, M. W.; Endicott, J. F. *The Journal of Physical Chemistry* 1990, *94*, 1217.

(4) Perkovic, M. W.; Heeg, M. J.; Endicott, J. F. *Inorganic Chemistry* 1991, *30*, 3140-3147.

(5) Macoas, E. M. S.; Kananavicius, R.; Myllyperkio, P.; Pettersson, M.; Kunttu, H. *Journal of the American Chemical Society* 2007, *129*, 8934-8935.

(6) Fehir, R. J., Ph.D Thesis, Michigan State University, 2009.

(7) Fehir, R. J.; McCusker, J. K. *Journal Of Physical Chemistry A* 2009, *113*, 9249-9260.

(8) Fehir, R. J.; Krzyaniak, M.; Schrauben, J. N.; McCracken, J. L.; McCusker, J. K. *Journal of Physical Chemistry B* 2010, *to be submitted.*

(9) Rodriguez, J. H.; Wheeler, D. E.; McCusker, J. K. *Journal of the American Chemical Society* 1998, *120*, 12051-12068.

APPENDICES

Appendix A: Additional Figures for Chapter 1

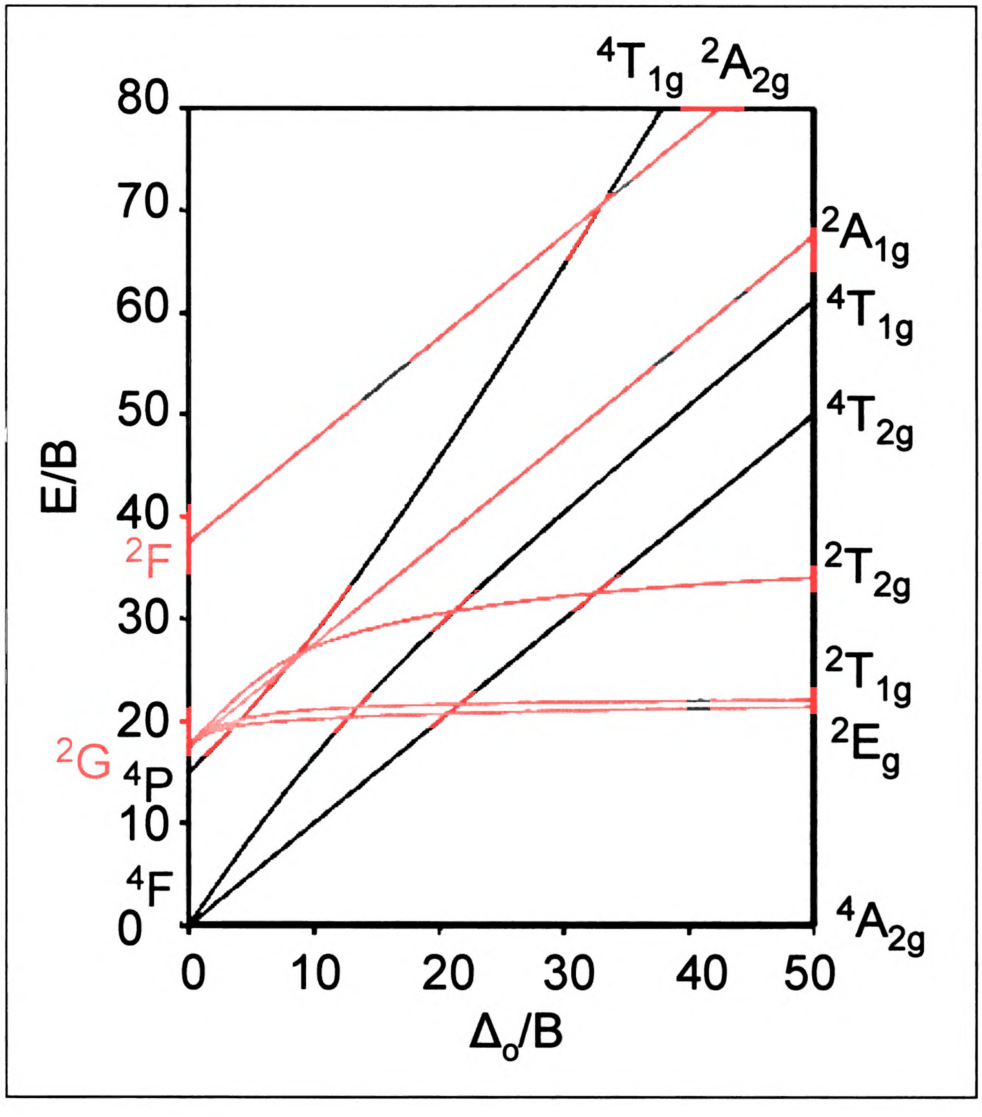

Figure A-1: Tanabe-Sugano diagram of a d^3 system.

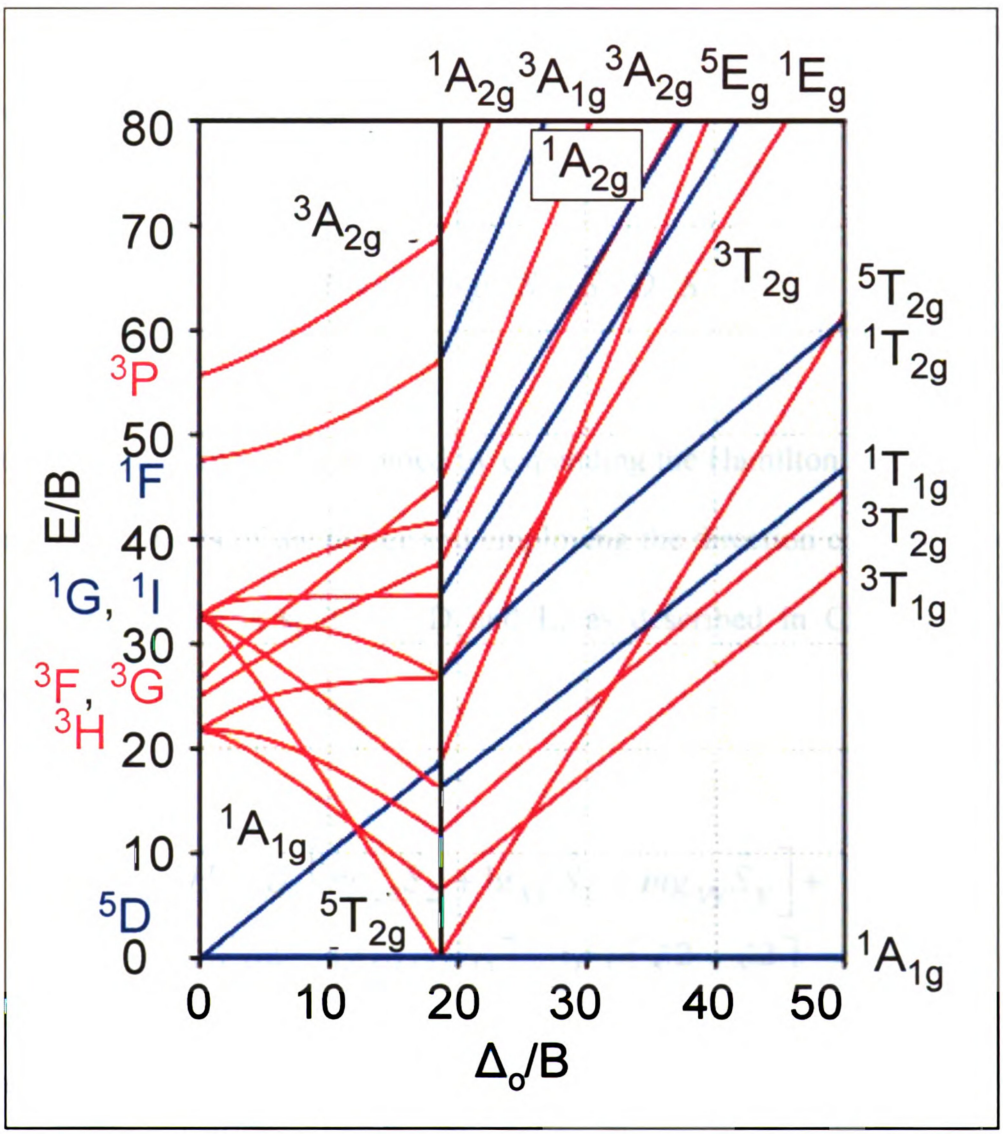

Figure A-2: Tanabe-Sugano diagram of a d^6 system.

Appendix B: Development of Characteristic Equations for Isolated Spin Systems

Considering only the electronic Zeeman and zero-field splitting interactions, the following Hamiltonian is used:

$$H = \beta_e \vec{B} \cdot \tilde{g} \cdot \vec{S} + \vec{S} \cdot \tilde{D} \cdot \vec{S}$$

The tensor formalism can be avoided by expanding the Hamiltonian to include the diagonal components of the tensor and employing the direction cosines. The zero field splitting tensor is split into D and E, as described in Chapter 2 of this dissertation.

$$H = \beta_e \left[n g_{zz} \hat{S}_z + \lg_{xx} \hat{S}_x + m g_{yy} \hat{S}_y \right] +$$
$$D\left[\hat{S}_z^2 - \tfrac{1}{3} S(S+1) \right] + \tfrac{1}{2} E \left[\hat{S}_+^2 + \hat{S}_-^2 \right]$$

Where the direction cosines are:

$$n = \cos\theta$$
$$l = \sin\theta\cos\phi$$
$$m = \sin\theta\sin\phi$$

The spin raising and lowering operators are then substituted into the Zeeman component:

$$\hat{S}_x = \tfrac{1}{2}\left(\hat{S}_+ + \hat{S}_-\right)$$
$$\hat{S}_y = \tfrac{-i}{2}\left(\hat{S}_+ + \hat{S}_-\right)$$

$$H = \beta_e\left[ng_{zz}\hat{S}_z + \tfrac{1}{2}\lg_{xx}\hat{S}_+ + \tfrac{1}{2}\lg_{xx}\hat{S}_- - \tfrac{i}{2}mg_{yy}\hat{S}_+ + \tfrac{i}{2}mg_{yy}\hat{S}_-\right]$$
$$+ D\left[\hat{S}_z^2 - \tfrac{1}{3}S(S+1)\right] + \tfrac{1}{2}E\left[\hat{S}_+^2 + \hat{S}_-^2\right]$$

This can be reduced to the final, usable form

$$H = \beta_e\left[ng_{zz}\hat{S}_z + g_-\hat{S}_+ + g_+\hat{S}_-\right] +$$
$$D\left[\hat{S}_z^2 - \tfrac{1}{3}S(S+1)\right] + \tfrac{1}{2}E\left[\hat{S}_+^2 + \hat{S}_-^2\right]$$

Where

$$g_- = \tfrac{1}{2}\left(\lg_{xx} - img_{yy}\right)$$
$$g_+ = \tfrac{1}{2}\left(\lg_{xx} + img_{yy}\right)$$

Spin eigenfunctions are represented as comprised of the total spin and all of the 2S+1 spin components, i.e. $|S,m_s\rangle$. For example, for a triplet spin state, the three eigenfunctions are:

$$|1,1\rangle$$
$$|1,-1\rangle$$
$$|1,0\rangle$$

The interactions of the various m_s levels are setup in a square matrix and the spin operators are applied in the usual fashion to yield the secular determinant. For a triplet state this equation (for the given Hamiltonian) is:

$$\begin{array}{c} \\ \langle 1,1| \\ \langle 1,0| \\ \langle 1,-1| \end{array} \begin{array}{c} \begin{array}{ccc} |1,1\rangle & |1,0\rangle & |1,-1\rangle \end{array} \\ \begin{vmatrix} g_{zz}\beta_e Bn + \frac{1}{3}D - \varepsilon & \frac{1}{\sqrt{2}}g_-\beta_e Bm & E \\ \frac{1}{\sqrt{2}}g_+\beta_e Bm & -\frac{2}{3}D - \varepsilon & \frac{1}{\sqrt{2}}g_-\beta_e Bm \\ E & \frac{1}{\sqrt{2}}g_+\beta_e Bm & -g_{zz}\beta_e Bn + \frac{1}{3}D - \varepsilon \end{vmatrix} \end{array} = 0$$

For a quartet spin state the characteristic equation for this Hamiltonian is:

$$
\begin{array}{c|cccc}
 & \left|\tfrac{3}{2},\tfrac{3}{2}\right\rangle & \left|\tfrac{3}{2},\tfrac{1}{2}\right\rangle & \left|\tfrac{3}{2},\tfrac{-1}{2}\right\rangle & \left|\tfrac{3}{2},\tfrac{-3}{2}\right\rangle \\
\left\langle\tfrac{3}{2},\tfrac{3}{2}\right| & +\frac{3}{2}g_{zz}\beta_e Bn + D - \varepsilon & +\frac{3}{2}g_{zz}\beta_e Bn + D - \varepsilon & \sqrt{3}E & 0 \\
\left\langle\tfrac{3}{2},\tfrac{1}{2}\right| & \frac{\sqrt{3}}{2}\beta_e Bg_+ & \frac{1}{2}g_{zz}\beta_e Bn - D - \varepsilon & \beta_e Bg_- & \sqrt{3}E \\
\left\langle\tfrac{3}{2},\tfrac{-1}{2}\right| & \sqrt{3}E & \beta_e Bg_+ & -\frac{1}{2}g_{zz}\beta_e Bn - D - \varepsilon & \frac{\sqrt{3}}{2}\beta_e Bg_- \\
\left\langle\tfrac{3}{2},\tfrac{-3}{2}\right| & 0 & \sqrt{3}E & \frac{\sqrt{3}}{2}\beta_e Bg_+ & -\frac{3}{2}g_{zz}\beta_e Bn + D - \varepsilon
\end{array}
= 0
$$

Appendix C. Crystallographic Data for Chapters 3 and 4

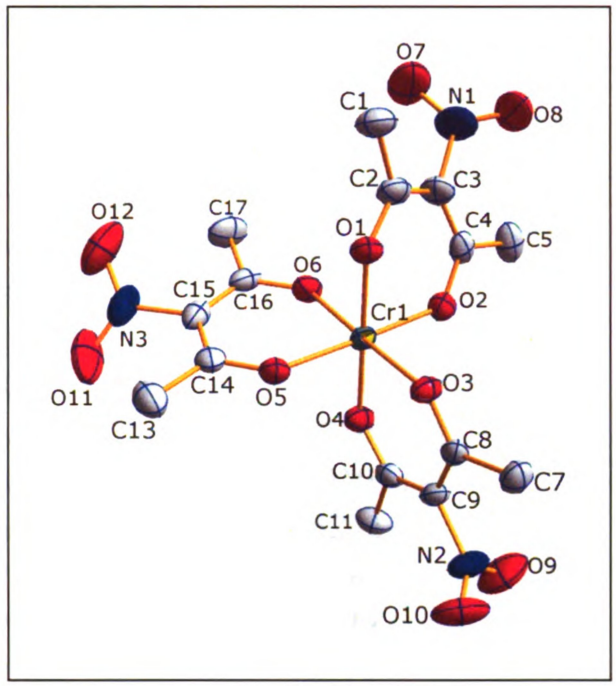

Figure C-1: Crystal structure for $Cr(3\text{-}NO_2ac)_3$.

Table C-1: Select bond lengths and angles for $Cr(3\text{-}NO_2ac)_3$.

Cr-O Bonds (Å)	Cr1-O1	1.9450
	Cr1-O2	1.9414
	Cr1-O3	1.9428
	Cr1-O4	1.9530
	Cr1-O5	1.9551
	Cr1-O6	1.9416
O-Cr-O Angles (°)	O1-Cr1-O4	179.63
	O2-Cr1-O5	177.68
	O3-Cr1-O6	178.11
	O1-Cr1-O5	91.32
	O1-Cr1-O6	87.77
	O2-Cr1-O4	90.94
	O2-Cr1-O6	88.59

Table C-2: Crystallographic data for $Cr(3\text{-}NO_2ac)_3$ and $Cr(3\text{-}Phac)_3$.

	$Cr(3\text{-}NO_2ac)_3$	**$Cr(3\text{-}Phac)_3$**
Formula	$C_{15}H_{18}CrN_3O_{12}$	$C_{99}H_{99}Cr_3O_{18}$
Mw	484.32	1732.78
cryst syst		Monoclinic
space group		*C2/c*
T/K	293	173
a/Å	33.0109 (4)	19.0021 (4)
b/Å	33.0109 (4)	13.8617 (3)
c/Å	7.5242 (2)	34.0764 (7)
α/°	90	
β/°	90	91.4740 (10)
γ/°	90	
V/Å^3	8199.3 (3)	8972.8 (3)
Z	16	4
D_c/g cm^{-1}	1.569	1.283
$2\Theta_{max}$	56.6	56.6
Reflns measured	26701	54629
Indepdendent reflns	5059	11143
Observed reflns [I>2σ(I)]	4786	9402
μ(Mo Kα)/ cm^{-1}	0.71073	0.71073
R_{int}	0.032	0.061
R1	0.040	0.056
ωR2	0.110	0.165
GOF	1.09	1.03

$$w = 1/[\sigma^2(F_o^2) + (0.0989P)^2 + 0.8945P]$$
where $P = (F_o^2 + 2F_c^2)/3$

Table C-3: Crystallographic data for $Cr(DBM)_3$ and $Ga(DBM)_3$.

	$Cr(dbm)_3$	**$Ga(dbm)_3$**
Formula	$C_{22.50}H_{16.50}Cr_{0.50}O_3$	$C_{45}H_{33}GaO_6$
Mw	360.86	739.43
cryst syst		
space group		
T/K	173(2)	173(2)
a/Å	17.0031(2)	9.7821(3)
b/Å	9.77730(10)	10.4784(3)
c/Å	21.2772(2)	18.1320(5)
α/°	90	93.3500(10)
β/°	92.6920(10)	93.9350(10)
γ/°	90	106.2230(10)
V/Å^3	3533.31(6)	1774.48(9)
Z	8	2
D_c/g cm^{-1}	1.357	1.384
$2\Theta_{max}$	68.15	68.27
Reflns measured	27409	23613
Indepdendent reflns	6386	6260
Observed reflns [I>2σ(I)]	5660	6113
μ(Cu Kα)/ cm^{-1}	1.54178	1.54178
R_{int}	0.0308	0.025
R1	0.0376	0.0305
ωR2	0.1022	0.0804
GOF	1.032	1.052

$$w = 1/[\sigma^2(F_o^2) + (0.0989P)^2 + 0.8945P]$$
where $P = (F_o^2 + 2F_c^2)/3$

Table C-4: Crystallographic data for [Cr(tren)(pycat)](BPh_4) and [Cr(tren)(3,6-1,2-orthocatecholate)](BPh_4).

	[Cr(tren)(pycat)]$^+$	**[Cr(tren)(CNcat)]$^+$**
Formula	$C_{38}H_{42}BCrN_4O_4$	$C_{40}H_{43}BCrN_6O_2$
Mw	681.57	716.62
cryst syst		Monoclinic
space group		P2(1)/c
T/K	293	173
a/Å	9.8957 (2)	18.4129 (3)
b/Å	10.0280 (2)	10.7008 (2)
c/Å	19.2369 (3)	18.8264 (3)
α/°	92.7190 (10)°	
β/°	99.0650 (10)°	104.4090 (10)°
γ/°	106.6950 (10)°	
V/Å^3	1796.96 (6)	3592.73 (11)
Z	2	4
D_c/g cm^{-1}	1.260	1.325
$2\Theta_{max}$	55	55
Reflns measured	38895	40650
Indepdendent reflns	8211	8242
Observed reflns [I>2σ(I)]	7007	6789
μ(Mo Kα)/ Å	0.71073	0.71073
R_{int}	0.057	0.084
R1	0.061	0.072
ωR2	0.183	0.202
GOF	1.01	1.08

$w = 1/[\sigma^2(F_o^2) + (0.0989P)^2 + 0.8945P]$
where $P = (F_o^2 + 2F_c^2)/3$